Preparation and investigation of an *in vitro* model system for the $GABA_A$ receptor organisation machinery of inhibitory post synapses

DISSERTATION

for the award of the degree

Doctor rerum naturalium

of the Georg-August-Universität Göttingen

within the doctoral program

Physics of Biological and Complex Systems

of the Georg-August-University School of Science (GAUSS)

submitted by

Jonas K. Schäfer

from Glandorf

Göttingen 2020

Members of the Thesis Advisory Committee

Prof. Dr. Claudia Steinem
Institute of Organic and Biomolecular Chemistry
Georg-August-University Göttingen

Prof. Dr. Nils Brose
Max-Planck Institute of Experimental Medicine
Göttingen

Prof. Dr. Reinhard Jahn
Max-Planck Institute for Biophysical Chemistry
Göttingen

Further Members of the Examination Board

Prof. Dr. Silvio Rizzoli
Department of Neuro- and Sensory Physiology
University Medical Centre Göttingen

Prof. Dr. Michael Meinecke
Department of Cellular Biochemistry
University Medical Centre Göttingen

Prof. Dr. Burkhard Geil
Institute of Physical Chemistry
Georg-August-University Göttingen

Date of Oral Examination

1st July 2020

Statutory Declaration

I, Jonas Schäfer, hereby certify that my doctoral thesis entitled “Preparation and investigation of an *in vitro* model system for the $GABA_A$ receptor organisation machinery of inhibitory post synapses” has been written independently and with no other sources and aids than quoted.

Göttingen, 2020

Jonas Schäfer

Meiner wunderbaren Familie

"The greatest enemy of knowledge is not ignorance,
it is the illusion of knowledge."
Daniel J. Boorstin

Table of Contents

Abstract. The synaptic communication between neuronal cells is based on the release and uptake of neurotransmitters. In the mammalian brain inhibitory signal transduction relies on the neurotransmitter γ-amino butyric acid (GABA) which is recognised by specific receptors in the post synaptic plasma membrane. These receptors experience high spatio-temporal fluctuations and thus need to be accumulated in direct opposition to the presynaptic active site to facilitate fast communication. Malfunctions in this process are origin of multiple neuronal diseases. A protein machinery composed of the cell adhesion protein neuroligin 2 (NL2), the scaffolding protein gephyrin and the adaptor protein collybistin 2 (CB2), that interacts with phosphoinositides (PtdInsPs) in the plasma membrane, is assumed to be responsible for the receptor organisation in the postsynaptic specialisations. The complex has been examined only *in vivo* so far, yet to characterise each constituent in detail and to investigate their intermolecular interactions an *in vitro* system is required. Therefore, this work focusses on the preparation of a model system, based on membranes supported by SiO_2 substrates. In solid-supported lipid bilayers (SLBs) a heterogeneous distribution of the bisphosphorylated phosphoinositide (PtdIns[4,5]P_2) was detected, thus solid-supported hybrid membranes (SHMs) prepared by spreading of small unilamellar vesicles (SUVs) on hydrophobically functionalised SiO_2 were deployed to guarantee homogeneous distribution and comparability of all PtdInsPs (PtdIns[3]P, PtdIns[4,5]P_2 and PtdIns[3,4,5]P_3) tested.

The adsorption of recombinantly expressed CB2 to SHMs containing the different PtdInsPs was examined by means of reflectometric interference spectroscopy (RIfS) and atomic force microscopy (AFM). In this way the isolated PH domain ($CB2_{PH}$) and the point-mutated, active full-length isoform ($CB2_{SH3/W24A-E262A}$) were characterised as unspecific, moderate PtdInsP interation partners, while the wild-type of CB2 ($CB2_{SH3}$) was incapable of binding. Furthermore, it was shown that the height of the adsorbed protein is dictated by the *C*-terminal PH domain.

The addition of a second receptor lipid (DGS), specific for a NL2 protein construct mimicking its intracellular domain (His-*cyt*NL2) introduced a positive charge but did not affect the established membrane system. After fixation of His-*cyt*NL2 to SHMs doped with DGS and PtdInsP also adsorption of $CB2_{SH3}$ was detected. Thereby, the activation of the wild-type by interaction with the intracellular domain of NL2 was proven. Additionally, the activated wild-type exhibited a higher specificity compared to that of $CB2_{SH3/W24A-E262A}$.

Zusammenfassung. Die Inhibition der Reizweiterleitung im Gehirn von Säugetieren beruht auf der Ausschüttung und Aufnahme von γ-Aminobuttersäure (GABA). Die Detektion dieses Neurotransmitters erfolgt durch spezifische Rezeptoren, die in der postsynaptischen Plasmamembran lokalisiert sind. Für eine schnelle und effiziente Inhibition ist die Akkumulation dieser Rezeptoren gegenüberliegend zur aktiven Zone der Präsynapse notwendig. Es wird angenommen, dass dieser Organisationsprozess auf den Proteinen Neuroligin 2 (NL2), Gephyrin und Collybistin 2 (CB2) beruht. Letzteres fungiert als Adapterprotein zwischen dem Proteinkomplex und Phosphatidylinositolphosphaten (PtdInsPs) in der Membrane. Zur genauen Characterisierung der einzelnen Bestandteile dieses Komplexes und ihrer Wechselwirkungen wurde im Rahmen dieser Arbeit ein *in vitro* Modell entwickelt. Dieses basiert auf festkörperunterstützten Lipidmonoschichten (SHMs), die durch das Spreiten von kleinen unilamellaren Vesikeln auf hydrophob funktionalisierten SiO_2 Oberflächen erzeugt wurden. Es konnte im Vergleich mit festkörperunterstützten Lipiddoppelschichten (SLBs) gezeigt werden, dass es in letzteren zu einer heterogenen Verteilung von PtdIns[4,5]P_2 kommt. Diese äußerte sich in einer Verarmung an zugänglichen Rezeptorlipiden, die unter der Verwendung von Markerproteinen mittels reflektometrischer Interferenzspektroskopie (RIfS) und Rasterkraftmikroskopie (AFM) detektiert wurde.

Auf Grund der ermittelten Vorteile wurden nochfolgend Adsorptionsstudien von CB2 auf SHMs durchgeführt, welche mit verschiedenen PtdInsPs dotiert waren. Dadurch konnte gezeigt werden, dass es sich bei allen CB2 Isoformen um unspezifische PtdInsP-Interaktionspartner handelt. Lediglich der CB2 Wildtyp zeigte keine Bindungsaktivität. Desweiteren wurde die *C*-terminale PH Domäne als höhenbestimmendes Proteinmodul identifiziert. Zusätzlich konnte gezeigt werden, dass neben der Proteinhöhe auch die Größe der adsorbierten Proteinstrukturen unabhängig vom vorliegenden PtdInsP ist.

Die Erweiterung des Modellsystems um NL2 in Form der *C*-terminalen intrazellulären Domäne, erforderte die Dotierung mit DGS als spezifisches Rezeptorlipid zusätzlich zu PtdInsP. Für SHMs, die beide Rezeptorlipide enthielten, wurden lediglich ein um die Hälfte reduzierte Diffussionskoeffizienten detektiert. Anhand von Co-Adsorptionsstudien von CB2 nach vorheriger NL2-Injektion, konnte gezeigt werden, dass der Wildtyp durch NL2 aktiviert wird und somit in der Lage ist mit PtdInsPs zu interagieren. Somit konnte anhand des entwickelten System ein Nachweis für die Aktivierung von CB2 durch NL2 erbracht werden.

1 Introduction

1.1 Neuronal communication

The nervous system can be divided into the peripheral nervous system (PNS) and the central nervous system (CNS) in which neurons represent the principle building blocks. These cells were identified right before the turn from 19th to 20th century by CAJAL, who visualized their dendritic spines via various staining techniques, thereby proving the predominant reticular theory of that time to be wrong.[1,2] Based on his results fundamental characteristics of neurons could be identified despite their large anatomical variations which is schematically shown in Figure 1.1. In most cases neurons consist of the central soma to which one or multiple dendrites and a unique axon are attached.[3] Both, dendrites and axon can be ramified to a different degree.

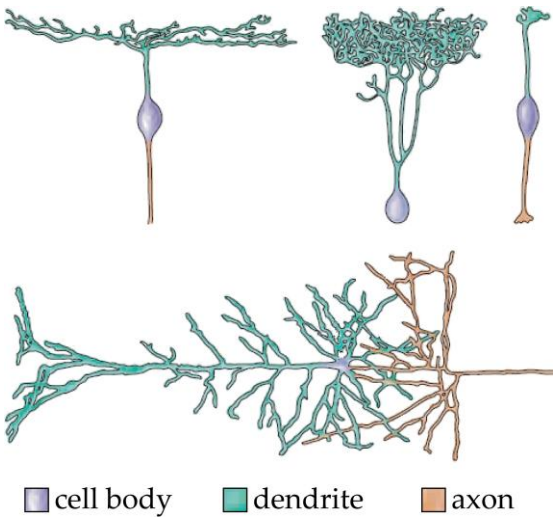

Figure 1.1: Variety in neuron morphology illustrated by schemes of a retinal ganglion cell, a retinal amacrine cell, a retinal bipolar cell, and a cortical pyramidal cell. Modified from PURVES *et al*.[3]

While the PNS mainly executes the transport of external sensory stimuli and corresponding motoric responses, the CNS functions as the controlling unit, where information is integrated, processed and afterwards transmitted to the PNS again. It is composed of the spinal cord and the brain. Due to its diverse functions the brain is presumed to be the most complex organ in the human body which is also reflected in the huge number of neurons inside. A rough estimation by WILLIAMS and HERRUP assumed 85 billion neurons to be contained in the adult human brain in addition to other cells like the glial cell, which do not participate in synaptic transition, yet, serve a supportive function and are essential in neuronal migration.[4]

The inter-neuronal contact sites are called synapses. They constitute the neuronal network in which signal transduction is either obtained via chemical transmission or, less common, by electrical coupling. While at electrical synapses gap junctions connect the cytoplasm of pre- and postsynaptic neurons, chemical synapses are composed of a presynaptic axon that is in close apposition to a postsynaptic dendrite or dendritic spine. Both are separated by a small

interval of extracellular space, the so-called synaptic cleft. To pass information across this extracellular area neurotransmitters are secreted via exocytosis of synaptic vesicles at the presynaptic terminal and diffuse to specialisations inside the post synaptic membrane where they bind and activate specific receptors.[5]

Two types of transmitter receptors are known. One class are the metabotropic, G-protein coupled receptors and the other one are ionotropic neurotransmitter receptors. The latter are ion channels which open their pore upon ligand binding and selectively allow ions to flow along the electrochemical gradient. This ion transfer changes the membrane potential of the postsynaptic dendrite. Spatiotemporal integration of all synaptic stimuli on the respective neuron results in an action potential that, in case a certain threshold value in potential is reached, propagates down the axon. Thereby the firing behaviour of this neuron is determined via all synaptic inputs and its activity in the neuronal network is controlled.[6–8]

It has been estimated that each neuron in the human brain is connected via more than 10,000 synapses to others.[5] The accurate communication and its underlying mechanism are critical for the well-being of the whole organism as the exchange controls virtually all internal body processes and functions. The necessity of its accurate function is confirmed by diseases like Alzheimer's and major depressions, shown to be a result of any malfunction in the information transmission process.[3] Thus, understanding the details of the processes underlying synaptic transmission is a prerequisite to get further insights in complex brain functions and to investigate rational treatments for the aforementioned and all other diseases who originate from dysfunctions in neuronal communication.

1.2 Excitatory and inhibitory synapses

The signal transduction between neurons takes place at either chemical or electrical synapses. While at the latter gap junctions are used for signal transfer, at chemical synapses secretion of a great variety of neurotransmitters occurs via vesicle fusion at the exon terminal. All types of neurotransmitters experience a similar circuit of use with synthesis, transport to synaptic vesicles, exocytosis and release in the synaptic cleft, binding to specific postsynaptic receptors and finally fast removal or degradation. The binding and simultaneous activation of specific neurotransmitter receptors lead to ionic permeability in the postsynaptic membrane determining

whether the actions at the dendrite are excitatory or inhibitory. The permeability of the dendritic membrane and a transmembrane ion concentration gradient, maintained for the most part via Na^+/K^+-ATPase, result in a negative membrane potential of circa -60 mV to -70 mV at rest.[9] Upon binding of neurotransmitters like glutamate to excitatory ionotropic receptors, Na^+ influx causes a depolarisation of the membrane potential resulting in an action potential if the threshold of approximately -40 mV is reached. Yet, the activity of neurons must be controlled. Therefore, an inhibition has to take place that is based on γ-amino butyric acid (GABA) and glycine release at synapses in the brain and the spinal cord, respectively.[10] The specific receptors for both neurotransmitters are ligand-gated Cl^- channels, whose opening and the accompanying Cl^- influx result in hyperpolarisation of postsynaptic membrane potentials. This hyperpolarisation antagonises the depolarisation of excitatory inputs and in this way leads to an inhibitory effect on the firing probability.

GRAY studied cerebrocortical tissues of rats and identified two different types of synapses. The electron micrographs presented in Figure 1.2 A-C clearly indicate a thickening of the postsynaptic membranes at synapses expressed between axons and dendrites or dendritic spines (type I) whereas no asymmetric thickening is detected in axosomatic synapses (type II).[11] Posterior studies showed that GRAY's synaptic types I and II accord with excitatory and inhibitory synapses, respectively.[12] Thus, there is also a structural difference between the two synaptic types. What was detected as a thickening of the postsynaptic membrane in excitatory synapses, later was identified as an electron-dense area composed of many proteins referred to as the postsynaptic density (PSD).[13–15] Only 10 % of the great protein diversity in the PSD were ion channels and receptors.[16,17] This small fraction stresses the importance of other constituents in the receptor organisation process at the excitatory postsynaptic membranes. In contrast to the rigorously investigated principles of excitatory synapses at the molecular and cell biological level, this information is lacking in most

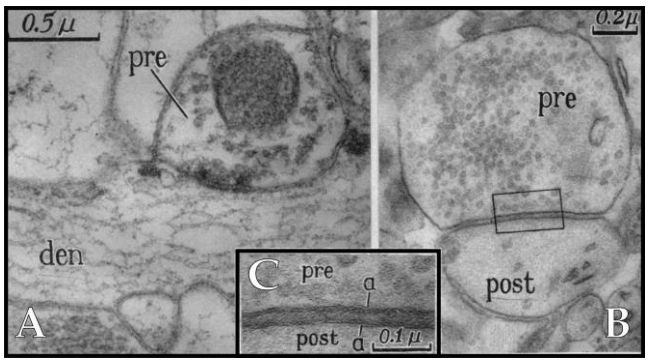

Figure 1.2: Electron micrographs of an axo-dendritic excitatory synapse (**A**) and an axo-somatic inhibitory synapse (**B**). Inset (**C**) highlights the reduced electron density in PSDs of inhibitory synapses in contrast to excitatory ones. "Pre" marks the axon while "den"/"post" labels the signal receiving neuron. Modified from GRAY.[11]

instances for inhibitory synapses relying on GABA as neurotransmitter, due to their challenging isolation and sparse character.[18] For this reason, a detailed look in the basics of GABAergic synapse formation and its molecular processes seems to be reasonable.

1.3 GABAergic inhibitory post synapses

Chemical synapses are defined by the neurotransmitter that is released from the axon and detected on the other side of the synaptic cleft at the postsynaptic membrane. The inhibition of neurons in the brain is induced by GABA detection that leads to hyperpolarisation of the postsynaptic neuron. Based on these two facts, one class of neuronal communication sites is referred to as GABAergic inhibitory synapses. These synapses have shown to provide a brake to neural firing and are relevant in various other purposes like action potential pattern modulation and synaptic strength modification.[19–23] Moreover, the fidelity of GABA transmission directly depends on the number of postsynaptic GABA receptors (GABARs) as GABA saturates them.[24,25] Hence, even slight changes in GABAR expression or their concentration in the synaptic specialisations of the postsynaptic membrane influence the signal trafficking, leading to behavioural consequences and direct physiological effects.[26,27] On these grounds a focus on this type of synapse is necessary. Despite the lack of information on them, in contrast to the excitatory PSD, former studies already identified potential proteins that contribute to the GABAergic synapse formation. Ideally, their number ranges in an amount manageable in *in vitro* experiments by which basic characteristics for each constituent part and for all together can be determined. The assumed composition of the receptor organisation machinery and its operation mechanism is outlined in the following section.

1.3.1 $GABA_AR$ organisation mechanism

As mentioned before, it is necessary for fast signal transduction that the postsynaptic specialisation is in direct apposition to the presynaptic terminal. This is ensured by the interaction of the cell adhesion molecules (CAMs) neurexin (presynaptic) and neuroligin (post synaptic) across the synaptic cleft. Additionally, the latter exhibits a gephyrin-binding site which is highly conserved in all its four isoforms, yet, only neuroligin 2 (NL2) holds a poly-proline segment (cf. Figure 1.5 A) being capable of interacting with collybistin 2 (CB2).[28,29] Such an interaction is src homology 3 (SH3) domain-dependent and causes the dissipation of the auto-

inhibition and opening of collybistin into an active conformation. In the open state the pleckstrin homology (PH) domain can bind to phosphoinositides in the plasma membrane. It is known that inactive CB2 can still interact with gephyrin via its B-cell lymphoma (Dbl) homology (DH) domain and forms cytosolic aggregates, though, after CB2 is switched in its active state these aggregates are adsorbed to the postsynaptic membrane (Figure 1.3 B) thereby, building the basis for the formation of gephyrin clusters underneath it (Figure 1.3 C).

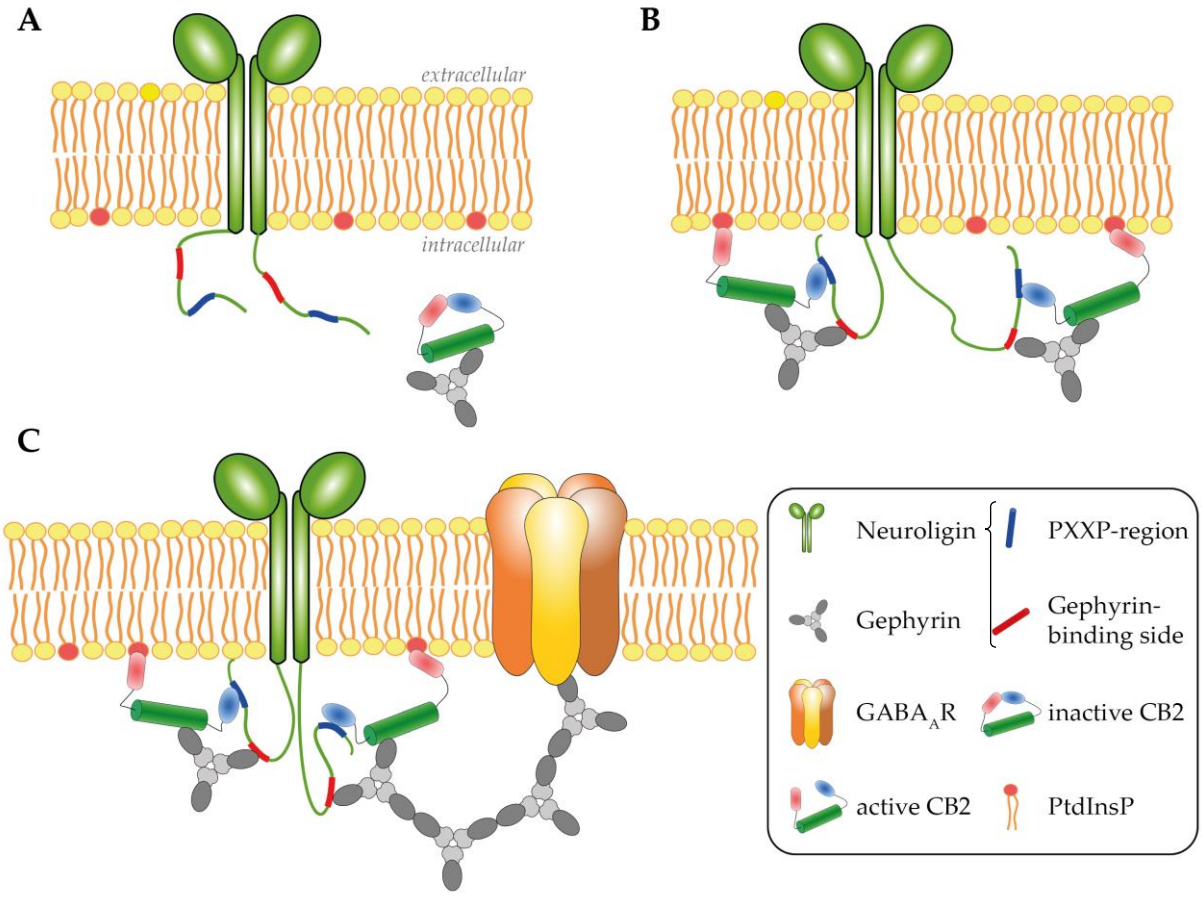

Figure 1.3: Postulated three-protein two-step mechanism of GABA$_A$R organisation in the post synaptic membrane of inhibitory synapses. (**A**) Cytosolic gephyrin-collybistin aggregates can interact with the *C*-terminal parts of a NL2 dimer via a specific gephyrin binding site and a poly proline sequence. (**B**) The interaction leads to an opening of CB2 and facilitates the adsorption of the aggregate to the plasma membrane via binding of the PH domain of CB2 to PtdInsPs. (**C**) Further gephyrin molecules adsorb to the anchored gephyrin-collybistin aggregate because of the high oligomerisation potential of gephyrin's terminal G- and E-domains and thereby form a hexagonal scaffold which causes the accumulation of GABA$_A$Rs at the synaptic specialisation.

Because of the oligomerisation potentials of both terminal domains of gephyrin a hexagonal shape of the sub membraneous scaffold is hypothesized, that is formed in the area of the synaptic specialisation and accumulates GABA receptors type A (GABA$_A$Rs). With this organisation process a fast signal transduction can occur. Yet, no direct evidence for this mechanism in the *in vivo* systems has been detected so far. An indication for the proposed protein machinery

and along with it the activation of collybistin via an interaction with NL2 was presented by POULOPOULOS *et al.* in co-expression experiments of all three proteins in COS7 cells.[30]

1.3.2 $GABA_A$ receptors

The inhibition of neuronal signal trafficking is largely a result of γ-aminobutyric acid transmission. Its fast-inhibitory functions are mediated by activation of specific GABA receptors in the brain. The GABA-specific receptors are composed of a heteropentameric stoichiometry of subunits ($\alpha_{1\text{-}6}$, $\beta_{1\text{-}3}$, $\gamma_{1\text{-}3}$, δ, $\varepsilon_{1\text{-}3}$, π, θ)[31] as shown in Figure 1.4 and belong to a ligand-gated ion channel superfamily, which as well includes nicotinic acetylcholine and glycine receptors.[32,33] Correlating with their variety in subunit composition, these receptors exhibit different physiological and pharmacological properties, yet the most abundant ones at synapses consist of two α subunits, two β subunits and one γ subunit (cf. Figure 1.4). These types of GABARs referred to as $GABA_A$Rs, are drug targets in clinical daily routine for anti-convulsant, anxiolytic and sedative-hypnotic agents. Furthermore, disease patterns like epilepsy[34], Huntington's disease[35], anxiety disorders[36], schizophrenia[37] and Autism spectrum disorders[38] are provoked by deficits in the functional expression of them.

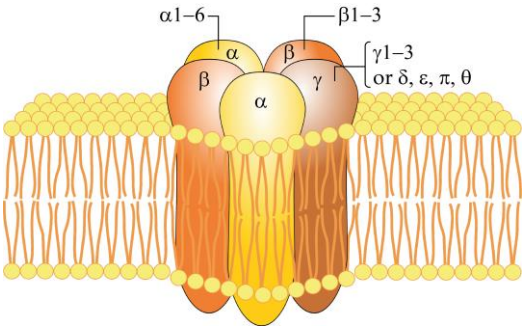

Figure 1.4: Schematic image of the pentameric composition in a GABA-receptor. The receptor consists in variations of $\alpha_{1\text{-}6}$, $\beta_{1\text{-}3}$, $\gamma_{1\text{-}3}$, δ, $\varepsilon_{1\text{-}3}$, π, and θ subunits.

After their formation in the endoplasmic reticulum and navigation through the secretory pathway, $GABA_A$Rs are inserted in the neuronal plasma membrane and can either access inhibitory postsynaptic specialisations or extra synaptic areas.[32] Due to the large surface area of extrasynaptic versus synaptic membrane the total number of extrasynaptic receptors is likely to be larger than that of synaptic ones.[39] Thus, the accumulation mechanism of $GABA_A$Rs in the active areas of postsynaptic membranes is essential for fast synaptic transmission between neurons, whilst a malfunction in this process can cause the aforementioned diseases. Therefore, the understanding of the organisation processes and their underlying molecular machinery has been in researchers' focus within the last decades to identify possible treatment sites.

$GABA_A$Rs experience the omnipresent BROWNIAN motion in the form of lateral diffusion in plasma membranes,[40] yet, the concerted spatial and temporary accumulation of the receptors

cannot exclusively be obtained by this process.[41] A further trapping of the receptors in the synaptic clusters is required, leading to an increase in this population due to reduced mobilities, as most $GABA_A$Rs are delivered to extra synaptic sites.[42–44] Specialisation in excitatory post synapses form via receptor-associated proteins and cytoskeletal elements located in the PSD.[15,45,46] In contrast to that, $GABA_A$ergic, inhibitory synapse formation is based on the tubulin binding protein gephyrin. It reduces the receptor diffusion velocity from high (10^{-1} -10^{-2} $\mu m^2 s^{-1}$), while moving between synaptic specialisations, to low ($<10^{-3}$ $\mu m^2 s^{-1}$) diffusion rates when interacting with scaffold aggregates.[41] The interaction of $GABA_A$Rs with gephyrin was also shown by *in vivo* experiments with gephyrin-deficient cortical neurons of mice by ESSRICH *et al*.[47] However, this trapping mechanism for $GABA_A$Rs is altered by collybistin and thus, must be composed of further components in addition to gephyrin.[48]

1.3.3 Neuroligin

For $GABA_A$Rs organisation in postsynaptic specialisations, in direct apposition to presynaptic neurotransmitter release-sites, the interaction of cell adhesion molecules (CAMs) is among the earliest and most indispensable events of synaptogenesis to guarantee faithful information transmission across the synaptic cleft. CAMs are localized on both sides of the synapse and execute strong transsynaptical interactions which align pre- and postsynaptic specialisations even when biochemically copurified in the presence of detergents.[13]

One brain-specific group of CAMs are neuroligins (NL) located at the postsynaptic site in neurons.[49,50] The group consists of four major members NL 1, 2, 3, and 4 which show great structural similarities and high homologies in their amino acid sequences as depicted in Figure 1.5 A.

A

```
Neuroligin          Transmembrane domain
1   YSTEL SCTIA VGASL LFLNI LAFAA LYYKK DKRRH DVH-R RCSPQ RTT-- ----- ----- TNDLT HAPEE EIMSL QMKHT DLDHE   764
2   YSTEL SVTVA VGASL LFLNI LAFAA LYYKR D-RRQ ELRCR RLSPP GGSGS GVPGG GPLLP TAGRE LPPEE ELVSL QLK-- --RGG   753
3   YSTEL SVTIA VGASL LFLNV LAFAA LYYRK DKRRQ EPL-R QPSPQ RGTG- ----- ----- APELG TAPEE ELAAL QLG-- PTHHE   755
4   YSTEL SVTIA VGASL LFLNI LAFAA LYYKK DKRRH ETH-R RPSPQ RNT-- ----- ----- TNDIA HIQNE EIMSL QMKQL EHDHE   743

Neuroligin                  Gephyrin-binding side          Poly-proline sequence                    PDZ
1   CESIH PHEVV LRTAC PPDYT LAMRR SPDDV PLMTP NTITM IPNTI PGIQP ----- LHTFN TFTGG QNNTL PHPHP HPHSH STTRV   843
2   GVGAD PAEA- LRPAC PPDYT LALRR APDDV PLLAP GALTL LPSGL GPPPP PPPPS LHPFG PFPPP PPTAT SHNNT LPHPH STTRV   836
3   CEAGP PHDT- LRLTA LPDYT LTLRR SPDDI PLMTP NTITM IPNSL VGLQT ----- LHPYN TFAAG FNSTG ----- LPNSH STTRV   828
4   CESLQ AHDT- LRLTC PPDYT LTLRR SPDDI PLMTP NTITM IPNTL TGMQP ----- LHTFN TFSGG QNSTN ----- LPHGH STTRV   816
```

B

Extra cellular	Neuroligin2	Neuroligin3	Neuroligin4
Neuroligin1	66 %	70 %	71 %
Neuroligin2		67 %	66 %
Neuroligin3			74 %

Intra cellular	Neuroligin2	Neuroligin3	Neuroligin4
Neuroligin1	38 %	56 %	71 %
Neuroligin2		36 %	35 %
Neuroligin3			64 %

Figure 1.5: (**A**) Alignment of amino acid sequences of NL1-4, where the sequences correspond to mouse NL1, rat NL2, and human NL3 and NL4.[53] (**B**) Matrices representing the approximate percent identity of the different human neuroligin protein sequences separated by domains (extra- and intracellular).[54]

The structural similarities are based on the fact that each member has a single transmembrane region, that separates a highly conserved, extracellular esterase-like domain from a short intrinsically disordered cytoplasmic tail (cf. Figure 1.5 B).[51–54] The different subtypes of NL are located each at unique membrane areas. While NL1 and NL2 are exclusively found at excitatory glutamatergic and inhibitory GABAergic synapses, respectively, NL3 is localised at both types of synapses.[54,55] Nevertheless, the primary adhesion partner of neuroligins inside the presynaptic axon is the neurexin family with a vast number of splice variants.[56] Furthermore, it has been shown that the primary species of NLs in the cell is a dimer and its formation is assumed to be a crucial step in NL trafficking.[57,58]

At GABAergic synapses, NL2 was shown to recruit the scaffolding protein gephyrin via a specific binding motif in its *C*-terminus.[55,59] Furthermore, the proline-rich area in the amino acid sequence of the cytosolic loop is a possible interaction site for the adaptor protein collybistin.[30,60] Based on these interactions, NL2 is believed to be the starting point of a two-step, three-protein organisation machinery for $GABA_A$Rs in postsynaptic specialisations during synaptogenesis as presented in Figure 1.3.[53]

1.3.4 Gephyrin

The tubulin binding protein gephyrin is the most prominent scaffolding protein in inhibitory post synapses as it is crucial for the localisation of both glycine and GABA specific receptors at synaptic sites.[47,61,62] Its interaction with the latter is based on binding to the α1-3 and β2-3 subunits with lower affinities, however, it is not less important.[63–67] Additional to its scaffolding character, it also interacts with cell adhesion molecules, signalling molecules and motor protein complexes, all contributing during anchoring of $GABA_A$Rs to synaptic specialisations of the neuronal membrane.[68–70] Beyond its participation in receptor organisation gephyrin catalyses the terminal steps of the molybdenum cofactor biosynthesis.[71] Both gephyrin functions turned out to be essential as shown by FENG *et al*.[72]

The protein itself is composed of a *N*-terminal G domain connected via a linker of ~150 amino acids to a *C*-terminal E domain.[73] Several studies based on crystal structure analysis showed that the G domain is capable of trimerisation,[74,75] while the E domain tends to form dimers.[76,77] This oligomerisation potential is essential for the synaptic clustering of gephyrin.[78] Furthermore, successive publications postulated the formation of a so-called hexagonal lattice when all oligomerisation interfaces of both domains are utilised.[79,80] Yet, structural analysis of hologephyrin indicates a prevention of the E domain dimerisation in full-length gephyrin and suggests different compact and extended states depending on the flexible linker region.[81] SPECHT and co-workers used different single-molecule based imaging techniques to gain insights in the three-dimensional organisation of gephyrin and detected a two-dimensional lattice with different gephyrin densities in constant proximity to the neuronal membrane that can be explained with the aforementioned compact and extended linker region states.[82] Notwithstanding gephyrin's spatial arrangement at synaptic sites, it was shown that the complexation of receptors with gephyrin *per se* is not sufficient for receptor cluster formation, as these complexes were also detected in extrasynaptic membrane parts and cytosolic compartments.[83,84] Additional factors, influencing receptor clustering, were found by observation of trapped $GABA_A$Rs at excitatory synapses and on the other hand trapped AMPA receptors at inhibitory synapses by RENNER *et al*.[85] These hint at a higher complexity of the receptor organisation process composed of further participants next to gephyrin like the aforementioned cytoskeleton and the adaptor protein collybistin, on which the following paragraph will focus on.

1.3.5 Collybistin

The structure of collybistin (CB) consists of an *N*-terminal SH3 domain connected to a so-called tandem domain of a DH and a PH domain (cf. Figure 1.6), which classifies CB as a member of the Dbl protein-family. The DH-domain enables collybistin's function as a guanine-nucleotide exchange factor (GEF) for small rat sarcoma homologue (Rho) GTPases. To be precise, CB regulates the small GTPase Cdc42 (cell division control protein 42 homologue) that is implicated in the control of the cytoskeleton and filopodia formation.[86] As illustrated in Figure 1.6 there are three isoforms of collybistin, CB1-3, exhibiting high sequence homology except for differences in their *C*-termini. Furthermore, for CB2 a splice variant exists lacking the *N*-terminal SH3 domain (CB2$_{-SH3}$).[48] Figure 1.6 schematically illustrates the structure of all collybistin isoforms.

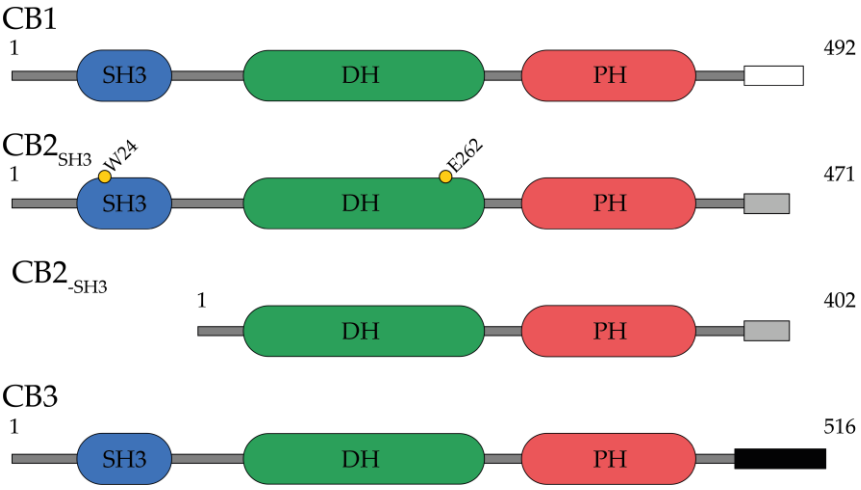

Figure 1.6: Schematic illustration of the three splice variants of collybistin (CB1-3) which vary in their *C*-termini only. All consist of a SH3 domain connected to a tandem domain made up from DH and PH domain except for a splice variant of CB2 that lacks the *N*-terminal SH3 domain.

In its duty as a GEF, CB has a second small Rho GTPases, TC10, next to Cdc42 as a substrate. Both enzymes share 67.4 % of sequence identity and structural similarities which are also represented in common cellular functions.[87,88] Yet, in contrast to Cdc42, which is ubiquitously expressed in the brain, TC10 is located only in specific areas like the CA1 region of the hippocampus.[89] Nevertheless, both GTPases are activated upon guanosine 5′-triphosphate (GTP) binding and deactivated via its hydrolysis to guanosine 5′-diphosphate (GDP) in the presence of GTPase activating proteins (GAPs). Collybistin afterwards regenerates the enzymes' activities by substitution of the nucleotides. Due to this function it was called collybistin from the ancient Greek word κολλυβιστομαι for "exchange".[90] It is highly expressed throughout the brain and is specifically enriched in neuronal dendrites.[91,92]

In 2000, KINS *et al*. first proved a connection between CB function and synaptic cluster formation of gephyrin. They were able to detect two splice variants of collybistin (CB1 and CB2)

and showed that the longer transcript variant CB1 co-expressed with gephyrin caused cytosolic aggregate formation in non-neuronal cells. In case of the shorter variant CB2 co-expression led to CB-gephyrin cluster formation underneath the plasma membrane.[90] These results built the base for the assumption that collybistin functions as a molecular switch and is relevant for neuronal receptor accumulation at inhibitory synaptic specialisations by regulating gephyrin clustering. This characteristic results from an intramolecular interaction between the *N*-terminal SH3 and the *C*-terminal PH domain that blocks the relevant binding sites necessary for fixation of CB to the plasma membrane via specific receptor lipids.[60] In case of CB these receptor lipids are the phosphorylated metabolic products of phosphatidylinositol (PI), the so-called phosphatidylinositol phosphates or phosphoinositides (PtdInsPs).[93] Additional studies determined that CB2$_{\text{-SH3}}$ displays the strongest binding to PtdIns(3)P in a PH domain-dependent manner, while the longer splice variant CB2$_{\text{SH3}}$ expresses no specific preference for a particular phosphoinositide and lower affinities.[60,94] The binding site for PtdInsPs is positioned in the loop between the β3- and β4-sheets of the PH-domain that is composed of seven antiparallel β-sheets in total.[93,95,96] Via its interaction with the different PtdInsPs, that are widely distributed in the cell,[97] CB can be specifically localised in different cellular compartments.
Even though, the potential activation of CB has been outlined, the exact interaction sites stay enigmatic and proof for the precise mechanism is missing. To focus this uncertainty in such a detail necessary for clarification a simplification or a model for the topic in question is reasonable. This can be done by a transfer into *in vitro* systems in which control of all relevant parameters is possible. A widely distributed tool are model membrane systems that are used to broaden the understanding of processes occurring in or at the plasma membrane. Therefore, chapter 1.4 will deal with these specific *in vitro* systems in detail.

1.4 Model membrane systems

The examination of processes and interaction *in vivo* has the advantage to present the object of study in its natural environment. However, in many cases investigations of protein-lipid or protein-protein interactions in their original environment and conditions are inappropriate for determinations of specific features or characterisations of these processes. This is based on difficulties like low abundance, high turnover or the molecular complexity of *in vivo* systems.[98]

Therefore, a plethora of studies focussing on a precise process or interaction have been performed in *in vitro* systems. They are usually composed step-by-step in a bottom-up approach which allows the control of all parameters and constituents resulting in the exact determination of characteristics underlying the respective research object. It is e.g. possible to extract natural lipids and built up a membrane by mixing chemically defined lipid species. This leads to a complete control of the membrane composition. There is a wide range of model membrane systems available differing in their features. Some of these are schematically illustrated in Figure 1.7.

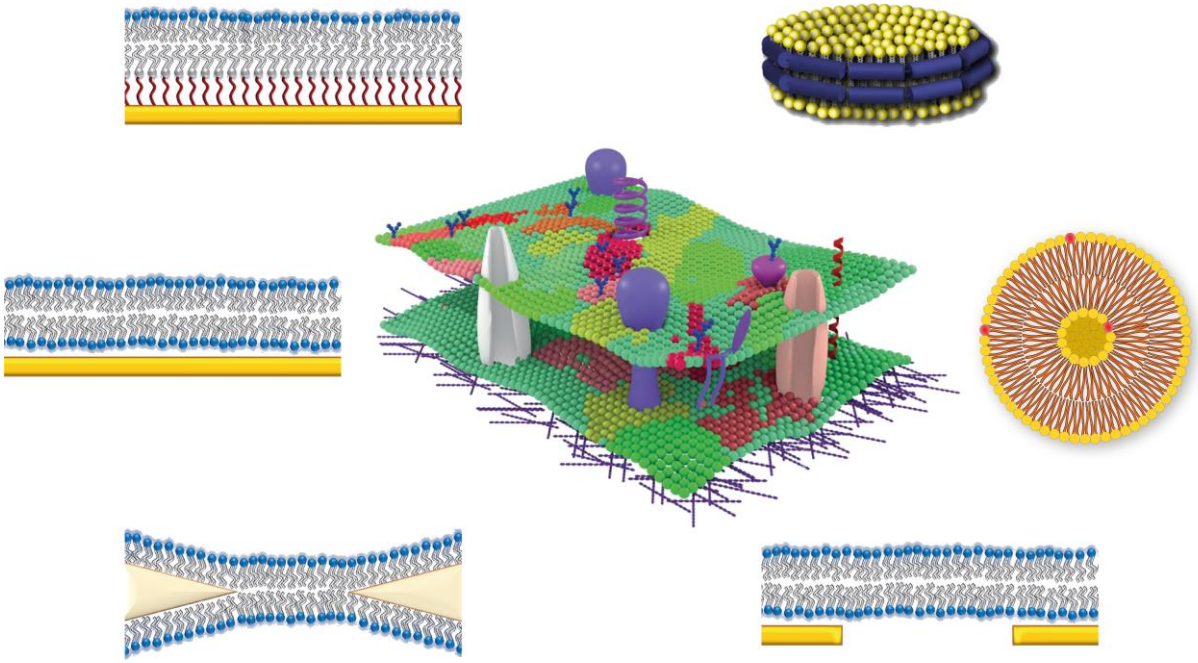

Figure 1.7: Schematically illustrations of various model membrane systems (a unilamellar vesicle, a lipid nanodisc, a black lipid membrane and diverse forms of solid-supported membrane systems)[100-102] that are arranged in an orbit around a scheme of the cellular plasma membrane modified from SEZGIN *et al*.[103]

The choice can be made between vesicles of different sizes and lamellarity,[99] adhered or freely floating, and lipid nanodiscs.[100] Furthermore, black lipid membranes, pore-spanning membranes, tethered double bilayers, solid-supported bilayers, solid-supported monolayers or polymer-cushion tethered bilayers are possible option for a model system of the plasma membrane.[101–103] Hence, the choice depends on the properties required for experimentation. Polymer-cushion tethered layers e.g. were used by TAMM and colleagues to perform reconstitution experiments with SNARE-proteins.[104] However in most cases the model system of choice is the solid-supported lipid bilayer (SLB) due to its simple preparation via spontaneous spreading of small unilamellar vesicles (SUVs) on hydrophilic surfaces.[105,106] This type of model mem-

brane system allows the use of surface sensitive methods to characterise interactions and processes mentioned before in a label-free and time-resolved manner.[107,108] Therefore, the solid-supported lipid membrane represented by either the standard lipid bilayer or a hybrid lipid membrane on top of a hydrophobically functionalised substrate will represent the basis for the experimental work of this study.

2 Scope of Thesis

The mammalian nervous system is composed of a plethora of neuronal cells which communicate via electrical or chemical synapses to guarantee proper signal transduction. In case of the second synapse type a differentiation between excitatory and inhibitory characteristics is feasible, depending on the induced post synaptic potential that either forwards information or stops its transduction. While excitatory synapses have been investigated rigorously at the molecular and cell biological level, similar characterisation is missing for inhibitory synapses relying on γ-amino butyric acid (GABA) which is a neurotransmitter prevalently used in the brain. This is owed to their challenging isolation and sparse character.

Therefore, this work aims on the preparation of an *in vitro* model system for the organisation machinery of specific GABA receptors in the postsynaptic plasma membrane. The organisation complex is assumed to consist of the cell adhesion protein neuroligin 2 (NL2), the scaffolding protein gephyrin and the adaptor protein (CB2). The latter is capable to interact with phosphoinositides (PtdInsPs) present in the postsynaptic membrane. For this reason, a bottom-up approach based on two different membrane systems, supported by silicon dioxide substrates with either hydrophilic or hydrophobic surface features, will be applied to characterise the anchoring CB2-PtdInsP interaction. Moreover, the impact of the phosphorylation pattern of PtdInsP will be examined by deploying three exemplary variants (PtdIns[3]P, PtdIns[4,5]P_2 and PtdIns[3,4,5]P_3). The preparation of solid-supported lipid bilayers (SLBs) and solid-supported hybrid membranes (SHMs) will facilitate their comparison and thus, examination of the support's impact on the receptor lipid distribution and other membrane features.

The investigation of CB2 adsorption to the PtdInsP containing model membranes by means of reflectometric interference spectroscopy (RIfS) and atomic force microscopy (AFM) will give insights in the adsorption behaviour of the adaptor protein and its organisation when attached to a membrane.

After detailed characterisation of the protein-lipid interaction, the model system will be expanded by an additional receptor lipid specific for a protein construct that mimics the intracellular domain of NL2. When the expansion does not impede the established model, the NL2—CB2 interaction will be investigated in order to elucidate if this interaction induces a intramolecular cleavage in CB2 that renders the protein active.

3 Materials and Methods

3.1 Used Materials

3.1.1 Lipids

In this thesis artificial membrane systems were used to mimic the plasma membrane. The model membranes were composed of varying lipid mixtures to investigate their impact on the proteins involved in post synaptic $GABA_A$ receptor organisation. All mixtures were composed of a matrix lipid in combination with at least one receptor lipid species and in some cases a fluorescent probe.

3.1.1.1 Matrix Lipids

The matrix lipid represents the mayor part of all lipid compositions but should not have a significant interaction with the attached proteins. Dependent on the used technique and the physical properties required for the experimental setup, two different phospholipids were utilised as matrix lipids in this work. On one hand, 1-palmitoyl-2-oleoyl-*sn*-glycero-phosphocholine (POPC) was used when fluid characteristic at room temperature were inevitable as it is the case for *in situ* membrane formation during reflectometric interference spectroscopy (RIfS, cf. Chapter 3.5). Alternatively, 1,2-dipalmitoyl-*sn*-glycero-3-phosphocholine (DPPC), which is in the gel phase at room temperature, was employed to simplify protein imaging via atomic force microscopy because of reduced lateral motion inside the more rigid system. These lipids

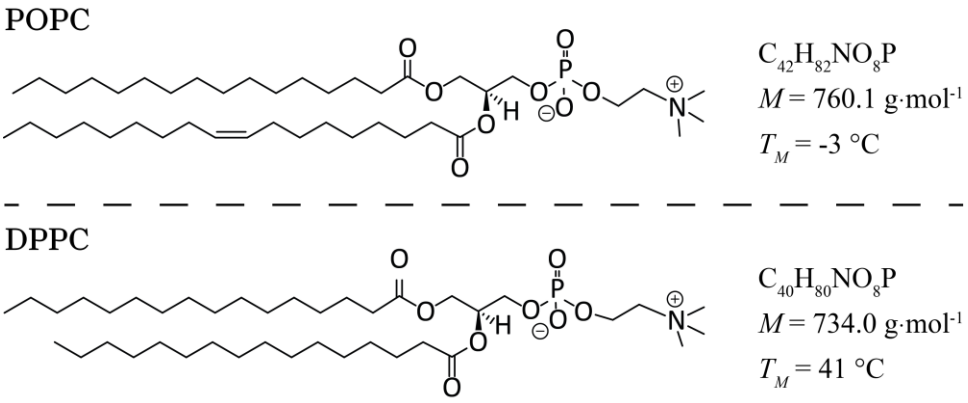

Scheme 3.1: Structures of the matrix lipids 1-palmitoyl-2-oleoyl-*sn*-glycero-phosphocholine (POPC) and 1,2-dipalmitoyl-*sn*-glycero-3-phosphocholine (DPPC) with their molecular formulas, molecular weights and main transition temperature.

show different main transition temperatures T_M (POPC: T_M = -3 °C; DPPC: T_M = 41 °C)[109,110] due to variations in their fatty acid chains attached to their glycerol backbone with POPC having

a palmitic acid (16:0) esterified on position 1 and an oleic acid (18:1 Δ^9-*cis*) on position 2 whereas DPPC only carries two palmitic acid chains on both positions (cf. Scheme 3.1). Nonetheless, both express a high structural similarity and provide no charge as glycerol is substituted with a phosphocholine headgroup at position 3.

3.1.1.2 Receptor Lipids

The artificial membrane systems contained in addition to the matrix lipids specific lipids which enabled an adsorption of the investigated proteins to the lipid layers. These lipids that are intended to affect the tested proteins are referred to as receptor lipids. While one class of them has been shown to be relevant physiological interaction partners inside the plasma membrane for collybistin and N-ERMAD, the second class employed are synthetic lipids that were used for the fixation of the protein construct mimicking the intracellular domain of neuroligin.

Phosphoinositides

Phosphoinositides (PtdInsP) are the phosphorylated products of phosphoinositol (PI). They are generated by reversible phosphorylation of the inositol ring at positions 3, 4 and 5 yielding seven different phosphoinositides that are either mono-, bis- or tris-phosphorylated. In Scheme 3.2 the three phosphoinositides are shown which were employed in this work. While L-α-phosphatidylinositol-4,5-bisphosphate (PtdIns[4,5]P_2) is the most abundant representative of this lipid group with 1 mol% of all phospholipids inside human erythrocytes,[111,112] the monophosphorylated PtdIns[3]P has been shown to express the highest binding affinity to collybistin.[113] To evaluate the influence of the degree of phosphorylation also the lipid PtdIns[3,4,5]P_3 was employed. All three share the characteristic of two palmitic acid chains that are esterified

at positions 1 and 2 of their glycerol backbone. Due to the phosphate groups of the inositol headgroup all PtdInsPs are negatively charged.

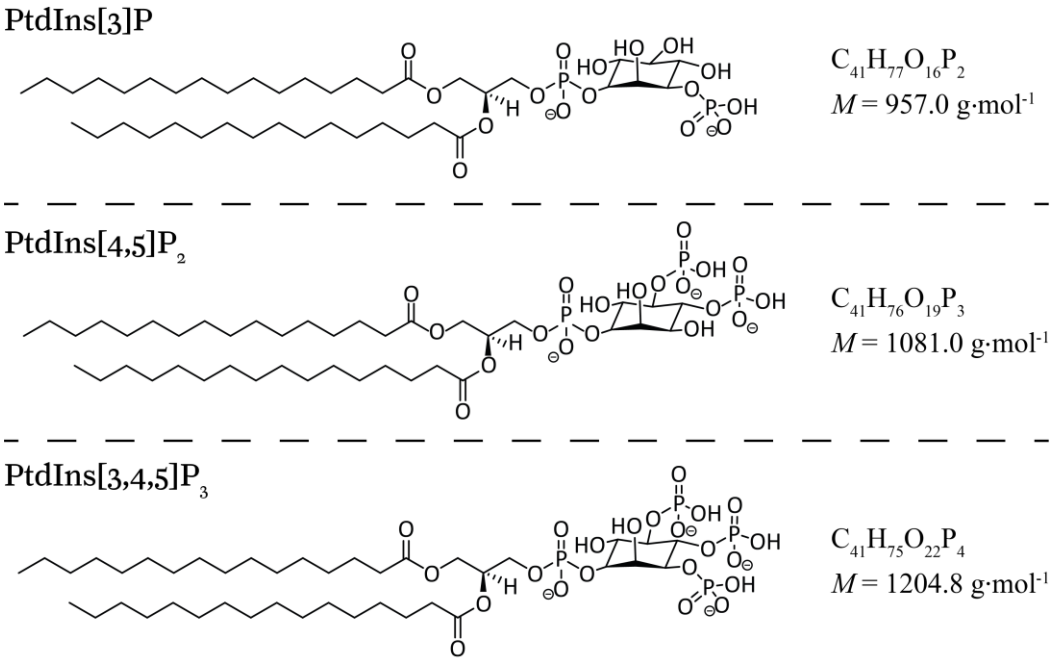

Scheme 3.2: Structural framework of the phosphoinositides PtdIns[3]P, PtdIns[4,5]P_2 and PtdIns[3,4,5]P_3 with their molecular formulas and weights.

1,2-dioleoyl-*sn*-glycero-3-{[*N*-(5-amino-1-carboxypentyl)iminodiacetic acid]succinyl} nickel salt

In contrast to the aforementioned phosphoinositides with physiological relevance the second receptor lipid used is the synthetic 1,2-dioleoyl-*sn*-glycero-3-{[*N*-(5-amino-1-carboxypentyl)iminodiacetic acid]succinyl} nickel salt (DGS). As shown in Scheme 3.3 it consists of two oleic acids (18:1 Δ^9-*cis*) that are esterified to the central glycerol at position 1 and 2. Additionally, nitrilotriacetic acid (NTA) is esterified via a linker to position 3 of the glycerol.

The NTA headgroup is a tetra dental ligand and can coordinate cations in an octahedral fash-

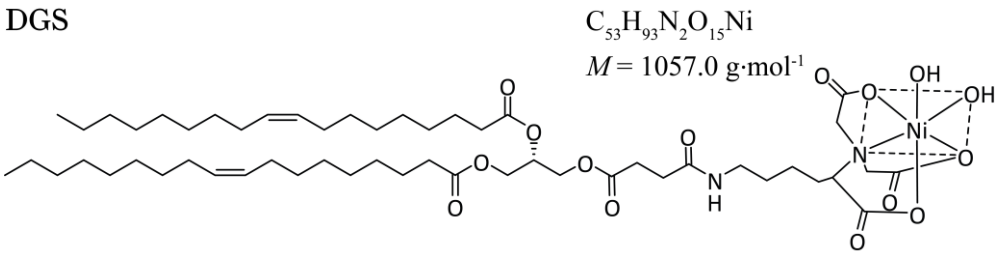

Scheme 3.3: Structures of the synthetic lipid 1,2-dioleoyl-*sn*-glycero-3-{*N*-5-amino-1-carboxypentyl)iminodiacetic acid]succinyl] nickel salt with its molecular formula and weight.

ion leaving two coordination sites vacant. Therefore, further coordination of other ligands

such as histidine-residues is possible and enables adsorption of proteins carrying a poly-histidine tag.

3.1.1.3 Fluorescent Probes

Fluorescent microscopy was used in this work to determine the quality of the artificial membrane systems and to investigate the lateral mobility of the lipids therein. To do so different lipid coupled dyes were introduced in small amounts into the lipid compositions.

Texas Red®

The fluorophore Texas Red® (TxR) was used in this work to determine the homogeneity of the model lipid layers and to check for defect formation. For this reason, the fluorescent molecule TxR coupled to 1,2-dihexadecanoyl-*sn*-glycero-3-phosphoethanolamine (TxR-DHPE, cf. Scheme 3.4) was employed for detection. The excitation wavelength of this dye is λ_{ex} = 561 nm and the emitted light was detected in a range of 585-630 nm.

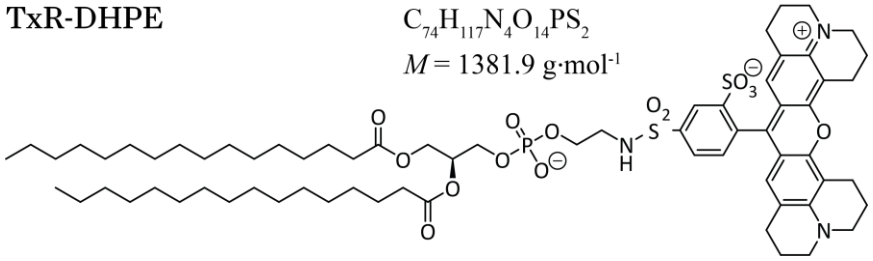

Scheme 3.4: Structure of the fluorescent probe TxR-DHPE with its molecular formula and weight.

BODIPY®-TMR labelled PtdInsPs

Furthermore, labelled receptor lipids are an interesting tool to investigate the lipid's behaviour inside the model membrane under varying conditions. Therefore, all three phosphoinositides tested in this work were purchased with a fluorescent dye, BODIPY®-TMR, coupled to one of

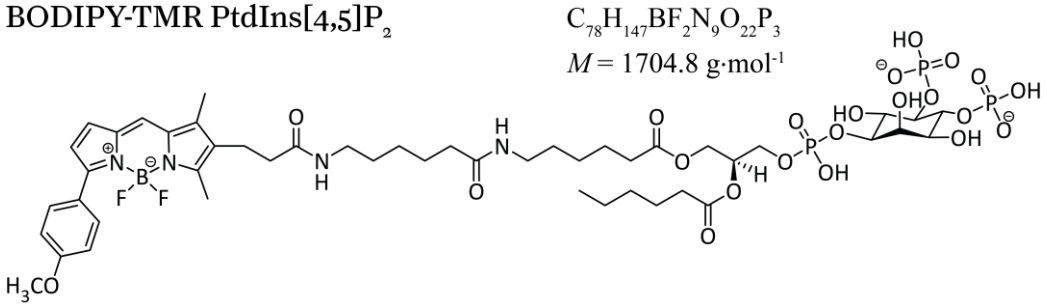

Scheme 3.5: Structure of BODIPY®-TMR PtdIns[4,5]P_2 with its molecular formula and weight as an example for fluorescently labelled phosphoinositides. The dye is coupled to the fatty acid chain of the lipid molecule.

the fatty acid chains as exemplary shown in Scheme 3.5 for PtdIns[4,5]P_2. While in position 1 of the glycerol the palmitic acid is substituted by a caproic acid, in position 2 the fluorophore BODIPY®-TMR is esterified via a linker to the lipid. In analogy to this, labelled version of the mono- and tris-phosphorylated phosphoinositides were also employed in this work.

3.1.2 Materials for the Solid Support

In this work solid-supported model membrane systems were prepared on top of a silicon base. The silicon wafers used for this purpose were purchased from *Silicon Materials Inc.* (Glenshow, USA) and exhibited SiO_2 layers with thickness of 100 nm or 5 µm on their surfaces. While the substrates with a thinner layer were applied for experimentation with atomic force microscopy (AFM) and fluorescence microscopy, the 5 µm layer of SiO_2 was a prerequisite for the application of RIfS (cf. Chapter 3.5). Furthermore, the Si-SiO_2 substrate's surface features can be manipulated via functionalisation which facilitates the employment of model membrane systems supported by either a hydrophilic or a hydrophobic base.

3.2 Biochemical Methods

The study of protein characteristics and their interaction with other partners such as lipids or other proteins consumes a high amount of resources in the sense of the proteins themselves. Therefore, a method of recombinant protein expression based on the application of bacteria is widely spread. In doing so *Escherichia coli* (*E. coli*) is the most frequently used prokaryotic expression system as it exhibits fast growth rates and a well-functioning protein biosynthesis.[114] Furthermore, *E. coli* is available in various mutated strains and can be combined with a plethora of cloning vectors.[115] Nonetheless, there are also disadvantages like the formation of inclusion bodies and the lack of post-translational modifications.[116] However, all proteins investigated within this thesis were expressed in *E. coli*, to be precise in the cells of the BL21(DE3) strain that contains the T7-RNA-polymerase promotor system.

3.2.1 Preparation of chemical competent cells

Under physiological conditions bacterial cells can take genetic material up with low efficiencies. Therefore, it is necessary to temporary enhance this process by increasing the permeability of the cellular membrane for exogeneous uptake. For gram-negative bacteria such as *E. coli*

this can be achieved by electroporation or the use competent cells. For the later different methods of preparation are known of which the cell treatment with calcium chloride is the most prominent one. For the preparation of competent cells different *E. coli* strains can be used. This section will focus on the process with cell from the DH5α strain that are preferably employed for plasmid copying due to their high transformation efficiency.[117]

First DH5α cells of a former preparation were placed on a LB (*lysogeny broth*) agar plate (for composition cf. Table 3.3) without any antibiotics contained and incubated at 37 °C in an incubator hood (Edmund Bühler GmbH, Bodelshausen, Germany) overnight. Then a single colony from the plate was selected and used for inoculation of an overnight culture (25 mL LB medium, cf. Table 3.3) which was subsequently incubated at 37 °C and 185 rpm overnight. 1 mL of this culture was used on the next day to inoculate the main culture (100 mL LB medium) that grew at 37 °C and 185 rpm till an optical density OD_{600} of 0.4 was reached. Growth was stopped by placing the culture on ice. Afterwards the cell suspension was centrifuged (2700 x g, 10 min, 4 °C), the resulting pellet was resuspended in 1.6 mL of $CaCl_2$ solution (100 mM) and stored on ice for 30 min. This process was repeated a second time and thereafter 0.5 mL of glycerol were added to the cell suspension in $CaCl_2$-solution followed by fractionation to 100 µL aliquots that were frozen in liquid N_2 and stored at -80 °C until use for plasmid transformation.

3.2.2 Plasmid Transformation

All plasmids (cf. Table 3.1) utilised within this work were reproduced in the DH5α cell system prior to transformation into the recombinant expression system.

Table 3.1: Overview of the employed vectors with their affinity tags, cleavage sites and antibiotic resistance.

Vector	DNA-Sequence	Affinity tag	Cleavage site	Resistance
pET28a+	N-ERMAD	His_6	Thrombin	Kanamycin, Chloramphenicol
pETM11	His-*cyt*NL2	His_6	TEV	Kanamycin
pTXB1	$CB2_{SH3}$ $CB2_{SH3/W24A-E262A}$	Chitin binding domain	Intein (DTT induced)	Ampicillin
pTYB21	$CB2_{PH}$	Chitin binding domain	Intein (DTT induced)	Ampicillin

The plasmids encoding collybistin and neuroligin were kindly provide by the group of Hermann Schindelin (Rudolph-Virchow-Zentrum, Würzburg, Germany). To achieve sufficient protein yields different *E. coli* strains were used that matched with the specific vectors (cf. Table 3.2) as some proteins show cell-toxic effects at critical concentrations.[118,119]

Table 3.2: Overview of the different *E. coli* strains used for protein expression with their genotypes and distributors.

Strain	Genotype	Expressed proteins	Distributor
BL21(DE3)	F^- ompT $hsdS_B$ ($r_{B-}m_{B-}$) gal dcm (DE3)	$CB2_{SH3}$ $CB2_{SH3/W24A-E262A}$ $CB2_{PH}$	Invitrogen
BL21(DE3) pLysS	F^- ompT $hsdS_B$($r_{B-}m_{B-}$) gal dcm (DE3) pLysS (Cam^R)	N-ERMAD	Invitrogen
BL21(DE3) Rosetta	F^- ompT $hsdS_B$(r_{B^-} m_{B^-}) gal dcm (DE3) pRARE (Cam^R)	His-*cyt*NL2	Novagen

Experimental procedure

A solution of plasmid in ultrapure H_2O (5 µL) was added to an aliquot of competent cells (50 µL) on ice and incubated for at least 30 min. After this duration the cell solution was placed for 45 s in a 42 °C water bath to induce exogeneous uptake via heat shock. Subsequently the solution was again stored on ice for 4 min and then 250 µL of SOC medium (*super optimal broth with catabolite repression*, for composition cf. Table 3.3) were added. For fast cell growth the culture was incubated at 37 °C and 150 rpm for one hour. Afterwards the cells were distributed on LB-agar plates, containing the specific antibiotic to guarantee selective growth of only successfully transformed bacterial cells, which were then incubated at 37 °C overnight.

Table 3.3: Composition of the nutrient solutions used for plasmid reproduction and protein expression.

LB medium	1.0 %(*w/v)* tryptone	**LB-agar**	1.0 %(*w/v)* tryptone
pH 7.0 or pH	1.0 %(*w/v)* NaCl	**(1.5 %)**	1.0 %(*w/v)* NaCl
7.4	0.5 %(*w/v*) yeast extract	pH 7.0 or pH	0.5 %(*w/v*) yeast extract
		7.4	1.5 %(*w/v)* Agar-agar
SOC medium	2.0 %(*w/v)* tryptone		
pH 7.0	0.5 %(*w/v*) yeast extract		
	10 mM NaCl		
	2.5 mM KCl		
	10 mM $MgCl_2$		
	10 mM $MgSO_4$		
	20 mM glucose		

3.2.3 Plasmid Isolation

The isolation of the plasmid DNA was essential to guarantee a sufficient stock as protein expression was only conducted with freshly transformed *E. coli* cells. The vector isolation was performed using a Nucleobond® Xtra Midi EF-Kit (*Macherey-Nagel*, Düren, Germany).[120] A single successfully transformed colony (as describe in Chapter 3.2.2) was picked from a LB-agar plate and used for inoculation of 100 mL LB medium at 37 °C and 185 rpm overnight. The cell suspension was then centrifuged (4500 rpm, 20 min, 4 °C) and the obtained pellet was resuspended in 8 mL RES-EF buffer which included RNase A. Further addition of 8 mL LYS-EF buffer induced the alkaline lysis of the cell that was followed by incubation at room temperature for 5 min. Meanwhile, a silica-based anion-exchange chromatography column was equilibrated by rinsing with 15 mL EQU-EF buffer. The lysate was then diluted with 8 mL NEU-EF buffer to neutralise the solutions pH and incubated for 5 min on ice. The separation of cell debris and lysate was achieved by centrifugation (4500 rpm, 10 min, 20 °C). The later was applied to the equilibrated column which was subsequently washed with 5 mL FIL-EF buffer, 35 mL ENDO-EF buffer and 15 mL WASH-EF buffer. After all impurities were removed the vector DNA was eluted with 5 mL ELU-EF buffer. A last purification step was performed by addition of 3.5 mL isopropyl alcohol to the plasmid solution and a further centrifugation (4500 rpm, 45 min, 4 °C). The resulting pellet was dissolved in endotoxin-free ethanol and

again centrifuged (13000 rpm, 5 min, 20 °C). After solvent removal the plasmid was solved in 1.2 mL ultrapure water, divided in aliquots, frozen in liquid N_2 and stored at -20 °C until further use. All buffer solution mentioned in this Chapter were ingredients of the initially mentioned isolation kit which included no information on the buffers' compositions.

3.2.4 Plasmid Sequencing

All plasmids were sequenced directly after their purification to avoid the use of any false DNA sequence that would impede the whole protein expression process. The sequencing of the vector DNA was implemented by the company *SeqLab, Inc*. (Göttingen, Germany). The primers (predominantly T7 promoter and T7 terminator, cf. Table 3.4) were directly provided by the sequencing company.

Table 3.4: Primers used for plasmid sequencing.

Name	Sequence
T7 promotor primer	5-TAATACGACTCACTATAGGG-3
T7 terminator primer	5-GCTAGTTATTGCTCAGCGG-3

3.2.5 Heterologous Protein Expression

As mentioned in Chapter 3.2.2 it is necessary to consider the combination of host system and vector when planning a heterologous protein expression because some proteins are toxic to the bacterial cells when expressed in higher concentrations. Therefore, the aim is to reduce basal expression to a minimum which was achieved by employment of *E. coli* strains containing the lysogen λDE3. This gen originates from bacteriophage T7 and encodes the T7-RNA polymerase which solely is capable of binding to the T7-promoter sequence of the vectors used, thus, transcribing the gen of the target proteins. Though, the expression of the T7 enzyme is initially inhibited by binding of the lac1-repressor to the lac-operon during growing period of the host system. Furthermore, the repressor binds to the lac-operon of the vector sequence hindering a transcription of the target protein's DNA. This fact ensures no expression of target protein even in the presence of slight amounts of basal T7-RNA polymerase.

With the addition of isopropyl-β-D-thiogalactopyranoside (IPTG), which is a molecular mimic of the lactose metabolite allolactose and binds to the lac1-repressor, interaction of the later with the lac-operon is cleaved and expression of the T7-RNA polymerase is induced. Additionally,

the expression of the target protein starts because of the accessibility of T7-promoter for the RNA polymerase.

Experimental procedure

At the beginning of every protein expression a fresh transformation (cf. Chapter 3.2.2) of the vector (cf. Table 3.1) in the appropriate *E. coli* strain as stated in Table 3.2 was performed. In the process the specific antibiotic (cf. see Table 3.5) was added to the LB-agar solution prior to plate preparation to guarantee selective cell growth.

Table 3.5: Proteins with their corresponding antibiotic for selective growth including final concentrations.

Protein	N-ERMAD	His-*cyt*NL2	CB isoforms
$c_{Antibiotic}$ per mL LB medium	60 µg kanamycin 34 µg chloramphenicol	50 µg kanamycin	100 µg ampicillin

A single culture from the LB agar plate was picked and used for inoculation of 50 mL LB medium (incl. the appropriate antibiotics, cf. Table 3.5) at 37 °C and 185 rpm overnight. From this overnight culture a glycerol-stock was taken consisting of a 1:1 mixture of culture and glycerol (95 %). This stock was frozen in liquid N_2 and stored as backup at –80 °C.

For the main culture the overnight culture was diluted with antibiotic containing LB medium in a ratio of 1:50 to result in total volume of 250 mL. In doing so, it had to be considered that for N-ERMAD expression only kanamycin was added to the main culture. After inoculation the main culture was placed in an Innova® 44 orbital shaker (*New Brunswick Scientific*, Enfield, USA) at 37 °C and 185 rpm and growth of the *E. coli* cells was controlled via OD_{600} measurements. While for His-*cyt*NL2 and all CB2 isoforms cultivation took place until an OD_{600} of 0.8 to 1.0 was reached, growth of cells transformed with pET28a+ (N-ERMAD) was already stopped at an OD_{600} of 0.5 to 0.6. The cultivation of cells was brought to a standstill via addition of IPTG (1 mM for N-ERMAD and 0.5 mM for His-*cyt*NL2 and all CB2 isoforms) which induced the heterologous expression of the target proteins. For sufficient expression of the target proteins different conditions that are described in Table 3.6 were required.

Table 3.6: Working conditions for expression of the target proteins

Protein	N-ERMAD	His-*cyt*NL2	CB isoforms
Time (*t*) / h	4	≥15	≥15
Temperature (*T*) / °C	37	4	4
Panning / rpm	175	200	185

After expression, the main culture was place on ice for 10 min to stop the expression machinery, then was poured in sterile centrifuge tubes and the cells were harvested via centrifugation at 4 °C and 4000 rpm for 20 min. The obtain cell pellets were either directly used for cell lysis as described in the following Chapter or stored at -20 °C until use.

3.2.6 Cell Lysis

The protein expression is performed within the cells, therefore it is necessary to overcome the plasma membrane which functions as a barrier. There are different approaches to break down the membrane which can be allocated to two subclasses, the mechanical and non-mechanical lysis techniques. Ultrasonic treatment and the use of high-pressure homogenisers among other belong to the first class. While the cells bump against each other and open during exposition to ultrasonic, the lysis in a high-pressure homogeniser relies upon strong shear forces by pumping the cell suspension under high pressure (up to 1.5 kbar) through capillary tubes of defined geometry. In contrast to that non-mechanical lysis methods are based on destabilisation of the cellular membrane by the utilisation of lysis agents like lysozymes and ethylenediaminetetraacetic acid (EDTA).

Experimental procedure

The freshly harvested pellet or one stored at -20 °C was resuspended in lysis buffer (with specific compositions for the target proteins, cf. Table 3.7) and 80 mg of DNaseI (in DNaseI buffer, cf. Table 3.7) added in case of all collybistin isoforms. For those and the resuspensions of His-*cyt*NL2 containing cells a high homogeneity of the suspensions without any bigger pellet residues was achieved by stirring for 1 h at 4 °C. These suspensions were afterwards lysed under high pressure in a homogeniser LM10 processor (Microfluidics, Westwood, USA). For lysis the suspensions were treated in three consecutive cycles at either 1 kbar or 1.5 kbar for collybistin

or His-*cyt*NL2, respectively. In contrast to that cells containing N-ERMAD were lysed via five cycles of 30 s tip sonification pulses (Sonopuls, *Bandelin electronic GmbH&Co. KG*, Berlin; 60 % power) followed by 15 s resting phases on ice. All lysates then were clarified by centrifugation (100,000 × g, 45 min to 1 h, 4 °C) and afterwards applied to French press columns containing specific resins to which each target protein expressed high affinity enabling the purification of the target proteins. This process is described in detail in the following section.

Table 3.7: Compositions of the lysis buffers used during lysis of cell suspension.

Lysis buffer	300 mM NaCl	**Lysis buffer**	500 mM NaCl
N-ERMAD	40 mM HEPES	His-*cyt*NL2	100 mM HEPES
pH 7.4	20 mM imidazole	pH 8.0	10 %(*w*/*v*) glycerol
	1 mM EDTA		*5 mM β-mercaptoethanol
	*10 mM β-mercaptoethanol		*6 mM benzamidine
	*Roche® cOmplete		*2 mM PMSF
			*Roche® cOmplete
Lysis buffer	250 mM NaCl	**DNaseI buffer**	20 mM TRIS
CB2	20 mM TRIS	CB2	50 %(*w*/*v*) glycerol
pH 8.0	10 %(*w*/*v*) glycerol	pH 7.5	1 mM $MgCl_2$
	2 mM EDTA		

* addition of reagents directly prior to use

3.2.7 Protein Purification

The aim of protein purification processes is to obtain solely the target protein in solution to ensure experimentation on it without distortions by any contaminations. There is a great variety of fractioning techniques available that exploit the physical and chemical characteristics (charge, polarity, size, and specific affinity) of the desired protein to stepwise separate it from other substances like basal proteins present in the cell lysate. These separation methods are referred to as chromatography and are classified by the type of interaction with the protein and the employed stationary phase.

3.2.7.1 Affinity Chromatography

This type of chromatography employs the capability of some protein parts to bind non-covalently, yet specifically to ligand molecules that are coupled to a chromatography matrix in a reversible fashion. After adequate washing steps to erase contaminations that are not strongly attached to the chromatography column, the target protein can be eluted from the stationary phase by changing the buffer conditions e.g. via pH variation or addition of a competitive reagent.

In the cases of N-ERMAD and His-*cyt*NL2 a special variant of affinity chromatography, the immobilized metal ion affinity chromatography (IMAC) was applied for purification as both proteins exhibit an *N*-terminal fused hexa-histidine tag (His_6 tag). This fusion tag is able to interact with divalent cations, especially Ni^{2+}, and thereby can bind to a ligand in which this cation is chelated by NTA. These interaction partners build up a complex with an octahedral structure in which to binding sites are either occupied by water molecules or histidine residues of the fusion tag as shown in Figure 3.1. The association of the His is achieved via its free electron pair and can be disrupted by introducing imidazole to the system which expresses a high affinity to Ni^{2+}. The isolation of the His_6-tagged proteins is conducted with NTA(Ni^{2+})-coupled agarose (Protino®, *Macherey-Nagel*, Düren, Germany) with a capacity of around 50 mg/mL.

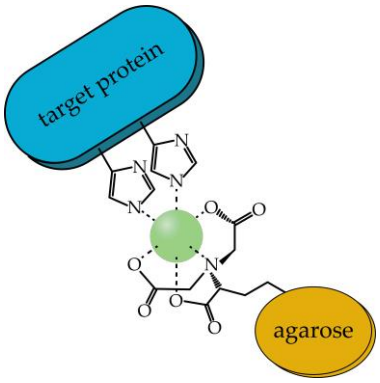

Figure 3.1: Schematic illustration of the interaction between the target protein containing a His_6-tag and the NTA(Ni^{2+}) functional group of an agarose matrix utilised in IMAC.

It has already been mentioned that the genes encoding the target proteins of this work were cloned into vector DNA which was well suited to the expression systems. In case of the collybistin isoforms the used vectors also encoded an Intein tag which was fused either *N*- or *C*-terminally for the pTXB1 or pTYB21 vector, respectively. This tag consists of a so-called Chitin binding domain (CBD) and can be used to adsorb the protein to a chitin resin (*New England BioLabs Inc.*, Ipswich, USA). The resin used for all collybistin isolations exhibited a capacity of 2 mg/mL. After adsorption as illustrated in Figure 3.2 an intramolecular *N,S*-acyl shift in the linker region between target protein and Intein tag takes place.[121] This facilitates thiolysis of the target protein from the tag when a thiol is introduced to the system. While the Intein tag

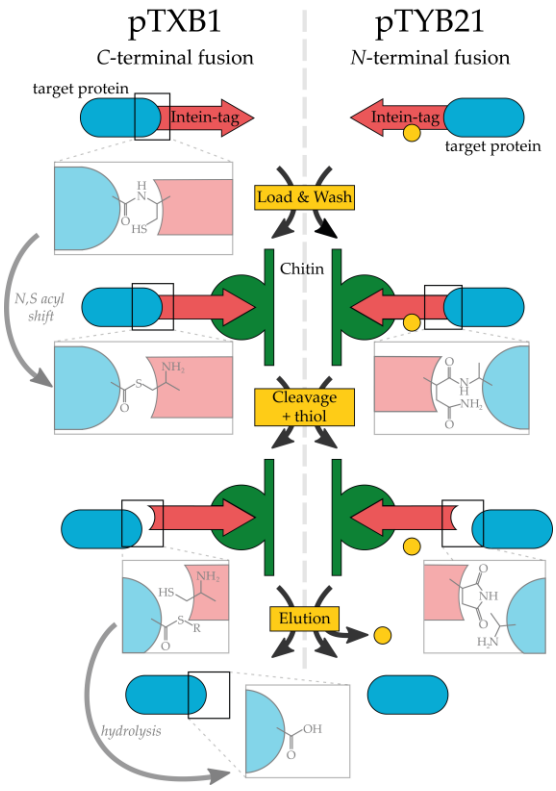

Figure 3.2: Schematic illustration of the protein purification via a CBD carrying Intein-tag that is either *C*- or *N*-terminal fused to the target protein.

remains at the chitin matrix, the protein carries a thioester moiety which is directly hydrolysed to a carboxylic acid under aqueous conditions. Subsequently, the desired collybistin can be eluted.[122]

Experimental procedure

For the isolation of the target proteins from the lysates, each French press column was loaded with the specific resin. Thereby, the column volume (CV) depended on the capacity of the matrix material, its capacity and of course on the scheduled quantity. The resin was washed with lysis- (cf. Table 3.7) or equilibration buffer (10 CV, cf. Table 3.8) prior to loading with the clarified lysate (cf. Chapter 3.2.6). The matrix-lysate suspension was then incubated under constant swivelling for 1 h at 4 °C. Subsequent, the column was placed in a vertical position and after the descent of the matrix particles the supernatant liquid (flow through, FT) was collected for posterior analysis. This was followed by a varying quantity of washing steps with wash buffers (15-20 CV) of specific compositions (cf. Table 3.8) which all were collected as washing fractions (WF). While CB2 isoforms were not eluted before the chitin resin was incubated in the second washing buffer (50 mM dithiothreitol, DTT) for on-column cleavage for at least 24 h at 4 °C the elution of both N-ERMAD and His-*cyt*NL2 was conducted immediately after the washing steps. For protein elution buffers (10-15 CV) with compositions stated in detail in Table 3.8 were used. The eluted protein was finally collected in fractions (elution fractions, E) of either 1.5 mL or 10 mL volumes for N-ERMAD or His-*cyt*NL2 and CB2, respectively. Storage of the proteins in elution buffer at 4 °C was possible for a duration of ca. three month. The success of this purification step was controlled by SDS-PAGE which is described in detail in Chapter 3.2.8. Though, the conditions of the elution buffers were incompatible with the prerequisites of further experimentation. Therefore, a change of the buffer system prior to adsorption studies was

necessary in all cases. This was achieved either via dialysis or spin concentration as described in Chapter 3.2.10.

Table 3.8: Overview of buffers and their compositions applied in affinity chromatography.

Equilibration buffer	300 mM NaCl 40 mM HEPES	**Elution buffer**	250 mM Imidazol
N-ERMAD	20 mM imidazole	N-ERMAD	50 mM KCl
pH 7.4		pH 7.4	20 mM Tris
Wash buffer I	300 mM NaCl	**Wash buffer II**	300 mM NaCl
N-ERMAD	40 mM HEPES	N-ERMAD	40 mM HEPES
pH 7.4	30 mM imidazole	pH 7.4	40 mM imidazole
	1 mM $MgCl_2$		1 mM $MgCl_2$
	*10 mM β-mercaptoethanol		*10 mM β-mercaptoethanol
Wash buffer	500 mM NaCl	**Elution buffer**	250 mM NaCl
His-*cyt*NL2	100 mM HEPES	His-*cyt*NL2	250 mM imidazole
pH 8.0	10 %(*w*/*v*) glycerol	pH 8.0	50 mM HEPES
	*5 mM β-mercaptoethanol		*5 mM β-mercaptoethanol
Wash buffer I	1 M NaCl	**Wash buffer II**	250 mM NaCl
CB2	20 mM HEPES	CB2	*50 mM DTT
pH 8.0	2 mM EDTA	pH 8.0	20 mM HEPES
			2 mM EDTA
Elution buffer	250 mM NaCl		
CB2	*5 mM DTT		
pH 8.0	20 mM HEPES		
	2 mM EDTA		

* addition of reagents immediately before use

3.2.7.2 Anion exchange chromatography

The ion exchange chromatography (IEC) is divided into two classes either anion- or cation-exchange chromatography based on the stationary phase utilised for immobilisation of charged molecules. While cation-exchange columns bind positively charge particles, the anion-exchange is used for immobilisation of negatively charged ions. The binding capability of proteins depends on their net charge which in turn is influenced by the pH. Furthermore, the presence of other ions has an impact on the proteins' binding affinities as they compete for binding sites of the ion exchanger. Therefore, the choice for the suitable stationary phase depends on the isoelectric point (pI, is the pH at which a molecule exhibits no net charge) of the target protein. As the amino acids that make up proteins are zwitterionic containing both positively and negatively charged residues each protein has a specific pI. In general, a good estimation is to use buffer conditions with pH values either at least 1 higher than the pI of the target protein or 1 lower than the specific pI when working with anion- or cation-exchangers, respectively.

After the affinity chromatography of His-*cyt*NL2, contaminations were still detected via SDS-PAGE. Therefore, a subsequent anion-exchange chromatography was performed, although His-*cyt*NL2 exhibits a relative neutral pI of 7.31. For this purpose, a Mono Q 5/50 GL column (*GE Healthcare*, Uppsala, Sweden) was used in combination with a ÄKTA purifier 10 system (*GE Healthcare*, Uppsala, Sweden). The stationary phase of the column consists of mono-disperse, porous beads out of styrene-divinylbenzene copolymer carrying quaternary ammonium ligands. The elution of the protein was achieved by a gradual increase of ion strength (c_{NaCl}) within the mobile phase.

Experimental procedure

All solutions (cf. Table 3.9) were filtrated and degassed before being applied to the ÄKTA system. The column was rinsed with buffer A (5 CV), buffer B (5 CV) and again buffer A (5 CV) to guarantee the absence of potential contaminations caused by previous use. Afterwards the column was rinsed with a buffer mixture of A : B (97.5 : 2.5) matching the ionic strength of the His-*cyt*NL2 solution which was first dialysed to pre-ÄKTA buffer (cf. Table 3.9), then diluted in a 1:1 ratio with ultrapure water and after that applied to the column at a flow velocity of 2 mL/min. While the protein solution was loaded to the anion-exchanger the flow through was

collected to ensure no protein loss. The column was washed with aforementioned buffer ratio (2 CV) to get rid of weakly bound molecules. The purification of the protein was then conducted via a linear gradient of buffer B (starting from 50 mM to 2 M NaCl) over a duration of 25 CV with a flow velocity of 3 mL/min. The process of elution was controlled by UV/VIS adsorption (λ = 280 nm) and conductivity detection. During elution fractions of 1 mL volume were collected by a sampler. Fractions that showed activity in the UV/VIS spectrum together with those collected during the loading and washing process were subsequently analysed by SDS-PAGE as described in the following paragraph.

Table 3.9: Buffers applied during anion-exchange chromatography of His-*cyt*NL2

Buffer A	20 mM HEPES	**Buffer B**	2 M NaCl
His-*cyt*NL2	1 mM EDTA	His-*cyt*NL2	25 mM HEPES
pH 8.0	5 mM β-mercaptoethanol	pH 8.0	1 mM EDTA
			5 mM β-mercaptoethanol
pre-ÄKTA	50 mM NaCl		
buffer	25 mM HEPES		
His-*cyt*NL2	1 mM EDTA		
pH 8.0			

3.2.8 Sodium Dodecyl Sulfate-Polyacrylamide Gel Electrophoresis

The success of an isolation was determined by sodium dodecyl sulfate-polyacrylamide gel electrophoresis (SDS-PAGE) which relies upon the movement of charged particles within an electric field and is well suited for molecular weight determination. The detergent sodium dodecyl sulfate (SDS) interacts with the non-polar parts of proteins via its hydrophobic residues, not only supporting the denaturing process but also inducing a linearization and introducing an anionic surplus charge to the proteins. By the latter effect SDS covers the intrinsic charge of the proteins and enables the separation based only on their mass as it guarantees a constant mass-to-charge ratio.[123] Yet, SDS alone is not sufficient for complete denaturing of the proteins, therefore, all protein samples were diluted with sample buffer containing dithiothreitol (DTT) which is a reducing agent and dissolves intramolecular disulfide bridges within proteins.

The separation during electrophoresis is carried out in porous polyacrylamide gels that consist of a stacking and a resolving gel. This differentiation is the reason why this method is also referred to as a discontinuous PAGE. The pore size differs between stacking and resolving gel due to varying ratios of acrylamide monomers (AA) to cross-linking N,N′-methylenebisacrylamide (Bis-AA) and has next to the constant mass-to-charge ratio the biggest influence on protein separation. The separation itself occurs in the close meshed resolving gel while a band focussing takes place in the stacking gel that also has a lower pH and contains chloride ions. These move with high velocity within the electric field due to their pH-independent anionic character in contrast to the glycine-ions that are present in the running buffer and express a zwitterionic character at low pH values. Zwitterionic particles are effectively uncharged. This discrepancy in velocity generates an electric field gradient inside the stacking gel causing the aforementioned focussing of protein bands owing to their electrophoretic mobility. When the glycine-ions are transferred from the stacking to the resolving gel they lose their zwitterionic character because of deprotonation and pass the protein bands whose velocities are reduced due to the smaller pore size in the resolving gel. These processes result in a high separation with sharp signals for the individual protein bands. In addition to the protein sample a mass standard (PageRuler Plus Prestained Protein Ladder, *Thermo Fisher Scientific*, Waltham, USA) has to be present in the gel to allow molecular weight estimations of the resulting protein bands. These fundamentals of the SDS-PAGE were first presented by U. K. LAEMMLI in 1970, however, a slightly changed method was utilised in this work.[123] By following the modifications of SCHÄGGER and VON JAGOW who used tricine instead of glycine resulting in a reduced electrophoretic mobility and thereby caused an increased separation for proteins with masses varying in the range of 1 to 100 kDa better results for the proteins in focus of this work were expected.[124,125]

Experimental procedure

The polyacrylamide gels were prepared under the use of the vertical gel electrophoresis kit Mini-PROTEAN® Tetra Cell (*Bio-Rad Laboratories Inc.*, Hercules, USA). The glass panels making up the preparation chambers were cleaned with ultrapure H_2O and ethanol p.a. and afterwards mounted in the gear. Initially the resolving gel solution (10 %, cf. Table 3.10) was injected into the chamber and covered during polymerisation with isopropyl alcohol for 1 h. The

polymerisation of the gels is initialised by ammonium peroxydisulfate (APS, 10 %(*w*/*v*)) and is catalysed by *N,N,N´,N´*-tetramethyl ethylenediamine (TEMED). After removal of the alcohol the stacking gel (4 %, cf. Table 3.10) was added and a comb was inserted that functioned as space holder for sample pockets. The polymerisation reaction was finished after 1 h. The polyacrylamide gel was then mounted into the electrophoresis chamber and the comb removed. Adjacent the inside of the chamber was filled with cathode buffer (cf. Table 3.10) while anode buffer (cf. Table 3.10) was poured into the outer compartment.

Table 3.10: Composition of stacking and resolving gel following the protocol of SCHÄGGER and VON JAGOW

Stacking gel	570 µL ultrapure H_2O	**Resolving gel**	1.23 mL ultrapure H_2O
4 %	1.06 mL glycerol (50 %(*v*/*v*))	10 %	500 µL gel buffer (pH 8.45)
	1.68 mL gel buffer (pH 8.45)		267 µL AA-mix*
	*1.66 mL AA-mix		13.4 µL APS (10 %(*w*/*v*))
	25 µL APS (10 %(*w*/*v*))		2.65 µL TEMED
	3 µL TEMED		

* AA-mix contains AA and Bis-AA in the ratio of 37.5:1

The protein samples (10 µL) that needed testing were merged with sample buffer (10 µL) and scalded to 85 °C for 5 min at 350 rpm. After complete denaturation the merges were pipetted into the sample pockets of the gel. The electrophoresis chamber was then connected to a power source applying a constant voltage of 210 V for ca. 90 min. Progress control of the electrophoresis was possible because of the bromophenol blue dye (0.02 %(*v*/*v*)) inside the sample buffer highlighting the migration. The gel was washed with ultrapure water, heated up in a microwave (800 W, 45 s) after electrophoresis and subsequently dyed with staining solution (cf. Table 3.11) that contains Coomassie brilliant blue capable of binding to alkaline amino acid residues. After washing with ultrapure water, the gel was incubated in destaining solution (cf. Table 3.11) overnight.

Table 3.11: Composition of the relevant buffers and solutions for SDS-PAGE.

Sample buffer (2 x) pH 6.8	175 mM Tris/HCl 100 mM DTT 15 %(*w*/*v*) SDS 2 %(*w*/*v*) SDS 0.02 %(*w*/*v*) bromophenol blue	**Gel buffer** pH 8.45	3 M Tris 0.3 %(*w*/*v*) SDS
Cathode buffer pH 8.25	100 mM Tris 100 mM tricine 0.1 %(*w*/*v*) SDS	**Anode buffer** pH 8.9	200 mM Tris
Staining solution	0.05 %(*w*/*v*) Coomassie brilliant blue G250 45 %(*v*/*v*) methanol 45 %(*v*/*v*) acetic acid	**Destaining solution**	5 %(*v*/*v*) ethanol 7.5 %(*v*/*v*) acetic acid

Afterwards the gels were rinsed with ultrapure water, either photographs of the discoloured gels were taken with a Nikon D600 (*Nikon Corporation*, Minato, Japan) or they were imaged with an Azure c300 gel imaging system (*Azure Biosystems, Inc*., Dublin, USA).

3.2.9 Western Blot

The Western blot (WB) is an additional and continuative method for the analysis of isolated proteins based on immune staining. For this type of immune blotting a previous electrophoresis is inevitable to separate the protein sample based on their molecular weight as described in detail in Chapter 3.2.8. The separated protein bands are then transferred or blotted to a nitrocellulose membrane via electrophoresis in orthogonal direction of the prior step. The blot can be controlled by staining with the azo-dye Ponceau S that reversibly and unspecifically binds to proteins and therefore enables the detection of the weight standard. The visualisation for protein identification is conducted via a two-step labelling process with selective antibodies. In this work the used antibodies varied depending on the protein that was analysed:

Table 3.12: Antibodies employed during Western blot for detection of the different proteins.

Protein	1st antibody antigen	Epitope	2nd antibody antigen	Epitope
His-*cyt*NL2	Polyclonal rabbit purified antibody	Amino acids 826 to 843 of mouse neuroligin1	Goat Anti-Rabbit IgG H&L (HRP)	Rabbit IgG, whole molecule
$CB2_{PH}$	Monoclonal mouse purified IgG	Amino acids 44 to 229 of rat colly-bistin	HRP Goat Anti-Mouse Ig	Not available
$CB2_{SH3}$				
$CB2_{SH3/W24A-E262A}$				
N-ERMAD/ His-*cyt*NL2	Monoclonal mouse purified IgG2b	Hexa-histidine sequences	Goat Anti-Mouse IgG H&L (HRP)	Not available

The second antibodies that were added after non bound primary antibodies have been removed did not only bind selectively to the later but also carried a horse radish peroxidase (HRP). The enzyme catalyses in presence of H_2O_2 the oxidation of luminol whereupon an excited 3-aminophtalat-dianion is form. The electron transition in this molecule from the excited into the ground state causes emission of light with a wavelength of 428 nm that can be detected.

Experimental procedure

The protein samples were first separated by SDS-PAGE. In contrast to the process described in Chapter 3.2.8 no staining after electrophoresis took place since the gel was used for the second orthogonal electrophoresis. Simultaneous to the SDS-PAGE two Whatman-paper and a nitrocellulose membrane (*Bio-Rad Laboratories Inc.*, Hercules, USA) were cut to the size of the gel and incubated for 30 min in blotting buffer (for composition cf. Table 3.13). Afterwards the platin electrode of the blotting gear Trans-Blot® (*Bio-Rad Laboratories Inc.*, Hercules, USA) was moistened with blotting buffer and the first soaked Whatman-paper was placed upon the electrode. In this work the semidry method introduced by KYHSE-ANDERSEN was applied.[126] On top of the Whatman-paper the nitrocellulose membrane was placed followed by the gel and

the second Whatman-paper. During the stacking process the enclosure of air was avoided. The blotting gear was closed with a stainless-steel electrode above the pile (compare Figure 3.3). By appling 180 mA for 45 min the blot was conducted.

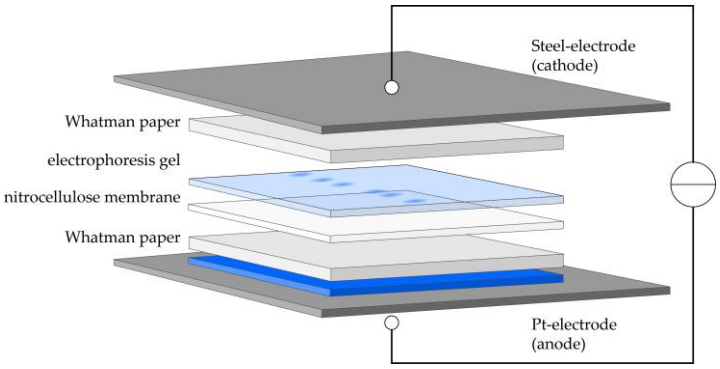

Figure 3.3: Schematic illustration of the layer order in the stack during a semidry Western blot.

The success of the blot was controlled after a 3 min incubation of the nitrocellulose membrane in Ponceau S solution (cf. Table 3.13). Subsequently the membrane was washed with ultrapure H_2O and then incubated in a suspension of low-fat dry milk (5 %(*w*/*v*)) in TBST buffer (tris buffer saline Tween-20, cf. Table 3.13) for 1 h at room temperature. The proteins within the milk suspension block vacant binding sites on the nitrocellulose membrane which otherwise would have been used by the first antibody leading to no specific detection. Afterwards the interaction of the primary antibody with the proteins takes place during incubation of the membrane with a solution of the antibody in a suspension of low-fat dry milk (5 %(*w*/*v*)) in TBST buffer overnight at 4 °C under constant fluctuation. The concentration of the antibody varied in the range of 0.8 to 1.0 µg/mL. Rinsing the membrane three times with TBST buffer (50 mL for 10 min) removed the excess of antibody and was followed by incubation with the second antibody for 1 h at 4 °C with gentle agitation, again solved in a 5 %(*w*/*v*) dry milk suspension in TBST buffer (1:2500 (*w*/*w*)). Unbound secondary antibody was removed by rinsing with TBST buffer (50 mL for 20 min) followed by incubation of the membrane for 2 min in a 1:1 mixture of enhanced chemiluminescence (ECL) solution 1 and 2 (for composition cf. Table 3.13). This initiated the oxidation of luminol and the resulting chemiluminescence was detected with imaging system Azure 300 (*azure biosystems*, Dublin, USA). Additionally, a marker image (comparable to a normal image of the nitrocellulose membrane) was taken to enable a correlation or overlay of luminescence and marker image and by that simplifying the estimation of molecular weights.

Table 3.13: Compositions of buffers and solutions used during Western blot.

Blotting buffer pH 7.4	20 mM Tris 150 mM glycine 0.05 %(*w*/*v*) SDS 20 %(*v*/*v*) methanol	**TBST buffer** pH 7.4	10 mM Tris 150 mM NaCl 0.2 %(*w*/*v*) Tween 20
ECL 1	100 mM Tris 2.5 mM luminol 0.4 mM *p*-coumaric acid	**ECL 2**	100 mM Tris 0.02 %(*w*/*v*) H_2O_2
Ponceau S solution	0.2 %(*w*/*v*) Ponceau S 3 %(*w*/*v*) acetic acid		

3.2.10 Buffer System Transfer

Since most proteins exhibit an intrinsically order structure dictated by their amino acid sequence and its capability to form intramolecular hydrogen bonds. To maintain these secondary structures a stabilization via appropriate buffer conditions is necessary. Furthermore, some buffers can contain reagents which are inevitable for their application areas, yet, these might perturb further experimentation as is the case for imidazole. Imidazole is used to systematically elute target proteins from an NTA(Ni^{2+})-matrix during IMAC (cf. Chapter 3.2.7.1) but its presence would impede adsorption experiments that rely on the interaction of His_6-tagged proteins to e.g. lipids like DGS (cf. Scheme 3.3).

The change from one buffer system to another can be achieved in different ways which will be described in the next sections.

3.2.10.1 Dialysis

Dialysis is used to exchange low molecular substances across a semipermeable membrane with a defined molecular weight cut-off (MWCO). By this transfer, which is based upon osmotic pressure, generated through concentration gradients of two solutions, the composition of a protein-containing solution can be change to desired conditions.

The elution fractions of the target protein (cf. Chapter 3.2.7) were combined in ZelluTrans® dialysis-tubes (MWCO = 14 kDa, *Carl Roth GmbH+Co. KG*, Karlsruhe, Germany) and dialyzed at 4 °C and constant stirring against a 50-fold excess of E1- or HEPES A-buffer (cf. Table 3.14)

for N-ERMAD or His-*cyt*NL2, respectively. The buffer was exchanged at least two times while the 24 h duration. Afterwards the protein solution was collected, its concentration determined and stored at 4 °C until use.

3.2.10.2 Spin Concentration

For the CB2 isoforms the protein stability was a critical factor as the protein exhibits a good lifetime in the elution buffer, but this buffer was not compatible with surface sensitive methods like reflectometric interference spectroscopy. Therefore, an empirical study was performed to identify buffer compositions combining a compatibility to the utilised techniques with a sufficient lifetime of CB2. This search resulted in the HEPES- and its DTT-free modification HEPES-A buffer (cf. Table 3.14). Dependent on the experimental setup both buffers were also used as EDTA-free versions. To reduce the duration of buffer exchange in case of CB2 an alternative to dialysis was used that obtains buffer exchange and an increase in protein concentration via centrifugation.

A volume of 500 µL elution fractions of CB2 was injected in Vivaspin® 500 centrifugal concentrator (MWCO = 5 kDa, *Sartorius GmbH*, Göttingen, Germany) and centrifuged for 10 min at 4 °C and 17,000 x g (Heraeus Fresco 17, *Thermo Scientific*, Darmstadt, Germany). Afterwards the flow-through was discharged, the volume within the concentrator adjusted to 500µL with the desired buffer and again centrifuged at similar conditions. This process was repeated a second time to ensure a complete buffer exchange. The protein solution was collected, and its concentrations determined by UV/VIS measurements as describe in the following chapter.

Table 3.14: Buffers and their compositions which were used during adsorption experiments.

E1-buffer	50 mM KCl	**HEPES buffer**	100 mM NaCl
N-ERMAD	20 mM Tris/HCl	CB2	25 mM HEPES
pH 7.4	0.1 mM EDTA	pH 8.0	5 mM DTT
	0.1 mM NaN_3		*0.5 mM EDTA

HEPES-A	100 mM NaCl
buffer	25 mM HEPES
His-*cyt*NL2/	*0.5 mM EDTA
CB2	
pH 8.0	

*when working with DGS containing membranes EDTA was left out

3.2.11 Determination of Protein Concentration

It is necessary for the planning, the reproducibility, and the analysis of experiments to exactly know the concentration of protein within the experimental setup. This can only be guaranteed by knowing the amount of protein inside its stock solution. There are different ways to determine such concentration, in this work either the method based on light absorption of aromatic amino acids or the one developed by M. BRADFORD were applied.

3.2.11.1 Concentration Determination via UV/VIS Spectroscopy

The determination of protein concentrations within a solution via UV/VIS spectroscopy relies upon the fact that aromatic amino acids like trypsin, tryptophan and phenylalanine absorbed light at a wavelength of 280 nm. Considering the law of LAMBERT and BEER (Equation 3.2) that describes the correlation of intensities before (I_0) and after (I_0) passing through an absorbing medium as the decadic logarithm of their proportion, concentration calculations for the absorbing species inside the medium is possible with Equation 3.3.

$$I = I_0 \cdot e^{-\varepsilon \cdot c \cdot d} \quad \textbf{3.1}$$

$$A = \log \frac{I_0}{I} = \varepsilon \cdot c \cdot d \quad \textbf{3.2}$$

$$c = \frac{A_{280}}{\varepsilon \cdot d} \qquad \textbf{3.3}$$

Yet, to calculate the exact concentrations one has to know the specific extinction coefficients ε_{280} for the proteins under investigation. These characteristic values were computed with the PROTPARAM tool based on the amino acid sequence (cf. Appendix A.4) for each protein and are in Table 3.15. The absorption at a wavelength of 280 nm (A_{280}) was detected in a photometric measurement in which the optical path length (d) was dictated to be 1 mm by the utilised instrument in this work.

Table 3.15: Extinction coefficients of all proteins investigated calculated with the PROTPARAM tool.

Protein	N-ERMAD	$CB2_{SH3}$	$CB2_{SH3/W24A-E262A}$	$CB2_{PH}$	His-*cyt*NL2
ε [$M^{-1} \cdot cm^{-1}$]	52,400	98,945	93,445	37,930	6,000

3.2.11.2 Concentration Determination via Bradford-Test

The technique described in the preceding Chapter is a fast and easy way to determine concentrations of proteins solution. However, some small proteins or protein fragments do not contain any aromatic amino acids, hence a concentration calculation based on the absorbance at 280 nm results in imprecise values. This is the case for the protein construct mimicking the intracellular domain of neuroligin 2, therefore an alternative technique was applied first introduced by MARION M. BRADFORD.[127] It uses Coomassie Brilliant Blue G-250 dye that is able to bind to proteins via electrostatic interactions of its sulfonic acid residues together with VAN DER WAALS and hydrophobic interactions and thereby switches from its cationic to its anionic form. This change in charge results in an adsorption maximum shift from 465 nm for the cationic form to 595 nm for the anionic one. Therefore, the amount of protein-dye complexes directly correlates with the absorbance at the latter wavelength.

For concentration calculation a calibration curve was required that was generated with bovine serum albumin (BSA) in a concentration range from 0.1 to 0.8 mg/mL. The photometric measurements were conducted in disposable cuvettes as the dye interacts with regular quartz cuvettes using a Cary 50 UV/VIS spectrometer (*Agilent Technologies*, Santa Clara, USA).

3.3 Preparative Methods

The investigation of protein adsorption processes and their interactions with either lipids or other proteins is dependent on multiple factors. To characterise these a differentiation among

them is a prerequisite. Yet, such distinction is not possible *in vivo* because of the features already mentioned in the introductory section (cf. Chapter 1.4). Therefore, a common tool to study adsorption processes to e.g. receptor lipid molecules are solid-supported membrane systems. In this work two different types of supported model membrane were applied. On the one hand solid-supported lipid bilayers (SLBs) were prepared on hydrophilic silicon dioxide substrates while on the other hand supported lipid monolayers or hybrid membranes (SHMs) formed on hydrophobically functionalised SiO_2 substrates. Different functionalisation strategies were tested to obtain optimal conditions for SHM-formation. Both model membrane types formed by spreading of small unilamellar vesicles (SUVs), hence their preparation process will be described in the following part.

3.3.1 Preparation of Small Unilamellar Vesicles

Lipid molecules cluster in an aqueous environment due to their amphiphilic character and can arrange in aggregates of different shape.[128] If the lipid concentration is beyond a critical point (critical micelle concentration, CMC) lipid bilayer formation is feasible in the form of lipid vesicles. These vesicles appear in a widely ranging size that depends, inter alia, on the solution's composition and the preparation method.[129–131] The smallest representatives of this aggregate type are the SUVs that exhibit diameters of up to 100 nm and a high membrane curvature. They can be formed by sonification of rehydrated lipid films and are often utilised to prepare supported lipid membranes. The application of lipid films as starting material for vesicle formation facilitates well defined compositions and known ratios of matrix to receptor lipids. Furthermore, not only the amount of lipid material can be adjusted to match the requirements, but also additional components can be enclosed. In this work lipid films with material quantities ranging from 0.2 to 0.8 mg were prepared with a wide selection of desired lipid mixtures.

Experimental procedure

Starting from stock solutions of the desired lipids with concentration ranging from 1.0 to 15.0 mg/mL the particular volumes were added to a test tube filled with 100 µL chloroform in requested molar ratios. Furthermore, a small amount of methanol (10-15 µL) was added to

increase the mixture's polarity, thus preventing lipid precipitation. The solvents were removed under a steady N_2 stream in a water bath at temperatures above T_M of the employed matrix lipid (cf. Chapter 3.1.1.1). Afterwards the lipid films were dried in vacuum ($T > T_M$) for at least 3 h to guarantee complete solvent removal and then stored at 4 °C until use.

On purpose of vesicle preparation, the lipid films were rehydrated with 200-800 µL low pH buffers (Na-citrate buffer, cf. Table 3.16) while taking particular care that EDTA-free buffer was applied when working with DGS containing films. Afterwards the films were incubated for 30 min at $T > T_M$ and subsequently multilamellar vesicles (MLVs) were obtained by vortexing 3 x 30 s at 5 min intervals. The MLV suspensions were transferred into Eppendorf cups and sonicated for 30 min at $T > T_M$ using a SONOPULS HD2070 ultrasonic homogeniser (*Bandelin electronic GmbH & Co. KG*, Berlin, Germany) to obtain SUVs. The SUV suspensions were used the same day for supported lipid membrane formation on either hydrophilic or hydrophobic SiO_2 substrates. The procedures of substrate treatment prior to incubation with SUVs will be focussed in the following section.

Table 3.16: Composition of Na-citrate buffer used for rehydration of lipid films and vesicle spreading.

Na-citrate	50 mM KCl
buffer	20 mM Na citrate
pH 4.8	*0.1 mM EDTA
	0.1 mM NaN_3

*when working with DGS containing lipid films EDTA was left out

3.3.2 Preparation of Hydrophilic Silicon Substrates

Lipid bilayers were prepared on silicon substrates, that exhibited a SiO_2 layer on their surfaces, because of the relatively low roughness. This layer had a thickness of either 100 nm or 5 µm dependent on the measuring technique subsequently applied. Due to uniform measurement chamber dimensions all substrates were cut into rectangle pieces (1.95 cm x 0.7 cm). They were rinsed with ethanol p.a. and ultrapure water prior to incubation in an ammoniacal solution (H_2O : NH_3 : H_2O_2, 5:1:1 (*v*/*v*/*v*)) at 70 °C for 20 min. After this treatment, the substrate's surface was clean and rendered hydrophilic. A storage until utilisation was possible in ultrapure water. Immediately before the experimental start the substrates were dried in N_2 stream and

treated with O_2 plasma in a Zepto LF PC (*Diener electronic GmbH & Co. KG*, Ebhausen, Germany) at 60 % power for 30 s.

3.3.3 Preparation of Hydrophobic Silicon Substrates

In contrast to the simple preliminary cleaning steps prior to SLB formation, the SiO_2 substrates that were used to support the SHMs had to be functionalised additionally to render their surfaces hydrophobic. The manipulation of surface characteristics is a commonly used way to obtain additional information on surface-related subject of matter. Therefore, different approaches like the functionalisation of gold surfaces with reagents containing reactive thiol groups or the reaction of silicon substrates with chloro-, alkoxysilanes or silyl amines are widely distributed.[132–134] As RIfS was one of the main techniques applied in the protein adsorption studies of this work and as it relies upon the interference of reflected and transmitted light, described in detail in section 3.5, substrates with a high reflectivity such as gold or other metal surfaces were not suitable. Therefore, the method of choice to obtain substrates with hydrophobic surface features was the treatment of Si-SiO_2 wafers with silyl amine 1,1,1-trimethyl-N-(trimethylsilyl)silanamine (HMDS). Its reaction with accessible hydroxy groups of the SiO_2 surface are illustrated in Scheme 3.6. Different functionalisation strategies, direct incubation with HMDS solution (cf. Chapter 3.3.3.1), plasma deposition (cf. Chapter 3.3.3.2) and vapour deposition (cf. Chapter 3.3.3.3) were tested to ascertain a functionalisation strategy leading to low surface roughness and high hydrophobicity. In the beginning of all functionalisation pathways the silicon substrates were cleaned by three cycles of sonification for 15 min during which the wafers were incubated in detergent solution (Hellmanex III, 0.5 %(*v*/*v*), 1st cycle) and two times in ultrapure water (2nd and 3rd cycle). Afterwards the wafers were dried in a N_2-stream and treated with O_2 plasma (p_{O2} = 0.2 mbar) for 30 s at 60 % power. Subsequently the substrates could be functionalised with HMDS. Independent of the followed functionalisation strategy all substrates were tested for their hydrophobic character via contact angle measurement after the functionalisation process (cf. Chapter 3.4).

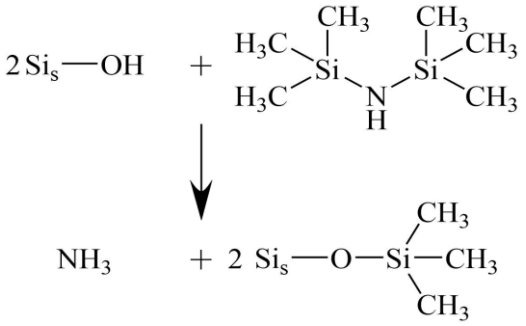

Scheme 3.6: Chemical equation of the surface functionalisation reaction of HMDS with the accessible hydroxyl groups of the SiO_2 surface.

3.3.3.1 Direct Incubation with HMDS

The cleaned silicon wafers were mounted in a reaction chamber and HMDS solution was added directly on top of the substrates. The reaction chamber was closed and incubated over night at room temperature. This ensured a preparation without deposition of dust on the surface.

3.3.3.2 Plasma Deposition of HMDS

The substrates remained in the plasma cleaner after first treatment with oxygen plasma (cf. Chapter 3.3.3) and a HMDS-reservoir was attached via vacuum tubing directly to the gas inlet of the cleaner. Afterwards multiple evacuation and ventilation cycles below the desired pressure of 0.2 mbar were conducted to rinse the reaction chamber, then HMDS deposition was started at 0.2 mbar for at least 120 s in a 100 % HMDS plasma at 60% power.

3.3.3.3 Vapour Deposition of HMDS

The wafers were stored upright in a glass chamber together with a test tube filled with 65 µL HMDS. Afterwards the chamber was sealed and placed overnight in a VD 23 drying cabinet (*Binder GmbH*, Tuttlingen, Germany) at 120 °C under reduced pressure. The next day the substrates were slowly cooled down and remained in the glass chamber until they were mounted in the experimental setup. This secured the functionalised substrates from contaminations and prevented aging processes.

3.3.4 Preparation of Solid-Supported Model Membranes

The substrates with their two opposing surface features (cf. Chapters 3.3.2 and 3.3.3) were treated in the same way to prepare two types of solid-supported model membranes, SLBs and SHMs. The substrates were mounted in the method specific reaction chambers, covered with Na-citrate buffer (cf. Table 3.16) and the SUV suspension was added in a final concentration of at least 0.2 mg lipid material per substrate. The addition of SUV induced their spreading on the substrate's surface. In case of preparations for AFM or fluorescence microscopy the substrates were incubated for a duration of minimum 30 min. The membrane formed *in situ* during RIfS measurements, enabling the control of the formation process in real time. After spreading the reaction chambers were rinsed with buffer which composition depended on the

continuing experiments (cf. Table 3.14). This rinsing guaranteed the removal of excess and attached, non-spread vesicles and facilitates the change to optimal buffer conditions for protein adsorption. In case of the gel-phase matrix lipid DPPC all preparation steps were performed at 55 °C, thus DPPC containing lipid mixtures were not suitable for RIfS-experiments. For all non-RIfS preparations, after changing the buffer conditions the membrane formation was controlled via fluorescence microscopy. In case of a homogenous fluorescence intensity with only a small number of defects or none at all visible inside the membrane, the volume above the preparation was reduced and protein was added to the solution ($c_{Protein} \geq 1$ µm) and incubated at room temperature for minimal 1 h. Afterwards, imaging of the adsorbed protein structures via AFM or determination of the protein's effect on fluorescence-quality and lipid mobility was feasible.

3.4 Contact Angle Determination

A tool to determine the hydrophobic character of a surface is the measurement of static contact angles (θ) that appear in sessile water droplets upon such surfaces. A water drop that easily spreads on a substrate exhibits a small contact angle, which is the angle made up by the liquid-solid interface and the liquid-gas interface (cf. Figure 3.4). This indicates a high wettability caused by a low hydrophobic character. In contrast to that high contact angles are detected on substrates that express a low wettability.[135] Therefore, this method is a good tool to evaluate the different strategies for substrate functionalisation described in Chapter 3.3.3.

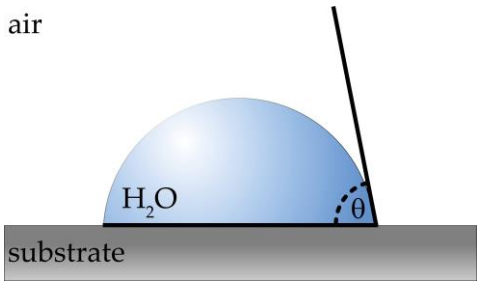

Figure 3.4: Scheme of a sessile droplet on a solid substrate with the contact angle θ connecting the liquid-solid and liquid-gas interfaces highlighted.

Experimental procedure

A custom-build contact angle goniometer setup, inspired by the one applied by STALDER *et al.*,[136] was utilized to determine contact angles of sessile water droplets (5 µL) on top of the hydrophobically functionalised SiO_2 substrates and on non-functionalised Si-SiO_2 wafers. The measurements were performed after rising each substrate with ethanol and drying it in a stream of nitrogen. The droplets were imaged with a Nikon D600 (*Nikon Corporation*, Minato,

Japan) that was equipped with an AF-S Nikkor 18/300 mm objective (*Nikon Corporation*, Minato, Japan) and fronted by a custom-made lens (*Scientific Precision Instruments GmbH*, Oppenheim, Germany). Analysis of gathered data was conducted by fitting a YOUNG-LAPLACE equation to the contour of the droplets using the ImageJ plugin Drop Shape Analysis.[136]

3.5 Reflectometric Interference Spectroscopy

Nowadays direct optical sensors make up an important class of detectors operating without invasive components like fluorophores that in many cases alter the activity and structure of physiological-relevant target molecules. Therefore, these non-invasive techniques represent an interesting tool to examine sensitive biomolecular interactions. The optical detection principles of the methods can be partitioned into two classes,[137] while the one is based on evanescent fields, like surface plasmon resonance (SPR), other methods among them the reflectometric interference spectroscopy (RIfS) rely on reflecto- or refractometry. RIfS is based on the reflection of white light at interfaces of transparent layers and thereby detects the interference pattern resulting from superposition of partially reflected beams.[138] The superposition of reflected and transmitted partial beams leads to either destructive or constructive interference depending on the angle of incidence, the wavelength and the optical thickness of the transparent layers investigated.[139] Therefore, changes in these factors alter the interference pattern facilitating e.g. the detection of optical thickness changes caused by adsorption processes like that of proteins to lipid membranes in real time.

3.5.1 Physical background

The basic principle of reflectometry is described in SNELL's law (cf. Equation 3.4)[140] focussing on the relationship between angle of incidence (α) and refraction (β) at interfaces of media with different refractive indices (n).

$$\frac{\sin\beta}{\sin\alpha} = \frac{n_1}{n_2} \qquad \textbf{3.4}$$

$$n_1 \sin\alpha = n_2 \sin\beta \qquad \textbf{3.5}$$

This fundamental law distinguishes between three different cases depending on the proportion of the refractive indices schematically illustrated in Figure 3.5.

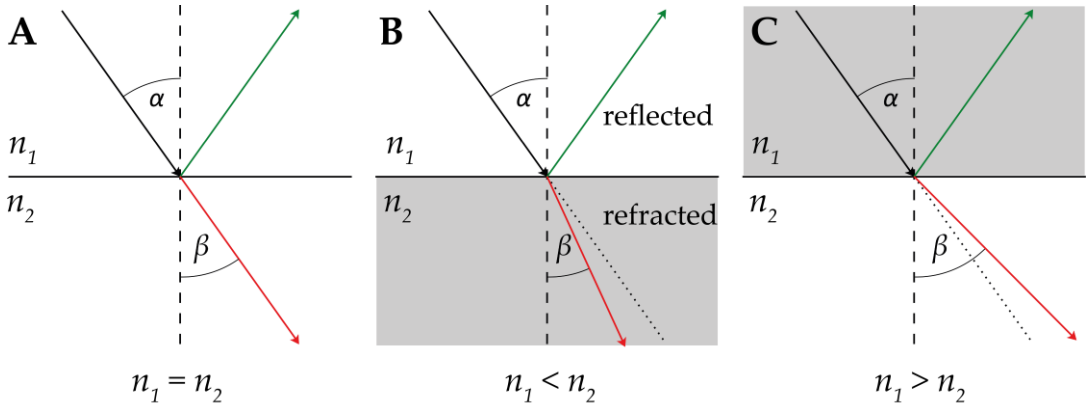

Figure 3.5: Principles described by the law of SNELL. Refraction of incident light with the angle α from a medium with a refractive index n_1 into a medium with n_2 by a refractive angle β. **A**: In case of identical refractive indices no refraction occurs. The incident light is transmitted. **B**: If n_2 is higher than n_1 the partial beam in the second medium is refracted towards the normal of the interface causing $\alpha > \beta$. **C**: The relation of incident and refractive angles is changed to $\alpha < \beta$ if $n_1 > n_2$.

Figure 3.5 A clearly shows that incident light is not only reflected by the incident angle α but also is transmitted without refraction as $\alpha = \beta$ when the refractive indices of both media are identical. In the cases of media with different refractive indices the transmitted light is either refracted towards or away from the normal of their interface for $n_1 < n_2$ (cf. Figure 3.5 B) or $n_1 > n_2$ (cf. Figure 3.5 C), respectively.

In this work the experimental setup was composed of three different phases separated by two interfaces (cf. Figure 3.6). The corresponding media were aqueous buffer solutions with $n_1 = 1.333$ ($T = 20$ °C, $\lambda = 589$ nm, $p = 0.1$ MPa)[141], a silicon dioxide layer with $n_2 = 1.458$ ($T = 20$ °C, $\lambda = 589$ nm, $p = 0.1$ MPa)[142] and an opaque silicon layer. The intermediate SiO_2 layer has a thickness (d) of 5 µm that functioned as the interference medium. This thickness is important as interference can only be detected when the path difference of the partial beams and consequently the reflecting interfaces are within the coherence length of white light with 0.5 to 30 µm.[143,144] The employment of such substrates guarantees a

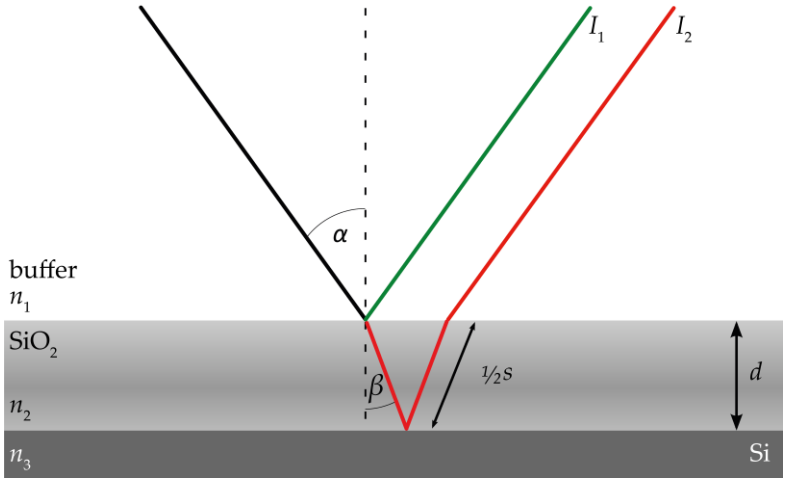

Figure 3.6: Scheme of the optical path in RIfS. The incident light is partially reflected (I_1) and transmitted (I_2). The later part is refracted by the angle β towards the normal of the interface due to the higher refractive index of the SiO_2-layer. The transmitted partial beam encounters the interface between SiO_2 and the opaque Si where it is reflected and after that gets refracted a second time at the first interface between buffer and SiO_2.

detection of monomolecular adsorption processes when the interference layer is extended by a biological layer, e.g. a lipid membrane or membrane-bound proteins with a refractive index (n = 1.46)[145] similar to that of SiO_2 (n_2). Either way, based on the mentioned refractive indices the experimental setup of this work represents the type of interfaces corresponding to Figure 3.5 B. Therefore, white light that hits the interface to the SiO_2 is in one part reflected (I_1) in the same angle as the incident one while a second part (I_2) is transmitted under refraction by the angle β as schematically presented in Figure 3.6. After the latter partial beam passes the interference layer it encounters the second interface (SiO_2-Si) at which it is reflected due to the opaque character of silicon. This causes a second refraction when leaving the interference layer resulting in a parallel travel direction of both partial beams but with I_2 covering a longer distance s to that of I_1. The path difference of the refracted partial beam is defined by:

$$s = \frac{2d}{\cos\beta} \qquad \textbf{3.6}$$

Under consideration of the refractive index n_2 of the interference layer and the distance s the difference in the optical path (Δs) can be calculated via:

$$\Delta s = \frac{2n_2 d}{\cos\beta} \qquad \textbf{3.7}$$

This equation can be simplified because of the experimental setup used in this work in which light is emitted perpendicular to the substrate altering the incident and refractive angles to $\alpha = \beta = 0°$ and resulting in Equation 3.8.

$$\Delta s = 2n_2 d \qquad \textbf{3.8}$$

Caused by the aforementioned difference in path length between I_1 and I_2 a phase shift ($\Delta\varphi$) is present that leads to a mutual displacement of maxima and minima of the partial beams. This displacement results during superposition of both waves in a specific interference pattern. The extreme case of maximum intensity that arises if the optical path is a multiple (m) of the emitted wavelength λ can be described by:

$$m\lambda_{max} = 2n_2 d \quad \text{with} \quad m \in \mathbb{N} \qquad \textbf{3.9}$$

In contrast to that minimum intensity occurs in case of:

$$\left(m + \tfrac{1}{2}\right)\lambda_{min} = 2n_2 d \quad \text{with} \quad m \in \mathbb{N} \qquad \textbf{3.10}$$

The phase shift of the two partial beams (I_1 and I_2) is defined by Equation 3.11 with:

$$\Delta\varphi(\lambda) = \frac{2\pi}{\lambda}\Delta s = \frac{2\pi}{\lambda} \cdot \frac{n_2 d}{\cos\beta} \quad \textbf{3.11}$$

Due to angle of incident light $\alpha = 0°$ in the experimental setup $\cos\beta = 1$ converting Equation 3.11 to:

$$\Delta\varphi(\lambda) = \frac{2\pi}{\lambda} n_2 d = \frac{2\pi}{\lambda} OT \quad \textbf{3.12}$$

The optical thickness *(OT)* is the product of the refractive index *n* and the physical thickness *d* as stated in Equation 3.12. Therefore, it is a parameter that is affected by adsorption processes causing an increase in *d* or a change of *n*, thus with Equation 3.12 at hand *OT* can be tracked by the phase shift.

3.5.2 Evaluation of the Data

All RIfS-measurements are based on the detection of the reflectivity, therefore, the connection between this parameter and *OT* will be highlighted within this paragraph. Prior to all RIfS adsorption studies reference spectra were detected for the extreme cases of complete and no reflectivity. While the bright spectrum (I_r) was determined under the use of a silver-sputtered glass substrate (reflectivity ≥ 98.5 %, *Chroma Technology GmbH*, Olching, Germany) the dark spectrum (I_d) was recorded when the light source was deactivated. The reflectivity spectrum of each substrate was displayed with Spectra Suite (Ocean Insight, Duiven, Netherlands) in consideration of the specific intensity spectrum of the substrate and both reference spectra following Equation 3.13.

$$\mathrm{R}(\lambda) = \frac{I_m(\lambda) - I_d(\lambda)}{I_r(\lambda) - I_d(\lambda)} \quad \textbf{3.13}$$

For non-absorbing substances the reflectivity can be described by the reflectivity coefficients of FRESNEL (r_{xy}) that are defined as:

$$r_{xy} = \frac{n_x - n_y}{n_x + n_y} \quad \textbf{3.14}$$

$$\mathrm{R}(\varphi) \equiv |r_{123}|^2 = \frac{r_{12}^2 + r_{23}^2 + 2r_{12}r_{23}\cos(2\Delta\varphi)}{1 + r_{12}^2 r_{23}^2 + 2r_{12}r_{23}\cos(2\Delta\varphi)} \quad \textbf{3.15}$$

Considering the definition of the phase shift and inserting it into Equation 3.15 leads to the direct correlation of reflectivity and *OT*:

$$R(\lambda, OT) = \frac{r_{12}^2 + r_{23}^2 + 2r_{12}r_{23}\cos\left(\frac{4\pi}{\lambda}OT\right)}{1 + r_{12}^2 r_{23}^2 + 2r_{12}r_{23}\cos\left(\frac{4\pi}{\lambda}OT\right)} \quad \textbf{3.16}$$

If this equation is fitted to the reflectivity spectra during RIfS-measurements a temporal change in optical thickness (ΔOT) can be determined. The detected changes are for the most part cause by variations in the physical thickness d because of the aforementioned very similar refractive indices of the interference layer SiO_2 and adsorbed biological material, thus being a good read-out parameter for surface coverages by those adsorbed substances.

3.5.3 Experimental Setup

The measuring chamber used for RIfS as illustrated in Figure 3.7 is composed of an alumina

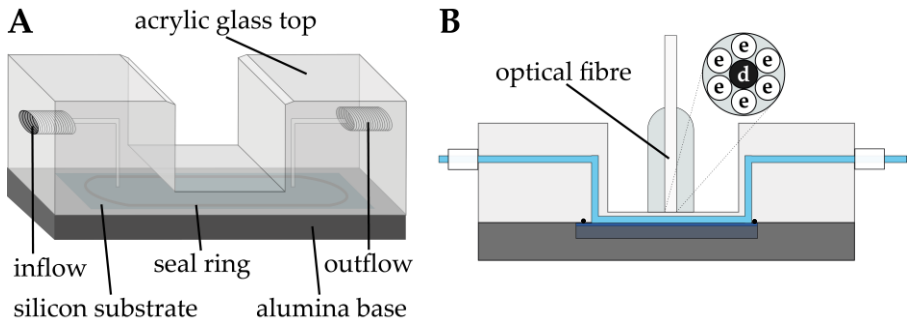

Figure 3.7: Scheme of the measuring chamber used in RIfS. **A**: Illustration of the composed flow-through chamber with the acrylic glass top and the alumina base between which the silicon substrate is fixed. The actual reaction volume is defined by a sealing ring that is embedded in the top. **B**: Schematic sideview of the chamber to which the optical fibre is attached that consist of six light-emitting fibres (e) around a detection fibre (d).

base with an inlet (2 cm x 2 cm, depth: 2 mm) in which the substrates can be placed and an acrylic glass top that can be mounted to the base with screws. The top exhibits a milling groove exactly fitting the size of a seal ring with dimension of 12 mm in radius and a thickness of 1 mm, thereby defining the actual reaction volume. Furthermore, the acrylic glass construct contains screw threads enabling attachment of tubing for the in- and outflow of solutions. This flow was generated by a peristaltic pump (*IDEX Health & Science*, Wertheim, Germany) with a velocity of ca. 0.5 mL/min. On top of the composed measuring chamber an optical fibre is placed perpendicular to the substrates surface (cf. Figure 3.7 B), thus guaranteeing the angles of incident and reflected light to be 0°, as described in the former chapter. The fibre is made up by six light-emitting fibres (e) that circle one detection fibre (d). While the later transmits the detected light to a FLAME-S spectrometer (Ocean Insight, Duiven, Netherlands) the other

fibres emit light (λ = 360-950 nm) that was generated by a tungsten-halogen light source (Ocean Insight, Duiven, Netherlands).

3.5.4 Experimental Procedure

After the composition of the measuring chamber and the attachment to the tubing system the whole setup was rinsed with ultrapure water to remove all air from inside. Remaining bubbles were removed by changing the direction and velocity of flow. Then the system was rinsed and equilibrated with the respective Na-citrate buffer. All rinsing processes were conducted in an open system configuration while vesicle spreading and some of the adsorption experiments took place in a closed one. The recording of change in optical thickness (ΔOT) was performed with the software Spectra Suite. After a base line was determined addition of SUV suspension (m = 0.2 mg) led to adsorption of lipid material and thus an adlayer formation on the interface. It was tracked until a plateau indicated successful membrane formation. Then the system was rinsed with the specific buffer (cf. Table 3.14) to remove adhered vesicles and change the buffer conditions to an optimum for protein adsorption. After that protein addition followed with varying concentrations. Depending on the experimental design either a single protein injection or multiple successive additions (referred to as adsorption isotherms) took place as schematically shown in Figure 3.8 A and B, respectively.

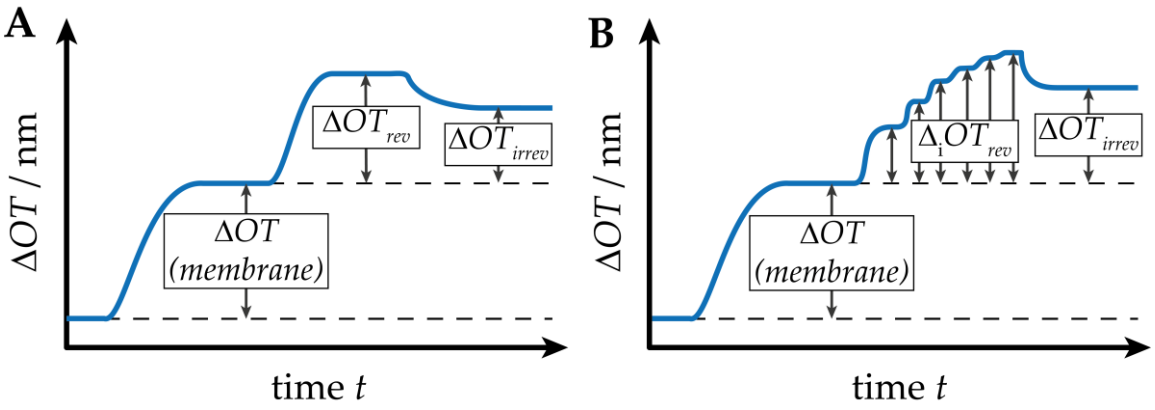

Figure 3.8: Schematic illustrations of RIfS-spectra gathered either in a single injection experiment (**A**) or during subsequent increase of protein concentration by multiple injections (**B**).

After another plateau was reached (closed configuration) or the whole protein solution was applied (open one) the complete setup was again rinsed with buffer to determine the amount of irreversible bound protein to the membrane. When the detection was stopped the tubing system was vigorously rinsed with ultrapure water and the acrylic glass tops together with

the seal rings were cleaned three times in an ultrasonic bath for 15 min (1st pass in 5 % Mucasol® solution, 2nd and 3rd passes in ultrapure water).

3.6 Atomic Force Microscopy

The atomic force microscopy (AFM) is another technique in addition to RIfS capable to determine surface adsorption processes as it detects forces on an atomic level. It was developed in 1985 by G. BINNIG, C. QUATE and C. GERBER based on the scanning tunnelling microscope (STM) to allow high resolutions in all three dimensions not only in *x*- and *y*-direction like fluorescence microscopy.[146] To be precise, its detection is limited to a lateral resolution of 1.0 nm while the axial resolution limit is 0.1 nm with the measuring probe being the decisive factor.[147,148] Therefore, in this work AFM aided to characterise the surface roughness of the substrates used as solid support for the model membranes before and after functionalisation with HMDS. Furthermore, data on the surface coverage by adsorbed proteins, their lateral organisations and their specific heights on top of the membrane systems were gathered via this technique making it an essential part of this study.

3.6.1 Principle of an AFM

The measuring probe dictating the resolution of the AFM by its radius is attached to a cantilever. The forces that occur either in proximity or in contact of probe and specimen cause a deflection of the cantilever that can be detected whereby the topography can be expressed in the relation of this deflection to the position on the specimen. The force necessary for cantilever manipulation is described by the law of HOOK:

$$F = k \cdot z_C \qquad \textbf{3.17}$$

Accordingly, the required force *F* depends on the spring constant *k* of the cantilever and the deflection z_C. In addition to the aforementioned atomic forces between probe and specimen there are also macroscopic, repulsive and attractive interactions taking place depending in various ratios on the distance *r* between both. In case of close proximity these forces are well described by the LENNARD-JONES potential (V_{LJ}) for neutral atoms or molecules:

$$V_{LJ}(r) = 4\varepsilon \left[\left(\frac{\sigma}{r}\right)^{12} - \left(\frac{\sigma}{r}\right)^{6} \right] \qquad \textbf{3.18}$$

With σ being the finite distance at which the potential between the two molecules is zero, ε describing the depth of the potential well whereas r represents the distance between both particles. Consequently, if two particles move closer together, they first experience attractive van-der-Waals interactions, though during further distance decrease the electron orbitals start to overlap inducing a repulsive force following the principle of PAULI.

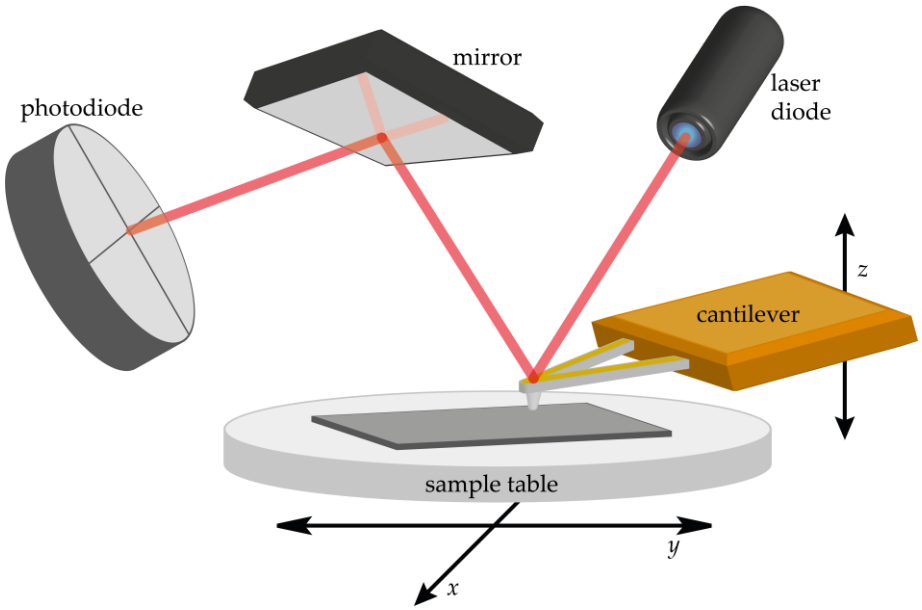

Figure 3.9: Schematic setup of atomic force microscope. A light beam is reflected from the back of the cantilever and detected via a position-sensitive photodiode. Scanning of specimen is possible by movement of the sample table in x- and y-direction while the distance between sample surface and cantilever is adjusted by a z-piezo actuator in the cantilever holder.

The experimental setup utilized in this work was a MFP-3D (*Asylum Research*, Santa Barbara, USA), therein the cantilever with the measuring probe is moved by an z-piezo while the specimen inside a reaction chamber can be moved in x- and y-direction via a piezo actuator underneath the sample table (cf. Figure 3.9). The actuators enable not only the scanning of the specimen but also allow adjustments of the distance between probe and surface. The later feature facilitates measurements either with constant distance or constant force. The vertical and lateral deflection is determined by the displacement of a laser beam that is pointed on the reflective back of the cantilever and detected via a four-quadrant diode (photodiode, cf. Figure 3.9).

3.6.2 Imaging modes

In contrast to samples investigated via STM the ones tested with AFM do not need to express any conductivity. Furthermore, AFM-imaging is possible not only in air but also in liquids, yet it is worthwhile to mention that in aqueous surroundings the imaging is more challenging due

to attenuating interaction between cantilever and the liquid itself. Another aspect that necessary to considered when working with AFM is the character of the sample under investigation which vary not only in the sense of stability or rigidity but also in adherence and intrinsic height differences. Due to these reasons one must choose an imaging mode that suits most the given sample characteristics. Therefore, the contact and the intermittent-contact mode were applied to the preparations tested in this thesis. Both are described in depth within the following paragraphs.

3.6.2.1 Contact mode

The continuous contact of the cantilever with the surface of the specimen during the whole scanning cycle is eponymous for this type of imaging. In a static fashion the cantilever can either be moved across the surface at a constant height or with an invariable force. Due to this features the contact mode is most suitable for rigid probes.[147] Furthermore, this mode enables determination of mechanic characteristics e.g. by force-distance curves or indentation experiments.

3.6.2.2 Intermittent-contact mode

The contact mode tends to either manipulated or to destroy softer preparations like cell or proteins, whereas in the intermittent-contact or tapping mode the forces induced by the cantilever are drastically reduced. This is achieved by a decrease in contact time as the cantilever is stimulated in the range of its resonance frequency and thus sinusoidally oscillates with a constant amplitude.[149] The determination of the exact resonance frequency is performed for each cantilever before the beginning of the experiment by recording the thermal noise. At the minimum of the oscillation the cantilever tip touches the sample's surface and afterwards is removed directly. These dynamics are the reason for the reduction of induced shear forces.

3.6.3 Experimental Procedure

For the different substrate types three cantilevers were utilized which varied in their characteristics as shown in Table 3.17.

Table 3.17: Cantilevers and their properties utilized in this work for the different sample types.

Cantilever	Shape	Res. frequency [kHz]	Spring constant [N/m^{-1}]	Length [µm]	Width [µm]	Mode
NCH-50	rectangular	250-390	42	125	30	contact
MSCT	triangular	90-160	0.6	85	18	tapping
MSNL-10	triangular	90-160	0.6	85	18	tapping

The cantilever applied in contact mode was purchased from *Nano World* (Neuchâtel, Switzerland) while the tapping-cantilevers both were produced by *Bruker AFM Probes* (Camarillo, USA).

At the start of all AFM measurements the cantilever was mounted to a glass prism functioning as a holder and fixed with a screw. All time the cantilever was handled with care to avoid any damage that might have impeded subsequent surface imaging. The sample of interest, being either a plain silicon substrate with or without HMDS functionalisation (cf. Chapters 3.3.2 and 3.3.3) on air or a solid-supported model membrane in buffer solution before or after incubation with protein (cf. Chapter 3.3.4) prepared in a home-build measuring chamber, were placed on top of the sample table as schematically shown in Figure 3.9. After that the prism was attached to the microscope head and place above the sample. In case of liquid samples, the head was lower until the cantilever is just in contact with the liquid whereby inclusion of air underneath the cantilever's tip was avoided. In the liquid the cantilever equilibrated for 30 min.

Before the tip approached the surface no matter if on air or in solution, the light spot had been focussed on the spike of the cantilever directly above the measuring tip to obtain maximum signal intensity. Additionally, the deflection was set to zero by adjustment of the reflecting mirror to the centre of the position-sensitive diode (PSD). When deflection stayed constant after equilibration, the resonance frequency was determined, and the probe approached to the sample. In contact the measuring parameters were adjusted using the software Igor – MFP3D. The obtained images were processed with Gwyddion 2.49 and analysed in detail with MATLAB R2017b and OriginPro 8.5G. To determine the roughness of the substrates the root mean square (RMS) of the surface heights (h) was calculated following Equation 3.19:

$$rms = \sqrt{\frac{1}{n}\sum_{i=1}^{n} h_i^2} \qquad \textbf{3.19}$$

The analyses of surface coverage, lateral protein organisation and protein heights were conducted under the use of a MATLAB script established by DR. INGO MEY. This routine distinguished between membrane and adsorbed protein by applying a threshold and identified protein structures with a 2D-peak detection function marking local maxima. These detected extreme values led to a histogram representing the distribution of their respective heights. To these data either a GAUSS-distribution (Equation 3.20) or a logarithmic normal distribution (Equation 3.21) was fitted to determine the mean protein height as the maximum value of the distribution x_c and its error ($w = 2 \cdot \sigma$).

$$y = y_0 + \frac{A}{w \cdot \sqrt{\frac{\pi}{2}}} \cdot \exp\left[-2 \cdot \left(\frac{x - x_c}{w}\right)^2\right] \qquad \textbf{3.20}$$

$$y = y_0 + \frac{A}{w \cdot x \cdot \sqrt{2\pi}} \cdot \exp\left[\frac{-\left(\ln\frac{x}{x_c}\right)^2}{2 \cdot w^2}\right] \qquad \textbf{3.21}$$

The logarithmic normal distribution was solely applied if the height distribution was not symmetric.

3.7 Fluorescence Microscopy

Fluorescence microscopy is a special form of light microscopy that relies on the ability of specific molecules, so called fluorophores, to adsorb light at one wavelength and emit it at a different wavelength after a short duration. This wavelength change is based upon a vibronic transition of the fluorophore after excitation from an electronic ground state S_0 to an excited vibrational and electronic one (S_1). The relaxation into the vibrational ground state of the excited electronic state is a fast process caused by collisions with surrounding molecules. Unlike this, the lifetime of the excited electronic state is in the range of nanoseconds before the molecule emits a red-shifted photon and thus returns to its ground state. This phenomenon is called STOKES shift and is frequently applied in life science to obtain high contrast even when working with simultaneous excitation and emission.[150] Within this work different types of fluorescence microscopy setups were used to determine membrane quality and lipid diffusion inside the model systems before and after protein adsorption exploiting the presence of fluorescently labelled lipids (cf. Chapter 3.1.1.3). The following sections will deal with those setups in more detail.

3.7.1 Epifluorescence microscopy

An epifluorescence microscope is characterised by a straightforward setup design prompting light at sample in a straight angle which leads to a maximum in illumination. Due to this feature it is also referred to as widefield microscopy. In general, a high-intensity light source such as a light-emitting diode (LED) is used emitting a continuous light spectrum schematically illustrated in Figure 3.10. The eradiated light hits an excitation filter, only passed by light of the corresponding excitation wavelength to the fluorophore present in the specimen to test. The monochromatic beam is reflected by a dichroic mirror onto the specimen and excites the fluorophores in a wide area. The emitted fluorescence of the sample then passes the objective and the dichroic mirror, since the mirror functions as a beam splitter only reflecting light of shorter wavelengths while irradiation with longer wavelengths is transmitted. After that the fluorescence is separated from scattered light by an emission filter guaranteeing the detection of the relevant spectral range solely. The resolution of an epifluorescence microscope is limited to half of the applied wavelength at best (ABBÉ diffraction limit) due to the optical components of the microscope that do not lead to illumination of a single spot in the specimen but a broader area as mentioned before.

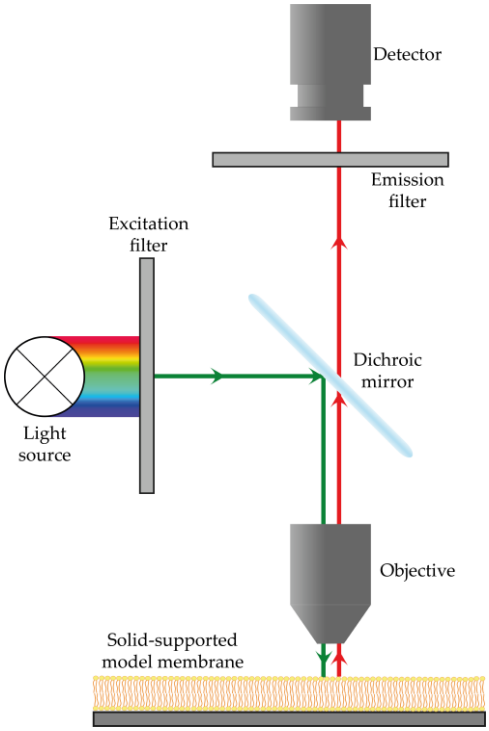

Figure 3.10: Schematic drawing of the setup of an epifluorescence microscope.

3.7.2 Confocal Laser Scanning Microscopy

The confocal laser scanning microscope (CLSM) achieves a better resolution in comparison to the epifluorescence microscopy as it reduces the background noise by cutting off scattered light before detection. The main difference to widefield microscopy is the application of pinholes and the use of a laser eradiating coherent light for fluorophore excitation. Furthermore, instead of a complete illumination of the sample only a small focal volume is irradiated, reducing photo damage and bleaching to a minimum. The CLSM technique is based on the principles presented in 1955 by MINSKY.[151] A scheme of a laser scanning microscope is shown in Figure 3.11. The coherent light is emitted by a laser at a specific wavelength and passes a collimator creating a parallel path of beams towards the dichroic mirror. At the mirror the excitation light is reflected on the lens inside the objective which refracts the light to focus plane resulting in light absorption by the fluorophores. When the photo-active molecules emit the light of lower wavelength, it afterwards is refracted at the lens and transmitted by the beam splitter. It is then separated by the adjustable pinhole from the out-of-focus scattered light before detection with a photomultiplier. The resolution of a CLSM depends on the width of the opened pinhole and in the extreme event of full opening the lateral resolution is similar to that of an epifluorescence microscope. Nonetheless, due to the differentiation between focal and scattered light the depth definition is drastically reduced and also enables a scanning in *z*-direction resulting in a 3D-reconstruction of the sample.[152]

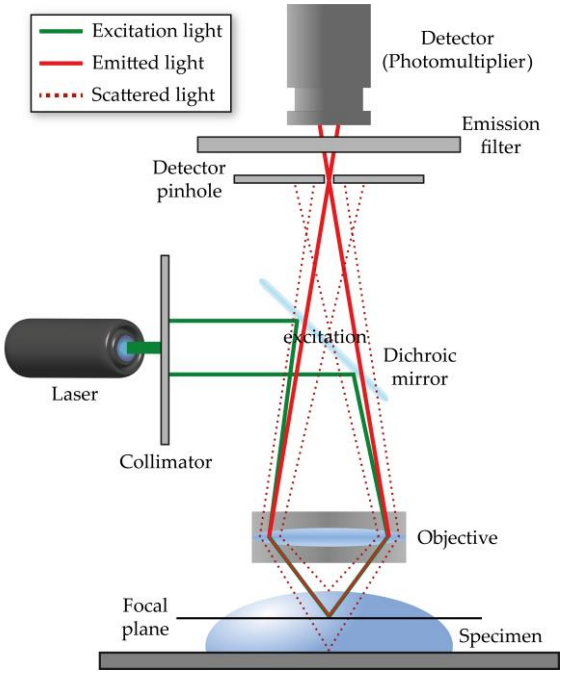

Figure 3.11: Setup of a confocal laser scanning microscope schematically illustrated.

3.7.3 Experimental Procedure

The control of model membrane quality after its formation process (cf. Chapter 3.3.4) and prior to AFM measurements was performed with a BX 51 epifluorescence microscope (*Olympus*, Hamburg, Germany). On this purpose the specimen was irradiated with green light (λ = 580 nm) to excite the TxR-fluorophores in the lipid layers.

For detailed characterisation of the prepared model membrane systems by high-resolution imaging and fluorescence recovery after photobleaching experiments, a confocal LSM 880 Examiner (*Carl Zeiss*, Jena, Germany) equipped with a 40 x water immersion objective (W Plan-Apochromat, NA = 1, *Carl Zeiss*, Jena, Germany) was utilised. After the formation process of the membranes the distribution and the mobility of the employed fluorophores were examined. To do this, either TxR or BODIPY®-TMR PtdInsPs were excited using a laser with λ = 561 nm of emission. For bleaching of the fluorophores an additional laser (λ = 488 nm) was employed to induce a grout amount of energy in a short duration. Although, the detection parameters varied, in all recovery experiments the bleach spot was placed in the centre of the detection area to guarantee an accurate analysis. This procedure is described in detail in the next chapter.

3.7.4 Fluorescence Recovery after Photobleaching

The method of fluorescence recovery after photobleaching (FRAP) is frequently used to determine lateral mobilities and binding kinetics of fluorescently labelled molecules inside a solution or liquid aggregate.[153–155] By exposition to high-energy radiation fluorophore molecules are destructed (non-filled red circles in Figure 3.12 A to D) in the corresponding area resulting

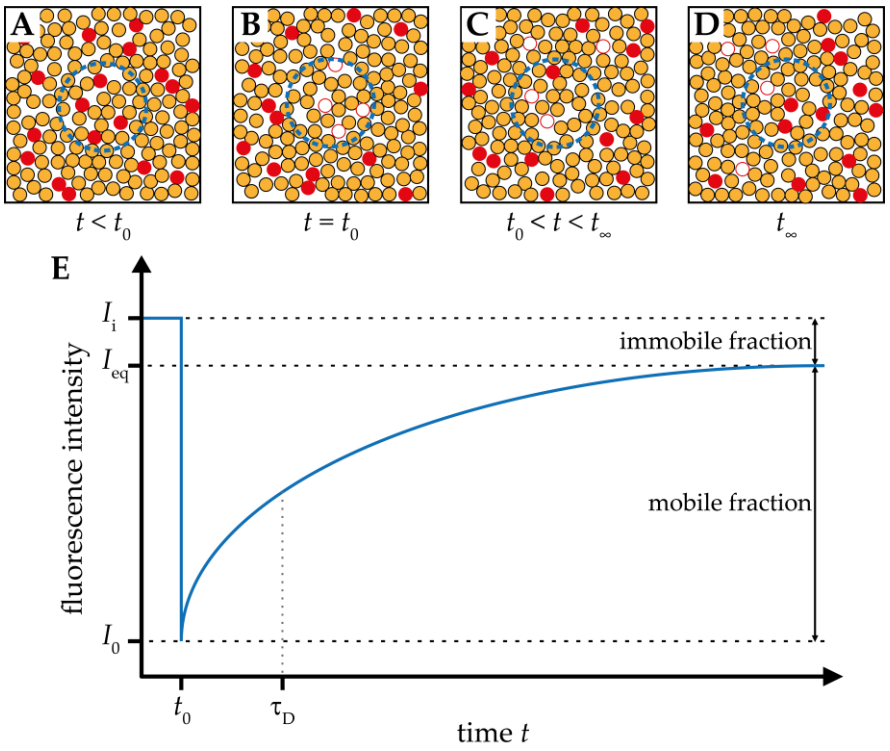

Figure 3.12: Schematic illustration of a FRAP experiment with the ROI highlighted as a dashed blue circle while fluorescently labelled lipid molecules are represented as red circles, unlabelled ones in orange while bleached fluorophores are presented as non-filled red circles. **A**: Initial fluorescence intensity I_i is detected in the ROI. **B**: Bleaching of fluorophores in the ROI (I_0) by inducing a high-energy laser pulse. **C**: Diffusion of lipid molecules in and out of the ROI cause recovery of the fluorescence intensity. **D**: A new intensity plateau is reached with I_{eq} when in and out diffusion of lipids is in an equilibrium. **E**: Schematic intensity spectrum correlating to the time series illustrated in A to D.

(represented by the dashed blue circle in Figure 3.12 A to D). Due to the lack of fluorescent molecules the spot referred to as region of interest (ROI) appears dark (Figure 3.12 B) and the respective intensity minimum immediately after bleaching is I_0. Determinations of the recovery-duration and the regenerated, final fluorescence intensity I_{eq} enable the characterisation of the fluorophore mobility inside the specimen.[156] To facilitate exact determinations the initial fluorescence intensity I_i of e.g. SLBs and SHMs, like in this work, is measured. The bleached area exhibited a circular shape to facilitate analysis with a HANKEL transform.[157] All parameters in combination with the time t and the time constant of the fluorescence recovery t_F can be

used to describe the time dependent fluorescence intensity $I(t)$ as shown in Figure 3.12 E via the following equation:

$$I(t) = I_{\mathrm{eq}} - \left(I_{\mathrm{eq}} - I_0\right) \cdot \exp\left(\frac{-t}{t_{\mathrm{F}}}\right) \qquad \textbf{3.22}$$

Between the time constant of the fluorescence recovery and the characteristic diffusion time τ_D a relation exists as shown in Equation 3.23:

$$\tau_{\mathrm{D}} = \ln(0.5) \cdot (-t_{\mathrm{F}}) \qquad \textbf{3.23}$$

With known radius of the circular ROI the diffusion time can be used to calculate the diffusion coefficient D as followed:

$$D = \frac{r^2}{4\tau_{\mathrm{D}}} \qquad \textbf{3.24}$$

In case of solid-supported model membranes there is always an interaction taking place between lipid molecules and substrate resulting in a proportion of immobilised lipid molecules. The exact amount of mobile lipids F_m correlates with the intensity ratios as stated in Equation 3.25.

$$F_{\mathrm{m}} = \frac{I_{\mathrm{eq}} - I_0}{I_{\mathrm{i}} - I_0} \qquad \textbf{3.25}$$

The detailed analysis of all FRAP experiments to calculate the specific diffusion coefficients and immobile fractions was conducted by application of a MATLAB script that was established by JÖNSSEN *et al.*[157]

4 Results and Discussion

This work aimed on the development on an *in vitro* model system of the GABA$_A$ergic postsynaptic receptor organisation machinery to enable characterisation of its constituents and their interactions. Different solid-supported membrane systems are envisioned to establish the bottom-up approach. These were prepared on top of silicon dioxide wafers which provided different surface features due to modification with 1,1,1-trimethyl-N-(trimethylsilyl)silanamine (HMDS). The functionalisation process together with the characterisation of the obtained surfaces and the subsequently prepared model membranes will be the focus of Chapter 4.1. The application of two different model membrane systems allowed determination of the leaflet-dependent PtdIns[4,5]P_2 distribution in solid-supported lipid bilayer (SLBs). The adsorption of marker proteins, both the *N*-terminal domain of ezrin (N-ERMAD) and the *C*-terminal PH domain of collybistin 2 (CB2$_{PH}$), was used to examine the accessibility of the specific receptor lipid in SLBs as well as in solid-supported hybrid membranes (SHMs). Having outlined the adsorption results and thus the advantages of SHMs in Chapter 4.2, the following section (cf. Chapter 4.3) will deal with the adsorption behaviour of the adapter protein collybistin 2 (CB2) to this model membrane system. On the account of binding specificity different PtdInsP-species have been deployed as receptor lipids and a detailed look on CB2's topographical features will be presented to evaluate their impact on the protein organisation. Afterwards, this characterisation allows the expansion of the *in vitro* model system by addition of neuroligin 2 (NL2). The protein-protein (NL2—CB2) interaction is believed to induce the activation of the latter under physiological conditions which has been investigated in co-adsorption experiments presented in Chapter 4.4.

4.1 Functionalisation of silicon dioxide surfaces for preparation of supported model membrane systems

-Some of the results presented in this Chapter have been published in "Leaflet-Dependent Distribution of PtdIns[4,5]P_2 in Supported Model Membranes" by J.Schäfer et al., Langmuir, ***2020****, 36, 1320-1328.*[158]*-*

4.1.1 Surface characterisation of hydrophilic silicon dioxide substrates

The preparation of solid-supported lipid bilayers is a widely distributed and frequently used method to obtain a simple model membrane which can be applied to examine protein-lipid interactions.[159–161] A prerequisite for the material used as solid support is an inert and smooth surface with a hydrophilic character. Next to mica these features are presented by silicon substrates with a SiO_2 surface. In this work SiO_2 wafers with a surface layer thickness of either 100 nm or 5 µm were used (cf. Chapter 3.5.1). A good model system requires the knowledge of all its constituents, therefore a detailed look on the substrate's surface features has been taken. Figure 4.1 A presents an exemplary atomic force micrograph of a hydrophilic functionalised SiO_2 substrate (with a layer thickness of 100 nm, cf. Chapter 3.3.2). The image shows a smooth surface with few aggregates of small heights on top of it. As the surface was imaged in air, these deposits might correlate to dust particles upon the otherwise clean surface. The surface roughness was determined as root mean square (RMS, cf. Equation 3.19) by atomic force microscopy (AFM) while imaging in intermittent-contact mode (cf. Chapter 3.6). For both hydrophilic silicon substrates (with different SiO_2 layer thicknesses of 100 nm and 5 µm) RMS was (0.88 ± 0.24) nm, based on eight independent measurements gathered on five different substrates. The results were combined due to an insignificant deviation.

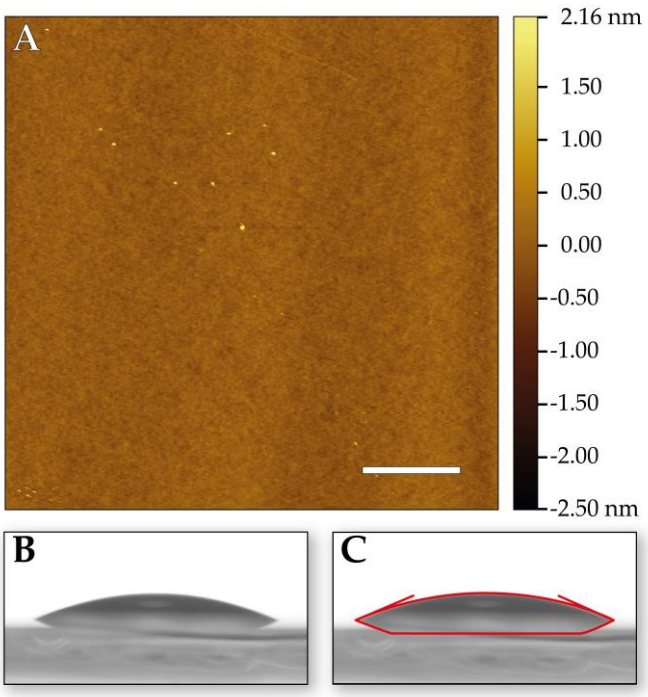

Figure 4.1: A: Atomic force micrograph of an unfunctionalised SiO_2 wafer surface. Scale bar: 2 µm. **B**: Exemplary image of a sessile water droplet on top of such a surface. **C**: Water droplet modulation (red) by the LB-ADSA ImageJ plug-in to determine the contact angle.

In addition to roughness determinations also the hydrophilicity of the substrates was studied by contact angle measurements of sessile water droplets (cf. Figure 4.1 B). The analysis of the contact angle was conducted by the ImageJ plug-in LB-ADSA as demonstrated in Figure 4.1 C and described in detail in Chapter 3.4. The mean of the determined angles is (16 ± 6)° with the

corresponding standard error. It is an evidence for the high hydrophilicity of the silicon dioxide surface.

4.1.2 Strategies of substrate functionalisation with HMDS

The functionalisation of the silicon substrates with HMDS as inspired by HERTL and HAIR[162] was performed following three different strategies. The cleaned wafers were either directly incubated with HMDS-solution, or exposed to HMDS-plasma for at least 120 seconds or to an HMDS-atmosphere at increased temperature und reduced pressure overnight (cf. Chapter 3.3.3). In analogy to the characterisation of hydrophilic SiO_2 surfaces, these substrates were also examined according to surface roughness and hydrophilicity. In Figure 4.2 atomic force micrographs are presented exemplary for each functionalisation strategy. The corresponding contact angle measurements are displayed in the respective inset.

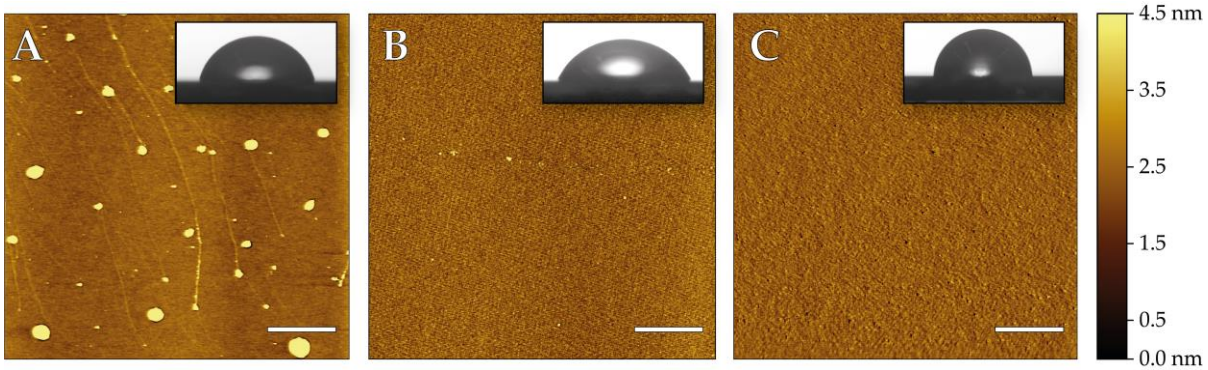

Figure 4.2: Atomic force micrographs of the functionalised substrate surfaces. **A**: Silicon dioxide wafer after direct incubation with HMDS-solution. **B**: Surface image after HMDS-plasma treatment (for 120 s). **C**: Surface imaged after exposure to HMDS-vapour overnight under reduced pressure and increased temperature. Scale bars: 2 µm. Insets represent the corresponding sessile water droplet experiments to determine the substrate's hydrophilicity by contact angle measurements.

While the direct incubation of the solid support to HMDS-solution resulted in a very heterogenous surface with plenty deposits on top (cf. Figure 4.2 A), the exposure to HMDS plasma reduced the amount of deposits on the surface (cf. Figure 4.2 B). However, the hydrophobic character of substrates functionalised following the plasma protocol is reduced with a contact angle of (61 ± 12)° (n = 12) compared to those directly incubated (69 ± 7)° (n = 8). The substrates exposed to the HMDS-vapour (cf. Figure 4.2 C) in turn exhibited the highest hydrophobicity with contact angles of (87 ± 1)° (n = 12). Furthermore, there were large discrepancies in the roughness of the hydrophobically functionalised surfaces. The direct incubation and plasma treatment led to aggregate formation during the deposition process resulting in RMS of

(1.97 ± 1.54) nm (n = 13) and (1.18 ± 0.67) nm (n = 8), respectively. Even though, higher roughness might reduce the hydrophilicity of a surface,[163] the detected heterogeneities had to be avoided. Otherwise, their broad height- and shape-distribution would have perturbed subsequent AFM studies of adsorbed proteins. In that scenario a precise distinction between functionalisation deposits and protein aggregates would have been possible only by using specific markers for the proteins, like antibodies or previously fused fluorescent labels. Fortunately, the strategy of substrate treatment with HMDS-vapour resulted not only in highest hydrophobicity but also led to a surface roughness of (0.40 ± 0.07) nm (n = 4). This value is even lower than that determined for the untreated SiO_2 substrates with (0.88 ± 0.24) nm, as shown in the prior Chapter 4.1.1. Additionally, none of the substrates functionalised following this strategy exhibited any aggregates. The determined features for the untreated silicon dioxide surfaces as reference were in good agreement with those determined for a smooth silicon wafer.[164] However, the roughness of the untreated substrate is vigorously larger than that determined for a freshly cleaved mica sheet, which is atomically smooth.[165] A model considering the net energy decrease during spreading of a droplet on a rough surface,[166] describes the well-known trend of very even surfaces to exhibit the highest hydrophilicity.[163] Yet, the data gathered after vapour deposition contradict this trend when compared to the results of the other functionalisation strategies as illustrated in Figure 4.3. Moreover, in surface surveys the discrimination between hydrophilic and hydrophobic characteristics is based on contact angles being <90° and >90°, respectively.[167] Therefore, the designation of the HMDS treated substrates as "hydrophobic" is incorrect in its general sense. Due to drastic increases in hydrophobicity after HMDS functionalisation this connotation will still be maintained.

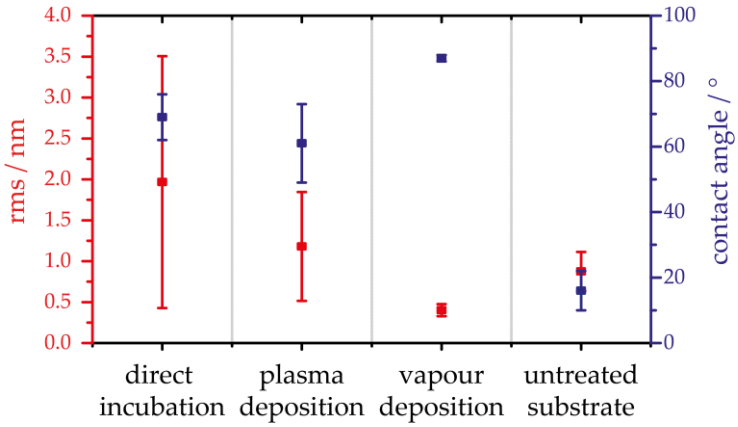

Figure 4.3: Illustration of the surface characteristics RMS (red) and hydrophilicity (contact angle, blue) for the different functionalisation techniques compared to an untreated SiO_2 substrate. Error bars are the standard error of the mean with $n \geq 4$.

The choice of HMDS as reagent for surface functionalisation instead of other substances leading to a self-assembled monolayer (SAM) was based on its good compatibility with the SiO_2

substrates. Examples for SAM formation are on one hand the adsorption of thiols on gold as introduced by NUZZO and ALLARA in 1983,[168] or on the other hand the functionalisation of hydrophilized silicon dioxide by covalent adsorption of trichlorosilanes.[169] The first possibility was inadequate for the application in RIfS due to the lack of an interference layer (cf. Chapter 3.5.1), yet, the second options would have been compatible with the deployed techniques as shown in former studies.[170] CAPEL-SANCHEZ and colleagues discovered in comprehensive examinations by means of diffuse reflectance infrared Fourier transform (DRIFTS), solid-state nuclear magnetic resonance (NMR) and photoelectron spectroscopy that chemically grafting of silica with both trimethylsilyl chloride (TMSCl) and HMDS leads to a complete removal of terminal and geminal hydroxyl groups on the functionalised substrate, thus causing full surface coverage by hydrophobic methyl groups.[171] Furthermore, they found higher hydrophobicity for surfaces treated with HMDS, showing its advantage compared to TMSCl. HMDS exhibits a single reaction site for interaction with the silicon dioxide, while other organosilicon compounds like the mentioned trichlorosilanes contain more of those sites. Therefore, such agents can form SAMs under ideal conditions, yet, other reaction pathways like covalent attachment or vertical polymerisation are possible, too.[172] The latter might result in an increased surface roughness and therefore was avoided by deploying HMDS to render the silicon dioxide substrates hydrophobic. When comparing the obtained surfaces, it becomes obvious that the substrate treatment with HMDS-vapour has been the most promising strategy. For this reason, subsequent hydrophobic solid supports preparation followed this protocol.

4.1.3 Formation and characterisation of SLBs and SHMs

-Some of the RIfS experiments have been performed by Jessica Nehls and Anna Lena Toschke as parts of their bachelor theses, and by Lucas Förster as part of his master thesis-

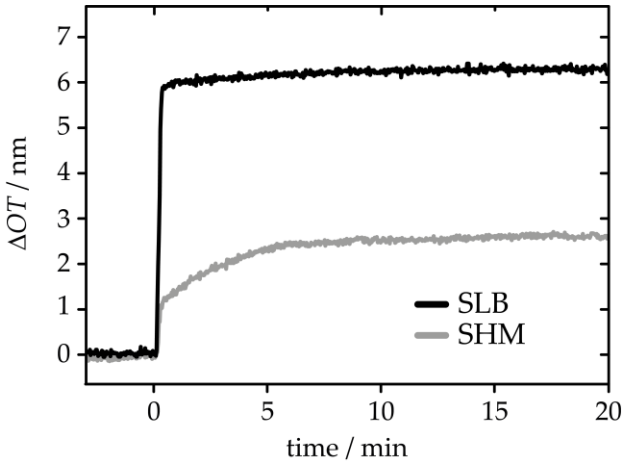

Figure 4.4: Exemplary plots of the change in optical thickness vs. the time during the process of model membrane formation after addition of SUV-suspension (POPC : PtdIns[4,5]P_2, 99 : 1, *n*/*n*) at $t = 0$ min on either hydrophilic (black) or hydrophobic (grey) silicon dioxide substrates.

Having determined the surface features of the silicon substrates that were applied as solid support in this work, it is now reasonable to examine and compare the two model membranes (SLBs and SHMs). Both were prepared via spreading of small unilamellar vesicles (SUVs) on the two substrate types (cf. Chapter 3.3.4). The membrane formation was performed either prior to the measurement in case of AFM and fluorescence microscopy experiments or *in situ* when working with reflectometric interference spectroscopy (RIfS). The latter concedes the characterisation of this process in detail. In Figure 4.4 exemplary plots of the change in optical thickness (ΔOT) vs. the time (t) are presented. These have been recorded during the incubation of both hydrophilic (black) and hydrophobic (grey) SiO_2 surfaces with POPC : PtdIns[4,5]P_2 (99 : 1, *n*/*n*) SUVs in a closed circuit. While the addition of vesicle suspension ($m = 0.2$ mg) to the reaction chamber at $t = 0$ min leads to a rapid increase in optical thickness (OT) when working on hydrophilic silicon surfaces (black graph), the change induced on hydrophobically functionalised substrates (grey graph) is reduced. The maxima recorded in these specific measurements for ΔOT are 6.3 nm and 2.8 nm for SLB and SHM, respectively. The statistics of ΔOT for the two membrane systems are displayed in Figure 4.5. Additional to the matrix- to receptor lipid ratio of 99 : 1 (cf. Figure 4.4), the ΔOT values with increased receptor lipid concentrations are presented. Thereby, the influence of the PtdIns[4,5]P_2 content on the resulting membrane thickness was assessed. The data represented in Figure 4.5 A correspond to the detected membrane thicknesses of SLBs while Figure 4.5 B shows ΔOT caused by SHM formation.

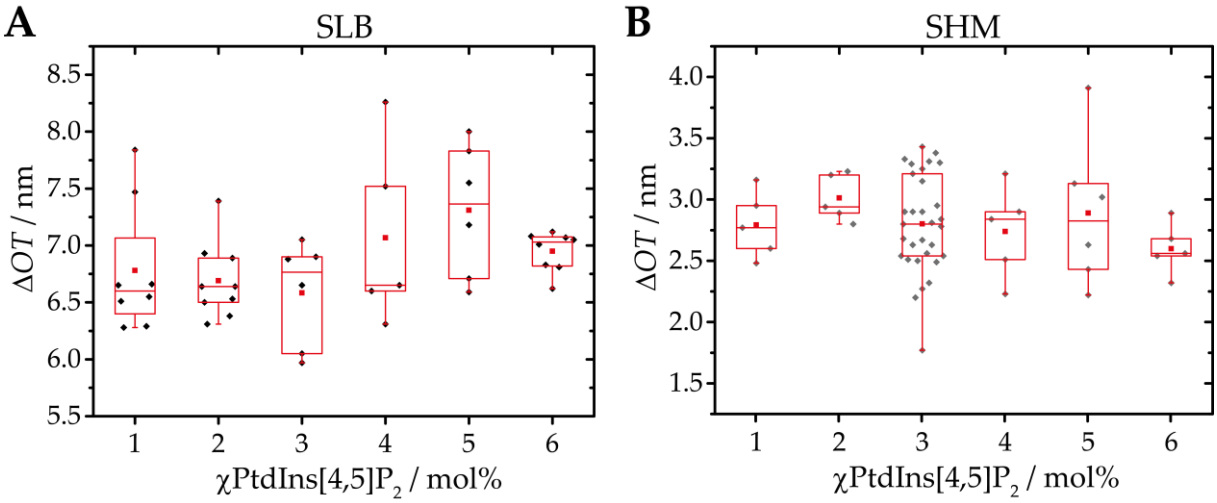

Figure 4.5: Box plots of the model membrane thickness of SLB (**A**) and SHM (**B**) dependent of the PtdIns[4,5]P_2 content in the small unilamellar vesicles used for membrane formation. The boxes extent from upper and lower quartile while the whiskers represent 1st and 99th percentiles. The medians are shown as horizontals inside the boxes and the means are represented by red squares within the respective data sets.

The means of layer thickness for lipid bilayers prepared on hydrophilic SiO_2 surfaces varies from a lower limit of (6.6 ± 0.5) nm for 3 mol% to (7.3 ± 0.6) nm for 5 mol% PtdIns[4,5]P_2. The values determined for SHM thickness rank from (2.6 ± 0.2) nm for 6 mol% to a maximum of (3.0 ± 0.2) nm for 2 mol% of the bisphosphorylated receptor lipid. These values match the expectations as the model membrane on hydrophilic substrates is composed of two lipid leaflets whereas on hydrophobic ones only one leaflet is formed. Therefore, half the thickness of SLB was expected for SHMs. All calculations comprise at least five independent measurements and data sets were analysed using an analysis of variance (ANOVA) to determine significant differences caused by the increased PtdIns[4,5]P_2 content. Though, the rejection of the null hypothesis was not possible as no significant difference between the membrane thicknesses could be detected. One can assume that the thickness of the formed lipid layer is independent of the amount of PtdIns[4,5]P_2.

According to Equation 3.12 the optical thickness is the product of the refractive index n and the physical thickness d. Hence, assuming $n = 1.49$[173–175] the determined changes in OT caused by lipid membrane formation correspond to membrane thicknesses d of (1.9 ± 0.3) nm or (4.5 ± 0.3) nm for SHMs or SLBs, respectively. This is in good agreement with literature values ranging from 4 to 5 nm in case of SLBs.[176] In contrast to that, also a thickness of (3.98 ± 0.08) nm has been reported for a bilayer investigated by means of small-angle neutron and X-ray scattering.[177] Those membranes, in contrast to the ones investigated in this work, were composed of POPC only and additionally were examined by techniques requiring other experimental

conditions. A better comparability is given to a study employing SUVs composed of POPC : PtdIns[4,5]P_2 (92 : 8, *n*/*n*) for membrane formation in RIfS-adsorption experiments, which found a SLB thickness of 4.2 nm.[170] This value not only directly matches to the one determined in this work, it also shows that even higher fractions of PtdIns[4,5]P_2 above the examined range of 0 to 6 mol% do not influence the resulting layer thickness. In case of the SHMs the determined values are slightly reduced compared to those found for erythrocyte membrane layers supported by alkanethiol monolayers on gold substrates.[178,179] This discrepancy is, however, reasonable as the lipid monolayer in the referred studies were prepared from erythrocytes and thus were not only composed of lipid molecules but also contained membrane proteins and other constituents which alter the thickness of a lipid membrane.

It has been shown by LUDOLPHS *et al.* in adsorption studies to SLBs containing 10 mol% receptor lipid, that collybistin 2 is not only specific for binding to PtdIns[4,5]P_2 but is also capable of interacting with other phosphoinositide species.[113] On this account also solid-supported membranes were prepared that were doped with either PtdIns[3]P or PtdIns[3,4,5]P_3. They were prepared in analogy to those of PtdIns[4,5]P_2 containing membranes (cf. Chapter 3.3.4). Therefore, it is possible to determine the effect of the phosphorylation degree on the lipid layer thickness. Multiple RIfS experiments were performed using SUVs composed of POPC : PtdIns[x]P (97 : 3, *n* / *n*) whose results are represented in Figure 4.6. The mean values of SHM thickness (red squares) calculated were (2.7 ± 0.6) nm for PtdIns[3]P ($n = 24$), (2.8 ± 0.4) nm for PtdIns[4,5]P_2 ($n = 31$) and (2.8 ± 0.5) nm for PtdIns[3,4,5]P_3 ($n = 22$). Furthermore, an ANOVA analysis was performed detecting no significant difference between the hybrid membrane thicknesses caused by variation of the receptor lipid. Taking these results and those represented in Figure 4.5 together, one can state that neither the concentration of phosphoinositides nor their phosphorylation degree influence the layer thickness of the model systems in an extent detectable by means of RIfS.

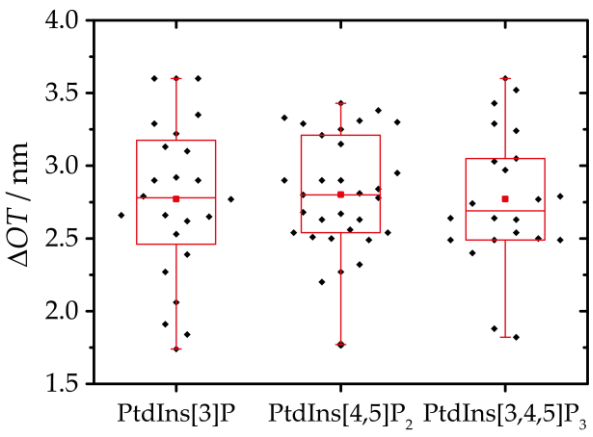

Figure 4.6: Box plots of SHM thicknesses containing 3 mol% of different phosphoinositides. The boxes extent from upper to lower quartile while the whiskers represent 1st and 99th percentiles. The medians are shown as horizontals inside the boxes and the means are represented by red squares within the respective data sets.

4.1.4 Fluidity and lipid mobility in SLBs and SHMs

With the knowledge that the resulting model membrane thicknesses are independent of both phosphoinositide species and their concentration, at least in a range from 1-6 mol%, it is important to examine another relevant feature of the SLBs and SHMs which is the lateral lipid mobility. This is a crucial characteristic as a reduced mobility directly affects e.g. the adsorption process of cytosolic proteins. Each adsorbed protein might cover multiple receptor lipids at once due to its specific footprint which leads to a depletion of pinning points in the membrane. To investigate the lipid mobility, fluorescence recovery after photobleaching (FRAP) experiments (cf. Chapter 3.7.4) were performed on membranes containing a small fraction (1 mol%, equal to 10 % of the total receptor lipid amount) of PtdIns[4,5]P_2 labelled with the fluorescent dye BODIPY®-TMR (cf. Chapter 3.1.1.3). The experiments were all conducted with a confocal LSM 880 Examiner under slightly varying instrumental settings. Nonetheless, the time series detected on an SHM as illustrated in Figure 4.7 A is representative for all measurements on both SLBs and SHMs.

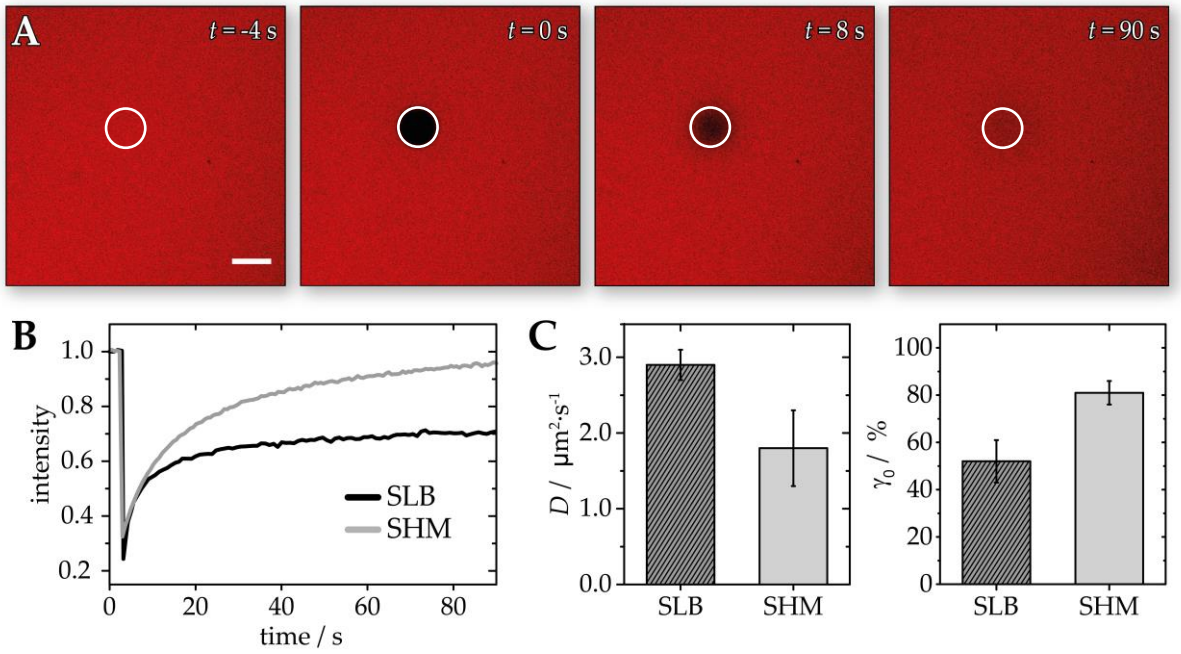

Figure 4.7: A: Time series exemplary displayed in four characteristic frames (t = -4 s, 0 s, 8 s, 90 s) showing the identical scanning area with a region of interest (ROI, highlighted with a white circle) during a fluorescence recovery after photobleaching experiment of an SHM (POPC : PtdIns[4,5]P_2 : BODIPY-TMR-PtdIns[4,5]P_2, 90 : 9 : 1, *n*/*n*/*n*) on a hydrophobically functionalised SiO_2 surface. Scale bar: 10 µm. **B**: FRAP experiments on either SLB (black) or SHM (grey) led to intensity time course as those exemplary shown here. There is a drastic discrepancy in fluorescence recovery detectable between the two model membranes. This is expressed in variations of the diffusion coefficient D and the mobile fraction γ_0, both being displayed in (**C**).

Prior to bleaching with a high intensity laser pulse, the membrane exhibited a homogeneously distributed fluorescence (t = -4 s). This indicates that no clusters of PtdIns[4,5]P_2 in a detectable

size were present within the membrane. Other studies focused on the receptor lipid distribution in the plasma membrane of PC12 cells. They determined inner-leaflet PtdIns[4,5]P_2 microdomains of about 65 nm or 73 nm in size detected either by direct stochastic optical reconstitution microscopy (dSTORM) or stimulated emission depletion (STED) microscopy.[180,181] Though, in both cases it can be assumed that clustering is induced by Ca^{2+} ions which are avoided within the model system applied in this work for this exact reason. Furthermore, the fluorescence images in Figure 4.7 A indicate that the duration of preparation did not lead to an aging process of the membranes. It would result in a great number of defects which would have been detected as areas without fluorescence. The laser pulse causes bleaching of dye molecules in the region of interest (ROI) in which the fluorescence intensity is detected over the whole experimental duration. After a characteristic time fluorescently labelled lipids laterally diffuse into while bleached ones leave the ROI causing a recovery of the fluorescence intensity. This process is vividly shown in the fluorescence micrographs at t = 8 s and t = 90 s. Exemplary background corrected intensity courses within the ROI during a FRAP-experiment for each membrane system are shown in Figure 4.7. The direct comparison visualises the presence of continuous lipid layers on both substrate functionalisations. But it also indicates a different recovery behaviour between SLB (black) and SHM (grey) that affects parameters like the diffusion coefficient D and mobile fraction γ_0. These parameters were calculated to be D_{SLB} = (2.9 ± 0.2) μm²/s with a mobile fraction of 54 ± 9 % (n = 10) for supported lipid bilayer, while the values of SHMs were determined to be D_{SHM} = (1.8 ± 0.5) μm²/s and γ_0 = 81 ± 5 % (n = 7) (cf. Figure 4.7 C). Both values are larger compared to the diffusion of BODIPY®-TMR PtdIns[4,5]P_2 in fibroblasts and epithelial cells with an average of D = (0.8 ± 0.2) μm²/s as determined by GOLEBIEWSKA *et al*. via fluorescence correlation spectroscopy.[182] Additionally, they examined the PtdIns[4,5]P_2 diffusion in Rat1 cells to be D = (2.5 ± 0.8) μm²/s which is in the same range as the diffusion determined for SLBs. The reduced diffusion constant within the SHM compared to that of the SLB is reasonable under the assumption of a stronger hydrophobic interaction between the HMDS-functionalised surface and the hydrophobic fatty acid chains of the lipid molecules. Furthermore, the mobile fraction of the lipid bilayer is only about 50 % and compared to that determined for SHMs considerably smaller. The same tendency has been recognised by BRAUNGER *et al*.,[170] who determined a mobile fraction of 64 ± 3 % for

SLBs and 98 ± 3 % for SHMs with a different fluorescently labelled PtdIns[4,5]P_2 on an alternative hydrophobic monolayer. The discrepancy can be explained with the direct interaction of the lower (proximal) leaflet in SLBs with the solid support resulting in an immobilisation of the PtdIns[4,5]P_2 derivative. In case of PtdIns[4,5]P_2 BAUMANN *et al.* assumed that the negative charge of the lipid (charge repulsion) and the steric demand of its head group (large hydration shell) are possible reasons for the mobility reduction in SLBs.[183] They suggested pits in the negatively charged substrate as potential wells of suitable dimensions for the receptor lipid leading to a reduced diffusion.

An additional aspect is the used labelled PtdIns[4,5]P_2 derivative which was non-natural and differed from natural PtdIns[4,5]P_2 due to shorter fatty acid chains. Therefore, the results did not report quantitative numbers of the latter's diffusive behaviour, still clearly expressed the different diffusion in both membrane systems and additionally are in good agreement with diffusive parameters found in similar systems.[170]

In conclusion the model membranes prepared on silicon dioxide substrates with two opposing surface features have shown to present all prerequisites necessary for detailed adsorption experiments. Furthermore, both SLBs and SHMs provide features which are close to those of *in vivo* systems even though the hybrid membrane is composed of only a single lipid layer and thus is in general more far away from physiology. Nonetheless, these models facilitate a closer look on the effect of the respective surface on the coating of lipid layers when compared under exact same conditions. On this account the accessibility of PtdIns[4,5]P_2 was addressed by adsorption studies of specific marker proteins. The corresponding results are presented in the subsequent chapter.

4.2 Characterisation of the leaflet-dependent distribution of PtdIns[4,5]P_2 in solid-supported lipid bilayers

-Some of the results presented in this Chapter have been published in "Leaflet-Dependent Distribution of PtdIns[4,5]P_2 in Supported Model Membranes" by J.Schäfer et al., Langmuir, ***2020****, 36, 1320-1328.*[158]*-*

-Some of the RIfS experiments have been performed by Jessica Nehls as part of her bachelor thesis-

-Atomic force micrographs of the SHMs were taken by Anna Lena Toschke as part of her bachelor thesis-

In Chapter 1.4 the importance of *in vitro* model systems to characterise crucial physiological processes and interactions has already been mentioned. This is equally true for investigations focussing on the receptor lipid PtdIns[4,5]P_2 which is the most abundant phosphoinositide in the plasma membrane.[111,184] It is a known source for the second messengers inositol triphosphate (IP_3) and diacylglycerol (DAG) and contributes to intracellular signalling processes.[185] Furthermore, it has a pivotal role in eukaryotic cell functions such as cytoskeletal dynamics, signal transduction, ion channel activation and endo- and exocytosis.[97,186–189] In part, these functions are based on the specific interaction of cytosolic proteins with PtdIns[4,5]P_2.[190–192] Some of these interaction partners harbouring protein domains of known and well-conserved structures like ENTH-, FERM-, FYVE-, PH-, PX-, and Tubby domains, while others bind via rather unstructured protein parts.[96,193–196] Due to a rather simple preparation protocol (cf. Chapter 3.3.4) SLBs doped with PtdIns[4,5]P_2, which are negatively charged at physiological pH, are often produced via spreading of SUV on surfaces providing low surface roughness.[105,197] The success of membrane formation depends on various factors among which the presence of divalent cations especially Ca^{2+}, the ionic strength and pH of the environment, the vesicle size and lipid composition are decisive parameters.[198–202] If the interplay of all these aspects is appropriate, spontaneous rupturing of absorbed vesicles leads to lipid bilayer formation.[203] Nevertheless, it is necessary to keep in mind that some factors directly influence the formed SLB, such as the presence of Ca^{2+} induces aggregation of PtdIns[4,5]P_2 in lipid monolayers and vesicles.[204,205] Unfortunately, the effect of the hydrophilic surface properties of the solid support and especially the surface charge density of e.g. SiO_2 or mica on the distribution of charged lipid molecules in the membrane leaflets has not been considered yet. Therefore, this Chapter will focus on the exact portion of accessible PtdIns[4,5]P_2 molecules in an SLB. On this purpose advantage will be taken of the two model membrane systems characterised before, enabling determination of PtdIns[4,5]P_2 accessibility via marker protein adsorption. The proteins utilised as markers in this work are the *N*-terminal domain of ezrin (N-ERMAD) and the *C*-terminal PH domain of collybistin 2 (CB2) both known to exhibit binding affinity to the phosphoinositide. They were expressed in a recombinant fashion as described in Chapter 3.2.5, purified

with affinity chromatography (cf. Chapter 3.2.7.1) and identified with polyacrylamide gel electrophoresis (PAGE) and Western blots (cf. Chapters 3.2.8 and 3.2.9). The results of this process are described in Chapter 4.2.1. The results of marker protein adsorption via RIfS experiments will be focus of Chapter 4.2.2, moreover, the examinations of surface coverage via AFM are shown in Chapter 4.2.3.

4.2.1 Isolation of the marker proteins N-ERMAD and CB2$_{PH}$

4.2.1.1 Isolation of N-ERMAD

The expression and isolation of the *N*-terminal domain of ezrin was conducted several times in the progress of this work following a protocol well consolidated throughout previous studies.[206–208] After protein expression the target protein was purified via immobilised metal ion affinity chromatography (IMAC, cf. Chapter 3.2.7.1) taking advantage of the *N*-terminally fused His$_6$-tag. A combination of sodium dodecyl sulfate-polyacrylamide gel electrophoresis (SDS-PAGE) with Western blot was performed to control the success of the target protein isolation. Examples for both, PAGE and blot, are shown in Figure 4.8 A and B, respectively.

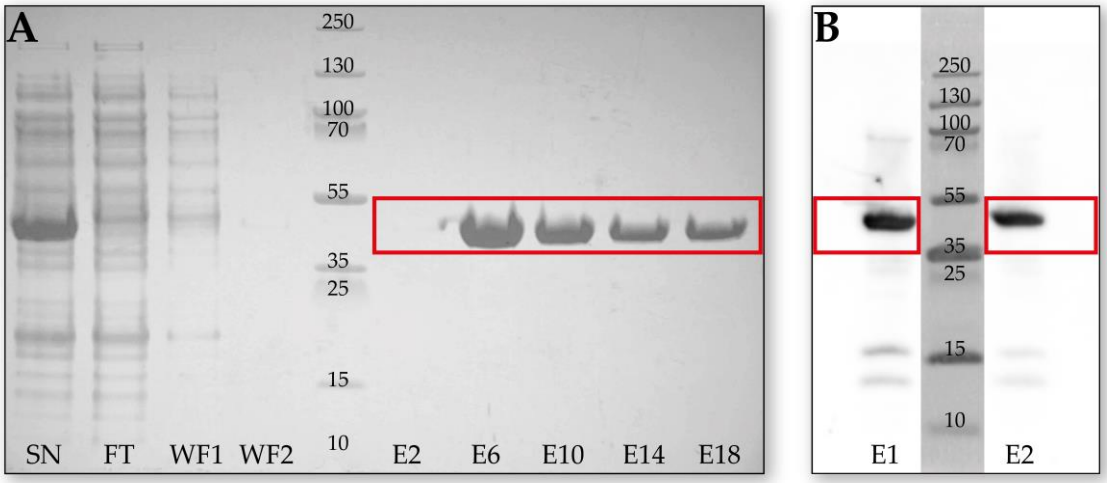

Figure 4.8: A: SDS-PAGE of N-ERMAD with the supernatant after ultra-centrifugation (SN), the flow through (FT) and washing fractions (WF), and multiple elution fractions (E) loaded to the polyacrylamide gel. **B**: Corresponding Western blot overlay (of luminescence and marker image) with two early elution fractions of N-ERMAD loaded to the gel and a specific primary antibody against the *N*-terminally fussed His$_6$-tag.

The SDS-PAGE allows a qualitative classification using a mass reference only. In the supernatant (SN) after lysate clarification a variety of bands over the whole mass range (10 to 250 kDa) was detected. This number of bands was reduced both in quantity and intensity when comparing the traces of flow through (FT) and washing fraction 1 (WF1). While in WF2 and the early elution fraction (E2) no bands were detected, in each of the other elution fractions (E6 to

E18) a single vigorous band with a mass between 35 and 55 kDa was exclusively visible. This band was also present in SN in a prevalent fashion while in FT, WF1 and 2 no correlating signal was detected. These results suggest that the incubation of the immobile IMAC phase (NTA(Ni^{2+}) agarose) with the clarified lysate led to a specific fixation of the proteins correlating with this band. Additionally, the gel shows that none of the other proteins interacted with the resin due to their detection in the flow through and WF1. These proteins were completely removed from the column as fraction WF2 did not show any signal within its trace. The lack of bands within the early elution fractions (represented by E2) can be explained by both the dead volume of the column outlet and a short duration of tag cleavage. Another reason for this can be accounted for the detection limit of SDS-PAGE, which was proven by an additional Western blot as shown in Figure 4.8 B. The WB exhibits an increased sensitivity, achieved through use of specific antibody (Anti-His), and is therefore capable of detecting in a lower concentration regime than PAGE,[209,210] resulting in a predominant signal for a His_6-tag carrying protein with a mass again ranging between 35 and 55 kDa. Also, bands with reduced intensity were detected in the lower molecular regime. These might correspond to not completely expressed protein fragments as the His_6-tag is *N*-terminally fused and thus expressed first.
The theoretical mass of N-ERMAD calculated with the PROTPARAM tool[211] is M_{theo} = 38.75 kDa based on the known amino acid sequence (cf. Appendix A.4.1), therefore it is reasonable to assume that the most intense band in both SDS-PAGE and WB correlates with the target protein, even though it appears at slightly higher masses. This tendency is also known for the full-length protein ezrin and is declared to be caused by the high intrinsic charge of the protein.[212] This can also be transferred to N-ERMAD, which contains 91 charges amino acids among the 332 in total, leading to an anomalous migration within the electric field during PAGE. Since the SDS-PAGE only shows this specific protein band in the elution fractions the isolation was successful, notwithstanding the fact that in WB slight contaminations of lower and higher molecular weights have been detected. Afterwards, the protein was dialysed against E1 buffer (cf. Table 3.14) and subsequently stored at 4 °C until further use in adsorption experiments.

4.2.1.2 Isolation of CB2PH

The *C*-terminal PH domain of collybistin 2 (CB2PH, M_{theo} = 20.96 kDa) was expressed from *E. coli* cells containing the vector pTYB21. After lysis and ultra-centrifugation, the clarified lysate was applied on an affinity chromatography column containing a chitin resin as immobile phase. The process and success of this purification steps were controlled via SDS-PAGE as exemplary shown in Figure 4.9 A.

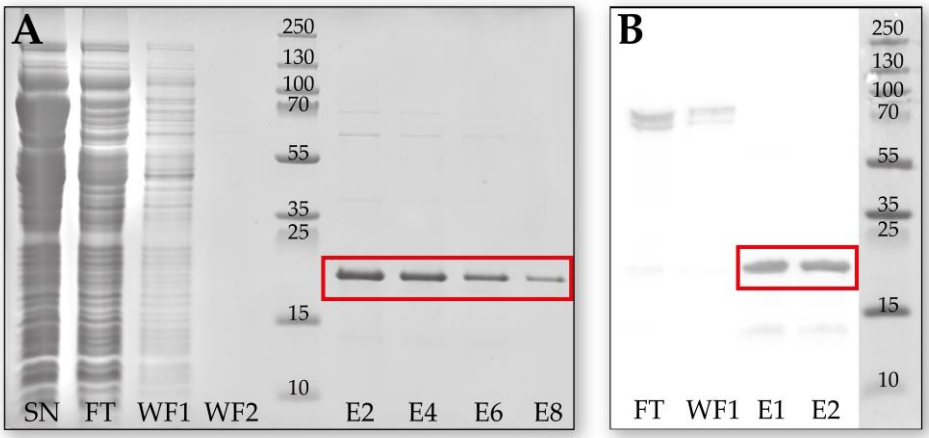

Figure 4.9: A: SDS-PAGE of the collybistin isoform CB2PH after purification via affinity chromatography against a chitin resin. The collected fractions of supernatant (SN), flow through (FT), washing (WF) and elution (E) were investigated to control the isolation of the target protein. **B**: Western blot overlay with isolation fractions tested for CB2PH under the use of a specific CB2 primary antibody.

In the exemplary SDS-PAGE multiple bands were detected in all traces of supernatant (SN), flow through (FT) and washing fraction 1 (WF1) with diminishing intensities. The fraction of the second washing step (WF2) presented no bands, while in all elution fractions (E2 to E8) three well separated bands were detected. The intensities of all signals decreased with higher fraction numbers suggesting a gradual removal from the chitin resin by elution. The prevalent band was located between the 15 and 25 kDa bands of the mass standard in contrast to the other two that were visible at higher molecular weights. These results suggest that the dominant band in E2 to E8 correlates with CB2PH based on the known calculated molecular weight. The SN clearly indicates that next to CB2PH a larger number of other proteins was expressed. The target protein was immobilised and remained on the column while the majority of proteins either directly flow through the column without retention (FT) or was washed from it in the first washing fraction (WF1). This assumption is based on the absence of a predominant signal within the corresponding mass range between 15 and 25 kDa in both traces. The second washing step not only was used to remove further contaminations but also increased the con-

centration of DTT on the column, thus, inducing the cleavage of the affinity tag from the protein allowing the elution of the later. Nonetheless, the extra signals needed additional examination to make sure whether they corresponded to oligomers of the PH domain or other collybistin isoforms. Thus, a Western blot was performed with a specific primary antibody against collybistin 2. As clearly shown in Figure 4.9 B the impurities of around 70 kDa were also present in the FT and WF1. Yet, they did not correspond to the similar proteins detected in the elution fractions of the SDS-PAGE because no such signal was visible in the elution fractions of the WB. In the elution fractions examined by WB, however a small contamination of 14 kDa was detected. Therefore, the protein corresponding to the signal must contain the epitope sequence to the used antibody suggesting the existence of an incomplete PH domain fragment. However, it was refrained from a subsequent application to an ion-exchange chromatography (IEC) due to no significant improvement in purity as shown in previous work.[213] A size-exclusion chromatography was also discarded as a successful separation of molecules with a molecular weight difference of around 6 kDa was unlikely. Accordingly, the protein solution was stored at 4 °C until it was transferred into another buffer system (cf. Chapter 3.2.10.2) directly before use in adsorption experiments which will also be focus of the following section.

4.2.2 Binding of the marker proteins to SLBs and SHMs

4.2.2.1 Adsorption of N-ERMAD to SLBs and SHMs with varying PtdIns[4,5]P_2 proportion

The issue of receptor lipid accessibility for marker protein adsorption in SLBs and SHMs as a function of different nominal PtdIns[4,5]P_2 concentrations in the SUVs was addressed by RIfS experiments. This allowed monitoring of the time-resolved change in *OT*, which is a good readout parameter for the amount of bound protein. *OT* is the product of the refractive index *n* and the physical thickness *d*. With the refractive indices for silicon dioxide, lipid membranes and proteins being in a similar range,[145,214,215] detected changes in *OT* can be correlated to changes of the physical layer thickness induced by deposition and adsorption in the scanning area (1 mm²). While the prepared membranes contained different nominal amounts of phosphoinositide the concentration of added N-ERMAD in solution remained constant. A typical graph of such an experiment is presented in Figure 4.10 A for an SLB prepared via SUV (POPC : PtdIns[4,5]P_2, 96 : 4, *n*/*n*) spreading on hydrophilic SiO_2. The arrows in this image indicate from left to right the incubation with SUV suspension, followed by rinsing with E1-buffer (cf. Table 3.14) and the addition of N-ERMAD (c = 850 nM). The experimental course was identical for all measurements independent of the solid support or the receptor lipid concentration resulting in N-ERMAD adsorption as exemplary portrayed in Figure 4.10 B on SLBs with increasing PtdIns[4,5]P_2 fractions from 0 to 6 mol%. The adsorption curves firstly show no nonspecific binding of N-ERMAD in the absence of PtdIns[4,5]P_2 and secondly indicate that with an increasing ratio of receptor lipid also the amount of adsorbed protein rose, represented by a higher Δ*OT* value. Only at higher

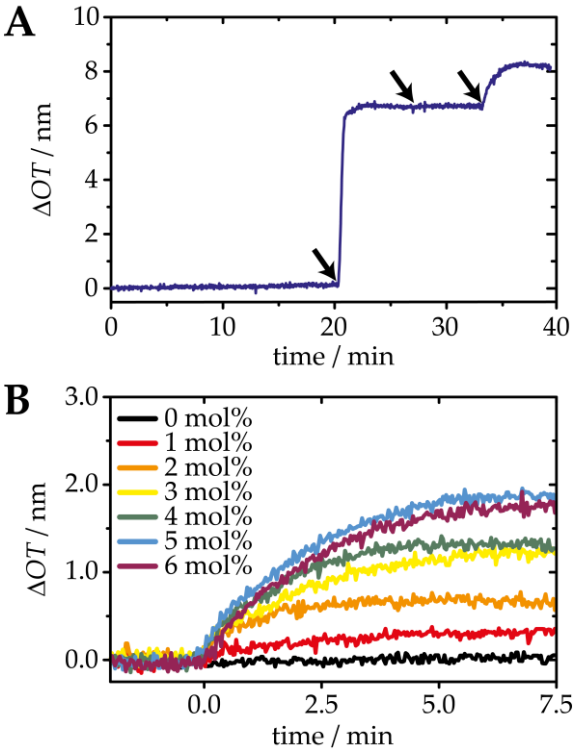

Figure 4.10: A: Exemplary plot of the change in optical thickness vs. the time of an adsorption experiment with N-ERMAD (850 nM) on an SLB formed via SUV (POPC : PtdIns[4,5]P_2, 96 : 4, *n*/*n*) spreading on a hydrophilic SiO_2 substrate. The arrows indicate from left to right: addition of SUV-suspension, buffer system change and incubation with N-ERMAD. **B**: Examples of N-ERMAD (c = 850 nM) adsorption to SLBs with receptor lipid concentrations from 0 to 6 mol% as indicated.

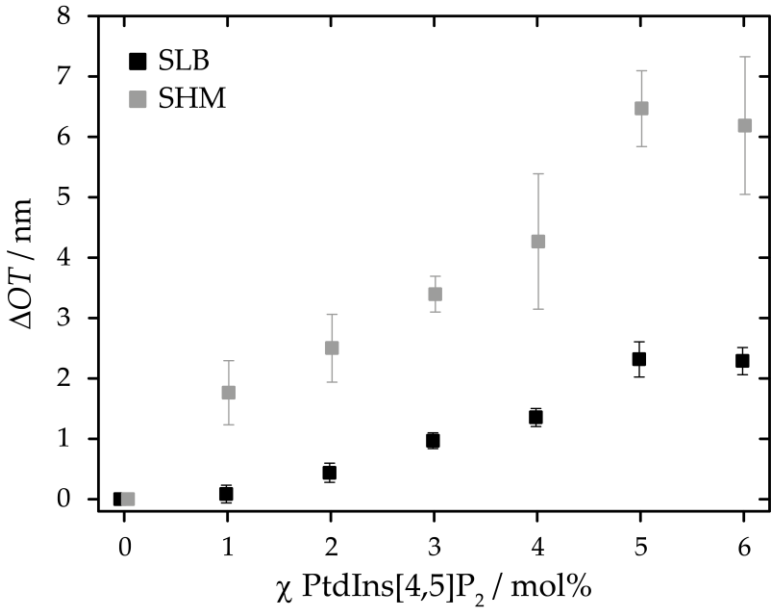

Figure 4.11: Statistical analysis of the maximum Δ*OT*s obtained for N-ERMAD adsorption on SLBs (black) and SHMs (grey), respectively, as a function of PtdIns[4,5]P_2 in the membrane. Error bars are the standard error of the mean with $n \geq 4$.

phosphoinositide concentrations of 5 and 6 mol% no further increase was detected. This might hint at maximum surface coverage by N-ERMAD. A similar trend was found for the ezrin mutant T567D in RIfS adsorption experiments.[187] By reading out the maximum change in optical thickness for the adsorption to both SLB and SHM under otherwise exact same conditions the amount of bound protein was determined as presented in Figure 4.11. The graph shows that incubation with N-ERMAD leads to larger changes in *OT* on hybrid membranes than those detected on lipid bilayers over all fractions of PtdIns[4,5]P_2. This clearly demonstrates that the concentration of accessible receptor lipid is higher in SHMs than in SLBs. To estimate a relation factor describing the accessibility discrepancy, the determined Δ*OT*s for SHMs were divided by the corresponding changes on SLBs at each receptor lipid content. The calculated asymmetry factors are summarised in Table 4.1.

Table 4.1: Asymmetry factors determined for N-ERMAD adsorption at different receptor lipid fractions.

χPtdIns[4,5]P_2	1	2	3	4	5	6
asymmetry factors	21.7	5.7	3.5	3.2	2.8	2.7

The values are evidence for the heterogeneous distribution of PtdIns[4,5]P_2 in silicon dioxide supported lipid bilayer resulting in an enrichment of the negatively charged lipid in the proximal leaflet. Consequently, a mismatch arises between nominal and accessible receptor lipid content.

4.2.2.2 Adsorption isotherms of N-ERMAD and $CB2_{PH}$ to SLBs and SHMs

In addition to the single injection experiments (cf. Figure 3.8 A) on varying PtdIns[4,5]P_2 fractions also measurements were performed in which a successive and stepwise increase in protein concentration took place while the receptor lipid concentration remained constant (cf. Figure 3.8 B). To rule out that the observed differences shown in Figure 4.11 and Table 4.1 are a function of the protein under investigation, two different proteins were used harbouring either the FERM domain (N-ERMAD) or a PH domain ($CB2_{PH}$). In case of N-ERMAD a receptor lipid concentration of 1 mol% was chosen to obtain on one hand a good signal to noise ratio but also to guarantee that no maximum protein surface coverage was reached. On the other hand, for $CB2_{PH}$ a higher phosphoinositide concentration of 10 mol% was employed to ensure a good signal to noise ratio and to obtain similar changes in optical thickness for both proteins.[113] The stepwise concentration increase from either 0 to 1.5 µM for N-ERMAD or from 0 to 3.5 µM for $CB2_{PH}$ resulted in adsorption curves like those exemplary shown in Figure 4.12 A or B, respectively. To highlight the adsorption process the established membrane plateaus were set to zero

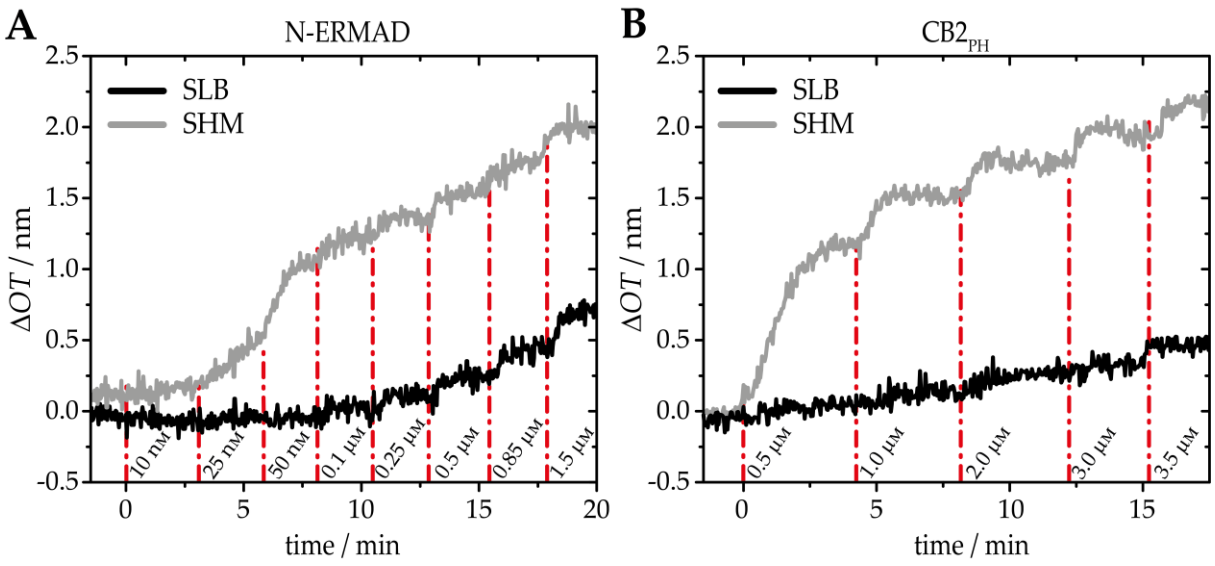

Figure 4.12: Exemplary plots of the change in optical thickness vs. the time during the adsorption of N-ERMAD (**A**) and $CB2_{PH}$ (**B**) on either SLBs (black) or SHMs (grey). In case of N-ERMAD the membranes were composed of (POPC : PtdIns[4,5]P_2, 99 : 1, *n*/*n*), while for $CB2_{PH}$ the membrane composition was (POPC : PtdIns[4,5]P_2, 9 : 1, *n*/*n*). The successive protein injections resulted in a stepwise concentration increase as indicated by the red dashed lines which also mark the moments of protein addition. The corresponding protein concentration is also indicated in each injection frame.

($\Delta OT_{SLB} = \Delta OT_{SHM} \stackrel{!}{=} 0$ nm, cf. Figure 3.8 B). The successive protein injections were performed in an open system configuration, therefore an adequate volume of protein solution had to be applied to ensure the detection of newly reached plateaus simplifying the ΔOT determinations. As shown in Figure 4.12 A the exposure of both membranes doped with 1 mol%

PtdIns[4,5]P_2 to small N-ERMAD concentration (c < 50 nm) led to no or only slight changes in optical thickness in case of SLB or SHM, respectively, indicating a very low amount of adsorbed protein. This is reasonable as the membranes also exhibited only a poor pinning point density at this receptor lipid content. Nevertheless, with increasing protein concentration the optical thickness is drastically raised on SHM compared to the signal changes on the lipid bilayer. These results are in good agreement with the trend detected on increasing PtdIns[4,5]P_2 concentrations as shown in Figure 4.11. Additionally, the graphs in Figure 4.12 B prove that the discrepancy in adsorbed protein is not a N-ERMAD specific feature but was also detected for CB2PH. This consequently indicates that there is a discrepancy in concentration of accessible receptor lipid between the solid-supported bilayer and the hybrid membrane. This effect seems to be more pronounced in case of CB2PH as the Δ*OT*s on the SHM are a multiple of those detected on the SLB after protein addition, although the pinning point density in the model membranes of these experiments was significantly increased. These findings are mirrored in the statistics of all multiple injection experiments that are summarised in Figure 4.13. For N-ERMAD (cf. Figure 4.13 A) each data point is based on at least four independent measurements, while the data set of CB2PH shown in Figure 4.13 B is composed of at least three individual results.

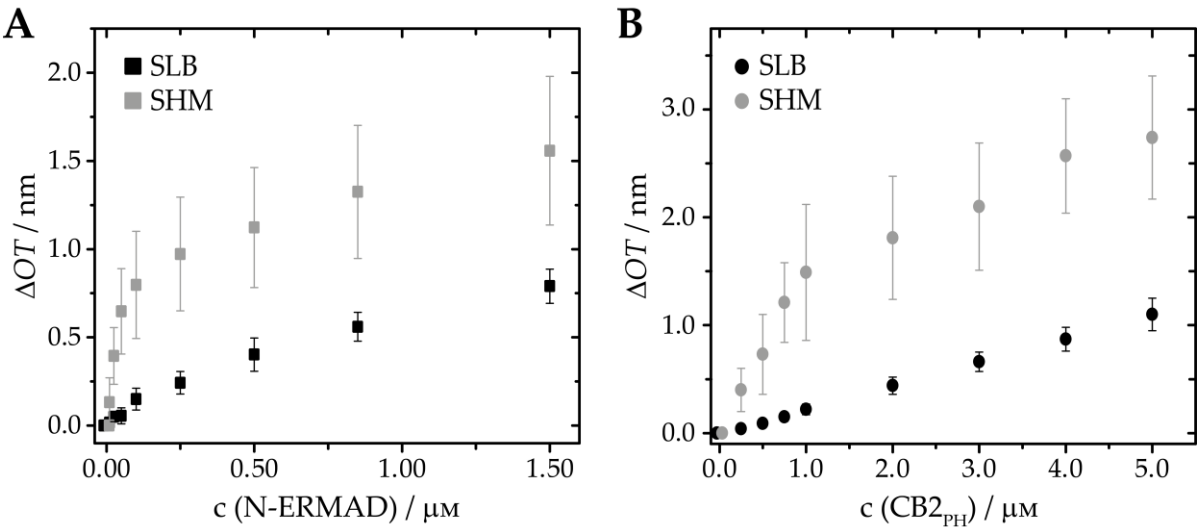

Figure 4.13: A: Adsorption isotherms of N-ERMAD on POPC : PtdIns[4,5]P_2 (99 : 1, *n*/*n*) membranes. Error bars are the standard error of the mean with $n \geq 4$. **B**: Adsorption isotherms of CB2PH on POPC/PtdIns[4,5]P_2 (9 : 1, *n*/*n*) membranes. Error bars are the standard error of the mean with $n \geq 3$.

Again, the graphs indicate a higher amount of adsorbed protein in the hybrid membrane system in contrast to that on the SLBs, allowing another determination of asymmetry factors for either N-ERMAD (cf. Table 4.2) or CB2PH (cf. Table 4.3).

Table 4.2: Asymmetry factors determined for adsorptions of various N-ERMAD concentrations at a constant receptor lipid fraction.

Protein	N-ERMAD							
χ(PtdIns[4,5]P_2) / mol%	1							
c(Protein) / μM	0.01	0.025	0.05	0.10	0.25	0.50	0.85	1.50
Asymmetry factor	7.6	7.9	11.8	5.3	4.0	2.8	2.4	2.0

Table 4.3: Asymmetry factors determined for adsorptions of various CB2PH concentrations at a constant receptor lipid fraction of 10 mol%.

Protein	CB2PH							
χ(PtdIns[4,5]P_2) / mol%	10							
c(Protein) / μM	0.25	0.50	0.75	1.00	2.00	3.00	4.00	5.00
Asymmetry factor	10.0	8.1	8.1	6.8	4.1	3.2	3.0	2.5

The calculated factors first of all support the assumption of a heterogeneous receptor lipid distribution inside an SLB. However, it appears that with higher amount of protein available the discrepancy is alleviated for both proteins. Whereby this tendency is more pronounced in case of N-ERMAD as it became obvious for lower protein concentrations tested than those applied during CB2PH examination.

Langmuir adsorption isotherm

Refocussing on Figure 4.13, it seems that only isotherms detected on lipid monolayers reach a saturation. Therefore, these data were used to determine thermodynamic parameters such as the affinities of both proteins for PtdIns[4,5]P_2. For this type of analysis, the adsorption isotherm of LANGMUIR describing the dynamic equilibrium of adsorption and desorption processes on interfaces in dependency of temperature and concentration can be deployed. It is based on the following assumptions:

- The adsorption of molecules on an interface leads to a mono molecular layer.
- The surface quality is uniform, and all pinning points are equal.
- The amount of pinning points is finite.
- The adsorption to each pinning point is independent of all other interaction sides.

In his theory LANGMUIR not only considered the adsorption process of a ligand L to pinning point P but also the transport of ligands to the interface. The concentration of freely diffusing ligands c_L in the interaction layer is reduced due to binding of L to P. This decrease must be compensated by transport of L to the interaction layer and only in case the transport is at least ten times faster than the adsorption, the latter is the rate-determining process. The dynamic equilibrium of freely diffusing (L) and adsorbed ligand (L-P) is described by:

$$\mathrm{L} + \mathrm{P} \underset{k^-}{\overset{k^+}{\rightleftharpoons}} \mathrm{L{-}P}$$

Here k^+ describes the rate constant of adsorption while k^- correlates to the desorption process. This leads to the following differential equation for the adsorption speed of L:

$$\frac{d\Gamma_{\mathrm{L-P}}(t)}{dt} = k^+\Gamma_{\mathrm{P}}(t)c_{\mathrm{L}}(t) - k^-\Gamma_{\mathrm{L-P}}(t) \qquad \textbf{4.1}$$

In Equation 4.1 $c_L(t)$ describes the concentration of free ligand, $\Gamma_P(t)$ and $\Gamma_{L\text{-}P}(t)$ the area concentrations of either vacant pinning points or bound L at moment t. When assuming an excess of L towards P, $c_L(t)$ equals the initial concentration $c_{L,0}$ at $t = 0$. Furthermore, the vacant pinning points $\Gamma_P(t)$ can be expressed by $\Gamma_{P,0}$-$\Gamma_{L\text{-}P}(t)$ with $\Gamma_{P,0}$ being the initial concentrations of pinning points. Both relations lead to a modification of Equation 4.1 resulting in Equation 4.2:

$$\frac{d\Gamma_{\mathrm{L-P}}(t)}{dt} + \left(k^+c_{\mathrm{L},0} + k^-\right)\Gamma_{\mathrm{L-P}}(t) = k^+c_{\mathrm{L},0}\Gamma_{\mathrm{P},0} \qquad \textbf{4.2}$$

When adsorption and desorption rates are equal in equilibrium, the change of occupied pinning points $d\Gamma_{L\text{-}P}(t)/d(t)$ is zero which simplifies the equation to:

$$k^+c_{\mathrm{L},0}\left(\Gamma_{\mathrm{P},0} - \Gamma_{\mathrm{L-P}}\right) = k^-\Gamma_{\mathrm{L-P}} \qquad \textbf{4.3}$$

In equation $\Gamma_{L\text{-}P}$ depicts the concentration of bound ligand in the equilibrium state. In general, the dissociation constant K_D is defined by the rate constant for adsorption and desorption by the following relation:

$$K_{\mathrm{D}} = \frac{k^-}{k^+} \qquad \textbf{4.4}$$

Additionally, the occupancy rate of the interface Θ varying between $0 \leq \Theta \leq 1$ is defined by:

$$\Theta = \frac{\Gamma_{\mathrm{L-P}}}{\Gamma_{\mathrm{P},0}} \qquad \textbf{4.5}$$

Substitutions in Equation 4.3 under consideration of the relation outlined in Equations 4.4 and 4.5 result in a term for the surface occupancy in the system:

$$\Theta = \frac{c_{\mathrm{L},0}}{K_{\mathrm{D}} + c_{\mathrm{L},0}} \qquad \textbf{4.6}$$

In this work the surface coverage was determined via RIfS as exemplary shown in Figure 4.13 in the change of optical thickness. Therefore, the surface occupancy in this case can also be described as:

$$\Theta = \frac{\Delta OT}{\Delta OT_{\max}} \qquad \textbf{4.7}$$

Therefore, Equation 4.6 can be modified to:

$$\Delta OT = \Delta OT_{\max} \frac{c_{\mathrm{L},0}}{K_{\mathrm{D}} + c_{\mathrm{L},0}} \qquad \textbf{4.8}$$

From an application of ΔOT against the concentration of ligand, being the concentration of injected marker proteins (both N-ERMAD and CB2$_{PH}$), an adsorption isotherm is obtained. By fitting Equation 4.8 to the resulting graph the thermodynamic parameter K_D can be determined.

This was done for the data of N-ERMAD adsorption to SHMs illustrated in Figure 4.13 resulting in a dissociation constant of K_D(N-ERMAD) = (72 ± 12) nM. No K_D value for N-ERMAD to PtdIns[4,5]P$_2$ has been reported so far. Though a former study examined a K_D value of 52 nM for the full-length protein of ezrin (wild-type) by means of quartz crystal microbalance (QCM) experiments which at least is in the same range.[216]

The RIfS examinations in total showed that there are effects on hydrophilic silicon dioxide substrates present leading to a heterogeneous PtdIns[4,5]P$_2$ distribution inside the two leaflets of SLBs. This distribution causes a depletion in accessible receptor lipid concentration in contrast to that of an SHM, resulting in a decreased amount of bound marker proteins on the SLB surface. But to guarantee that this discovery is a function of bound protein and not induced by, for example, an increased number of defects in the membrane owing to the different functionalisation strategies, the surface coverage was independently analysed by AFM. The results gathered by this experimental approach will be displayed in the subsequent section.

4.2.3 Topographical analysis of adsorbed marker proteins via AFM

Contrary to RIfS, atomic force microscopy is an invasive technique. It was used to verify the findings on protein adsorption discrepancy between solid-supported lipid bilayers and hybrid membranes, both on silicon dioxide substrates. Based on the results gathered by means of RIfS,

it remained elusive whether the determined trend was caused by heterogeneities, like for example membrane defects, in the model membranes. This option can be validated by AFM as a direct distinction between membrane surface and adsorbed deposits is possible. However, due to the invasive character caused by the direct interaction of the cantilever with the surface of the specimens their features had to be adjusted to obtain micrographs of optimum quality. On this account, next to POPC also DPPC (cf. Scheme 3.1) was deployed as matrix lipid. The latter is in the crystalline phase at room temperature because of the high main transition temperature of 41 °C. Thus, the DPPC membranes provide rigid features leading to a reduced lateral motion of the lipids and consequently of adsorbed proteins in case of N-ERMAD. This feature allows imaging at a reduced speed resulting in micrographs with high contrast and sharp resolution.[217] Two of these micrographs are presented in Figure 4.14 showing an SLB (A) and SHM (B) composed of DPPC : PtdIns[4,5]P_2 (97 : 3, *n*/*n*) before addition of N-ERMAD.

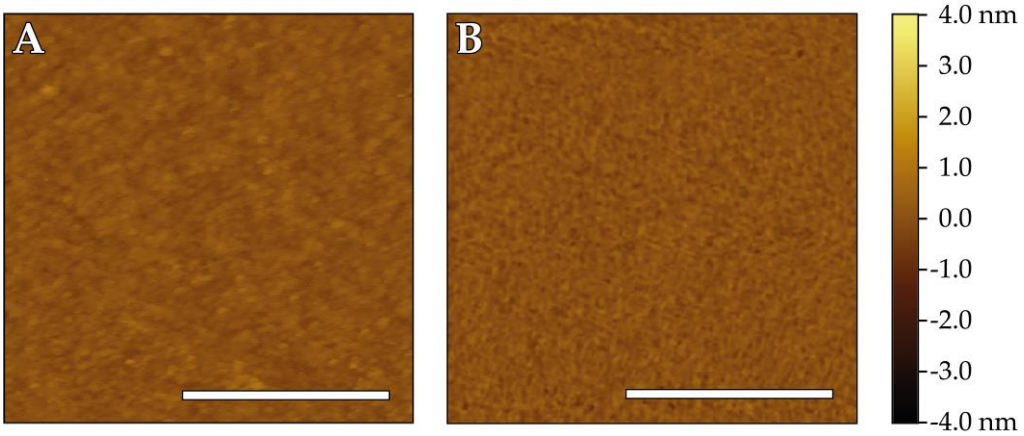

Figure 4.14: Atomic force micrographs of an SLB (**A**) and SHM (**B**) composed of DPPC : PtdIns[4,5]P_2 (97 : 3, *n*/*n*) prior to N-ERMAD addition. Scale bars: 500 nm.

Both images indicate homogeneous membrane surfaces with only slight fluctuations in height without any defects present, that would have been represented by black areas inside the otherwise uniform lipid layers. Based on these results obtained from membranes that were at least two hours old due to their preparation process and the subsequent control via fluorescence microscopy (cf. Chapter 3.3.4), it can be assumed that the membranes formed *in situ* during RIfS experiments exhibited similar qualities. Furthermore, resulting membrane features should be independent of the matrix lipid (DPPC or POPC) if all preparation steps were performed above the corresponding main transition temperature. Only the lipid mobility will be reduced in the resulting DPPC membranes. These identical qualities have been proven in various studies which employed different surface-sensitive technique such as RIFTS, AFM and

dissipation-enhanced QCM.[218–220] Moreover, LIND et al. were able to show, that the preparation of SLBs from DPPC-SUVs is even possible when working below the main transition temperature.[221]

The membranes of proven quality were subsequently exposed to the marker proteins for at least one hour at room temperature and then imaged in intermittent-contact mode (cf. Chapter 3.6.3). Examples of such micrographs presenting higher structures on the membrane surface, which were attributed to adsorbed N-ERMAD on either SLB (A) or SHM (B), are illustrated in Figure 4.15.

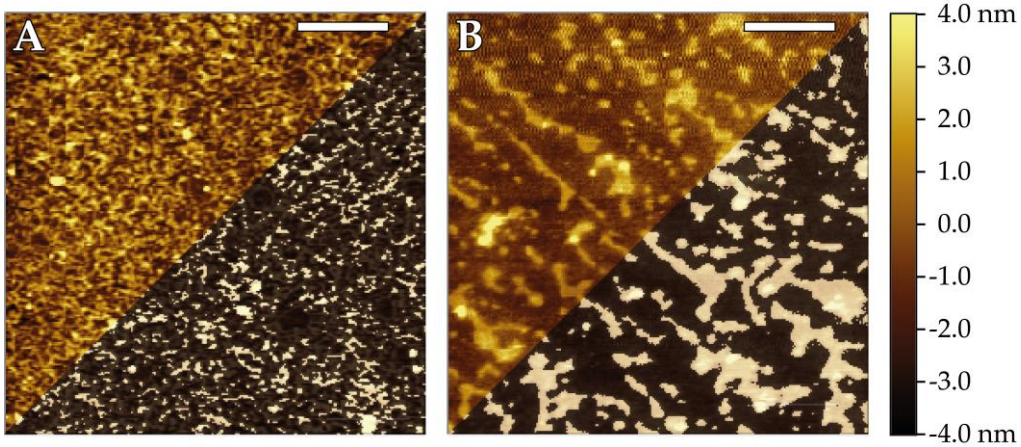

Figure 4.15: Atomic force micrographs of model membranes composed of DPPC : PtdIns[4,5]P_2 (97 : 3, *n*/*n*) with N-ERMAD adsorbed to an SLB (**A**) and SHM (**B**). Scale bars: 1 µm. The micrographs (original data represented in the upper left half) were analysed using a threshold to distinguish uncovered membrane (in black) from protein deposits (in white) shown as overlays in the lower right half of both micrographs.

Both micrographs (upper left) show adsorbed N-ERMAD structures (golden) on top of the membrane surfaces (brown). It is obvious that the protein arranges in different shapes on SLB and SHM. While the protein deposits on SLBs tend to form reticular structures (cf. Figure 4.15 A) which has also been observed by SHABARDINA *et al.*,[217] N-ERMAD on SHMs rather forms greater aggregates of no specific shape (cf. Figure 4.15 B). Nonetheless, in both cases adsorbed protein structures and membrane could be distinguished by applying a threshold. The thresholding process resulted in black and white images of the original data, with white representing the surface covered by protein. These are shown as overlays in the lower right half of both micrographs in Figure 4.15.

In analogy to these examinations, topographical experiments on SLBs and SHMs, containing a strongly increased amount of receptor lipid (10 mol%), after CB2PH adsorption have also been performed. Representative for the gathered results Figure 4.17 displays two micrographs of CB2PH on either SLB (A) or SHM (B).

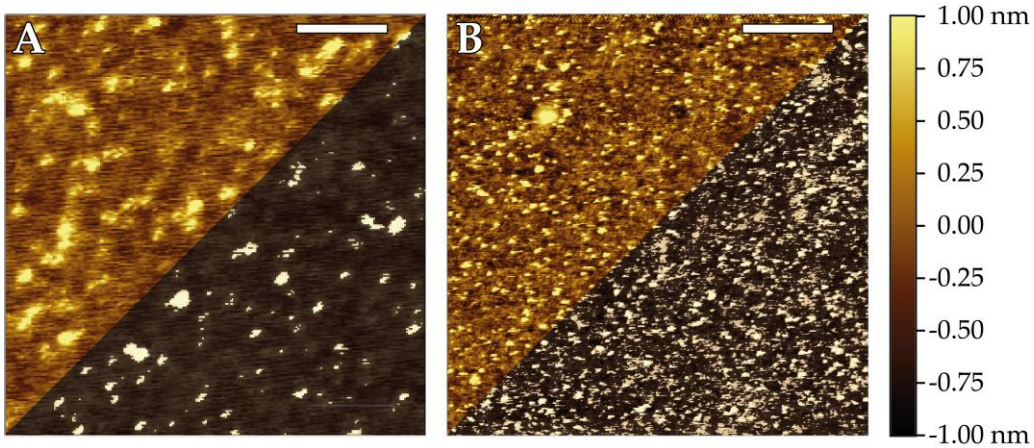

Figure 4.17: Atomic force micrographs of model membranes composed of POPC : PtdIns[4,5]P_2 (9 : 1, *n*/*n*) with CB2PH adsorbed to an SLB (**A**) and SHM (**B**). Scale bars: 500 nm. The micrographs (original data represented in the upper left half) were analysed using a threshold to distinguish uncovered membrane (in black) from protein deposits (in white) shown as overlays in the lower right half of both micrographs.

In contrast to the shape of the N-ERMAD deposits only small CB2PH aggregates were detected on both membrane systems. The direct comparison between Figure 4.17 A and B vividly demonstrate that the amount of adsorbed protein is increased on SHMs. This trend is better visible in the black and white images after thresholding. For both proteins, N-ERMAD and CB2PH, the analysed micrographs were used to determine the surface coverage by adsorbed protein as shown in Figure 4.16. It is based on the values of 14 ± 3 % surface coverage by N-ERMAD on the membrane in case of SLBs, whereas the occupancy was larger with 31 ± 6 % on SHMs determined from three individual experiments. The same holds true for the values calculated for CB2PH being 5.7 ± 1.2 % on SLBs and 31.0 ± 1.3 % on SHMs. Under consideration of the AFM data a third asymmetry factor calculation was performed whose results are reported in Table 4.4.

Consequently, Figure 4.16 also illustrates the drastic discrepancy in surface coverage by marker protein between the lipid bilayer and the hybrid system. These findings support the assumption based on the RIfS results that hydrophilic SiO_2 substrate surfaces affect the distribution of PtdIns[4,5]P_2 within SLBs causing a depletion of the receptor lipid in the distal leaflet and rendering the majority of these lipid inaccessible for specific binding partners.

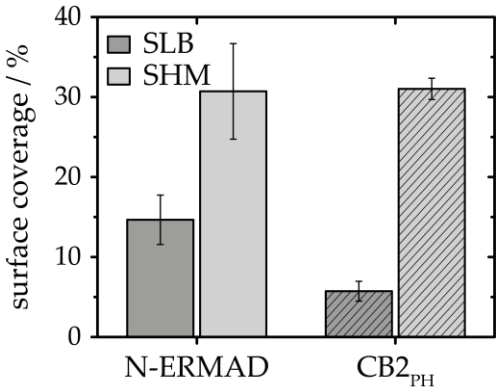

Figure 4.16: Protein surface coverage on SLBs and SHMS for N-ERMAD (DPPC : PtdIns[4,5]P_2 (97 : 3, *n*/*n*)) with (14 ± 3) % on SLBs and (31 ± 6) % on SHMs (*n* = 3) and for CB2PH adsorption to 10 mol% PtdIns[4,5]P_2 with (5.7± 1.2) % on SLBs and (31.0± 1.3) % on SHMs (*n* = 5).

Table 4.4: Calculated asymmetry factors based on the surface coverages determined via AFM.

Protein	N-ERMAD	CB2PH
χ(PtdIns[4,5]P_2) / mol%	3	10
Asymmetry factor	2.1	5.4

4.2.4 Asymmetric PtdIns[4,5]P_2 distribution in SLB on hydrophilic SiO_2 surfaces

Both data gathered by means of RIfS and AFM on the adsorption of marker proteins to PtdIns[4,5]P_2, indicate an intrinsic heterogeneity in the receptor lipid distribution within solid-supported lipid bilayers using silicon dioxide surfaces. This is a substantial finding as plenty of studies have been based on such SLBs. Among those were protein binding examinations from NÖDING *et al.* who applied SLBs with varying PtdIns[4,5]P_2 concentrations to build up a minimal actin cortex (MAC) and to correlate the actin architecture with its viscoelastic properties.[187] Apart from this, the complex membrane-binding mechanism of the phosphatase and tensin homolog (PTEN) was investigated on the same model membrane system.[222] While both surveys followed an SLB preparation protocol similar to the one applied in this work, DRÜCKER *et al.* also used a low pH of 4.6, but increased the sodium chloride concentration to 150 mM to prepare SLBs on SiO_2 and subsequently investigated the annexin A2—PtdIns[4,5]P_2 interaction.[223] Regardless of the membrane formation conditions, all previous results were interpreted under the premise of a homogeneous PtdIns[4,5]P_2 distribution in the model membrane. This was insofar reasonable when considering the results of RICHTER *et al.* whose QCM-D experiments proved a homogeneous distribution of the negatively charged lipid DOPS in SLBs generated by SUV spreading on SiO_2 surfaces.[224] However, they also found that spreading of the same vesicles on mica led to SLBs in which the accessible amount of DOPS is reduced to the nominal concentration of the negatively charged molecules. In this study they used the specific adsorption of prothrombin to DOPS as a readout parameter for accessibility of the latter. They concluded that the asymmetry is already produced during the spreading process and proposed a lipid transfer across the edges of bilayer patches (10^{-4} to 1 μm^2) that are formed during bilayer formation on mica,[225] which takes place on short time scales below 1 s. But on

silicon dioxide, the spreading process of vesicles follows a different track, starting with adhesion of intact SUVs up to a critical surface concentration followed by wave-like rupturing of the lipid spheres which was impressively shown by interferometric scattering microscopy (iSCAT) experiments.[226] Along this line, BISWAS *et al.* performed a comprehensive study in which they looked in detail at the different vesicle adsorption and spreading pathways. Their results indicated that the spreading of negatively charged phospholipid vesicles (DOPC : DOPS, 7 : 3, *n*/*n*) onto SiO_2 surfaces is dictated by interfacial forces (electrostatics and steric hydration forces) which they tested by systematically varying the pH and the membrane surface charge of the vesicles. Furthermore, they observed that bilayers only are formed within a pH range of 2 to 6, whereas larger pH values prevent the spreading process. Similar tendencies have been found by BRAUNGER *et al.* who detected that high PtdIns[4,5]P_2 concentrations (>4 mol%) prevent spreading on hydrophilic silicon dioxide surfaces if a pH of 7.4 is adjusted.[170] A decrease in pH of the buffer to 4.8 reduces the net charge of PtdIns[4,5]P_2 to -3,[227] and thereby facilitates the spreading of vesicles containing up to 10 mol% PtdIns[4,5]P_2 as shown in a former study on CB2 adsorption.[113] At pH 4.8 the net charge of POPC : PtdIns[4,5]P_2 (9 : 1) SUVs matches that of vesicles with a lipid composition of DOPC : DOPS (7 : 3) and both compositions indeed spread at low pH. Thus, both examples indicate the strong influence of the vesicles' negative surface charge density on the spreading process, which is even more comprehensible when considering that the SiO_2 support is negatively charged at this pH due to its isoelectric point ranging from 1.0 to 3.7.[228,229] However, it remains unknown to what extent the vesicle spreading pathway on SiO_2 affects the leaflet distribution of negatively charged lipids.

In the special case of PtdIns[4,5]P_2 containing membranes, another aspect has to be taken into account. Not only electrostatic repulsion but also attractive forces can occur due to the capability of PtdIns[4,5]P_2 to form hydrogen bonds,[230,231] further influencing the spreading pathway. This might be another cause for the increased immobility of labelled PtdIns[4,5]P_2 with only about 50 % in SLBs compared to 80 % in SHMs.

A third aspect that needs to be discussed is the high steric demand of the headgroup of PtdIns[4,5]P_2. The inositol ring with its phosphate substituents in 4- and 5-position demands an area of 70 $Å^2$ being slightly increased compared to the area occupied by the headgroup of phosphatidylserine (65 $Å^2$).[232,233] If compared to phosphatidylcholine, the headgroup of PtdIns[4,5]P_2 is even 40 % lager.[234] Furthermore, LI *et al.* reported an exposed position of the

phosphoinositide's headgroup into the aqueous phase when contained in a POPC lipid bilayer based on molecular dynamics (MD) simulations.[235] Thus, it is conceivable that owing to the large head group there is already an asymmetric PtdIns[4,5]P_2 distribution present in SUVs. This is supported by the findings of CHIANTIA *et al.* They showed that the large curvature of a vesicle with a radius smaller than 70 nm causes the lipid in the outer leaflet to be further apart from each other in contrast to those of the inner leaflet.[236] This suggests more available space in the outer leaflet for lipids with a high steric demand such as PtdIns[4,5]P_2. In the exact same direction point the results of SAKUMA *et al.* who observed an enrichment of cone-shaped lipids in the outer leaflet of SUVs.[237] Based on the outlined indications a lipid distribution dictated by that inside the vesicles could be assumed, yet in that case also the spreading mechanism has to be taken into account. The mechanism has been subject of extensive discussions since the preparation of solid-supported lipid bilayers via vesicle spreading was introduced by MCCONNELL *et al.* in the 1980s.[238,239] The dispute focusses on the question whether the spreading is an inside-up or outside-up process, meaning which lipid leaflet (inside or outside one) of the vesicles faces the bulk solution after membrane formation, and thus is accessible for potential interaction partners.[108,240] Arguments for an outside-up process have been presented in two studies deploying transmembrane protein containing liposomes to test either activity after proteolytic digestion[241] or binding capability.[242] In contrast to that, REIMHULT *et al.* found that at best 30 to 40 % of biotinylated lipids face the bulk solution after spreading of vesicles. The specific lipids were selectively incorporated in the outer monolayer of those vesicles.[243] They assumed a transient mixing process between inner and outer leaflets during rupturing process of the adsorbed vesicles, which accordingly is critically dependent on the bilayer formation rate. Furthermore, a lipid translocation across the established bilayer at a later stage is hindered by a high energy barrier composed of the high resistance of the polar headgroups to passage through the hydrophobic core and the increasing lateral tension arising in the receiving leaflet.[244] Considering these indications, the presented results hint at an inside-up SLB formation mechanism, however to which extend the PtdIns[4,5]P_2 asymmetry is a result of the spreading process or is already generated in the highly curved SUVs remains unclear. Therefore, subsequently further investigations should be conducted in which the surface properties of the solid support and the vesicle size will be varied. Notwithstanding these uncertainties, the results highlight the usability of SHMs to develop sensor surfaces that can be applied to

quantitatively study lipid-protein interactions although these type of model membranes do not fully resemble the natural bilayer situation.

4.2.4.1 Effects on the asymmetry factor between SLBs and SHMs

Based on the marker protein adsorption to both SLBs and SHMs studied by means of RIfS and AFM as presented in Chapters 4.2.2 and 4.2.3, respectively, the discrepancy in amount of adsorbed protein was calculated as asymmetry factors. These factors indicated that in case of an

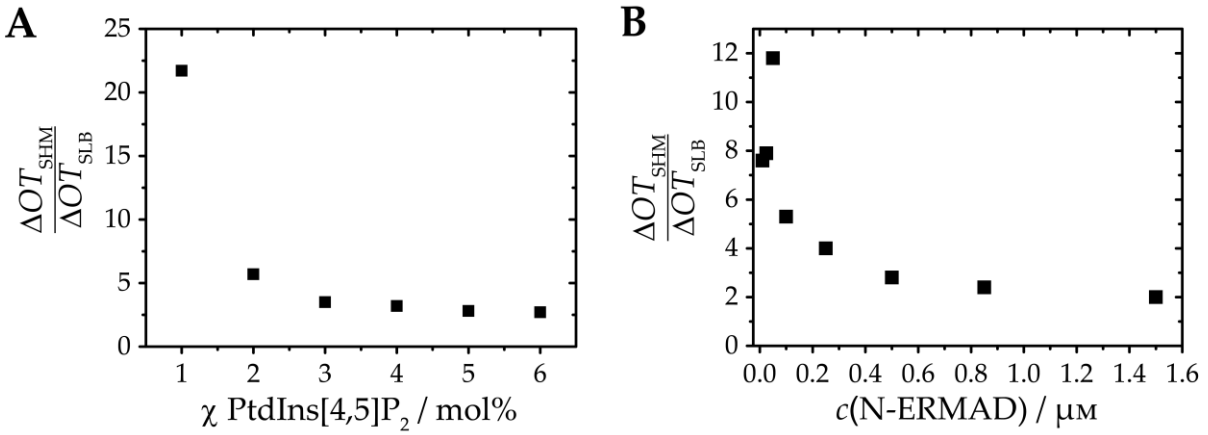

Figure 4.18: Asymmetry factors of N-ERMAD adsorption calculated as ratio of changes in optical thickness on SHMs and SLB determined either on POPC model membranes with different PtdIns[4,5]P_2 fractions (**A**) or on membranes composed of POPC : PtdIns[4,5]P_2 (99 : 1, *n*/*n*) exposed to ascending N-ERMAD concentrations (**B**).

increase for both receptor lipid fraction and marker protein concentration the discrepancy declined as illustrated in Figure 4.18 A and B.

This effect was more pronounced in case of ezrin's *N*-terminal domain compared to CB2PH and might be caused by the tendency of ezrin to laterally interact on the membrane surface. The ability results in an adsorption without a direct linkage to the receptor lipid.[245,246] This assumption is supported by another set of adsorption experiments with a successive increase in N-ERMAD concentration on SLBs and SHMs doped with 3 mol% PtdIns[4,5]P_2. The resulting adsorption isotherms show that there is no difference in the amount of bound protein between the two model membrane systems (cf. Figure 4.19), which has also been tested via a STUDENT's *t*-test for each protein concentra-

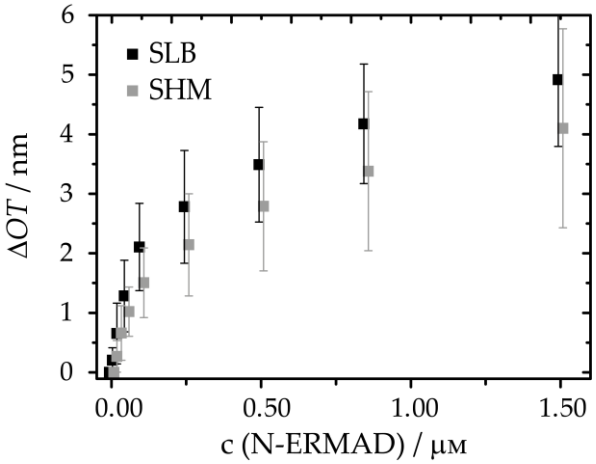

Figure 4.19: Adsorption isotherms of N-ERMAD on POPC : PtdIns[4,5]P_2 (97 : 3, *n*/*n*) membranes. Error bars are the standard error of the mean with $n \geq 10$.

tion, detecting no significant difference between the Δ*OT*s on both membranes. It is, however, not possible to quantitatively determine the impact of N-ERMAD's lateral interaction, therefore the exact asymmetry factor remains unidentified. Yet, based on all the results presented in the last sections at least a factor of two exists for the concentration differences of accessible PtdIns[4,5]P_2 in SHMs and SLBs. Therefore, SHMs were selected as the starting point of the model system for the organisation machinery of γ-amino butyric acid (GABA) receptors type A ($GABA_AR$) in the postsynaptic membrane. However, it was previously shown that CB2 as part of the organisation machinery can also interact with other phosphoinositide variants.[113] Thus, it was investigated via $CB2_{PH}$ adsorption experiments to PtdIns[3,4,5]P_3 if the heterogeneous receptor lipid distribution in SLBs also exists in case of other PtdInsPs. The corresponding results are presented in the next paragraph.

4.2.4.2 Distribution of PtdIns[3,4,5]P_3 in SLBs on SiO_2 substrates

Having previously outlined the variety of phosphoinositides due to phosphorylation of the inositol ring (cf. Chapter 3.1.1.2) and as the results on membrane formation indicate that neither receptor lipid concentration nor its phosphorylation degree have an influence on the resulting model membrane thickness (cf. Chapter 4.1.3), it was worth testing if the detected heterogeneous PtdIns[4,5]P_2 distribution in SLBs is likewise present in case of other phosphoinositides. That is why, the trisphosphorylated PtdIns[3,4,5]P_3 was deployed which functioned as another receptor lipid for the PH domain of collybistin 2. In analogy to the PtdIns[4,5]P_2 examinations (cf. Chapter 4.2.2), the model membranes contained 10 mol% PtdIns[3,4,5]P_3 and were exposed to increased $CB2_{PH}$ concentrations ranging from 0-5 μM. The protein adsorption was again followed by means of RIfS. The adsorption isotherms are depicted in Figure 4.20 and are based on at least three individual experiments. As indicated by the error bars, representing the standard error of the mean, for all protein concentrations rather large deviations of Δ*OT* were detected. However, it becomes

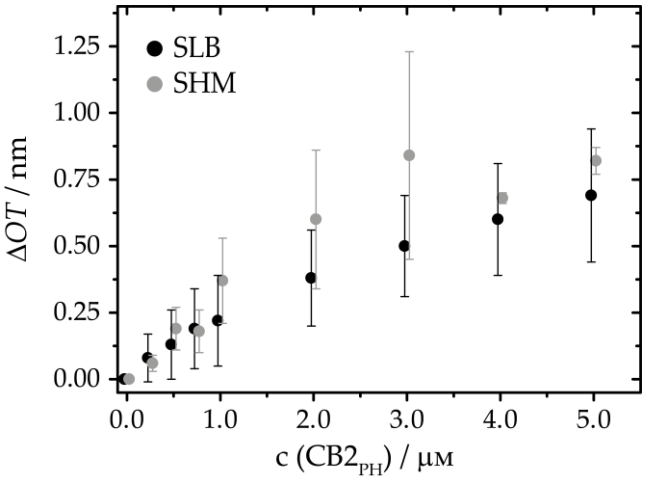

Figure 4.20: Adsorption isotherms of $CB2_{PH}$ on POPC : PtdIns[3,4,5]P_3 (9 : 1, *n*/*n*) membranes. Error bars are the standard error of the mean with $n \geq 3$.

obvious that there is no difference in those values between SLBs and SHMs. This meets the results of a STUDENT's *t*-test for each protein concentration detecting no significant differences. Referring to this data set, the conclusion of a homogeneous PtdIns[3,4,5]P_3 distribution seems reasonable. The is supported by findings of LUCCHINI *et al.* who investigated the structural effects of phosphatidylinositol trisphosphate on SLBs by means of QCM-D, AFM and Neutron Reflectometry (NR).[159] Not only did they show that spreading of SUVs containing 10 mol% PtdIns[3,4,5]P_3 leads to the formation of homogenous lipid bilayers, they also were able to detect an inclination of the inositol headgroup towards the layer of POPC headgroups matching the calculated 40° angle of former MD simulations.[235] Consequently, the question arises which differences between the two phosphoinositides lead to such opposing distribution tendencies.

On one hand the aforementioned simulations indicated that both phosphatidylinositol phosphates perturbed a POPC membrane to similar extends, with the ring phosphate in position 4 (P4) extending ~5.5 Å above the phosphate plane and ~1 Å above the other ring phosphates.[235] This is commensurate with the results for membrane formation gathered by means of RIfS and indicates that next to PtdIns[4,5]P_2 also PtdIns[3,4,5]P_3 can form intermolecular hydrogen bonds.[230,247,248] Then again, at least both phosphoinositides differ in their net charge due to their degree of phosphorylation. While for the bisphosphorylated phosphoinositide charges of -1.58 ± 0.05 and -1.41 ± 0.05 were detected for P4 and P5, respectively, leading to an overall charge (including the charge of the phosphodiester group) of -3.99 ± 0.10 at pH 7.0, PtdIns[3,4,5]P_3 exhibits a charge of -5.05 ± 0.15 under these conditions.[249] Due to the conditions applied for SUV spreading within this work the net charge of both was reduced to facilitate lipid membrane formation,[170,202] however, the charge difference between both phosphoinositides remains the same. Thus, increased repulsion will occur if a SiO_2 surface is exposed to vesicles composed of a great fraction of PtdIns[3,4,5]P_3 (10 mol%). The repulsion might be able to counteract those effects responsible for the enrichment of receptor lipids in the proximal SLB leaflet in case of PtdIns[4,5]P_2. Eventually, these determinations hint at a unique feature of PtdIns[4,5]P_2 that needs to be considered when working on SLBs, although, its exact origin remains elusive. At the same time these findings represent another reason for the selection of SHMs as basis for the model system preparation, because only in this model membrane system an equal accessibility for all phosphoinositides under investigation can be guaranteed. Even if

the heterogenous leaflet distribution is unique for PtdIns[4,5]P_2, it would still affect comparing adsorption studies to various phosphoinositides.

4.3 Adsorption experiments and topographical studies of collybistin 2 on PtdInsP-doped solid-supported hybrid membranes

The Dbl-family (diffuse B-cell lymphoma) guanine nucleotide exchange factor collybistin (CB) exists in several splice variants which differ in their *N*- and *C*-termini (CB1-CB3, cf. Figure 1.6) and the presence or absence of an exon encoding a regulatory src homology 3 (SH3) domain.[48] Furthermore, collybistin contains a so-called tandem-domain made up by a DH (Dbl homology) and a *C*-terminal PH (pleckstrin homology) domain. The latter is capable of interacting with phosphoinositides like many other members of this specific protein group.[250] Based on this ability, CB2 is believed to function as an adapter protein connecting the plasma membrane with other scaffolding proteins in inhibitory postsynapses.[63,251] However, former studies revealed that SH3 domain containing isoforms adopt a closed, autoinhibited conformation that prevents the interaction of CB2 with phosphatidylinositol phosphates (PtdInsPs).[60] Additionally, a series of recent studies focussed on *ARHGEF9*, the collybistin encoding gene, and missense mutations therein. For instance, PAPADOPOULOS *et al.* investigated the influence of a point mutation in position 290 of the Dbl-homology domain on the intramolecular interactions within the tandem domain and were able to detect an altered interaction strength and even more serious a reduced binding affinity of the PH domain to PtdIns[3]P.[252] Another example is the work of LONG *et al.* which concentrated on a family with X-linked intellectual disability.[253] They were able to identify a point mutation in position 338 causing a change from arginine (R) to tryptophan (W) as the origin of the symptoms. Furthermore, functional assays revealed a deficiency of the PH domain to interact with phosphoinositides for this missense mutation. Both results emphasise the importance of the proper interaction between collybistin's *C*-terminal domain and phosphoinositides and therefore the adsorption of CB2 to the postsynaptic plasma membrane. To illuminate the process and to gain insights in the behaviour of the adsorbed proteins, different isoforms of collybistin 2 were applied in this work. Their recombinant expression and purification will be presented in Chapter 4.3.1. The adsorption analysis was started with the isolated PH domain ($CB2_{PH}$) as the minimal prerequisite for CB2-PtdInsP

interaction. The experiments with the minimal system were performed to identify ideal experimental conditions and determine binding affinities to solid-supported hybrid membranes (SHMs) doped with the three different phosphoinositides mentioned before (PtdIns[3]P, PtdIns[4,5]P_2 and PtdIns[3,4,5]P_3). The gathered data on $CB2_{PH}$ will be focus of Chapter 4.3.2. The adsorption behaviour of the full-length protein was studied by deploying a point mutated isoform of collybistin 2 ($CB2_{SH3/W24A\text{-}E262A}$) which has already been investigated in former experiments.[60,113] Its application is inevitable as the wild-type of collybistin 2 ($CB2_{SH3}$) is not able to interact with phosphoinositides in the plasma membrane due to the reasons mentioned before in detail. The results obtained under the use of the mutant will be presented in Chapter 4.3.3. Furthermore, the orientation and lateral behaviour of the adsorbed isoforms were investigated by means of AFM to determine an influence of the various receptor lipids (cf. Chapter 4.3.4).

4.3.1 Recombinant expression and isolation of the different collybistin 2 isoforms

The isolation of the minimal adsorption fragment ($CB2_{PH}$) has already been presented in Chapter 4.2.1.2, as the PH domain was also applied as a marker protein to investigate the PtdIns[4,5]P_2 distribution in the two solid-supported model membrane systems. In contrast to that isolation protocol, the full-length proteins $CB2_{SH3}$ (M_{theo} = 55.93 kDa) and $CB2_{SH3/W24A\text{-}E262A}$ (M_{theo} = 55.76 kDa) were heterologously expressed in *E. coli* cells containing the corresponding pTXB1 vectors. After lysis and ultra-centrifugation, the clarified lysate was applied on a French press column containing chitin resin as immobile phase. The process and success of the purification steps were controlled via SDS-PAGE and Western blot analysis. In Figure 4.21 examples of a gel after electrophoresis (A) and an overlay after immunodetection (B) are presented.

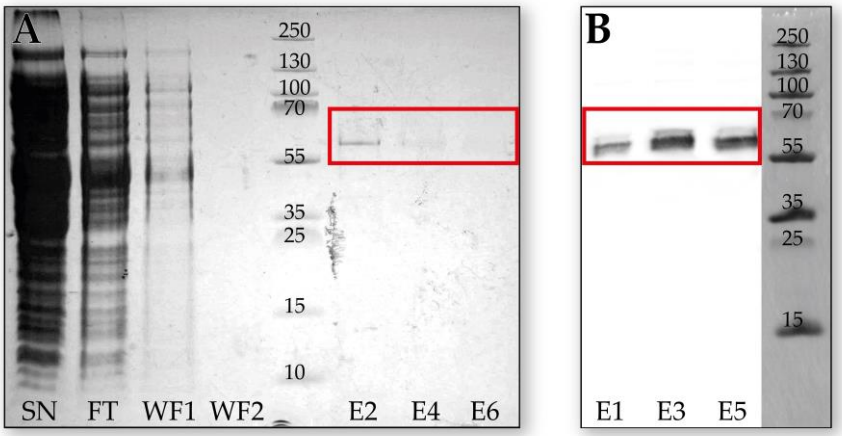

Figure 4.21: A: SDS-PAGE of $CB2_{SH3}$ after purification via affinity chromatography. The collected fractions of supernatant (SN), flow through (FT), washing (WF) and elution (E) were loaded on a polyacrylamide gel control the isolation of the collybistin 2 wild-type. **B**: Western blot overlay with elution fractions tested for $CB2_{SH3}$ using a CB2 specific primary antibody.

The exemplary gel of a $CB2_{SH3}$ isolation (cf. Figure 4.21 A) after electrophoresis showed a great number of bands of the supernatant (SN) after cell lysis, indicating the expression of basal proteins along with the target protein. Similar band quantities were present in the flow through (FT) and first washing fraction (WF1), which provided reduced intensities. In the second washing fraction (WF2) no signals were detected, while in the elution fraction (E2 and E4) a single band was visible between the 55 and 70 kDa bands of the mass standard. This specific band at around 60 kDa was assumed to correspond with the wild-type of CB2 due to its theoretical molecular mass calculated from the amino acid sequence (cf. Appendix A.4.2) via the PROTPARAM tool.[211] In addition, a similar band was detected in isolations, either recombinant or from cellular tissue, as part of former studies.[60,213] They also recognised a slight shift to higher molecular weights. Yet, the target protein band did not dominate the SN indicating that it was not overexpressed. Nonetheless, in FT as well as in WF1 a band was detected in this molar regime. This might indicate that the capacity of the chitin resin was exceeded due to a high amount of protein with a fused Chitin binding domain (CBD). Another possibility is that the band corresponds to a basal protein of similar weight. In this case the corresponding protein was incapable of interacting with the stationary phase and thus was removed from the column. However, the comparison of SN and FT together with WF1 shows that the different purification steps led to a reduction of undesired proteins as the number of bands and their intensities were successively decreased in these fractions. The purification was optimized to such an extent that WF2 did not contain any proteins at all, represented by the absence of band signals within the corresponding lane. The introduction of dithiothreitol (DTT) as composite

of the second wash buffer (cf. Table 3.8) induced the cleavage of the Intein-tag from the target protein and facilitated the elution of the latter. The early elution fractions (E2 and E4) contained the corresponding band but presented a declining signal intensity resulting in complete extinction of signal in E6. This hints at a total removal of the target protein from the column. The expression and purification of collybistin 2 wild-type can be considered as a success. These results indicate that the capacity of the resin was not exceeded. Consequently, the band at around 60 kDa in both FT and WF1 most probably corresponds to another protein with similar weight lacking the affinity tag. To identify further elution fraction that contained target protein also a Western blot was performed (cf. Figure 4.21 B) using a specific primary collybistin antibody. In the corresponding overlay all elution fraction (E1, E3 and E5) presented a single broad band in the same molecular weight regime as detected via SDS-PAGE. The signal intensities have their climax in E3. This indicates a retention of target protein in the beginning of elution but also shows that the protein amount on the column is reduced in course of it. Thus, the WB confirmed the correlation between the band of the elution fractions and the target protein and furthermore showed that it is also contained in later elution fractions.

The expression and isolation of the collybistin isoform with two point-mutations at positions 24 and 262 where tryptophan (W) and glutamine (E), respectively, are substituted by alanine were conducted following a protocol identical to that of the wild-type. An exemplary SDS-PAGE after the purification of $CB2_{SH3/W24-E262A}$ via affinity chromatography is illustrated in Figure 4.22 A.

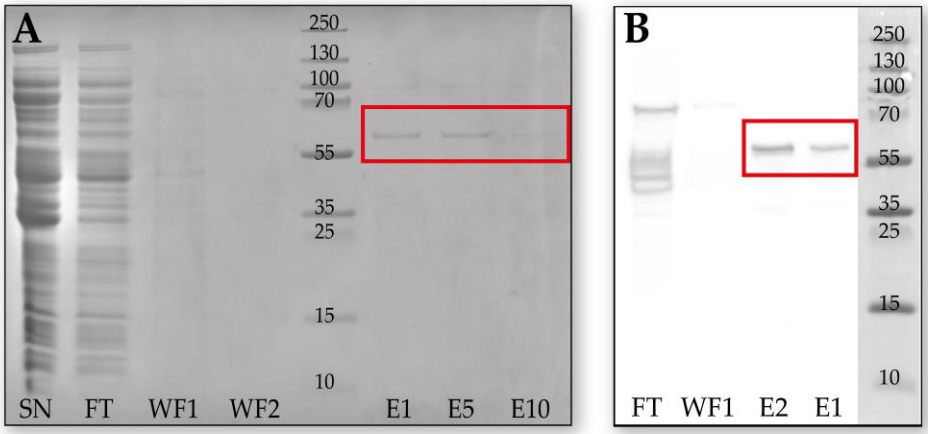

Figure 4.22: **A**: SDS-PAGE of CB2$_{SH3/W24A-E262A}$ after purification via affinity chromatography. The collected fractions of supernatant (SN), flow through (FT), washing (WF) and elution (E) were loaded on a polyacrylamide gel to control the isolation of the target protein. **B**: Western blot overlay with isolation fractions tested for CB2$_{SH3/W24A-E262A}$ using a CB2 specific primary antibody.

The illustrated gel of CB2$_{SH3/W24-E262A}$ highlights some differences to the one obtained from wild-type isolation (cf. Figure 4.21) as the band intensities in all traces of SN, FT and WF1 were reduced in case of the active mutant. Such a comparison is possible as the applied volumes of the tested fractions was constant (V = 10 µL) in all electrophoresis runs (cf. Chapter 3.2.8). The smaller intensities indicate lower protein amounts that were applied to the gel. This could correlate with a decreased expression yield of CB2$_{SH3/W24-E262A}$. However, the tendency of reduction in signal quantity and intensity is also apparent. The second washing fraction (WF2) presented no detectable bands which indicates a complete removal of unbound proteins from the stationary column phase. In the early elution fractions tested (E1 and E5) a narrow band was recorded which was located between the 55 and 70 kDa bands of the mass standard. Under consideration of the amino acid sequence of CB2$_{SH3/W24A-E262A}$ and the resulting molecular weight (cf. Appendix A.4.3) the signal in all elution fractions was assumed to correlate with the target protein. It was expressed together with basal proteins represented by the great number of bands in the SN. Yet, also for CB2$_{SH3/W24A-E262A}$ no overexpression was detected and again a band was present in the FT corresponding to a protein with a molecular weight of around 60 kDa. In contrast to the wild-type, the first washing step during the isolation of the mutant already contained nearly no proteins. Therefore, also in WF2 no protein bands were visualised. Because of the single band in the elution fractions that was assigned to the target protein, the isolation of CB2$_{SH3/W24A-E262A}$ was assumed to be successful. Yet again, only small amounts of target protein were obtained. This is concluded from the low band intensities for the early fractions while the corresponding band vanished in E10. Therefore, a complete cleavage of the

mutant from the affinity column was presumed. To ensure that no protein fragments in concentrations below the detection limit of the SDS-PAGE were present, a Western blot as shown in Figure 4.22 B was performed. By applying a specific primary CB2 antibody (cf. Table 3.12) FT, WF1 and early elution fractions were tested. While the FT contained both, protein fragments with lower molecular weight and proteins in the higher molecular regime exhibiting the specific antigen, in the elution fractions only the specific band was visualised which corresponded to $CB2_{SH3/W24A-E262A}$.

In Table 4.5 the average yields (per litre nutrient solution) for the three different isoforms of collybistin 2 after heterologous expression in *E. coli* are summarised based on at least three isolations.

Table 4.5: Averaged yields of the three different CB2 isoforms from heterologous expression in *E. coli.*

Protein	Yield [mg/mL]	Isolations *n*
$CB2_{PH}$	16.4 ± 7.2	8
$CB2_{SH3}$	1.8 ± 0.5	3
$CB2_{SH3/W24A-E262A}$	4.0 ± 2.3	7

Despite the different yields of target proteins, all isoforms were successfully isolated and thus were applicable for subsequent investigations which focussed on their interaction with solid-supported hybrid membranes containing phosphoinositides as specific receptor lipids. The results of such experiments will be presented in the following chapters.

4.3.2 Adsorption experiments with the PtdInsP-binding PH domain as minimal model system

The PH domain is a protein motif composed of approximately 120 amino acid residues that lacks primary sequence similarity.[254,255] Despite this minimal homology of the PH domain, the three-dimensional structures are well conserved and it is found in a great number of proteins.[256] Most of them participate either in cell signalling or cytoskeletal regulation. Among this quantity also collybistin harbours a PH domain required as the interacting domain with PtdInsP in the plasma membrane. This process is crucial for accurate neuronal functions as a malfunction can be related to various diseases which has been outlined before (cf. Chapter 1.3.2). Thus, this work concentrated on the interaction of collybistin's PH domain ($CB2_{PH}$) with different variants of phosphoinositides that were embedded in SHMs. The protein-lipid interaction was investigated by means of reflectometric interference spectroscopy (RIfS). In a first set of adsorption experiments on SHMs unspecific interactions of the PH domain with the matrix lipid POPC were excluded as no protein adsorption could be detected in absence of receptor lipid (cf. Figure 4.23 black spectrum). Additionally, it was investigated whether protein adsorption is caused by electrostatic interactions. On this purpose $CB2_{PH}$ was added to POPC SHMs doped with 30 mol% 1-palmitoyl-2-oleoyl-sn-glycero-3-phospho-L-serine (POPS) mimicking the net charge of a membrane containing 10 mol% PtdIns[4,5]P_2 (cf. Figure 4.23 grey graph).[227] A close look at both plots shown in Figure 4.23 reveals that addition of 1 μM protein (highlighted as point II) neither for pure POPC- nor for POPC : POPS (7 : 3, *n*/*n*) membranes leads to a change in optical thickness. Thus, the adsorption to PtdInsP doped membranes is exclusively caused by specific interactions with the receptor lipids.

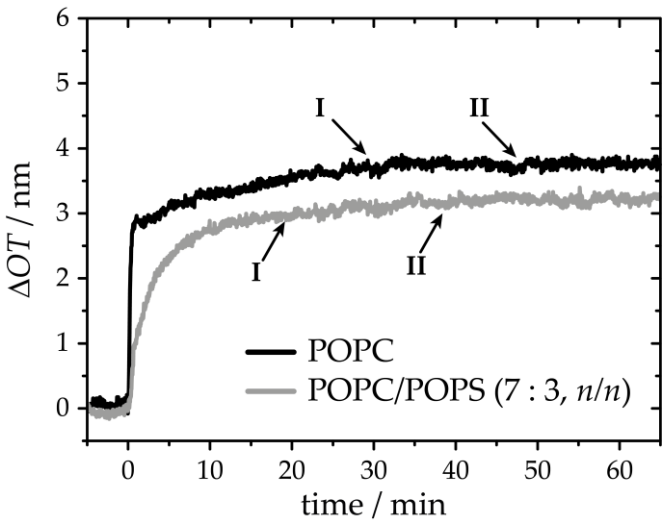

Figure 4.23: : Exemplary plots of the change in optical thickness vs. the time of an adsorption experiment with of $CB2_{PH}$ on either a pure POPC solid-supported hybrid membrane (black) or a POPC SHM doped with 30 mol% POPS (grey). SUV were added at t = 0 min which induced their adsorption and spreading to form the differently composed membranes. Subsequently the setup was rinsed with HEPES buffer (I). $CB2_{PH}$ injection with a concentration of 1 μM is indicated by II.

Parts of the data of CB2PH adsorption to such SHMs doped with 10 mol% of bis- and trisphosphorylated forms of PtdInsP have already been presented in Chapters 4.2.2.2 and 4.2.4.2, respectively. In addition to those adsorption experiments, the interaction with the monophosphorylated PtdIns[3]P was quantified by means of reflectometric interference spectroscopy (RIfS). The statistics for successive, stepwise increase in CB2PH concentration to SHMs doped with one of the PtdInsPs at a time is presented in Figure 4.24.

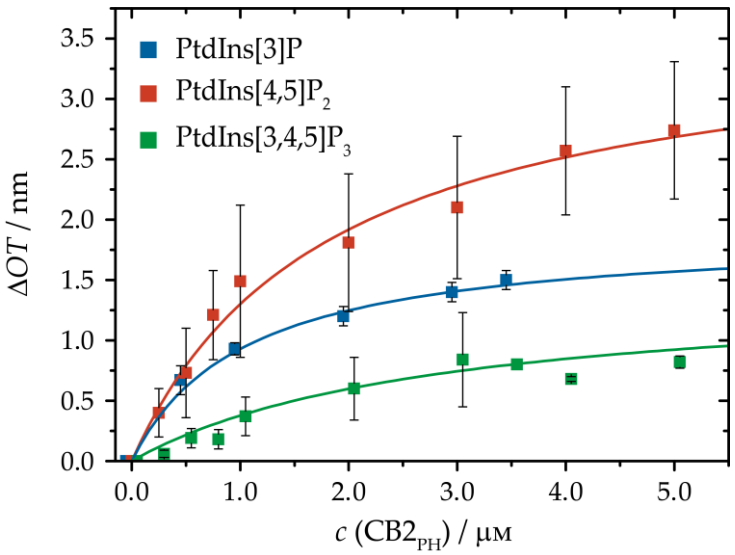

Figure 4.24: Adsorption isotherms of CB2PH to POPC SHMs doped with 10 mol% of either PtdIns[3]P (blue), PtdIns[4,5]P2 (red) or PtdIns[3,4,5]P3 (green). Error bars are the standard error of the mean with $n \geq 3$. The continuous curves in the corresponding colours represent the applied LANGMUIR fits.

In those experiments the protein concentration was increased from 0-5 µM. Each data point is an average of at least three independent measurements and error bars represent the standard error of the mean. A Langmuir adsorption isotherm was fit to the data (coloured curves, cf. Chapter 4.2.2.2 Equation 4.8) to determine the maximum change in optical thickness (ΔOT_{max}) and the dissociation constant K_D of CB2PH to the different phosphoinositides. The determined parameters are shown in Figure 4.25.

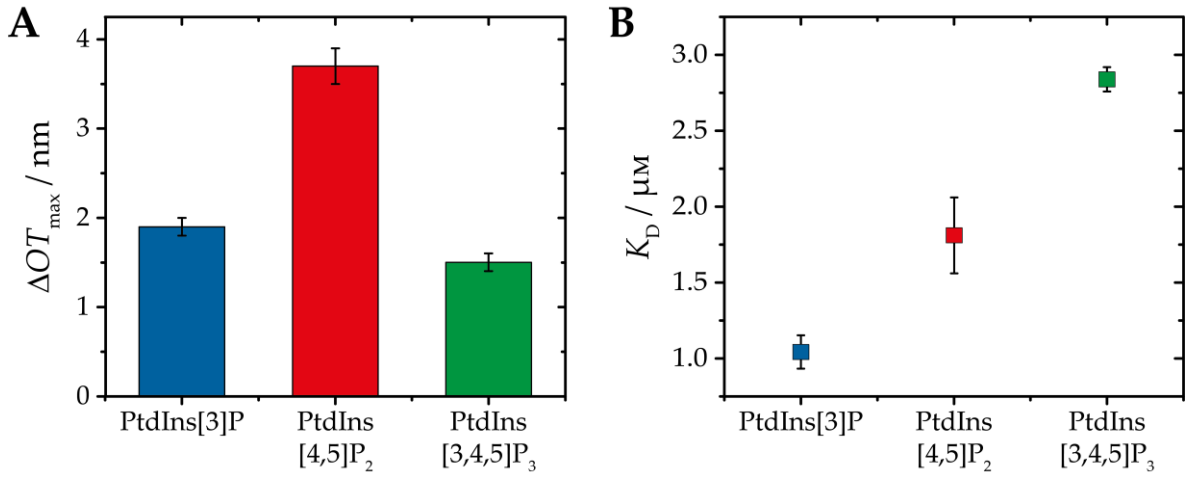

Figure 4.25: Determined ΔOT_{max} (**A**) and K_D values (**B**) of CB2PH on POPC SHMs doped with 10 mol% of either PtdIns[3]P (blue), PtdIns[4,5]P2 (red) or PtdIns[3,4,5]P3 (green). Error bars are the standard error of the mean with $n \geq 3$.

Both, Figure 4.24 and Figure 4.25 indicate a diverse adsorption behaviour of the *C*-terminal PH domain to the three PtdInsPs. While the adsorption to PtdIns[3]P and PtdIns[3,4,5]P_3 doped SHMs resulted in ΔOT_{max} values of (1.9 ± 0.1) nm and (1.5 ± 0.1) nm, respectively, the $CB2_{PH}$ layer thickness was calculated to be (3.7 ± 0.2) nm on PtdIns[4,5]P_2 doped membranes. Thus, the difference in adsorbed protein layer thickness varies with a factor of around two and reflects the different binding capacities of the membranes. Furthermore, the determined adsorption isotherms led to different affinities of the PH domain to the phosphoinositides (cf. Figure 4.25 B). These are independent of the calculated maximum layer thicknesses. $CB2_{PH}$ exhibits the highest affinity to PtdIns[3]P with a K_D of (1.0 ± 0.1) μM. The dissociation constants for PtdIns[3,4,5]P_3 and PtdIns[4,5]P_2 were determined to be (2.8 ± 0.1) μM and (1.8 ± 0.3) μM, respectively.

Due to the well conserved structure within the PH domain protein motif, a comparison of the determined values to those recognised for other representatives is reasonable. The determined affinity to PtdIns[4,5]P_2 is in accordance with the dissociation constant of phospholipase C-δ_1 (PLC-δ_1) as determined by LEMMON *et al.*[257] They were able to detect an average K_D of the isolated PH domain to PtdIns[4,5]P_2 of (1.66 ± 0.80) μM by means of isothermal titration calorimetry (ITC). This finding was supported by another study that investigated the amount of bound isolated PH domain (PLC-δ_1) to large unilamellar vesicles (LUVs) containing PtdIns[4,5]P_2 after ultracentrifugation via bicinchoninic acid (BCA) assays.[258] In contrast to that, the isolated *N*-terminal PH domain of pleckstrin investigated by HARLAN *et al.* exhibits a K_D of around 30 μM to PtdIns[4,5]P_2,[96] hence, showed lower affinity to the bisphosphorylated phosphoinositide. A third representative is Num1p which is one of the 33 proteins in baker's yeast (*S. cerevisiae*) harbouring this protein modulus.[259] For its isolated GST/Num1p-PH fusion form an equal affinity to PtdIns[4,5]P_2 has been measured as that detected for PLC-δ_1.

Affinities to PtdIns[3]P and PtdIns[3,4,5]P_3 for other PH domain containing proteins have also been determined. While the dissociation constants to the later range from 27 nM to ~1 μM,[260,261] showing high affinities and selectivity, those determined for the monophosphorylated phosphoinositide are reduced. For instance, K_Ds calculated for the tandem domain (DH and PH domain) of the guanine nucleotide exchange factor (GEF) Tiam1 are 5 μM to inositol 1,3-bisphosphate (Ins[1,3]P_2), which is the head group of PtdIns[3]P, or 10 μM to PtdIns[3]P it-

self.[262] Only the vacuolar protein-sorting-associated protein 36 (Vps36) as part of the endosomal sorting complexes required for transport II (ESCRT-II) contains a PtdIns[3]P-specific binding motif , the GLUE (GRAM-like ubiquitin-binding in EAP45) domain, that expresses a high affinity of 0.1 μM to the monophosphorylated phosphoinositide within the full-length protein.[263] Though, this domain has been reported to be a "split" PH domain that interacts with PtdIns[3]P in a distinct manner than that determined for PtdIns[4,5]P_2- and PtdIns[3,4,5]P_3-specific interactions.[261,263,264]

This selection of affinities and selectivity expressed by different PH domains already indicates their broad distributions. Thus, it qualifies the calculated K_D values of $CB2_{PH}$ to be consistent for all three phosphoinositides under investigation. Such a behaviour is also known for other proteins like those of the Osh1 and Osh2 (oxysterol-binding protein homologue) families found in yeast, who express affinities in the range of 1.1 to 6.2 μM to PtdIns[3]P and PtdIns[4,5]P_2.[259] They are characterised as proteins with moderate binding affinities yet low selectivity which can also be considered being true for the PH domain of collybistin 2 based on the adsorption behaviour detected within this work. Some of the related studies suggested that the interaction of PH domain and receptor lipid is affected when the whole protein is adsorbed instead of the isolated binding motif. Therefore, it was necessary to have a closer look on the adsorption process of the full-length protein which was achieved by using the active mutant $CB2_{SH3/W24A-E262A}$. Those results are in focus of the following section.

4.3.3 Adsorption behaviour of full-length CB2 to different phosphoinositides affected by its auto-inhibition

Already in 2000 when KINS *et al*. identified collybistin as a "brain-specific GEF", they were able to show, that splice variants containing the *N*-terminal SH3 domain were redistributed in the presence of gephyrin to cytoplasmic regions enriched with this scaffolding protein.[90] Apart from that, they detected sub-membraneous collybistin-gephyrin cluster formation for SH3-deficient collybistin in human embryonic kidney (HEK) 293 cells. This feature was also determined for subsequently identified collybistin isoforms generated by alternative splicing.[48] The results gathered in this work for the wild-type of collybistin 2 ($CB2_{SH3}$) are in accordance with the former findings, i.e., the addition of $CB2_{SH3}$ to SHMs doped with one of the tested phosphoinositides did not lead to a detectable adsorption signal during RIfS measurements.

One time course of such adsorption experiments of CB2 wild-type is presented in Figure 4.26 showing the addition of $CB2_{SH3}$ to a PtdIns[3]P doped solid-supported hybrid membrane (POPC : PtdIns[3]P, 9 : 1, *n*/*n*). The removal of excess lipid material by rinsing with HEPES buffer (cf. Table 3.14, highlighted by I) was followed by injection of $CB2_{SH3}$ ($c = 1$ μM, indicated by II). After protein addition a small rise in change of optical thickness (ΔOT) was recorded which was almost undetectable because of the signal noise. If protein molecules would have been adsorbed to the membrane surface, a large ΔOT would have been recorded. Thus, this result can be interpreted as no protein adsorption as the small fluctuation can originate from changes of the refractive index induced by protein addition. This result matches with the expectation of an inactive CB2 wildtype that is unable to interact with phosphoinositides in membranes because of an intramolecular interaction of its terminal domains.[28] Therefore, an active mutant was required to enable the investigation of the full-length protein adsorption. A possible option would have been the collybistin 2 isoform lacking the *N*-terminal SH3 domain (cf. Figure 1.6) which was proven to be active by HARVEY *et al*. who detected the aforementioned sub-membraneous collybistin-gephyrin clusters.[48] However, they also mentioned its very rare character, which is the reason why the protein is untraceable in mouse brain tissue.[60] To circumvent problems with this CB2 isoform, a double point-mutated one ($CB2_{SH3/W24A-E262A}$), being intrinsically active, was applied for the adsorption experiments of the full-length protein in analogy to those performed with the minimal adsorption system ($CB2_{PH}$, cf. Chapter 4.3.2). An exemplary plot of ΔOT vs. the time for an adsorption experiment of $CB2_{SH3/W24A-E262A}$ is illustrated in Figure 4.27.

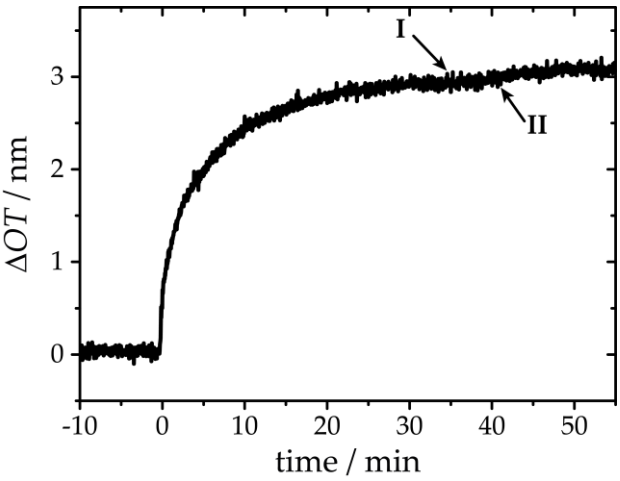

Figure 4.26: Exemplary plot of the change in optical thickness vs. the time of a $CB2_{SH3}$ adsorption experiment on a POPC solid-supported hybrid membrane doped with 10 mol% PtdIns[3]P. The model membrane was prepared via SUV spreading at $t = 0$ min and subsequently rinsed with HEPES buffer (I). $CB2_{SH3}$ injection with a concentration of 1 μM is indicated by II.

During the course of the experiment the protein concentration on the solid-supported hybrid membrane (POPC : PtdIns[4,5]P_2, 9 : 1, *n*/*n*) was increased in 1 µM-steps (starting at $t = 0$ min) to record an adsorption isotherm. The addition of CB2$_{SH3/W24A-E262A}$ in the lower concentration regime ($c \leq 3$ µM) resulted in relatively large ΔOT values. At higher protein concentrations ($c > 3$ µM) the rise of ΔOT was attenuated until the last protein injection ($c = 5$ µM) caused only a small increase in ΔOT (cf. Figure 4.27).

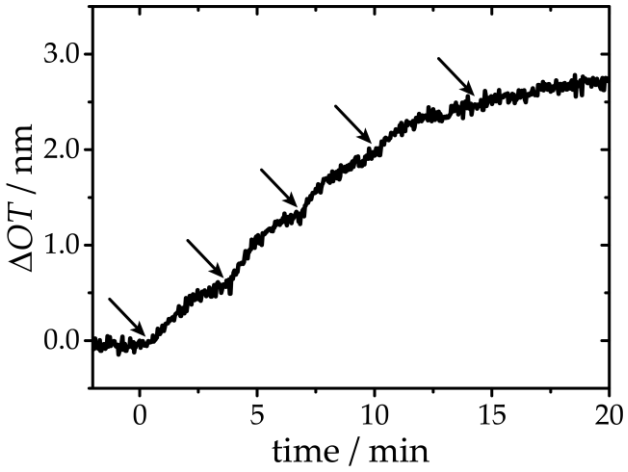

Figure 4.27: Exemplary plot of ΔOT vs. the time during an adsorption experiment of CB2$_{SH3/W24A-E262A}$ to an SHM composed of POPC : PtdIns[4,5]P_2 (9 . 1, *n*:*n*). The protein concentration was subsequently increased in 1 µM-steps (starting at $t = 0$ min, indicated by arrows) from 0-5 µM.

This indicates the saturation of accessible receptor lipids in the SHM and thus maximum surface coverage by the adsorbed protein. However, in the statistics of all adsorption isotherms recorded on PtdIns[4,5]P_2 containing SHMs a mitigation in ΔOT increase but no saturation is evident (cf. Figure 4.28 red curve). In contrast to that, when adsorbed to membranes doped with PtdIns[3]P and PtdIns[3,4,5]P_3 CB2$_{SH3/W24A-E262A}$ reached complete surface coverage at lower concentrations (cf. Figure 4.28 blue and green curves). To be precise, the fitted LANGMUIR adsorption isotherms (solid lines in Figure 4.28) indicate that complete surface coverage with the active mutant has been reached already at $c \geq 3$ µM. For all phosphoinositides under investigation at least four independent experiments were performed. The data points are the corresponding mean values while the error bars represent the error of the mean. In virtue of a lack of measurements with higher protein concentrations,

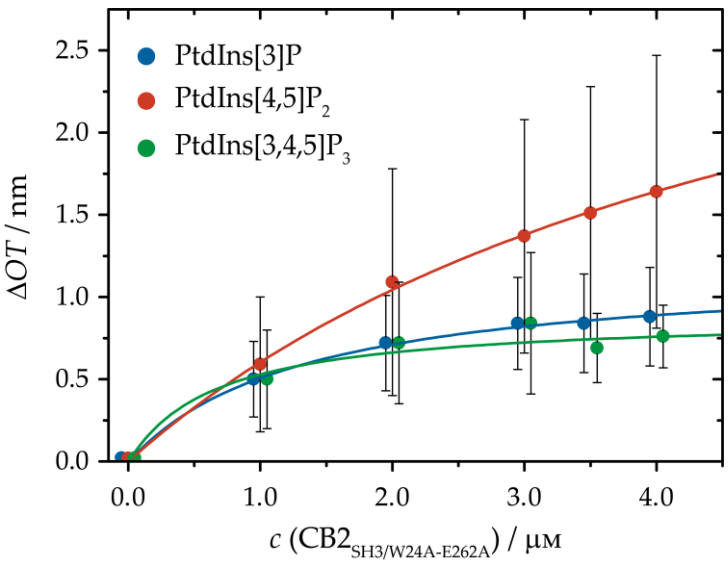

Figure 4.28: Adsorption isotherms of CB2$_{SH3/W24A-E262A}$ to POPC SHMs doped with 10 mol% of either PtdIns[3]P (blue), PtdIns[4,5]P_2 (red) or PtdIns[3,4,5]P_3 (green). Error bars are the standard error of the mean with $n \geq 4$. The continuous curves in the corresponding colours represent the applied LANGMUIR fits.

the adsorption isotherms only consider the range from 0 to max. 4 µM. This was owed to the low yield obtained from the heterologous expression (cf. Table 4.5). Furthermore, data gathering in the low concentration range ($c > 1$ µM) due to the signal-noise ratio of RIfS and challenging concentration adjustments. Nevertheless, the statistics were used to obtain the protein specific parameters ΔOT_{max} and the dissociation constant K_D which are illustrated in Figure 4.29.

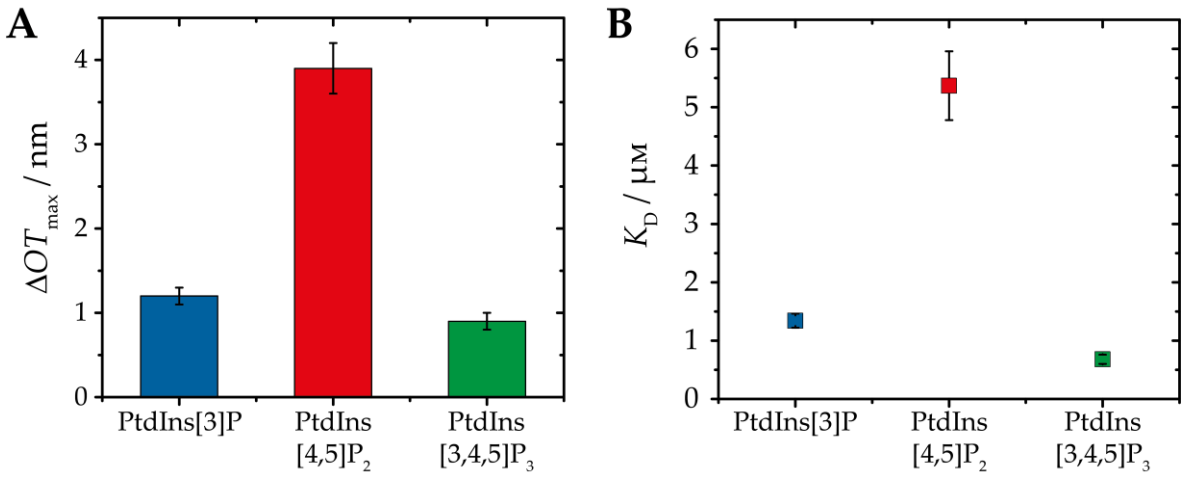

Figure 4.29: Determined ΔOT_{max} (**A**) and K_D values (**B**) of CB2$_{SH3/W24A-E262A}$ on POPC SHMs doped with 10 mol% of either PtdIns[3]P (blue), PtdIns[4,5]P$_2$ (red) or PtdIns[3,4,5]P$_3$ (green). Error bars are the standard error of the mean with $n \geq 3$.

The afore mentioned tendency of CB2$_{SH3/W24A-E262A}$ to induce maximum change in optical thickness already at concentrations of around 3 µM is also represented in the calculated ΔOT_{max} values (cf. Figure 4.29 A) with (1.2 ± 0.1) nm and (0.9 ± 0.1) nm for PtdIns[3]P and PtdIns[3,4,5]P$_3$, respectively. The maximum signal intensity on PtdIns[4,5]P$_2$ (ΔOT_{max} = (3.9 ± 0.3) nm) was by a factor of four larger than that determined for the trisphosphorylated PtdInsP. These calculations indicate an increased binding capacity for hybrid membranes doped with PtdIns[4,5]P$_2$. Furthermore, when compared to the values calculated for CB2$_{PH}$ with (1.9 ± 0.1) nm and (1.5 ± 0.1) nm on PtdIns[3]P and PtdIns[3,4,5]P$_3$, respectively, the ΔOT_{max} values of the active mutant suggest a reduced membrane binding capacity for SHMs containing the mono- and trisphosphorylated PtdInsP. Yet, no such impact was detected for PtdIns[4,5]P$_2$. Another difference in adsorption of the two collybistin 2 isoforms to phosphoinositide doped hybrid membranes is represented by the different affinities. While CB2$_{PH}$ exhibits highest affinity to the monophosphorylated PtdIns[3]P, the K_D of (0.7 ± 0.1) µM for PtdIns[3,4,5]P$_3$ depicts the strongest binding in case of CB2$_{SH3/W24A-E262A}$ adsorption (cf. Figure 4.29 B). The dissociation constants determined for either PtdIns[3]P or PtdIns[4,5]P$_2$ were (1.3 ± 0.1) µM or (5.4 ± 0.6) µM, respectively. Thus, the latter is the only combination of protein

and receptor lipid that can be described as a low affinity interaction when following the general categorisation.[259,260] A STUDENT's *t*-test was performed for the K_D values expressed by both isoforms ($CB2_{PH}$ and $CB2_{SH3/W24A-E262A}$) to each phosphoinositide and showed that all were significantly different. However, when reconsidering the great margin of affinities expressed by various PH domains to phosphoinositides (cf. Chapter 4.3.2) the values determined in this work do lie in a narrow range. Exclusively, the values of $CB2_{SH3/W24A-E262A}$ adsorption to PtdIns[4,5]P_2 do not match with the others. This mismatch might be caused by the heterogeneity in the detected adsorption signals leading to the error. Despite this, the calculated protein characteristics are considered to correspond well, as related fluctuations have also been shown for other isolated PH domains and their respective full-length proteins.[257]

One interesting aspect calls for precise investigation. When considering size or better say the molecular weights of the two proteins, the active mutant is by a factor of ~2.6 larger than the *C*-terminal PH domain. This difference must also be reflected in the dimensions of the proteins. Therefore, adsorption of the full-length protein should lead to a larger change in optical thickness assuming identical surface coverage. However, this is not the case contemplating the calculated ΔOT_{max} values. While the ones determined for adsorption of both isoforms to PtdIns[4,5]P_2 were similar, the ΔOT_{max} values of $CB2_{SH3/W24A-E262A}$ on PtdIns[3]P and PtdIns[3,4,5]P_3 doped SHMs were smaller than those calculated for $CB2_{PH}$ on the respective phosphoinositides. The tendencies of the adsorbed protein layers might originate from a smaller surface coverage or could be traced to a special protein organisation on the surface. This however could not be examined by means of RIfS. Hence the organisation of the adsorbed collybistin 2 isoforms was investigated by means of atomic force microscopy (AFM). The results gathered with this surface-sensitive technique are described within the next chapter.

4.3.4 Organisation of adsorbed CB2 on SHMs containing different phosphoinositides

-Some of the AFM experiments were performed by Anna Lena Toschke as part of her bachelor thesis-

For the characterisation of processes taking place at surfaces reflectometric interference spectroscopy (RIfS) is a valued technique to examine inter alia adsorption and deposition processes, such like those presented earlier. But as a consequence of its experimental setup (cf. Chapter 3.5.3), the spectroscope detects changes in a scanning area of around 1 mm². Therefore, the detected changes in reflectivity and consequently in optical thickness (ΔOT) are averaged over this zone. That is why the information gathered by means of RIfS can be used as an indicator for e.g. the amount of bound protein or other deposits. Yet, further details such as physical thickness (d) of the adlayer can only be determined in case of complete surface coverage by the adsorbate. In addition the prepared hybrid membranes were examined by means of atomic force microscopy (AFM, cf. Chapter 3.6) after addition of one of the collybistin 2 isoforms and incubation for at least one hour to obtain spatially resolved information. Imaging of the surface was conducted in intermittent-contact mode to reduce forces induced by the cantilever to a minimum. It is important to emphasise that after protein injection and incubation the preparations were not rinsed with buffer. In Figure 4.30 three exemplary micrographs are illustrated, showing the *C*-terminal PH domain of collybistin 2 ($CB2_{PH}$) adsorbed to solid-supported hybrid membranes (SHMs) composed of POPC and one of the three phosphoinositides (9 : 1, n/n) under investigation in this work.

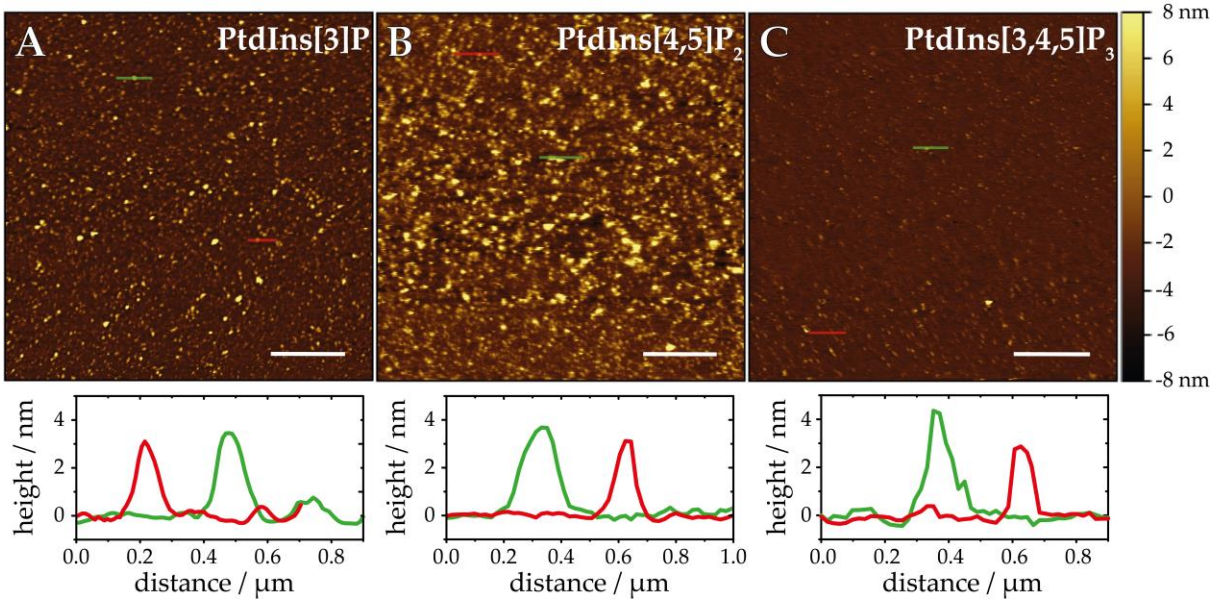

Figure 4.30: Atomic force micrographs of CB2PH ($c \geq 1$ µM) on POPC SHMs doped with either PtdIns[3]P (**A**), PtdIns[4,5]P2 (**B**) or PtdIns[3,4,5]P3 (**C**) (9 : 1, n/n) with the corresponding line scans below. The latter graphs present the height profile along the cross sections highlighted with red and green lines in the micrographs. Scale bars: 2 µm.

In all three micrographs high structures were presented in gold while brown areas provide a height equal to that of the membrane surface. Thus, on all SHMs containing the different PtdInsPs adsorbed structures, defined as CB2PH, are visible. Additionally, in all micrographs red and green lines highlight cross sections along which height profiles have been detected. These profiles are shown in graphs below the corresponding micrograph. In all cross sections, adsorbates with heights between 3-4 nm were detected independent of the phosphoinositide deployed as receptor lipid.

This homogeneity in height of the adsorbed structures is also reflected in the histograms illustrating the height distribution (cf. Figure 4.31) of the detected local maxima (cf. Chapter 3.6.3). In case of PtdIns[4,5]P_2 a very narrow distribution was recorded (cf. Figure 4.31 B), while for the two other phosphoinositides broader scatterings were determined with extended shoulders to higher values (cf. Figure 4.31 A and C).

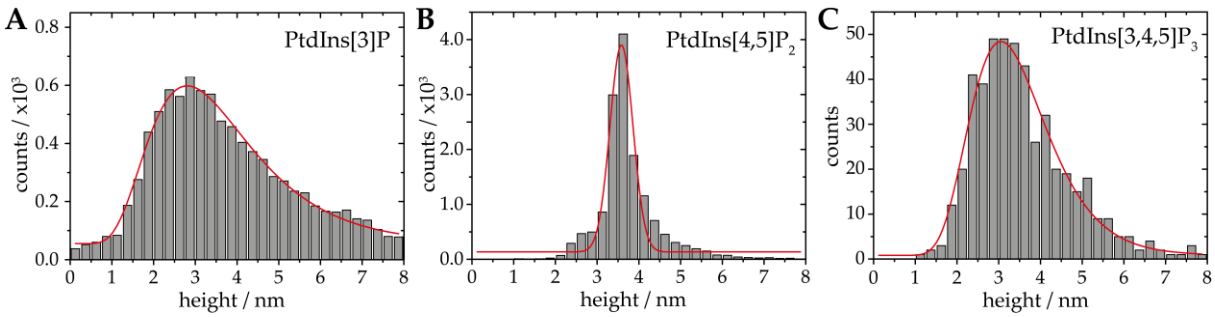

Figure 4.31: Histograms of the detected local maxima and their corresponding heights for CB2PH (c ≥ 1 µM) adsorbed to POPC solid-supported hybrid membranes doped with 10 mol% of either PtdIns[3]P (**A**), PtdIns[4,5]P2 (**B**) or PtdIns[3,4,5]P3 (**C**). Either normal or log-normal functions were fitted to the data indicated by the solid red lines to determine the average height.

To all data sets distribution-functions were adjusted to determine the mean height of the adsorbed aggregates. For PtdIns[3]P and PtdIns[3,4,5]P3 log-normal distributions were adapted whilst a normal distribution was fitted to the data gathered for CB2PH on PtdIns[4,5]P2. Based on this analysis an average protein height of CB2PH was determined on each of the three phosphoinositides, which are summarised in Table 4.6.

The height of the PH domain varies between 3.3 and 3.6 nm which is a very narrow range. Based on these results the height of adsorbed CB2PH can be assumed to be independent of the deployed phosphoinositide. When reconsidering the RIfS results such equality was not determined for ΔOT_{max} (cf. Figure 4.25 A). Yet, both findings are consistent when considering averaging effect in detection during RIfS experiments and the difference in surface coverage by CB2PH dependent on the deployed receptor lipid. This difference in surface occupancy is instantly evident when comparing the presented micrographs of the adsorbed *C*-terminal domain (cf. Figure 4.30). The variation in surface coverage was quantified by calculating the surface area ratio covered by protein via analysis of binary versions of the micrographs that distinguished between adsorbate and membrane surface via thresholding. The obtained occupancies are summarised in Table 4.6.

Table 4.6: Calculated heights of and surface coverages by CB2PH (c ≥ 1 µM) adsorbed to SHMs doped with 10 mol% phosphoinositide with the corresponding statistics. For comparative reasons, the determined ΔOT_{max} values are also included.

Receptor lipid	PtdIns[3]P	PtdIns[4,5]P_2	PtdIns[3,4,5]P_3
CB2PH height / nm	3.40 ± 0.04	3.58 ± 0.04	3.34 ± 0.13
n_{Image}	8	8	9
$N_{Preparations}$	2	3	2
Distribution	log-norm	Normal	log-norm
Surface coverage / %	20.0 ± 3.8	31.0 ± 1.3	2.6 ± 1.1
ΔOT_{max} / nm	1.9 ± 0.1	3.7 ± 0.2	1.5 ± 0.1

The relative amount of surface covered by CB2PH is maximum on PtdIns[4,5]P_2 doped SHMs (cf. Chapter 4.2.3). In case of PtdIns[3]P and PtdIns[3,4,5]P_3 containing membranes the occupancy by protein is lower. These values are in good agreement with the trend determined for ΔOT_{max}. But the rather high occupancy difference between the mono- and trisphosphorylated phosphoinositide is not reflected in the RIfS results. This can be explained by the affinity of CB2PH to the latter, being the lowest for all PtdInsPs tested within this work. The weaker interaction and the application of external forces by the cantilever might lead to the removal of a large amount of protein from the PtdIns[3,4,5]P_3 containing membrane surface and thus resulting in a reduced surface coverage. Higher fluctuation in SHMs doped with PtdIns[3,4,5]P_3 might be another explanation for the reduced occupancy, as imaging of adsorbed proteins would not be possible in a more dynamic system.

With this supporting and explanatory results for the RIfS data on CB2PH at hand, it is now necessary to have a closer look on the behaviour of the adsorbed active mutant to illuminate the discrepancy detected for CB2PH and CB2SH3/W24A-E262A adsorption via RIfS (cf. Chapters 4.3.2 and 4.3.3). In analogy to the experiments performed with CB2PH, also the active mutant of collybistin 2 was imaged after its adsorption to SHMs containing 10 mol% phosphoinositide. Representative micrographs are shown in Figure 4.32.

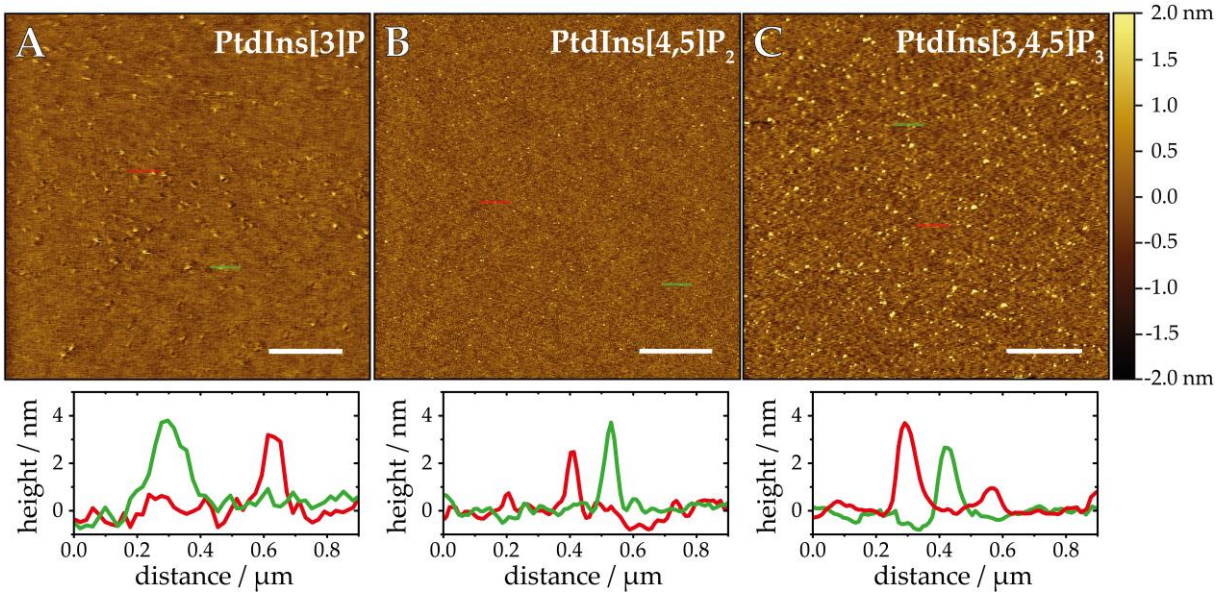

Figure 4.32: Atomic force micrographs of CB2SH3/W24A-E262A ($c \geq 1$ µM) on POPC SHMs doped with either PtdIns[3]P (**A**), PtdIns[4,5]P_2 (**B**) or PtdIns[3,4,5]P_3 (**C**) (9 : 1, *n*/*n*) with the corresponding line scans below. The latter graphs present the height profile along the cross sections highlighted with red and green lines in the micrographs. Scale bars: 2 µm.

Extra to the micrographs, height profiles of the adsorbed structures are displayed below the corresponding images. The respective line scans are visualised by red and green lines in the original surface images. Again, all profiles demonstrate deposits on top of the SHMs with height ranging between 2.5 and 4 nm independent of the deployed receptor lipid.

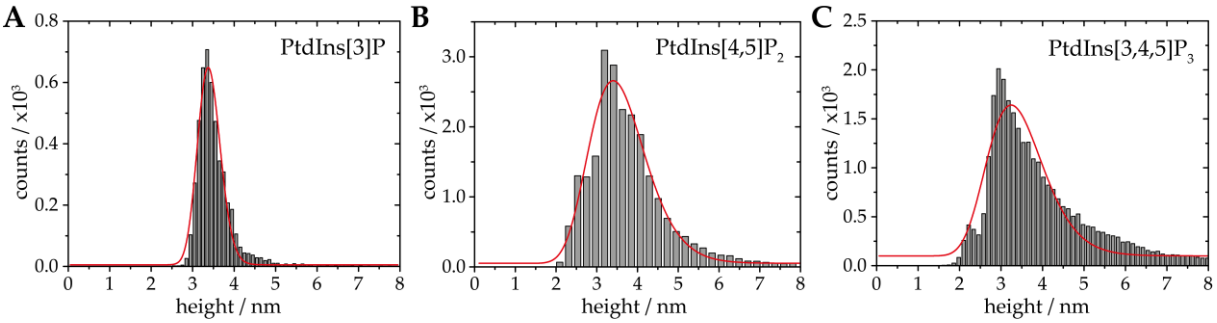

Figure 4.33: Histograms of the detected local maxima and their corresponding heights for CB2$_{SH3/W24A-E262A}$ ($c \geq 1$ µM) adsorbed to POPC solid-supported hybrid membranes doped with 10 mol% of either PtdIns[3]P (**A**), PtdIns[4,5]P$_2$ (**B**) or PtdIns[3,4,5]P$_3$ (**C**). Either normal or log-normal functions were fitted to the data indicated by the solid red lines to determine the average height.

This uniformity is also evident in the histograms (cf. Figure 4.33) that represent all detected local maxima and their corresponding heights of the absorbed active mutant to PtdIns[3]P, PtdIns[4,5]P$_2$ and PtdIns[3,4,5]P$_3$. A log-normal distribution-function was fitted to the data sets of the histograms to determine the height of adsorbed CB2$_{SH3/W24A-E262A}$. The results of the fits together with the underlying statistics are summarised in Table 4.7.

Like the findings on CB2$_{PH}$, also the height of the adsorbed active CB2 mutant is indifferent for SHMs doped with the three phosphoinositides. Surprisingly, the calculated heights for the latter match those determined for the PH domain as vividly illustrated in Figure 4.34. This finding was unexpected as the minimal adsorption fragment provides a molecular weight just slightly above a third of the mutant's mass, hence calls for further consideration. Yet, for the moment refocussing of the presented micrographs is more reasonable as also in case of CB2$_{SH3/W24A-E262A}$ heterogeneous amounts of adsorbed protein have been detected on the SHMs. This becomes obvious when comparing the quantity of golden structures on top of the membrane surfaces (represented in light brown) in Figure 4.32 A to C. Consequently, the surface occupancy by CB2$_{SH3/W24A-E262A}$ is also affected by the receptor lipids, as well as it is the case for CB2$_{PH}$. The calculated ratios of area occupied with CB2$_{SH3/W24A-E262A}$ to vacant membrane surface are summed up in Table 4.7.

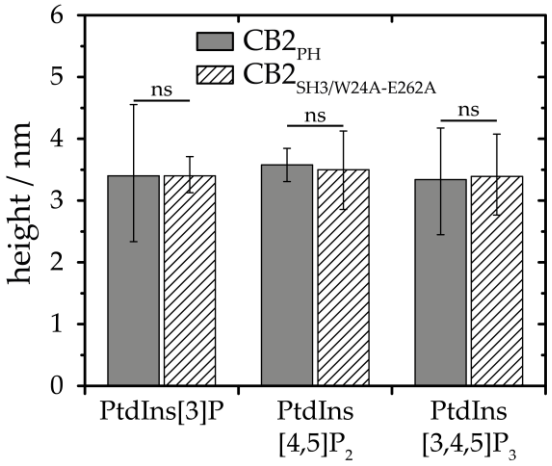

Figure 4.34: Protein heights of the collybistin 2 isoforms CB2$_{PH}$ (solid grey bars) and CB2$_{SH3/W24A-E262A}$ (shaded bars) on 10 mol% phosphoinositides containing POPC SHMs determined by AFM. Error bars indicate the standard deviations (σ) of the fitted distribution functions.

Table 4.7: Calculated heights of and surface coverages by $CB2_{SH3/W24A-E262A}$ ($c \geq 1$ μM) adsorbed to SHMs doped with 10 mol% phosphoinositide with the corresponding statistics. For comparative reasons, the determined ΔOT_{max} values are also included.

Receptor lipid	PtdIns[3]P	PtdIns[4,5]P_2	PtdIns[3,4,5]P_3
$CB2_{SH3/W24A-E262A}$ height / nm	3.40 ± 0.03	3.50 ± 0.04	3.39 ± 0.06
n_{Image}	6	10	9
$N_{Preparations}$	2	3	4
Distribution	normal	log-norm	log-norm
Surface coverage / %	1.1 ± 0.4	1.2 ± 0.8	3.0 ± 1.3
ΔOT_{max} / nm	1.2 ± 0.1	3.9 ± 0.3	0.9 ± 0.1

The occupancies in case of PtdIns[3]P and PtdIns[4,5]P_2 are an order of magnitude smaller than those determined for $CB2_{PH}$ under identical conditions. Only for PtdIns[3,4,5]P_3 no significant difference was detected between the two collybistin 2 isoforms. When compared to the RIfS data on $CB2_{SH3/W24A-E262A}$, it becomes obvious that the occupancy variation matches the determined affinities (cf. Chapter 4.3.3). At the same time the high fluctuations in ΔOT_{max} (cf. Figure 4.29 A and Table 4.7) cannot entirely be explained by the calculated coverages. While for PtdIns[3]P and PtdIns[3,4,5]P_3 the findings are in good accordance, there is a mismatch in case of the bisphosphorylated PtdIns[4,5]P_2. Such an effect might be explained with the low affinity of the active mutant to PtdIns[4,5]P_2 (cf. Figure 4.29 B) causing a wide spread of ΔOT induced by $CB2_{SH3/W24A-E262A}$ adsorption. This in turn affects the determination of ΔOT_{max} rendering it imprecise.

The identical height of $CB2_{PH}$ and the full-length active mutant with a 2.6 times higher molecular weight is remarkable and will be discussed below. To better understand the organisation of the proteins, CD (circular dichroism) spectroscopy or crystal structure analysis can be performed with the latter being the technique of choice to gain detailed structural information. However, neither for the PH domain nor for CB2 itself these data are available, whilst CB1 was characterised in detail by means of small angle X-ray scattering (SAXS).[60] The crystal structure in various orientations (PDB ID: 4MT6, turned around the *z*-axis) are illustrated in Figure 4.35.

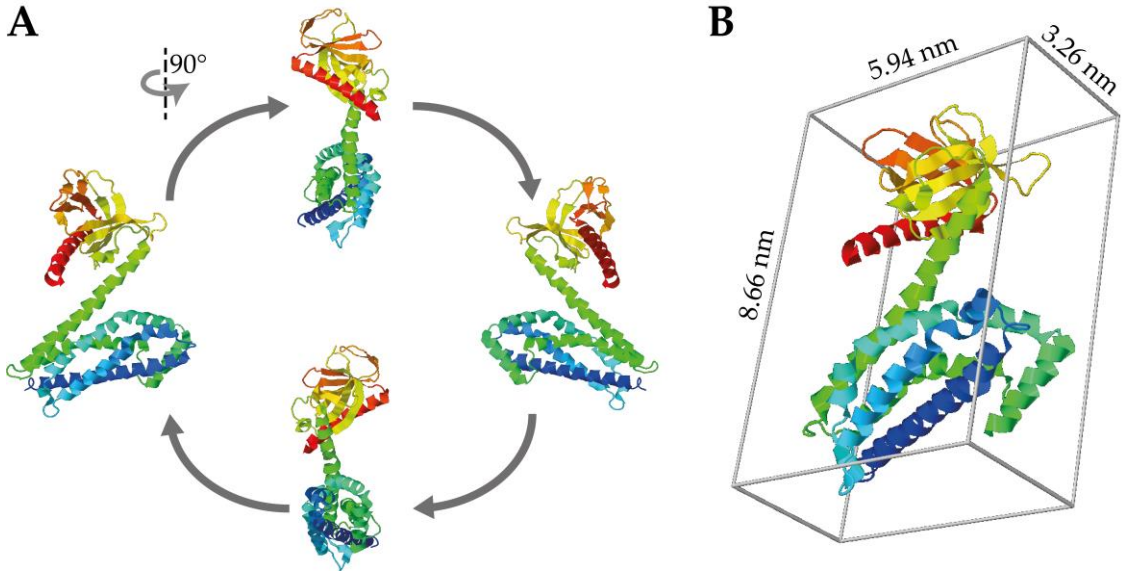

Figure 4.35: Crystal structure of the active collybistin 1 isoform (PDB ID: 4MT6) determined by means of SAXS at a resolution of 5.501 Å² by SOYKAN *et al.*[54] The PH domain is coloured in yellow, orange and red, while green and blue code the DH domain. **A**: 360° rotation of the structure around its *z*-axis. **B**: Visualisation of the protein dimensions by placement of the structure inside a box.

The dimensions of the protein structure become obvious when placed inside a box of corresponding side lengths (cf. Figure 4.35 B). These dimensions can also be attributed to CB2 in a good approximation as both proteins share an overall amino acid sequence homology of 95.5 %. To be more precise, 450 amino acids exhibit an overlap with a unity of 99.1 % when both sequences (for CB2 cf. Appendix A.4.3) are compared excluding the terminal domains.[60] The determined heights for both adsorbed CB2 isoforms range around 3.4 nm which fits to the smallest extension determined for CB1. The flat character of the structure in one dimension is evident in the complete rotation visualised in Figure 4.35 A. Therefore, only an adsorption behaviour for the full-length protein is possible in which the other subdomains (SH3 and DH) are arranged next to the PtdInsP-binding PH domain. This would be equal to a deposition of the "boxed" protein alongside the (8.66 x 5.94) plane which is schematically illustrated in Figure 4.36.

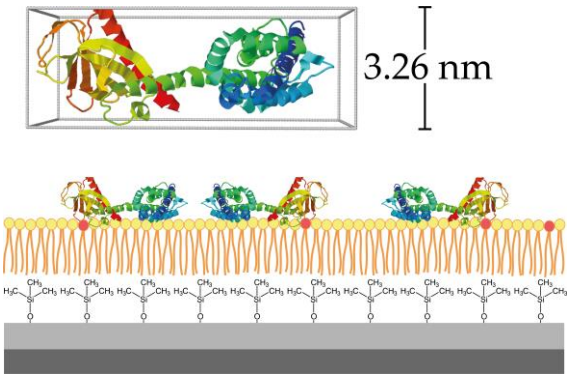

Figure 4.36: Scheme of the hypothised full-length collybistin orientation when adsorbed to PtdInsP containing solid-supported hybrid membranes.

This arrangement can be supported when considering structural similarities with other PtdInsP-interacting proteins. The PH domains usually share a low sequence identity. However, all possess a β-sandwich fold that is capped at one end with a *C*-terminal α-helix.[262] This motif is also present in the PH domains of both phospholipase C-δ_1 (PLC-δ_1) and CB1 as shown in Figure 4.37.[60,265] Focussing the structure of PLC-δ_1, it becomes obvious that the headgroup of PtdIns[4,5]P_2, Ins[1,4,5]P_3, is embedded in the mentioned cavity in a specific manner. This embedment would only allow the protein to be adsorbed to a PtdIns[4,5]P_2 doped membrane in the fashion previously suggested for CB based on the determined protein heights. In Figure 4.37 B the CB1 crystal structure is shown in an orientation that matches that of PLC-δ_1 and highlights its own PtdInsP binding site (red sphere). Thus, the detected protein heights for $CB2_{PH}$ and $CB2_{SH3/W24A-E262A}$ are confirmed by exact structure determinations of related proteins. One might argue on the incomparability of PLC-δ_1 and CB, due to the previously determined unspecific binding character for collybistin in contrast to the specificity of PLC-δ_1 to PtdIns[4,5]P_2. But this can be neglect as it has been shown by BARALDI *et al.* that the binding site for PtdIns[3,4,5]P_3 in the PH domain of Bruton's tyrosine kinase (Btk) is identical to that for PtdIns[4,5]P_2 in PLC-δ_1's pleckstrin homology domain.[264] Based on their results it is reasonable to consider the protein orientation on the model membranes independent of the used phosphoinositide, which is consistent with the results of this work. Thus, the presented crystal structure of CB provides a good explanation for the determined heights, however, also other explanations might be possible. It might be possible that the structure of CB is more flexible and therefore capable arranging in different conformations while bound to phosphoinositides on top of membranes. In a recent study CHIOU *et al*. were able to model the arrangement of CB in a PtdIns[3]P bound state with molecular dynamics (MD) simulations.[266] They detected different conformations for the wild-type of collybistin 1, among which an elongated

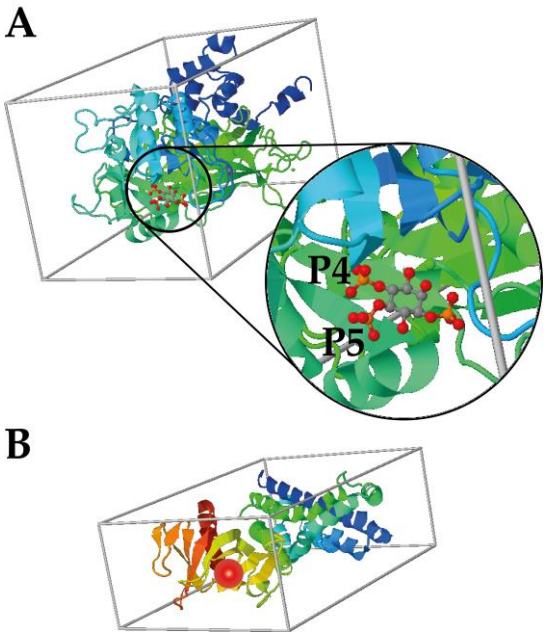

Figure 4.37: A: Boxed crystal structure of PLC-δ_1 with a zoom-in on the Ins[1,4,5]P_3 binding site (PDB ID: 1DJX).[249] **B**: Boxed CB1 in a similar orientation to highlight the PtdInsP binding site (red sphere).[54]

one was predominant with 68 %. The second most frequent conformation, which they referred to as an "open clam", was evident in 32 % of the cases. Both states diverged from the determined crystal structure (cf. Figure 4.35 B) thereby implying that structural flexibility might be possible.

Finally, the independency of the protein height from the used phosphoinositide allows investigations of other features that might be dependent on the receptor lipids like the lateral organisation of the adsorbed proteins. This becomes obvious when comparing the micrographs presented for both $CB2_{PH}$ and $CB2_{SH3/W24A\text{-}E262A}$ (cf. Figure 4.30 and Figure 4.32). It appears that the deposits were not only dependent on the deployed PtdInsP but were characteristic for the added collybistin isoform. To analyse this indications in detail, the available binary images of the original micrographs (cf. Chapters 3.6.3 and 4.2.3) have been deployed. The resulting size distributions of the deposits for both PH domain and $CB2_{SH3/W24A\text{-}E262A}$ were determined as vividly shown in Figure 4.38.

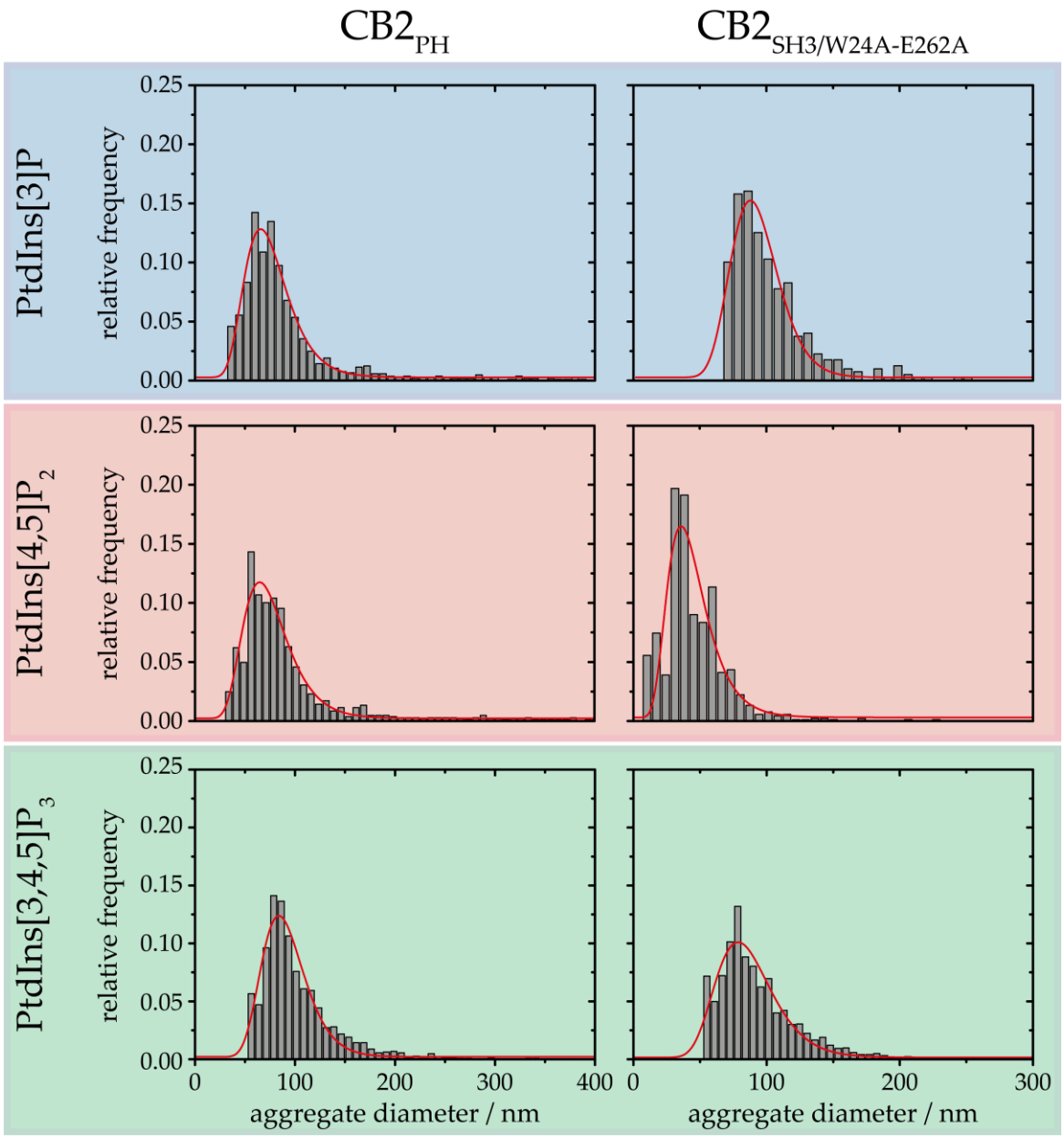

Figure 4.38: Histograms of the deposit diameters determined for $CB2_{PH}$ (left) and $CB2_{SH3/W24A-E262}$ (right) on top of SHMs composed of POPC and 10 mol% of either PtdIns[3]P (blue), PtdIns[4,5]P_2 (red) or PtdIns[3,4,5]P_3 (green). To each data set a log-normal distribution function was adjusted represented by red curves.

Log-normal distribution functions were adjusted to the presented probability density distributions enabling the determination of the corresponding medians. The fit functions are represented by red lines and the medians are summarised in Table 4.8.

Table 4.8: Overview of the determined $CB2_{PH}$ and $CB2_{SH3/W24A-E262A}$ aggregate sizes determined on SHMs doped with the different phosphoinositides.

	Deposit diameter / nm		
Receptor lipid	PtdIns[3]P	PtdIns[4,5]P_2	PtdIns[3,4,5]P_3
$CB2_{PH}$	73 ± 1	72 ± 1	89 ± 1
$CB2_{SH3/W24A-E262A}$	92 ± 1	42 ± 2	84 ± 1

It becomes clear that the defined clusters of $CB2_{PH}$ are uniform in size when the mono- and bisphosphorylated phosphoinositides function as receptor lipids. Solely, in case of PtdIns[3,4,5]P_3 the size is slightly increased to (89 ± 1) nm. This might originate from the different affinities determined for $CB2_{PH}$ to the phosphoinositides (cf. Figure 4.25). Because of weaker interactions, smaller aggregates might be removed from the membrane surface during imaging. In contrast to that larger aggregates that are composed of an increased number of protein molecules can interact with a greater number of receptor lipid molecules. The deposits with higher pinning-point quantity, hence, can resist the induced forces and are detected whilst the smaller ones are removed. This would also explain the drastically declined surface occupancy of 2.6 % (cf. Table 4.6 and Table 4.7). In addition, this is also supported by the fact that no clusters were detected with a diameter below 50 nm (cf. Figure 4.38). Another explanation might be a varying mobility of the adsorbed protein clusters. While large structures are more rigid, the smaller aggregates might diffuse on the membrane surface and thus would be indetectable by AFM.

In case of aggregates composed of full-length protein, the cluster size exhibits a wider range. The tendencies on the different PtdInsPs, however, do not show a correlation with the previous determined protein characteristics like affinity or binding capability of the SHMs (cf. Figure 4.29). A reason for this can be seen in the very low surface coverage by adsorbed protein that ranged between 1.1 and 3.0 % (cf. Table 4.7).

Nevertheless, the results presented within this chapter identified both isoforms of CB2, $CB2_{PH}$ and $CB2_{SH3/W24A-E262A}$, as unspecific interaction partners of phosphoinositides with moderate affinities. Furthermore, no specific lateral protein-protein interactions were detected in contrast to e.g. N-ERMAD (cf. Figure 4.15) or the full-length protein of ezrin.[217] A detailed analysis of the interaction between the adapter protein collybistin 2 and different variants of phosphoinositides was presented. Thereby, a firm foundation was established upon which the planned

in vitro model system for the post synaptic GABA$_A$ergic receptor machinery can be build. On this purpose, an additional receptor lipid was introduced to the model membrane. This lipid was used as a specific receptor for a protein construct mimicking the intracellular domain of neuroligin 2. This expansion allows a detailed characterisation of the interaction between the adaptor protein collybistin 2 and the cell adhesion protein neuroligin 2, which is believed to be a prerequisite for the activation of CB2 under physiological conditions. The results obtained in the expanded model complex are focus of Chapter 4.4

4.4 Neuroligin2—Collybistin2 interactions within the *in vitro* model system of GABA$_A$ergic receptor-organisation

-The RIfS data presented in this section contain results determined by Lucas Förster as part of his master thesis-

The adapter protein collybistin 2 is one of the constituents of the GABA$_A$ergic receptor organisation machinery and therein responsible for the interaction of the protein complex with the post synaptic plasma membrane. This interaction induces the accumulation of GABA$_A$ receptors in the postsynaptic specialisations and thus its fixation in direct apposition to the presynaptic terminals. Yet, in analogy to the findings on the homologous APC-stimulated guanine nucleotide exchange factors (Asef) 1 and 2,[267,268] also the SH3 domain of collybistin 2 forms an intramolecular interaction with the *C*-terminal PH domain. This renders the protein incapable of membrane binding as a closed conformation is exhibited. The consequences of such behaviour have been detected in coexpression experiments within HEK 293 cells in which CB1 (SH3 domain containing isoform) was redistributed to gephyrin-rich cytoplasmic regions, while CB2 (lacking the SH3 domain) induces sub-membraneous gephyrin clustering.[90] In contrast to that, both collybistin isoforms redistributed gephyrin into synaptic clusters in transfected cortical neurons.[48] These findings suggest a specific local activation of CB1 via a SH3-interacting partner. In 2009, neuroligin 2 (NL2) was identified by POULOPOULOS *et al.* to perform such an interaction and thereby inducing gephyrin in a neuron-specific manner.[30] Its short intracellular domain contains various motifs assumed to be necessary for the scaffolding process of postsynaptic components.[269,270] Among these, a gephyrin-specific binding side and poly-proline sections are found. The latter are missing in the CB-binding-deficient neuroligins 1 and 3,

hence the interaction of CB2 and NL2 is believed to be a typical SH3/poly-proline mode.[60] All known studies, focussing on this specific interaction in order to determine collybistin activation, were performed *in vivo*. Thus, other effectors cannot be ruled out completely. With the solid-supported hybrid membrane (SHM) system and its highlighted advantages (cf. Chapters 4.1 and 4.2) an isolated observation of the interaction process is possible. To allow the adsorption of both CB2 and NL2 to the SHM, the in-depth characterised system (cf. Chapter 4.3) had to be expanded with a second receptor lipid specific for neuroligin. The lipid of choice for this purpose was 1,2-dioleoyl-*sn*-glycero-3-{[*N*-(5-amino-1-carboxypentyl)iminodiacetic acid]succinyl} nickel salt (DGS, cf. Scheme 3.3) as the cell adhesion molecule (CAM) NL2 was mimicked by a protein construct that contained a *N*-terminally fused His_6-tag (His-*cyt*NL2). The pursued modelling strategy is schematically illustrated in Figure 4.39. In this scheme PtdInsPs are represented by lipid molecules with red headgroups while those with blue ones correspond to DGS. The effects of the latter, which introduces a positive charge to the model system, on the membrane formation and its features will be focus of subsection 4.4.1 while in 4.4.2 the results on His-*cyt*NL2 isolation and introduction are presented. Conclusively, the impact of NL2 on the adsorption behaviour of collybistin 2 will be highlighted in section 4.4.3.

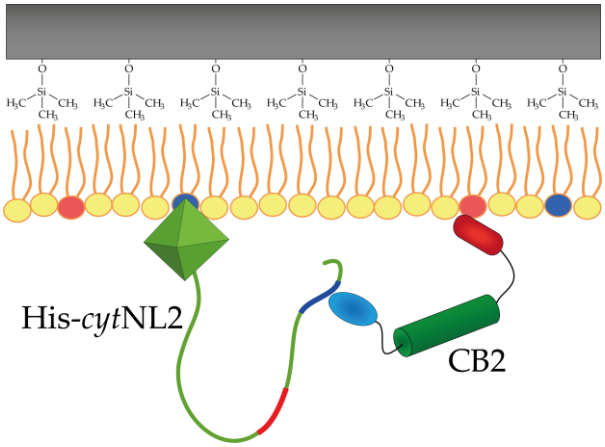

Figure 4.39: Scheme of the expanded model system containing both PtdInsP (red headgroup) and DGS (blue headgroup) in the solid-supported hybrid membrane to allow the simultaneous adsorption of NL2 and CB2.

4.4.1 Expansion of the model membrane system — Formation of PtdInsP and DGS containing SHMs

The preparation of solid-supported model membrane systems is either based on a combination of the LANGMUIR-BLODGETT and LANGMUIR-SCHÄFER techniques or on the adsorption and spreading of vesicles from aqueous solution to the substrate surface. The latter was the method applied within this work using hydrophobically functionalised silicon dioxide substrates. Obtained hybrid membranes containing different variants of phosphoinositides and changing concentrations thereof have been analysed extensively (cf. Chapter 4.1.3). These experiments showed no influence of either the PtdInsP amount nor the phosphorylation pattern of the phosphoinositide on the formation of SHMs or its layer thickness. To enable isolated examination of the interaction of NL2 with CB2 and the expected activation of the later, a second receptor lipid (DGS) was added to the system as schematically shown in Figure 4.39. Consequently, a detailed look has been taken at its influence on the hybrid membrane formation as DGS introduced a positive charge to the lipid layer which might have altered the membrane features because of electrostatic interactions with the negatively charged PtdInsPs. This was done by means of reflectometric interference spectroscopy (RIfS) enabling the *in situ* determination of the vesicle adsorption, spreading and membrane formation process. Furthermore, it had to be guaranteed that both receptor lipids were accessible in a sufficient amount to allow selective adsorption of both proteins even in case of consecutively injections. Therefore, POPC films, used for small unilamellar vesicle (SUV) preparation, contained 3 mol% of DGS with or without additional 3 mol% of PtdInsPs. The resulting hybrid membrane thicknesses are summarised in Figure 4.40. The calculated mean values of SHM thickness (represented by red squares) were (2.7 ± 0.3) nm for DGS/PtdIns[3]P (n = 38). Equally, the spreading of DGS and

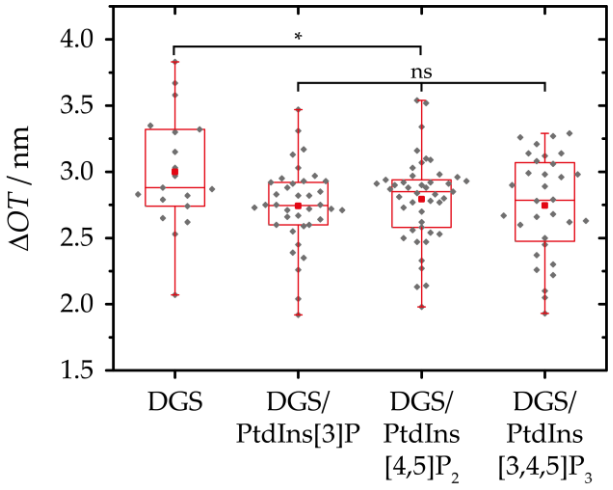

Figure 4.40: Box plots of the model membrane thickness of SHMs dependent on the receptor lipids in the small unilamellar vesicles used for membrane formation. The boxes extent from upper and lower quartile while the whiskers represent 1st and 99th percentiles. The medians are shown as horizontals inside the boxes and the means are represented by red squares within the respective data sets. A statistical ANOVA calculation determined no significant differences (*ns*) for SHMs containing combinations of DGS with PtdInsPs, while Δ*OT* of DGS doped SHMs is significantly different with **p* = 0.1.

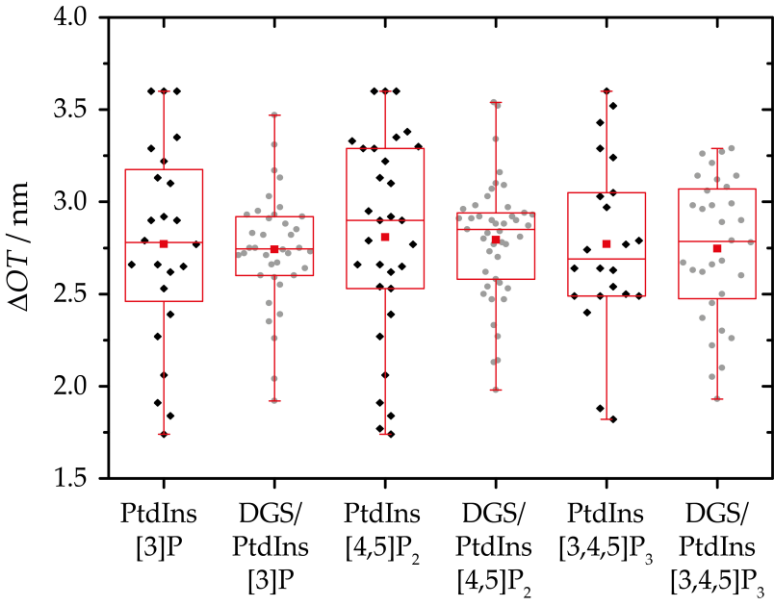

Figure 4.41: Box plots of the SHM thickness dependent on the presence or absence of DGS in PtdInsP containing SUVs used for membrane formation. The boxes extent from upper and lower quartile while the whiskers represent 1st and 99th percentiles. The medians are shown as horizontals inside the boxes and the means are represented by red squares within the respective data sets. A statistical ANOVA calculation determined no significant differences in ΔOT of the resulting SHMs.

PtdIns[4,5]P_2 (n = 45) or PtdIns[3,4,5]P_3 (n = 32) containing SUVs resulted in similar values, which was proven by an analysis of variance (ANOVA) that determined no significant differences among the DGS/PtdInsP containing SHMs. Then again, for membranes doped only with DGS a significant increase in resulting layer thickness was determined with a mean value of (3.0 ± 0.4) nm (n = 19, cf. Figure 4.40).

Furthermore, the obtained values for DGS/PtdInsP doped SHMs were compared to the ones for membranes containing only PtdInsPs (cf. Figure 4.41). Also, for this comparison an ANOVA determined no significant differences in the change of optical thickness correlating to the established hybrid membranes system. For this reason, it is assumed that DGS does not alter the membrane formation process. Even though the additional receptor lipid does not affect the resulting membrane thickness, it might still have an influence on its characteristics. In contrast to *in vivo* experiments supported membranes exhibit a reduced mobility of the lipids (cf. Chapter 4.1.4). This feature is commonly known; however, it might be affected due to the introduced positive charge by addition of DGS. Both receptor lipids provide opposing charges and might interact. Therefore, it was necessary to illuminate the resulting lipid mobility in presence of DGS. The mobility for BODIPY®-TMR labelled PtdIns[4,5]P_2 has already been determined the SHM and SLB as described in Chapter 4.1.4. Here, additional fluorescence recovery after photo bleaching (FRAP) experiments were performed with small fractions of the phosphoinositides being substituted by their BODIPY®-TMR labelled forms in presence and absence of DGS. Fluorescence images of SHMs composed of POPC : DGS : PtdInsP : BODIPY®-TMR PtdInsP (94.0 : 3.0 : 2.7 : 0.3, *n*/*n*/*n*/*n*) are shown in Figure 4.42.

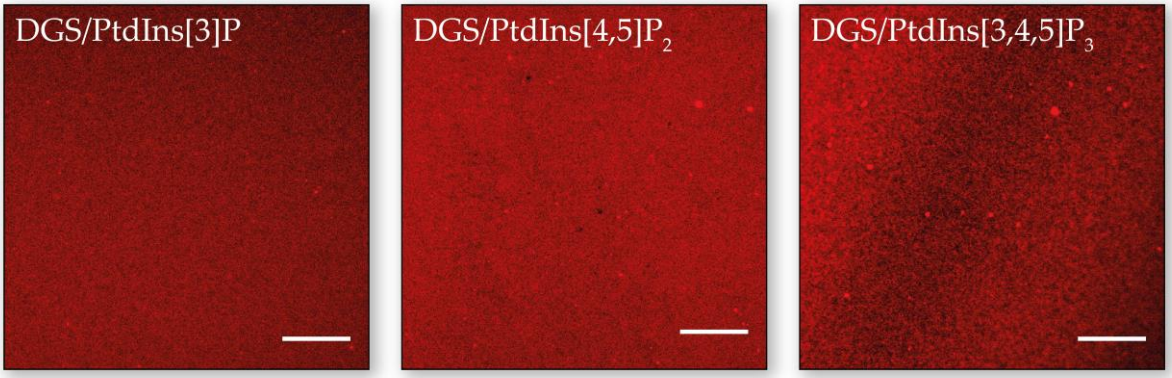

Figure 4.42: Exemplary fluorescence images obtained on solid-supported hybrid membranes composed of POPC : DGS : PtdInsP : BODIPY®-TMR PtdInsP (94.0 : 3.0 : 2.7 : 0.3, *n*/*n*/*n*/*n*). Scale bars: 20 µm.

The presented images are exemplary for hybrid membranes that contained the respective phosphoinositides in combination with DGS. In all preparations a homogenous fluorescence intensity distribution was detected while the quantity of defects (areas without fluorescence, black) remained low. Areas with higher intensities correlated are interpreted as adsorbed, un-spread lipid material which was proven by FRAP experiments. As the bright spots did not recovery it is concluded that they were not connected to the continuous lipid monolayer. The determined diffusion coefficients (D) and mobile fractions (γ_0) are summarised in Figure 4.43.

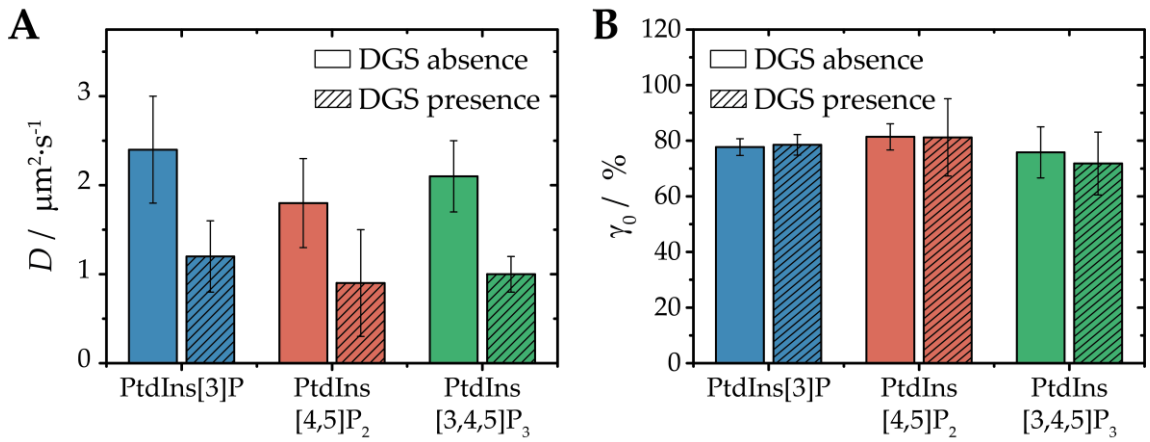

Figure 4.43: Overview on the effect of DGS absence in POPC/PtdInsP SHMs (97 : 3, *n*/*n*; solid bars) or its presence in POPC/DGS/PtdInsP SHMs (94 : 3 : 3, *n*/*n*/*n*, shaded bars) on the diffusion coefficients (**A**) and mobile fractions (**B**) of BODIPY®-TMR labelled phosphoinositides with 1 % of the corresponding PtdInsP being labelled. Scale bars represent the standard error of the mean with $n \geq 5$.

The calculated diffusion coefficients of the different labelled phosphoinositides do not show a significant difference as tested by ANOVA in case of either absence (solid bars) or presence of DGS (shaded bars, cf. Figure 4.43 A). This was expected because of identical fatty acid chains in all labelled PtdInsP-forms deployed in this work as exemplary shown in Scheme 3.5 for BODIPY®-TMR PtdIns[4,5]P2.

However, when specifically considering the effect of DGS on the lateral motion of each phosphoinositide, it becomes obvious that the diffusion coefficients significantly declined (tested by ANOVA) in all three cases. For PtdIns[3]P *D* has been reduced from (2.4 ± 0.6) $\mu m^2 s^{-1}$ without DGS to (1.2 ± 0.4) $\mu m^2 s^{-1}$ in its presence. A similar trend was detected for PtdIns[4,5]P_2 and PtdIns[3,4,5]P_3 with a decrease in *D* from (1.8 ± 0.5) $\mu m^2 s^{-1}$ to (0.9 ± 0.6) $\mu m^2 s^{-1}$ and from (2.1 ± 0.4) $\mu m^2 s^{-1}$ to (1.0 ± 0.2) $\mu m^2 s^{-1}$, respectively. Thus, the addition of DGS is accompanied by a bisection of lateral mobility of all phosphoinositides. This might be based on electrostatic interactions as DGS contains a divalent nickel cation (Ni^{2+}) in its headgroup which induces attractive forces on the phosphoinositides that present a high negative charge. However, no formation of PtdInsP-clusters within the confocal laser scanning microscope's (CLSM) resolution range was detectable, although it is common knowledge that divalent cations induce such processes especially in PtdIns[4,5]P_2 containing membranes.[204,205] It seems like the "caging" effect of the nitrilotriacetic acid (NTA) prevents such behaviour. In contrast to the diffusion coefficients, the presence of DGS does not influence the mobile fractions of the hybrid membranes that ranges around 80 % (cf. Figure 4.43 B). The independence of the mobile fractions of DGS can be understood as an additional prove for the absence of cluster, even of those with sizes beyond the detection limit. The presented effects of DGS on the model membrane system were considered admissible. Therefore, first adsorption experiments were performed with the well characterised protein collybistin 2 to determine the effect of the second receptor lipid on the interaction of the adapter protein with the phosphoinositides.

4.4.1.1 Impact of DGS on the collybistin 2 adsorption

The developed model system in this work aims on the imitation of the $GABA_A$ergic receptor ($GABA_AR$) organisation process. The involved proteins are anchored to specialisations in the postsynaptic plasma membrane by the adaptor protein collybistin. Therefore, it is necessary to ensure an unaffected adsorption of CB2 to its specific receptor lipid even if a further component is introduced to the model. On this purpose additional adsorption studies have been performed with full-length isoforms, $CB2_{SH3}$ and $CB2_{SH3/W24A-E262A}$. Even though the wild-type of CB2 ($CB2_{SH3}$) was already characterised as incapable of adsorption to phosphoinositides in the hybrid membranes of this work (cf. Figure 4.26 in Chapter 4.3.3), additional tests were required to eliminate unspecific interactions to the second receptor lipid DGS. The same holds

true for the point-mutated isoform CB2$_{SH3/W24A-E262A}$ as shown to be in a permanently opened conformation. For each of the full-length proteins an exemplary plot of the change in optical thickness (ΔOT) vs. the time during their adsorption to an SHM (POPC : PtdIns[3,4,5]P$_3$: DGS, 94 : 3 : 3, *n*/*n*/*n*) determined by means RIfS is shown in Figure 4.44.

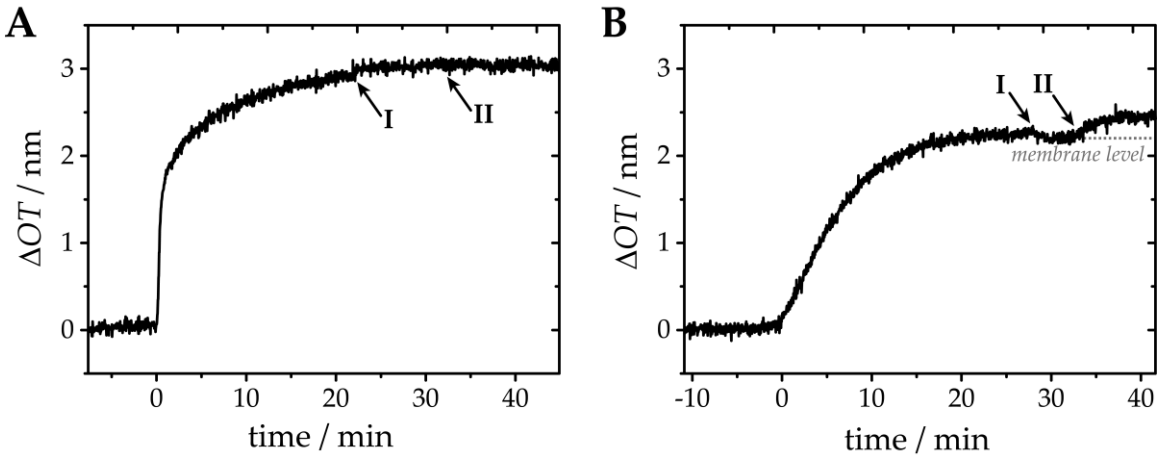

Figure 4.44: Exemplary plots of the change in optical thickness vs. the time during adsorption experiments of either CB2$_{SH3}$ (**A**) or CB2$_{SH3/W24A-E262A}$ (**B**) on POPC hybrid membranes doped with 3 mol% of each PtdIns[3,4,5]P$_3$ and DGS. The model membranes were prepared via SUV spreading at t = 0 min and subsequently rinsed with HEPES-A buffer (I). Protein injection with a concentration of 1 µM for both isoforms is indicated by II.

The incubation of the hydrophobically functionalised silicon dioxide substrates with suspensions of small unilamellar vesicles (SUV, t = 0 min) in Na-citrate buffer (cf. Table 3.16) at a pH of 4.8 caused a change in optical thickness (ΔOT) of around 2.5 to 3 nm in both measurements. This was correlated to solid-supported hybrid membrane formation in agreement with the previously determine layer thicknesses of various SHMs (cf. Chapters 4.1.3 and 4.4.1). Adsorbed, yet non-spread lipid material was removed from the SHMs by rinsing with HEPES-A buffer (highlighted by timepoint I, cf. Table 3.14) which affected ΔOT only to a minor extent. While the subsequent injection of CB2$_{SH3/W24A-E262A}$ (1 µM, represented by timepoint II) led to an increase in ΔOT, no such tendency was detected for collybistin wild-type (cf. Figure 4.44 A). This again illustrates the behavioural differences between CB2$_{SH3}$ exhibiting a closed, inactive conformation, and the point-mutated isoform that is open and capable of phosphoinositide interaction. In analogy to the presented adsorption experiments to PtdIns[3,4,5]P$_3$/DGS doped SHMs also measurements on other lipid compositions were conducted. The averaged ΔOTs relative to the established membrane level (as illustrated in Figure 4.44 B) are shown as a function of the corresponding receptor lipids in Figure 4.45.

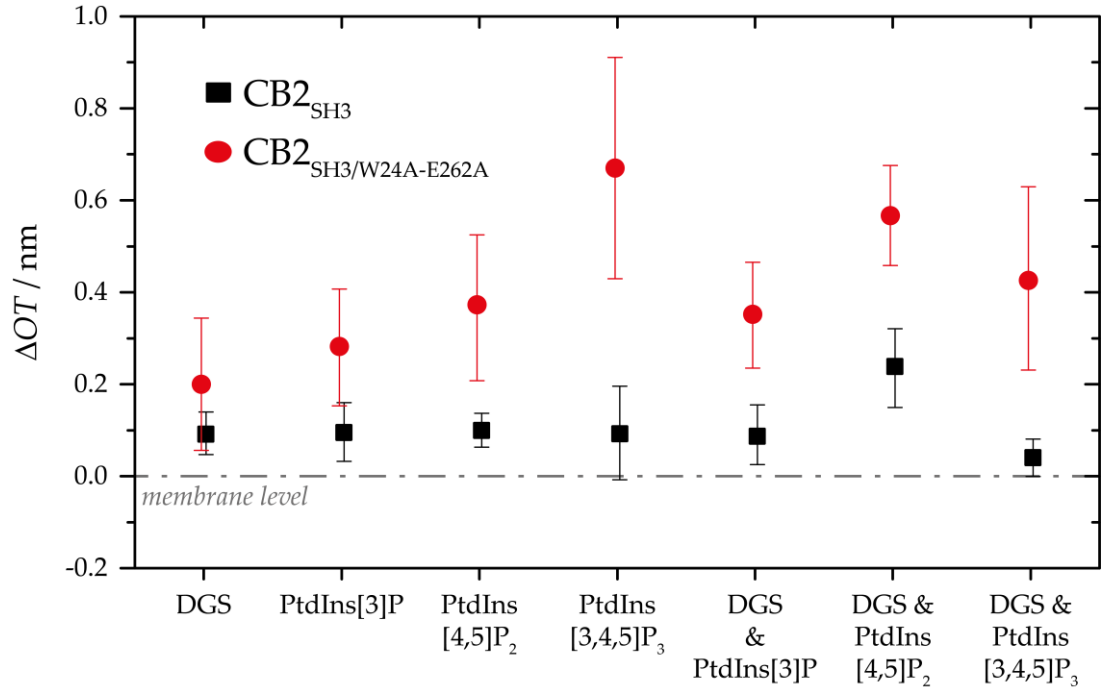

Figure 4.45: Change in ΔOT relative to the established membrane level (broken line) induced by adsorption of either CB2$_{SH3}$ (black) or CB2$_{SH3/W24A-E262A}$ (red) each at a concentration of 1 µM to SHMs containing the respective receptor lipids or combinations thereof.

Likewise, in case of the other phosphoinositides and their combinations with DGS the injection of CB2$_{SH3}$ resulted in only small changes of ΔOT which were considered as indication of no protein adsorption. This is feasible because already slight fluctuations in the refractive index n as induced by e.g. change in buffer solution or addition of protein within the detection area might alter ΔOT. Furthermore, it is evident, that all spectra present a background noise in the range of around 0.1 nm (cf. for example Figure 4.10, Figure 4.26 and Figure 4.44) which impedes the identification of a change in signal intensity with a similar amplitude as induced by protein adsorption. Opposing behaviour was detected for CB2$_{SH3/W24A-E262A}$ which induced increases in ΔOT when injected. This can be correlated to specific interactions with the phosphoinositides as no sufficient change in signal intensity was detected on SHMs doped with DGS alone. The detected trends for the adsorption of the active mutant to the different PtdInsPs is consistent to the previously determined protein specific parameters ΔOT_{max} and K_D (cf. Chapter 4.3.3), identifying the highest affinity for PtdIns[3,4,5]P$_3$. This, however, was unaffected by the presence of DGS. Therefore, the addition of DGS as a second receptor lipid to the existing model membrane system seems to be unproblematic. It represents the first step to the introduction of a further constituent, the cell adhesion molecule neuroligin 2, of the GABA$_A$R organisation machinery to the *in vitro* model complex of the later.

4.4.2 Introducing His-*cyt*NL2 to the model system

The cell adhesion molecule (CAM) neuroligin 2 (NL2) is responsible for the direct apposition of the post synaptic specialisations to the presynaptic release sites. This is accomplished by its interaction with neurexins inside the axon of the signal transmitting neuronal cell. Via this interaction the synaptic cleft is bridged by the extracellular domains of both CAM species. Additional to this part, NL2 consists of a single transmembrane region and an intrinsically disordered cytoplasmic tail. Its trans-membraneous character is, however, problematic for the application due to a challenging reconstitution process and the necessity of aqueous compartments on both sides of the model membrane missing in the system used in this work. Therefore, a protein construct was employed to mimic the intracellular domain of NL2. It was composed of all cytoplasmic amino acid residues of NL2 to which a hexa-histidine (His_6) tag was *N*-terminally fused, hence, it is referred to as His-*cyt*NL2 in this work.

4.4.2.1 Isolation of His-*cyt*NL2

The expression and isolation of the protein construct mimicking the cytoplasmic part of the transmembrane protein neuroligin 2 (His-*cyt*NL2) was conducted several times in the progress of this work. The protocol followed during this process was inspired by the isolations of N-ERMAD and collybistin 2 as described before (cf. Chapter 3.2.5). Additionally, previous work of DR. BODO SANDER was referred to for orientation.[271] The protein expression was performed in *E. coli* cells of the BL21(DE3) Rosetta strain. Afterwards target protein purification was achieved via immobilised metal ion affinity chromatography (IMAC, cf. Chapter 3.2.7.1) taking advantage of the *N*-terminally fused His_6-tag. Its success was controlled by SDS-PAGE in combination with Western blot. Examples for both, PAGE and blot, are shown in Figure 4.46.

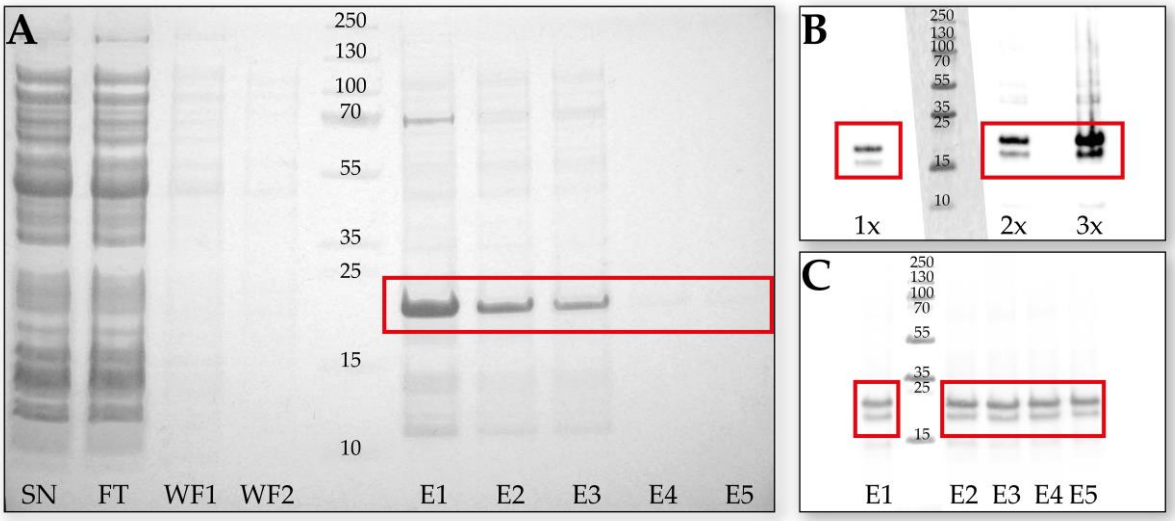

Figure 4.46: SDS-PAGE of His-*cyt*NL2 after purification via affinity chromatography against NTA(Ni^{2+}) agarose. The collected fractions of supernatant (SN), flow through (FT), washing (WF) and elution (E) were investigated to determine the distribution of the target protein (**A**). Western blot overlay with a concentration gradient (simple to tripled protein amount) of E1 using a specific primary antibody for the intracellular domain of NL2 (**B**). Western blot overlay of the early elution fractions (E1-E5) tested for His-*cyt*NL2 with a specific primary antibody against the *N*-terminally fussed His_6-tag (**C**).

The theoretical mass of His-*cyt*NL2 was calculated to M_{theo} = 17.31 kDa. Its calculation was based on the amino acid sequence (cf. Appendix A.4.5) determined via plasmid sequencing (cf. Chapter 3.2.4). The obtained sequence was in accordance to previous results.[271] While the trace for the supernatant (SN) and the flow through (FT) did not show a difference in the gel of the SDS-PAGE (cf. Figure 4.46 A), a drastic reduction of bands was evident in the fraction of the first washing step (WF1). The intensity decline was even more enhanced in the second washing step (WF2). The indifference between SN and FT indicated that most proteins expressed, did not interact with the solid phase of the column und thus were flushed through it. The small number of signals with only light intensities within the washing fractions confirms this and shows that nearly no proteins were hold back via unspecific interactions with the NTA(Ni^{2+}) agarose. However, all elution fractions (E1 to E5) present a dominant band located between the 15 and 25 kDa ones of the applied mass reference. The mass of this specific band was estimated to around 20 kDa and thus considered to correlate with the target protein. The shift to higher masses can be explained by the poly-proline section in the amino acid sequence, providing a rigidity that results in an increased retention within the polyacrylamide gel. Even though, the target protein was eluted successfully the isolation cannot be considered as a success. The reason for this is the co-elution of other unknown proteins that correspond to bands

detected over the whole separation range of the PAGE. To elucidate the character of the contaminations additional Western blots (WBs) of the elution fractions have been performed. While one was conducted using a primary antibody that was specific for the intracellular domain of neuroligin (cf. Figure 4.46 B), the second WB identified His_6-tag harbouring proteins via a primary antibody being specific for poly-histidine motifs in amino acid sequences (cf. Figure 4.46 C). In both cases and for all fractions tested a double band was detected in the molecular range of His-*cyt*NL2. This might either indicate an incompletely expressed protein fragment that contains a His_6-tag and is sufficient as epitope to the NL-specific antibody. Another more probable explanation for this band duplication is a defective reduction process prior to PAGE analysis. A fraction of all proteins may have been re-oxidised during or might not have been reduced at all in the denaturation process due to a deficiency in DTT.[272] This effect would result in doubling of all detected protein bands which was the case in both WBs presented in Figure 4.46 B and C. Therefore, the double bands were ignored and both overlays of the WBs showed intensive bands that were correlated to the target protein. Based on these results, the contained impurities were neglected, as only His-*cyt*NL2 exhibited the poly-histidine tag required for its adsorption to the DGS-doped solid-supported hybrid membrane system.

4.4.2.2 Adsorption experiments to DGS and PtdInsP containing SHMs

After the elution of the protein construct and its transfer into HEPES-A buffer via dialysis (cf. Chapter 3.2.10.1), its adsorption behaviour was analysed by means of RIfS to elucidate its interaction with the different receptor lipids inside the SHM (cf. Chapter 4.4.1). In addition to the receptor lipids PtdInsP and DGS, adsorption on POPC : POPS (94 : 6, *n*/*n*) SHMs was also analysed to identify potential non-specific, electrostatic interaction of His-*cyt*NL2. Exemplary time courses of the adsorption process to the hybrid membranes containing various receptor lipids are shown in Figure 4.47.

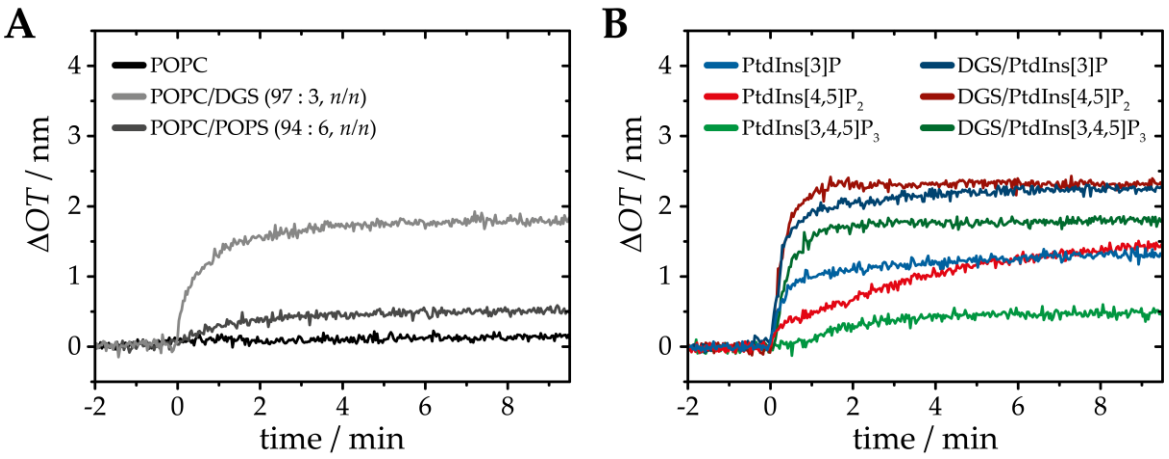

Figure 4.47: Exemplary plots of the change in optical thickness vs. the time during adsorption experiments of His-*cyt*NL2 (c = 1.36 µM, t = 0 min) on either pure POPC SHMs or on those doped with DGS and POPS (**A**), and POPC SHMs containing 3 mol% PtdInsP or DGS-PtdInsP (each 3 mol%) in combination (**B**).

As expected, the injection of His-*cyt*NL2 to POPC : DGS (97 : 3, *n*/*n*, cf. Figure 4.47 A, light grey spectrum) SHMs led to a significant change in signal intensity (Δ*OT*) as the protein is adsorbed to the membrane via the interaction of its *N*-terminal His_6-tag with DGS. Additionally, no unspecific interaction was detected with the matrix lipid POPC (represented by the black spectrum in Figure 4.47 A). However, also adsorption of the protein construct to membranes containing 6 mol% POPS was detected as vividly illustrated in Figure 4.47 A by the grey spectrum. A similar trend was monitored for SHMs doped with 3 mol% of phosphoinositide (cf. Figure 4.47 B). The change in Δ*OT* on PtdIns[3]P, PtdIns[4,5]P_2 and PtdIns[3,4,5]P_3 doped SHMs (represented by the blue, red and green curve, respectively) also indicated adsorption of His-*cyt*NL2. However, the changes in optical thickness did not correlated with the net charges of the membrane systems as a higher number of protein (expressed by a larger signal intensity change) was adsorbed to PtdIns[3]P and PtdIns[4,5]P_2 containing membranes than to ones doped with the trisphosphorylated PtdInsP. Even though the latter exhibits the highest net charge with each PtdIns[3,4,5]P_3 molecule being highly negatively charged (-7) at pH 8.[235] This suggests that the adsorption to phosphoinositides is not only based on electrostatic interactions. Nonetheless, also in presence of those receptor lipids the interaction of His-*cyt*NL2 with DGS still results in raises of the signal intensity. In such SHMs the tendency against the phosphoinositides mentioned before is evident, although at higher intensity levels due to the strong interactions with DGS.

Consequently, expansion of the established model membrane system in combination with His-*cyt*NL2 in the presented form is not feasible, as a specific interaction of the protein con-

struct with DGS only is needed to guarantee vacant phosphoinositides which function as pinning-points for collybistin 2. Therefore, a subsequent purification step was applied to increase the purity of the His-*cyt*NL2 protein solution.

4.4.2.3 Subsequent purification of His-*cyt*NL2

The protein construct mimicking the intracellular domain of neuroligin 2 (His-*cyt*NL2) was eluted together with various contaminations after IMAC (cf. Figure 4.46 A). The addition of this protein mixture to hybrid membranes containing phosphoinositide and DGS led to adsorbed proteins that were caused by unspecific interaction as shown in the prior sections. Thus, it was necessary to elucidate whether this behaviour was caused by His-*cyt*NL2 itself or might be a result from deposited contaminations. To do so, the protein mixture obtained from the IMAC elution fractions was applied to an anion exchange chromatography (IEC) column to separate the target protein from all contaminations. As this purification technique is based on electrostatic interactions, a NaCl-gradient was applied during the process in which the ion concentration in the buffer solution was stepwise, ranging from 0 to 2 M.[271] Simultaneously fractions were collected and then analysed by SDS-PAGE. The corresponding gel is shown in Figure 4.48 A.

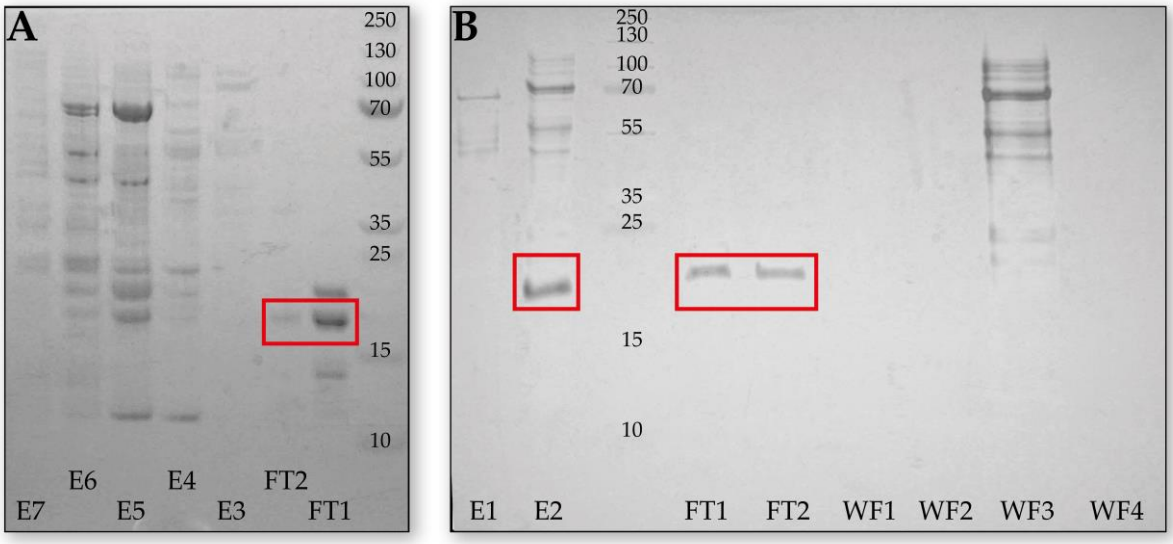

Figure 4.48: A: Examplary gel of a SDS-PAGE after anion exchange chromatography of His-*cyt*NL2 at a Mono Q 5/50 in an ÄKTA purification system. Together with the mass standard the flow through (FT) gathered during protein application to the column, and the elution fractions (E) collected during rinsing with a gradient of increasing NaCl concentration up to 2 M were applied. **B**: SDS-PAGE after repetition of the purification step yet without a gradual NaCl concentration increase. Elution fractions of the IMAC (E) as references were loaded to the gel together with the collected fractions of flow through (FT) and washing fractions (WF) of the Mono Q 5/50.

In the elution fractions (E3-E7) a great variety of bands was visible among which the band corresponding to His-*cyt*NL2 was detected in slight amounts, too. In contrast to that, the flow through (FT) fractions contained only minor quantity of bands. In these fractions the band corresponding to His-*cyt*NL2 with M_{theo} = 17.31 kDa was dominant. Therefore, a second run of the anion exchange chromatography was performed without the elution process and consequently the NaCl-gradient. The corresponding gel of the SDS-PAGE is presented in Figure 4.48 B. Additional, to the FT fractions also elution fractions from IMAC (E1 and E2, cf. Figure 4.46 A) as references and washing fractions (WF1-4) of the Mono Q column cleaning were applied. While the elution fraction contained the previously described band pattern (cf. Chapter 4.4.2.1), in the FT fractions only a single band of a molecular weight around 20 kDa was detected. On the other hand, all higher molecular bands were present in one of the washing fractions (WF3). Based on the presented gel it becomes clear, that the ion exchange column functioned as a filter, hindering the flow through of contaminations while the His-*cyt*NL2 was eluted without retention. Hence, the resulting protein solution contained the pure neuroligin 2 construct (cf. Figure 4.48 B, FT1 and FT2).

Furthermore, the specificity of the *N*-terminally fused His_6-tag had to be tested. To do that, the obtained pure His-*cyt*NL2 (after IEC) was treated with tobacco etch virus (TEV) to cleave the affinity tag and end up with the intracellular domain of neuroligin 2 (*cyt*NL2) alone. The separation of cleaved protein construct and His_6-tag harbouring one was again conducted using IMAC. The results are illustrated in Figure 4.49.

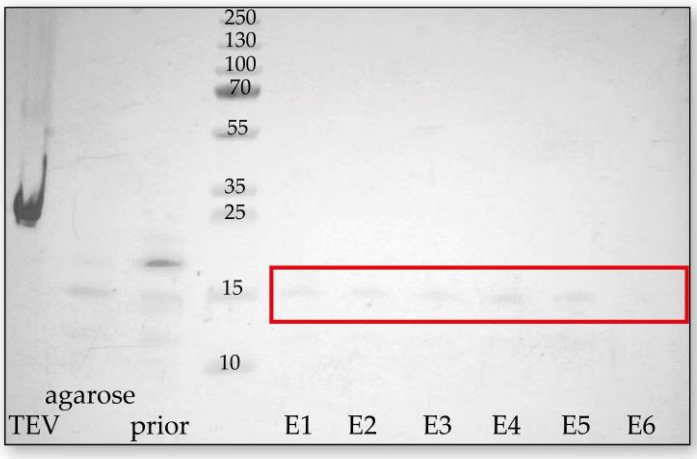

Figure 4.49: SDS-PAGE of His-*cyt*NL2 after the cleavage reaction with TEV to remove the *N*-terminal His_6-tag. As references the etching virus (TEV), the immobile phase of the IMAC (agarose) and the untreated elution fraction (prior) were of loaded to the gel together with various elution fraction (E1-E6).

In contrast to the His-*cyt*NL2 solution after anion exchange chromatography (represented by the trace labelled with *prior*), the trace of the immobile phase (agarose) and the elution fractions showed dominant bands with a molecular weight of around 15 kDa. These are assigned to bare *cyt*NL2 as the fragment cleavable by TEV has a theoretical

weight of M_{theo} = 2.76 kDa. The cleavage of the *N*-terminal His_6-tag was successful and the cleaved intracellular domain of neuroligin 2 was effectively isolated.

With these pure protein fragments (His-*cyt*NL2 and *cyt*NL2) at hand, once again adsorption experiments by means of RIfS have been performed. The adsorption behaviour of all three neuroligin 2 constructs (His-*cyt*NL2 after IMAC, His-*cyt*NL2 after IEC and *cyt*NL2) are summarised in Figure 4.50. While the bare intracellular domain of neuroligin 2 (*cyt*NL2) has not been adsorbed to any of the receptor lipids, the His_6-tag containing pure His-*cyt*NL2 (after IEC) showed only a specific interaction with DGS. Thus, an interaction of the tag with the phosphoinositides can be neglected indicating that the detected changes in optical thickness (cf. Figure 4.47) were results of impurity deposition on top of the SHMs. Hence, a selective protein adsorption of NL2 and CB2 can only be guaranteed when using His-*cyt*NL2 (after IEC) in the expanded model system.

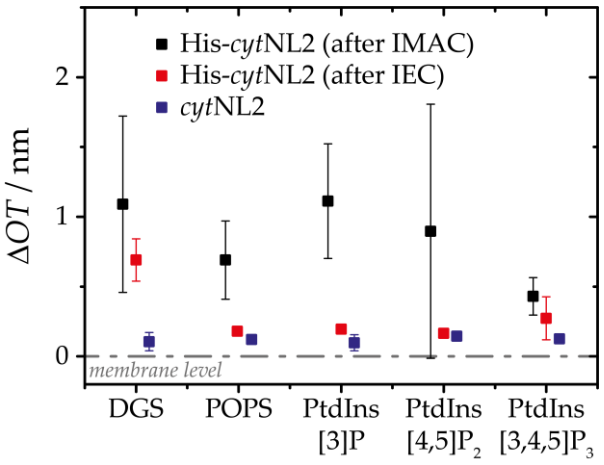

Figure 4.50: Change in optical thickness induced by the adsorption of the different neuroligin 2 constructs (impure His-*cyt*NL2: black; pure His-*cyt*NL2: red; *cyt*NL2: blue) each at a concentration of 1.36 µM to SHMs doped with different receptor lipids.

4.4.3 Activation of CB2 by its physiological interaction partner NL2

Having proven selective binding of His-*cyt*NL2 to DGS (cf. Chapter 4.4.2.3), the focus was switched to its interaction with the full-length isoforms of collybistin 2. On this purpose, the adsorption of both, the CB2 wild-type ($CB2_{SH3}$) and its active mutant ($CB2_{SH3/W24A-E262A}$), was investigated by means of reflectometric interference spectroscopy (RIfS) to hybrid membrane systems containing DGS and one of the phosphoinositides (PtdIns[3]P, PtdIns[4,5]P_2 or PtdIns[3,4,5]P_3). Prior to collybistin adsorption, His-*cyt*NL2 was added to the system and fixed to the membrane via its *N*-terminal His_6-tag. For both isoforms exemplary time courses of adsorption experiments are portrayed in Figure 4.51.

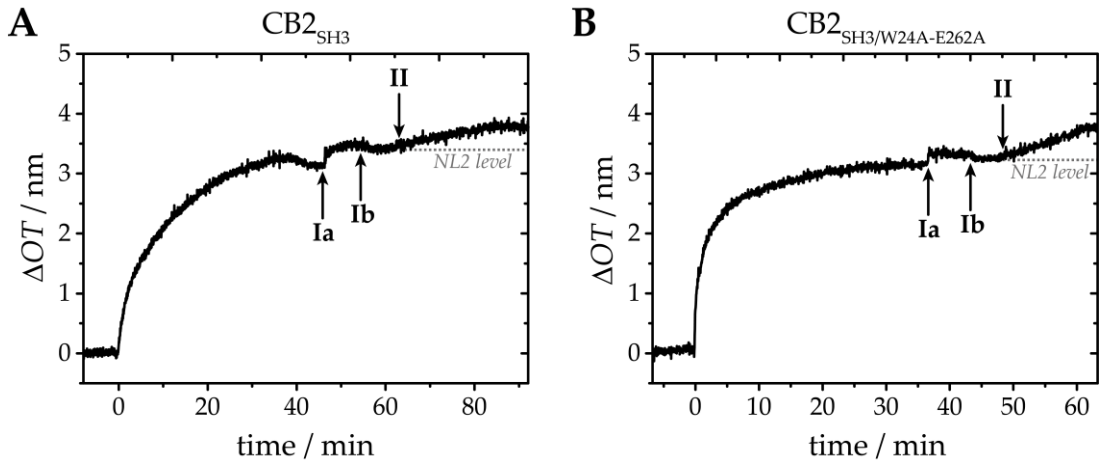

Figure 4.51: Exemplary plots of the change in optical thickness vs. the time during adsorption of either CB2$_{SH3}$ (**A**) or CB2$_{SH3/W24A-E262A}$ (**B**) on POPC hybrid membranes doped with PtdIns[3,4,5]P$_3$ and DGS (94 : 3 : 3, *n*/*n*/*n*). The model membranes were prepared via SUV spreading at t = 0 min and subsequently rinsed with buffer. Then His-*cyt*NL2 (c = 1.36 μM) was injected at timepoint Ia and unbound protein construct was removed by rinsing with HEPES-A buffer (Ib). CB2 injection with a concentration of 1 μM for both isoforms is indicated by timepoint II. The change in optical thickness caused by CB2 adsorption was determined relative to the established NL2 level (dotted line).

After the formation of the lipid hybrid membrane (beginning at t = 0 min) on top of the hydrophobically functionalised silicon dioxide substrates, excess lipid material was removed by rinsing with HEPES-A buffer (cf. Table 3.14). This also adjusted the conditions (pH) to an optimum for the protein adsorption process. Afterwards His-*cyt*NL2 (c = 1.36 μM) was injected (timepoint Ia). When a new level in Δ*OT* was reached (timepoint Ib) the system was rinsed with HEPES-A buffer for a second time. The resulting level was referred to as *NL2 level*. It functioned as reference for subsequent determinations of signal intensity changes. These changes were caused by the adsorption of CB2 (in form of CB2$_{SH3}$ and CB2$_{SH3/W24A-E262A}$) that was added to the system in concentrations of 1 μM (at timepoint II). The injection of CB2 wild-type led to a significant increase in signal intensity of Δ*OT* = 0.3 nm on the SHM after His-*cyt*NL2 adsorption (cf. Figure 4.51 A). This is a striking observation when compared to the determined incapability of CB2$_{SH3}$ to interact with DGS/PtdIns[3,4,5]P$_3$ containing SHMs (cf. Figure 4.44 A). On the other hand, the adsorption of CB2$_{SH3/W24A-E262A}$ as illustrated in Figure 4.51 B, was not or only to a small extend affected by the presence of His-*cyt*NL2 if compared to Figure 4.44 B.

In analogy to these experiments also the adsorption of both CB2 isoforms to the remaining two phosphoinositides in combination with DGS was examined. For each lipid composition at least four independent experiments were performed. The mean changes in Δ*OT* (relative to the *NL2-level*) are summarised in Figure 4.52 and compared to those induced by CB2 adsorption in absence of His-*cyt*NL2 (relative to the *membrane-level*).

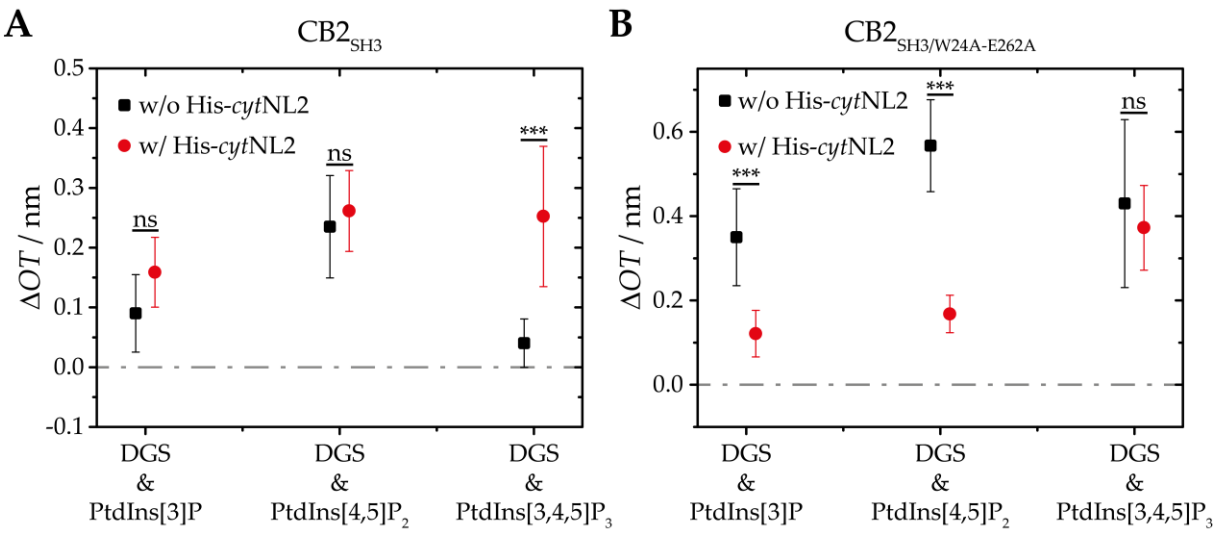

Figure 4.52: Overview on the induced changes in Δ*OT* by adsorption of CB2$_{SH3}$ (**A**) and CB2$_{SH3/W24A-E262A}$ (**B**) to POPC SHMs containing DGS and one of the phosphoinositides (94 : 3 : 3, *n*/*n*/*n*). While the data in absence of His-*cyt*NL2 (black, n(CB2$_{SH3}$) ≥ 3 and n(CB2$_{SH3/W24A-E262A}$) ≥ 7) was determined relative to the *membrane-level*, the changes in Δ*OT* after adsorption of 1.36 µM His-*cyt*NL2 (red, n(CB2$_{SH3}$) ≥ 7 and n(CB2$_{SH3/W24A-E262A}$) ≥ 5) were calculated relative to the *NL2-level*. The injected CB2 concentration for both isoforms was 1 µM.

The comparison of Δ*OT* caused by adsorption of CB2$_{SH3}$ to SHMs doped with both DGS and phosphoinositides with or without the intracellular domain of NL2 as presented in Figure 4.52 A hints at an interesting behaviour. While in case of PtdIns[3]P and PtdIns[4,5]P$_2$ containing SHMs no significant effect of His-*cyt*NL2 was detected, its presence affected the interaction of the wild-type with the tris-phosphorylated PtdInsP in a drastic fashion. After NL2 deposition a significant quantity of protein was adsorbed to PtdIns[3,4,5]P$_3$ doped model membranes. This indicates an opening of the autoinhibited conformation of CB2$_{SH3}$. The opening must be induced by the interaction with NL2 that renders the adapter protein capable of PtdIns[3,4,5]P$_3$ binding. Thus, this result supports the previously postulated activation of CB2 via intermolecular interactions with NL2.[60]

The preceding NL2 adsorption influences CB2$_{SH3/W24A-E262A}$ in a different way. While on DGS/PtdIns[3,4,5]P$_3$ doped membranes no significant difference was monitored, His-*cyt*NL2 altered the adsorption behaviour of CB2$_{SH3/W24A-E262A}$ to SHMs containing PtdIns[3]P and PtdIns[4,5]P$_2$. In both cases the quantity of adsorbed protein was declined when the active

mutant induced rather large Δ*OT* changes in the absence of the NL2 construct (cf. Figure 4.52 B). This hints at an inhibiting effect of His-*cyt*NL2, as PtdInsPs in direct vicinity to DGS-lipids might be blocked by the protein construct. In such a case, the phosphoinositides would be occupied without a specific interaction. Nonetheless, the amount of accessible, vacant phosphoinositides as pinning-points for collybistin 2 would be reduced. Thus, such an effect would also be present in the adsorption process of $CB2_{SH3}$ in case of a similar unspecific interaction behaviour. Either way, because of its intrinsically disordered character,[51] a size determination of the cytoplasmic part of NL2 is not possible due to the lack of a crystal structure. Consequently, an evaluation of the ratio of potentially blocked PtdInsP is unconvertible.

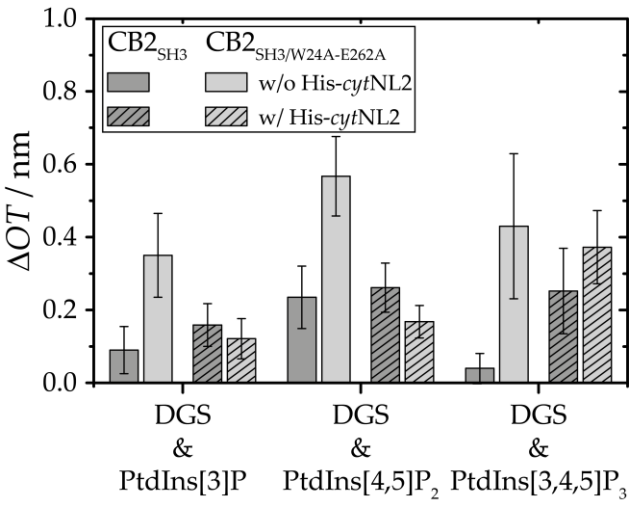

Figure 4.53: A: Comparison of the Δ*OT* values caused by adsorption of $CB2_{SH3}$ (dark grey) and $CB2_{SH3/W24A-E262A}$ (light grey) to SHMs in absence of His-*cyt*NL2 (solid bars) or its presence (dashed bars). The error bars indicate the standard error of the mean.

To simplify the comparison of $CB2_{SH3}$ and $CB2_{SH3/W24A-E262A}$ Figure 4.53 presents the RIfS data on CB2 adsorption depending on the presence of NL2 in another way. The addition of $CB2_{SH3}$ after adsorption His-*cyt*NL2 often resulted in similar Δ*OT* values as those recorded for $CB2_{SH3/W24A-E262A}$ with and without prior NL2 adsorption (cf. Figure 4.53). This indicates a related amount of adsorbed protein for both isoforms. It might also suggest a similar arrangement of the activated wild-type on the membrane surface (cf. Chapter 4.3.4). Though, this hypothesis cannot be proven by the RIfS results alone and requires further investigations. The combination of atomic force microscopy (AFM) with fluorescence labelling would be a promising way of examination as a differentiation of the adsorbed structures between His-*cyt*NL2 and $CB2_{SH3}$ would be impossible by simple AFM-studies.

Yet, it remains elusive whether the activated CB2 wild-type can also interact with the other phosphoinositides. Based only on the comparison of its adsorption influenced by NL2 (cf. Figure 4.52 A) $CB2_{SH3}$ could by classified as specific to $PtdIns[3,4,5]P_3$. Both CB2 isoforms exhibit identical adsorption behaviour on SHMs (cf. Figure 4.53), therefore, it is feasible to use $CB2_{SH3/W24A-E262A}$ as a benchmark. The Δ*OT*s induced by $CB2_{SH3}$ adsorption can be related to

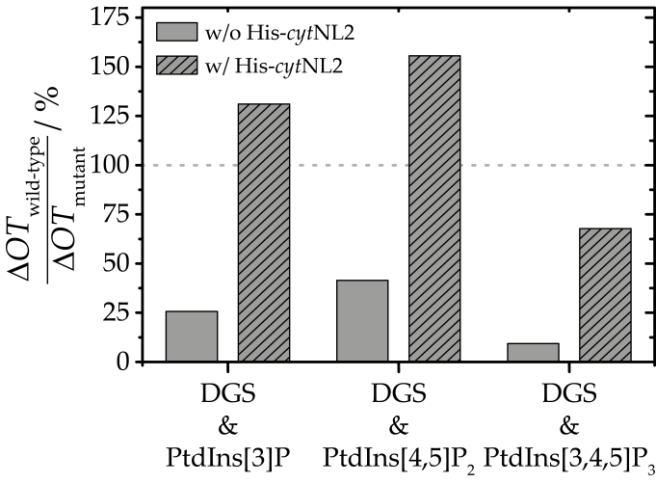

Figure 4.54: Change in optical thickness induced by CB2$_{SH3}$ adsorption to SHMs correlated to Δ*OT* caused by CB2$_{SH3/W24A-E262A}$ under similar conditions.

those determined for CB2$_{SH3/W24A-E262A}$ to exclude any impact of the reference layer (*membrane-* or *NL2-level*). The relative Δ*OT* of CB2$_{SH3}$ ($\Delta OT_{\text{wild-type}}$) correlated to $\Delta OT_{\text{mutant}}$ was calculated as shown in Figure 4.54.

In this form of presentation an increase in signal intensity on all receptor lipid combinations caused by the preceding His-*cyt*NL2 adsorption is evident. Thus, the activated CB2$_{SH3}$ can interact with all phosphoinositides. However, a qualified estimation of its PtdInsP-binding specificity cannot be made. This would have been an interesting piece of information as former studies presented different behaviour between the wild-type and point-mutated forms of collybistin. REDDY-ALLA *et al.* showed by variation of the amino acid residues 232 and 233 of CB2 that inhibition of the guanine nucleotide exchange factor (GEF) activity towards the small rat sarcoma homologue (Rho) GTPases Cdc42 occurred, while the phosphoinositide interaction was not affected.[93] On the other hand changes of amino acid residues in the PH domain abolished gephyrin recruitment to synaptic sites indicating their requirement for PtdInsP binding. This is supported by the finding that alterations in the DH domain (R290H and R338W)[252,253] of CB2 indirectly affect the interaction of its PH domain with the receptor lipids in the post synaptic membrane.

Another aspect that needs consideration is the fact that neuroligins *in vivo* tend to form homodimers.[58] In 2012, POULOPOULOS *et al*. focussed on the dimerisation of all neuroligin isoforms and were able to identify a transmembrane asparagine residue to be crucial for the dimer formation and thus the accumulation of neuroligin at synaptic site.[57] However, as the model setup established in course of this work only contains the *C*-terminal cytoplasmic domain of NL2 dimerisation is not possible. Nonetheless, the results gathered for CB2$_{SH3}$ after His-*cyt*NL2 adsorption (cf. Figure 4.54) suggest an activation by the NL2 construct proving the dispensability of NL2 dimerisation for this process. For this reason, it can be assumed that the

dimerisation is more relevant for the intercellular communication process with the presynaptic neurexins.

In order to test whether the activation of CB2 is based on its interaction with the poly-proline sequences inside the intracellular domain of NL2, it would be an interesting experiment to substitute His-*cyt*NL2 by a peptide that harbours at least one poly-proline sequence. The peptide could also be equipped with an accessible cysteine to allow coupling reactions to maleimide containing artificial lipids. This would provide the opportunity to renounce the use of DGS and thus the reduction of potential lateral lipid-lipid interactions.

In conclusion, the investigations performed during this work represent the establishing process of an *in vitro* model for the fundamental protein machinery responsible for $GABA_AR$ organisation in the inhibitory postsynaptic membrane. The results showed the advantages of a solid-supported hybrid membrane (SHM) system prepared on hydrophobically functionalised silicon dioxide substrates. Furthermore, it was proven that a combination of the receptor lipids DGS and various phosphoinositides inside such a model membrane is possible without detectable adverse effects except for a slight reductions of diffusion coefficients. Moreover, it was possible to selectively bind two constituents of the organisation machinery to the SHM. For this purpose, a protein construct (His-*cyt*NL2) mimicking the intracellular part of NL2 was isolated and specifically adsorbed to DGS. After its preceding adsorption it was possible to monitor an interaction of the usually inactive collybistin 2 wild-type with phosphoinositides. Thereby, proof of the activating interaction between NL2 and CB2 was generated in the absence of other proteins. While the active mutant ($CB2_{SH3/W24A-E262A}$) and the isolated PH domain ($CB2_{PH}$) were characterised as non-specific interaction partners for the three phosphoinositides, no qualified statement on the binding specificity of $CB2_{SH3}$ was possible.

Based on the accomplishments of this work it is the logical consequence to introduce a third protein, the scaffolding protein gephyrin, to the model system. Thereby the presumed protein machinery underlying $GABA_AR$ organisation would be complete. Already at its current state the model system is suitable for drug testing to examine the influence of chemical agents either on the adsorption of CB2 to the membrane or on the protein-protein interaction between NL2 and CB2. Furthermore, the *in vitro* system can be used to test the consequences of mutations within the respective proteins and thereby identify potential origins of diseases which hitherto had to be done in neuronal tissue or animal tests.

5 Conclusion

The communication at chemical synapses is based on the release and uptake of neurotransmitters. In the mammalian brain, inhibitory signal transduction relies on the neurotransmitter γ-amino butyric acid (GABA) which is recognised by specific receptors ($GABA_ARs$) in the post synaptic plasma membrane. Their accumulation in direct opposition to presynaptic active sites is required to facilitate fast communication. The cell adhesion protein neuroligin 2 (NL2), the scaffolding protein gephyrin and the adaptor protein collybistin 2 (CB2) are assumed to be part of this organisation process. CB2 interacts with phosphoinositides (PtdInsPs) in the plasma membrane and functions as an anchor for the protein complex. In this thesis an *in vitro* model system of the $GABA_A$ergic postsynaptic receptor organisation machinery was developed. The model system was based on solid-supported hybrid membranes (SHMs) that were prepared via spreading of small unilamellar vesicles (SUVs) on top of hydrophobically functionalised substrates. The surface features were modified by treating SiO_2 wafers with 1,1,1-trimethyl-N-(trimethylsilyl) silanamine (HMDS). Among other strategies, the functionalisation under reduced pressure and increased temperature was identified as most effective to obtain smooth hydrophobic surfaces with a root mean square (RMS) of (0.40 ± 1) nm and a mean contact angle of $(87 \pm 1)°$. Besides these substrates hydrophilic functionalised ones were used to prepare solid-supported lipid bilayer (SLBs). This allowed the comparison of the phosphatidylinositol-4,5-bisphosphate (PtdIns[4,5]P_2) distribution in both membrane systems influenced by the solid support. Via adsorption experiments of marker proteins by means of reflectometric interference spectroscopy (RIfS) and atomic force microscopy (AFM) a reduced accessibility of PtdIns[4,5]P_2 with an asymmetry factor of at least two was identified in SLBs. The enrichment of the receptor lipid in the substrate facing leaflet is believed to be caused by electrostatic interactions with the SiO_2 surface in combination with a pre-organisation of PtdIns[4,5]P_2 in the SUVs.

This heterogeneity was identified to be unique for PtdIns[4,5]P_2, therefore, the adsorption studies of CB2 to membranes containing one of three phosphoinositide variants (PtdIns[3]P, PtdIns[4,5]P_2 and PtdIns[3,4,5]P_3) were performed on SHMs. The adsorption of three different CB2 isoforms was examined. The isolated PH domain ($CB2_{PH}$) and the conformationally active point-mutated isoform ($CB2_{SH3/W24A-E262A}$) were characterised as unspecific interaction partners

with moderate affinities in the range of 0.7-5.6 μM for all three PtdInsPs. No adsorption of the CB2 wild type ($CB2_{SH3}$) was monitored, supporting the general assumption of a closed, inactive conformation. AFM imaging of the adsorbed protein structures ($CB2_{PH}$ and $CB2_{SH3/W24A-E262A}$) identified the *C*-terminal PH domain as height dictating part of CB2 with around 3.4 nm. Additional to the protein height, the size of the defined protein structures was characterised to be independent of the deployed phosphoinositide.

Subsequently, NL2 was added to the model system as a further constituent of the protein machinery. 1,2-dioleoyl-*sn*-glycero-3-{[*N*-(5-amino-1-carboxypentyl)iminodiacetic acid]succinyl} nickel salt (DGS) functioned as specific receptor lipid for a protein construct mimicking its intracellular domain (His-*cyt*NL2). The addition of DGS to PtdInsP containing membranes did not affect their formation processes nor the resulting layer thickness (ΔOT_{SHM} = 2.7 nm) but caused a reduction in diffusion coefficients by 50 % for labelled PtdInsPs. However, no influence of DGS was detected on the CB2—PtdInsP interaction. The purified His-*cyt*NL2 did not interact with phosphoinositides and thus was adsorbed to DGS/PtdInsP containing SHMs prior to injection of either $CB2_{SH3}$ or $CB2_{SH3/W24A-E262A}$. While the latter was unaffected by the presence of NL2, a drastically increased adsorption of $CB2_{SH3}$ was monitored after preceding His-*cyt*NL2 addition.

In conclusion, it was shown that the use of SHMs is beneficial to avoid undesired substrate influences. Deploying this system, the CB2—PtdInsP interaction was characterised in detail and $CB2_{PH}$ was identified as the height dictating protein part. Furthermore, the established model system provided convincing evidence for the activation of CB2 by its interaction with NL2.

6 Bibliography

(1) García-López, P.; García-Marín, V.; Freire, M. The Discovery of Dendritic Spines by Cajal in 1888 and Its Relevance in the Present Neuroscience. *Prog. Neurobiol.* **2007**, *83* (2), 110–130.

(2) Jones, E. G. Golgi, Cajal and the Neuron Doctrine. *J. Hist. Neurosci.* **1999**, *8* (2), 170–178.

(3) *Neuroscience*, 6th ed.; Purves, D., Augustine, G. J., Fitzpatrick, D., Hall, W. C., LaMantia, A.-S., Mooney, R. D., Platt, M. L., White, L. E., Eds.; Oxford University Press: New York, **2018**.

(4) Williams, R. W.; Herrup, K. The Control of Neuron Number. *Annu. Rev. Neurosci.* **1988**, *11* (1), 423–453.

(5) *The Synapse: A Subject Collection*, 1st ed.; Sheng, M., Sabatini, B., Südhof, T. C., Eds.; Cold Spring Harbor perspectives in biology; Cold Spring Harbor Laboratory Press: Cold Spring Harbor, N.Y, **2012**.

(6) Gaiarsa, J.-L.; Caillard, O.; Ben-Ari, Y. Long-Term Plasticity at GABAergic and Glycinergic Synapses: Mechanisms and Functional Significance. *Trends Neurosci.* **2002**, *25* (11), 564–570.

(7) Castillo, P. E. Presynaptic LTP and LTD of Excitatory and Inhibitory Synapses. *Cold Spring Harb. Perspect. Biol.* **2012**, *4* (2), a005728–a005728.

(8) Lüscher, C.; Malenka, R. C. NMDA Receptor-Dependent Long-Term Potentiation and Long-Term Depression (LTP/LTD). *Cold Spring Harb. Perspect. Biol.* **2012**, *4* (6), a005710–a005710.

(9) *Molecular Biology of the Cell*, 5th ed.; Alberts, B., Johnson, A., Lewis, J., Raff, M., Roberts, K., Walter, P., Eds.; Garland Science: New York, **2008**.

(10) Markram, H.; Toledo-Rodriguez, M.; Wang, Y.; Gupta, A.; Silberberg, G.; Wu, C. Interneurons of the Neocortical Inhibitory System. *Nat. Rev. Neurosci.* **2004**, *5* (10), 793–807.

(11) Gray, E. G. Axo-Somatic and Axo-Dendritic Synapses of the Cerebral Cortex: An Electron Microscope Study. *J. Anat.* **1959**, *93* (4), 420–433.

(12) Raviola, G.; Raviola, E. Light and Electron Microscopic Observations on the Inner Plexiform Layer of the Rabbit Retina. *Am. J. Anat.* **1967**, *120* (3), 403–425.

(13) Fiszer, S.; Robertis, E. de. Action of Triton X-100 on Ultrastructure and Membrane-Bound Enzymes of Isolated Nerve Endings from Rat Brain. *Brain Res.* **1967**, *5* (1), 31–44.

(14) Peters, A.; Kaiserman-Abramof, I. R. The Small Pyramidal Neuron of the Rat Cerebral Cortex: The Synapses upon Dendritic Spines. *Z. Für Zellforsch. Mikrosk. Anat.* **1969**, *100* (4), 487–506.

(15) Carlin, R. K.; Grab, D. J.; Cohen, R. S.; Siekevitz, P. Isolation and Characterization of Postsynaptic Densities from Various Brain Regions: Enrichment of Different Types of Postsynaptic Densities. *J. Cell Biol.* **1980**, *86* (3), 831–845.

(16) Collins, M. O.; Husi, H.; Yu, L.; Brandon, J. M.; Anderson, C. N. G.; Blackstock, W. P.; Choudhary, J. S.; Grant, S. G. N. Molecular Characterization and Comparison of the Components and Multiprotein Complexes in the Postsynaptic Proteome. *J. Neurochem.* **2006**, *97*, 16–23.

(17) Grant, S. G. N. SnapShot: Organizational Principles of the Postsynaptic Proteome. *Neuron* **2013**, *80* (2), 534-534.e1.

(18) Kuzirian, M. S.; Paradis, S. Emerging Themes in GABAergic Synapse Development. *Prog. Neurobiol.* **2011**, *95* (1), 68–87.

(19) Andersen, P.; Eccles, J. C.; Løyning, Y. Hippocampus of the Brain: Recurrent Inhibition in the Hippocampus with Identification of the Inhibitory Cell and Its Synapses. *Nature* **1963**, *198* (4880), 540–542.

(20) Buhl, E. H.; Halasy, K.; Somogyi, P. Diverse Sources of Hippocampal Unitary Inhibitory Postsynaptic Potentials and the Number of Synaptic Release Sites. *Nature* **1994**, *368* (6474), 823–828.

(21) Cobb, S. R.; Buhl, E. H.; Halasy, K.; Paulsen, O.; Somogyi, P. Synchronization of Neuronal Activity in Hippocampus by Individual GABAergic Interneurons. *Nature* **1995**, *378* (6552), 75–78.

(22) Miles, R.; Wong, R. K. Unitary Inhibitory Synaptic Potentials in the Guinea-Pig Hippocampus *in Vitro*. *J. Physiol.* **1984**, *356* (1), 97–113.

(23) Davies, C. H.; Starkey, S. J.; Pozza, M. F.; Collingridge, G. L. $GABA_B$ Autoreceptors Regulate the Induction of LTP. *Nature* **1991**, *349* (6310), 609–611.

(24) Otis, T. S.; De Koninck, Y.; Mody, I. Lasting Potentiation of Inhibition Is Associated with an Increased Number of γ-Aminobutyric Acid Type A Receptors Activated during Miniature Inhibitory Postsynaptic Currents. *Proc. Natl. Acad. Sci.* **1994**, *91* (16), 7698–7702.

(25) Nusser, Z.; Cull-Candy, S.; Farrant, M. Differences in Synaptic $GABA_A$ Receptor Number Underlie Variation in GABA Mini Amplitude. *Neuron* **1997**, *19* (3), 697–709.

(26) Crestani, F.; Lorez, M.; Baer, K.; Essrich, C.; Benke, D.; Laurent, J. P.; Belzung, C.; Fritschy, J.-M.; Luscher, B.; Mohler, H. Decreased $GABA_A$-Receptor Clustering Results in Enhanced Anxiety and a Bias for Threat Cues. *Nat. Neurosci.* **1999**, *2*, 833–839.

(27) Shen, Q.; Lal, R.; Luellen, B. A.; Earnheart, J. C.; Milasincic Andrews, A.; Luscher, B. γ-Aminobutyric Acid-Type A Receptor Deficits Cause Hypothalamic-Pituitary-Adrenal Axis Hyperactivity and Antidepressant Drug Sensitivity Reminiscent of Melancholic Forms of Depression. *Biol. Psychiatry* **2010**, *68* (6), 512–520.

(28) Papadopoulos, T.; Soykan, T. The Role of Collybistin in Gephyrin Clustering at Inhibitory Synapses: Facts and Open Questions. *Front. Cell. Neurosci.* **2011**, *5*, 11.

(29) Hoon, M.; Soykan, T.; Falkenburger, B.; Hammer, M.; Patrizi, A.; Schmidt, K.-F.; Sassoe-Pognetto, M.; Lowel, S.; Moser, T.; Taschenberger, H.; et al. Neuroligin-4 Is Localized to Glycinergic Postsynapses and Regulates Inhibition in the Retina. *Proc. Natl. Acad. Sci.* **2011**, *108* (7), 3053–3058.

(30) Poulopoulos, A.; Aramuni, G.; Meyer, G.; Soykan, T.; Hoon, M.; Papadopoulos, T.; Zhang, M.; Paarmann, I.; Fuchs, C.; Harvey, K.; et al. Neuroligin 2 Drives Postsynaptic Assembly at Perisomatic Inhibitory Synapses through Gephyrin and Collybistin. *Neuron* **2009**, *63* (5), 628–642.

(31) Barnard, E. A.; Skolnick, P.; Olsen, R. W.; Mohler, H.; Sieghart, W.; Biggio, G., Braestrup, C.; Bateson, A. N.; Langer, S. Z. International Union of Pharmacology: Subtypes of γ-Aminobutyric $Acid_A$ Receptors Classification on the Basis of Subunit Structure and Receptor Function. *Pharmacol. Rev.* **1998**, *50* (2), 291–313.

(32) Jacob, T. C.; Moss, S. J.; Jurd, R. $GABA_A$ Receptor Trafficking and Its Role in the Dynamic Modulation of Neuronal Inhibition. *Nat. Rev. Neurosci.* **2008**, *9* (5), 331–343.

(33) Unwin, N. The Structure of Ion Channels in Membranes of Excitable Cells. *Neuron* **1989**, *3* (6), 665–676.

(34) Benarroch, E. E. $GABA_A$ Receptor Heterogeneity, Function, and Implications for Epilepsy. *Neurology* **2007**, *68* (8), 612–614.

(35) Thompson-Vest, N. M.; Waldvogel, H. J.; Rees, M. I.; Faull, R. L. M. $GABA_A$ Receptor Subunit and Gephyrin Protein Changes Differ in the Globus Pallidus in Huntington's Diseased Brain. *Brain Res.* **2003**, *994* (2), 265–270.

(36) Rudolph, U.; Möhler, H. Analysis of $GABA_A$ Receptor Function and Dissection of the Pharmacology of Benzodiazepines and General Anesthetics Through Mouse Genetics. *Annu. Rev. Pharmacol. Toxicol.* **2004**, *44* (1), 475–498.

(37) Lewis, D. A.; Gonzalez-Burgos, G. Pathophysiologically Based Treatment Interventions in Schizophrenia. *Nat. Med.* **2006**, *12* (9), 1016–1022.

(38) *Autism Imaging and Devices*; Casanova, M. F., El-Baz, A. S., Suri, J. S., Eds.; CRC Press, Taylor & Francis Group: Boca Raton, **2017**.

(39) Rusakov, D. A.; Harrison, E.; Stewart, M. G. Synapses in Hippocampus Occupy Only 1–2% of Cell Membranes and Are Spaced Less than Half-Micron Apart: A Quantitative Ultrastructural Analysis with Discussion of Physiological Implications. *Neuropharmacology* **1998**, *37* (4–5), 513–521.

(40) Dahan, M.; Levi, S.; Luccardini, C.; Rostaing, P.; Riveau, B.; Triller, A. Diffusion Dynamics of Glycine Receptors Revealed by Single-Quantum Dot Tracking. *Science* **2003**, *302* (5644), 442–445.

(41) Triller, A.; Choquet, D. Surface Trafficking of Receptors between Synaptic and Extrasynaptic Membranes: And yet They Do Move! *Trends Neurosci.* **2005**, *28* (3), 133–139.

(42) Jacob, T. C.; Bogdanov, Y. D.; Magnus, C.; Saliba, R. S.; Kittler, J. T.; Haydon, P. G.; Moss, S. J. Gephyrin Regulates the Cell Surface Dynamics of Synaptic $GABA_A$ Receptors. *J. Neurosci. Off. J. Soc. Neurosci.* **2005**, *25* (45), 10469–10478.

(43) Thomas, P.; Mortensen, M.; Hosie, A. M.; Smart, T. G. Dynamic Mobility of Functional $GABA_A$ Receptors at Inhibitory Synapses. *Nat. Neurosci.* **2005**, *8* (7), 889–897.

(44) Meier, J.; Vannier, C.; Sergé, A.; Triller, A.; Choquet, D. Fast and Reversible Trapping of Surface Glycine Receptors by Gephyrin. *Nat. Neurosci.* **2001**, *4* (3), 253–260.

(45) Sheng, M. PDZs and Receptor/Channel Clustering: Rounding Up the Latest Suspects. *Neuron* **1996**, *17* (4), 575–578.

(46) Craven, S. E.; Bredt, D. S. PDZ Proteins Organize Synaptic Signaling Pathways. *Cell* **1998**, *93* (4), 495–498.

(47) Essrich, C.; Lorez, M.; Benson, J. A.; Fritschy, J.-M.; Lüscher, B. Postsynaptic Clustering of Major $GABA_A$ Receptor Subtypes Requires the Gamma 2 Subunit and Gephyrin. *Nat. Neurosci.* **1998**, *1* (7), 563–571.

(48) Harvey, K.; Duguid, I. C.; Alldred, M. J.; Beatty, S. E.; Ward, H.; Keep, N. H.; Lingenfelter, S. E.; Pearce, B. R.; Lundgren, J.; Owen, M. J.; et al. The GDP-GTP Exchange Factor Collybistin: An Essential Determinant of Neuronal Gephyrin Clustering. *J. Neurosci.* **2004**, *24* (25), 5816–5826.

(49) Nguyen, T.; Südhof, T. C. Binding Properties of Neuroligin 1 and Neurexin 1β Reveal Function as Heterophilic Cell Adhesion Molecules. *J. Biol. Chem.* **1997**, *272* (41), 26032–26039.

(50) Ichtchenko, K.; Nguyen, T.; Südhof, T. C. Structures, Alternative Splicing, and Neurexin Binding of Multiple Neuroligins. *J. Biol. Chem.* **1996**, *271* (5), 2676–2682.

(51) Choi, U. B.; McCann, J. J.; Weninger, K. R.; Bowen, M. E. Beyond the Random Coil: Stochastic Conformational Switching in Intrinsically Disordered Proteins. *Structure* **2011**, *19* (4), 566–576.

(52) Südhof, T. C. Neuroligins and Neurexins Link Synaptic Function to Cognitive Disease. *Nature* **2008**, *455* (7215), 903–911.
(53) Nguyen, Q.-A.; Horn, M. E.; Nicoll, R. A. Distinct Roles for Extracellular and Intracellular Domains in Neuroligin Function at Inhibitory Synapses. *eLife* **2016**, *5*, e19236.
(54) Bemben, M. A.; Shipman, S. L.; Nicoll, R. A.; Roche, K. W. The Cellular and Molecular Landscape of Neuroligins. *Trends Neurosci.* **2015**, *38* (8), 496–505.
(55) Varoqueaux, F.; Jamain, S.; Brose, N. Neuroligin 2 Is Exclusively Localized to Inhibitory Synapses. *Eur. J. Cell Biol.* **2004**, *83* (9), 449–456.
(56) Treutlein, B.; Gokce, O.; Quake, S. R.; Südhof, T. C. Cartography of Neurexin Alternative Splicing Mapped by Single-Molecule Long-Read mRNA Sequencing. *Proc. Natl. Acad. Sci.* **2014**, *111* (13), E1291–E1299.
(57) Poulopoulos, A.; Soykan, T.; Tuffy, L. P.; Hammer, M.; Varoqueaux, F.; Brose, N. Homodimerization and Isoform-Specific Heterodimerization of Neuroligins. *Biochem. J.* **2012**, *446* (2), 321–330.
(58) Shipman, S. L.; Nicoll, R. A. Dimerization of Postsynaptic Neuroligin Drives Synaptic Assembly via Transsynaptic Clustering of Neurexin. *Proc. Natl. Acad. Sci. U. S. A.* **2012**, *109* (47), 19432–19437.
(59) Graf, E. R.; Zhang, X. Z.; Jin, S.-X.; Linhoff, M. W.; Craig, A. M. Neurexins Induce Differentiation of GABA and Glutamate Postsynaptic Specializations via Neuroligins. *Cell* **2004**, *119* (7), 1013–1026.
(60) Soykan, T.; Schneeberger, D.; Tria, G.; Buechner, C.; Bader, N.; Svergun, D.; Tessmer, I.; Poulopoulos, A.; Papadopoulos, T.; Varoqueaux, F.; et al. A Conformational Switch in Collybistin Determines the Differentiation of Inhibitory Postsynapses. *EMBO J.* **2014**, *33*, 2113–2133.
(61) Kirsch, J.; Wolters, I.; Triller, A.; Betz, H. Gephyrin Antisense Oligonucleotides Prevent Glycine Receptor Clustering in Spinal Neurons. *Nature* **1993**, *366* (6457), 745–748.
(62) Kneussel, M.; Brandstätter, J. H.; Laube, B.; Stahl, S.; Müller, U.; Betz, H. Loss of Postsynaptic $GABA_A$ Receptor Clustering in Gephyrin-Deficient Mice. *J. Neurosci. Off. J. Soc. Neurosci.* **1999**, *21* (19), 9289–9297.
(63) Saiepour, L.; Fuchs, C.; Patrizi, A.; Sassoè-Pognetto, M.; Harvey, R. J.; Harvey, K. Complex Role of Collybistin and Gephyrin in $GABA_A$ Receptor Clustering. *J. Biol. Chem.* **2010**, *285* (38), 29623–29631.
(64) Tretter, V.; Kerschner, B.; Milenkovic, I.; Ramsden, S. L.; Ramerstorfer, J.; Saiepour, L.; Maric, H.-M.; Moss, S. J.; Schindelin, H.; Harvey, R. J.; et al. Molecular Basis of the γ-Aminobutyric Acid A Receptor α3 Subunit Interaction with the Clustering Protein Gephyrin. *J. Biol. Chem.* **2011**, *286* (43), 37702–37711.
(65) Maric, H.-M.; Mukherjee, J.; Tretter, V.; Moss, S. J.; Schindelin, H. Gephyrin-Mediated γ-Aminobutyric Acid Type A and Glycine Receptor Clustering Relies on a Common Binding Site. *J. Biol. Chem.* **2011**, *286* (49), 42105–42114.
(66) Tretter, V.; Jacob, T. C.; Mukherjee, J.; Fritschy, J.-M.; Pangalos, M. N.; Moss, S. J. The Clustering of $GABA_A$ Receptor Subtypes at Inhibitory Synapses Is Facilitated via the Direct Binding of Receptor 2 Subunits to Gephyrin. *J. Neurosci.* **2008**, *28* (6), 1356–1365.
(67) Kowalczyk, S.; Winkelmann, A.; Smolinsky, B.; Förstera, B.; Neundorf, I.; Schwarz, G.; Meier, J. C. Direct Binding of $GABA_A$ Receptor β2 and β3 Subunits to Gephyrin. *Eur. J. Neurosci.* **2013**, *37* (4), 544–554.

(68) Kirsch, J.; Kuhse, J.; Betz, H. Targeting of Glycine Receptor Subunits to Gephyrin-Rich Domains in Transfected Human Embryonic Kidney Cells. *Mol. Cell. Neurosci.* **1995**, *6* (5), 450–461.

(69) Ramming, M.; Kins, S.; Werner, N.; Hermann, A.; Betz, H.; Kirsch, J. Diversity and Phylogeny of Gephyrin: Tissue-Specific Splice Variants, Gene Structure, and Sequence Similarities to Molybdenum Cofactor-Synthesizing and Cytoskeleton-Associated Proteins. *Proc. Natl. Acad. Sci. U. S. A.* **2000**, *97* (18), 10266–10271.

(70) Mammoto, A.; Sasaki, T.; Asakura, T.; Hotta, I.; Imamura, H.; Takahashi, K.; Matsuura, Y.; Shirao, T.; Takai, Y. Interactions of Drebrin and Gephyrin with Profilin. *Biochem. Biophys. Res. Commun.* **1998**, *243* (1), 86–89.

(71) Schwarz, G.; Mendel, R. R.; Ribbe, M. W. Molybdenum Cofactors, Enzymes and Pathways. *Nature* **2009**, *460* (7257), 839–847.

(72) Feng, G.; Tintrup, H.; Kirsch, J.; Nichol, M. C.; Kuhse, J.; Betz, H.; Sanes, J. R. Dual Requirement for Gephyrin in Glycine Receptor Clustering and Molybdoenzyme Activity. *Science* **1998**, *282* (5392), 1321–1324.

(73) Kirsch, J.; Langosch, D.; Prior, P.; Littauer, U. Z.; Schmitt, B.; Betz, H. The 93-kDa Glycine Receptor-Associated Protein Binds to Tubulin. *J. Biol. Chem.* **1991**, *266* (33), 22242–22245.

(74) Schwarz, G.; Schrader, N.; Mendel, R. R.; Hecht, H.-J.; Schindelin, H. Crystal Structures of Human Gephyrin and Plant Cnx1 G Domains: Comparative Analysis and Functional Implications. *J. Mol. Biol.* **2001**, *312* (2), 405–418.

(75) Sola, M.; Kneussel, M.; Heck, I. S.; Betz, H.; Weissenhorn, W. X-Ray Crystal Structure of the Trimeric N-Terminal Domain of Gephyrin. *J. Biol. Chem.* **2001**, *276* (27), 25294–25301.

(76) Sola, M.; Bavro, V. N.; Timmins, J.; Franz, T.; Ricard-Blum, S.; Schoehn, G.; Ruigrok, R. W. H.; Paarmann, I.; Saiyed, T.; O'Sullivan, G. A.; et al. Structural Basis of Dynamic Glycine Receptor Clustering by Gephyrin. *EMBO J.* **2004**, *23* (13), 2510–2519.

(77) Kim, E. Y.; Schrader, N.; Smolinsky, B.; Bedet, C.; Vannier, C.; Schwarz, G.; Schindelin, H. Deciphering the Structural Framework of Glycine Receptor Anchoring by Gephyrin. *EMBO J.* **2006**, *25* (6), 1385–1395.

(78) Saiyed, T.; Paarmann, I.; Schmitt, B.; Haeger, S.; Sola, M.; Schmalzing, G.; Weissenhorn, W.; Betz, H. Molecular Basis of Gephyrin Clustering at Inhibitory Synapses: ROLE OF G- AND E-DOMAIN INTERACTIONS. *J. Biol. Chem.* **2007**, *282* (8), 5625–5632.

(79) Kneussel, M.; Betz, H. Clustering of Inhibitory Neurotransmitter Receptors at Developing Postsynaptic Sites: The Membrane Activation Model. *Trends Neurosci.* **2000**, *23* (9), 429–435.

(80) Xiang, S.; Nichols, J.; Rajagopalan, K. V.; Schindelin, H. The Crystal Structure of *Escherichia Coli* MoeA and Its Relationship to the Multifunctional Protein Gephyrin. *Structure* **2001**, *9* (4), 299–310.

(81) Sander, B.; Tria, G.; Shkumatov, A. V.; Kim, E.-Y.; Grossmann, J. G.; Tessmer, I.; Svergun, D. I.; Schindelin, H. Structural Characterization of Gephyrin by AFM and SAXS Reveals a Mixture of Compact and Extended States. *Acta Crystallogr. D Biol. Crystallogr.* **2013**, *69* (Pt 10), 2050–2060.

(82) Specht, C. G.; Izeddin, I.; Rodriguez, P. C.; El Beheiry, M.; Rostaing, P.; Darzacq, X.; Dahan, M.; Triller, A. Quantitative Nanoscopy of Inhibitory Synapses: Counting Gephyrin Molecules and Receptor Binding Sites. *Neuron* **2013**, *79* (2), 308–321.

(83) Maas, C.; Tagnaouti, N.; Loebrich, S.; Behrend, B.; Lappe-Siefke, C.; Kneussel, M. Neuronal Cotransport of Glycine Receptor and the Scaffold Protein Gephyrin. *J. Cell Biol.* **2006**, *172* (3), 441–451.

(84) Ehrensperger, M.-V.; Hanus, C.; Vannier, C.; Triller, A.; Dahan, M. Multiple Association States between Glycine Receptors and Gephyrin Identified by SPT Analysis. *Biophys. J.* **2007**, *92* (10), 3706–3718.

(85) Renner, M.; Schweizer, C.; Bannai, H.; Triller, A.; Lévi, S. Diffusion Barriers Constrain Receptors at Synapses. *PLoS ONE* **2012**, *7* (8), e43032.

(86) Reid, T.; Bathoorn, A.; Ahmadian, M. R.; Collard, J. G. Identification and Characterization of hPEM-2, a Guanine Nucleotide Exchange Factor Specific for Cdc42. *J. Biol. Chem.* **1999**, *274* (47), 33587–33593.

(87) Neudauer, C. L.; Joberty, G.; Tatsis, N.; Macara, I. G. Distinct Cellular Effects and Interactions of the Rho-Family GTPase TC10. *Curr. Biol.* **1998**, *8* (21), 1151–1161.

(88) Murphy, G. A.; Solski, P. A.; Jillian, S. A.; de la Ossa, P. P.; D'Eustachio, P.; Der, C. J.; Rush, M. G. Cellular Functions of TC10, a Rho Family GTPase: Regulation of Morphology, Signal Transduction and Cell Growth. *Oncogene* **1999**, *18* (26), 3831–3845.

(89) Tanabe, K.; Tachibana, T.; Yamashita, T.; Che, Y. H.; Yoneda, Y.; Ochi, T.; Tohyama, M.; Yoshikawa, H.; Kiyama, H. The Small GTP-Binding Protein TC10 Promotes Nerve Elongation in Neuronal Cells, and Its Expression Is Induced during Nerve Regeneration in Rats. *J. Neurosci.* **2000**, *20* (11), 4138–4144.

(90) Kins, S.; Betz, H.; Kirsch, J. Collybistin, a Newly Identified Brain-Specific GEF, Induces Submembrane Clustering of Gephyrin. *Nat. Neurosci.* **2000**, *3* (1), 22–29.

(91) Tyagarajan, S. K.; Ghosh, H.; Harvey, K.; Fritschy, J.-M. Collybistin Splice Variants Differentially Interact with Gephyrin and Cdc42 to Regulate Gephyrin Clustering at GABAergic Synapses. *J. Cell Sci.* **2011**, *124* (16), 2786–2796.

(92) Kneussel, M.; Engelkamp, D.; Betz, H. Distribution of Transcripts for the Brain-Specific GDP/GTP Exchange Factor Collybistin in the Developing Mouse Brain: Distribution of Collybistin Transcripts. *Eur. J. Neurosci.* **2001**, *13* (3), 487–492.

(93) Reddy-Alla, S.; Schmitt, B.; Birkenfeld, J.; Eulenburg, V.; Dutertre, S.; Böhringer, C.; Götz, M.; Betz, H.; Papadopoulos, T. PH-Domain-Driven Targeting of Collybistin but Not Cdc42 Activation Is Required for Synaptic Gephyrin Clustering. *Eur. J. Neurosci.* **2010**, *31* (7), 1173–1184.

(94) Kalscheuer, V. M.; Musante, L.; Fang, C.; Hoffmann, K.; Fuchs, C.; Carta, E.; Deas, E.; Venkateswarlu, K.; Menzel, C.; Ullmann, R.; et al. A Balanced Chromosomal Translocation Disrupting ARHGEF9 Is Associated with Epilepsy, Anxiety, Aggression, and Mental Retardation. *Hum. Mutat.* **2009**, *30* (1), 61–68.

(95) Hyvönen, M.; Macias, M. J.; Nilges, M.; Oschkinat, H.; Sarastel, M.; Wilmanns, M. Structure of the Binding Site for Inositol Phosphates in a PH Domain. *EMBO J.* **1995**, *14* (19), 4676–4685.

(96) Harlan, J. E.; Hajduk, P. J.; Yoon, H. S.; Fesik, S. W. Pleckstrin Homology Domains Bind to Phosphatidylinositol-4,5-Bisphosphate. *Nature* **1994**, *371*, 168–170.

(97) Di Paolo, G.; De Camilli, P. Phosphoinositides in Cell Regulation and Membrane Dynamics. *Nature* **2006**, *443*, 651–657.

(98) Corvera, S.; D'Arrigo, A.; Stenmark, H. Phosphoinositides in Membrane Traffic. *Curr Opin Cell Biol* **1999**, *11*, 460–465.

(99) Stein, H.; Spindler, S.; Bonakdar, N.; Wang, C.; Sandoghdar, V. Production of Isolated Giant Unilamellar Vesicles under High Salt Concentrations. *Front. Physiol.* **2017**, *8*, 1–16.

(100) Forschungszentrum Jülich - Research - Nanodiscs – Tool for membrane protein studies https://www.fz-juelich.de/ics/ics-6/EN/Research/Themen/04Nanodiscs/artikel.html?nn=1475680 (accessed Oct 2, 2019).

(101) Andersson, J.; Köper, I.; Knoll, W. Tethered Membrane Architectures—Design and Applications. *Front. Mater.* **2018**, *5*.

(102) Andersson, J.; Köper, I. Tethered and Polymer Supported Bilayer Lipid Membranes: Structure and Function. *Membranes* **2016**, *6* (2), 30.

(103) Sezgin, E.; Levental, I.; Mayor, S.; Eggeling, C. The Mystery of Membrane Organization: Composition, Regulation and Roles of Lipid Rafts. *Nat. Rev. Mol. Cell Biol.* **2017**, *18* (6), 361–374.

(104) Wagner, M. L.; Tamm, L. K. Tethered Polymer-Supported Planar Lipid Bilayers for Reconstitution of Integral Membrane Proteins: Silane-Polyethyleneglycol-Lipid as a Cushion and Covalent Linker. *Biophys. J.* **2000**, *79* (3), 1400–1414.

(105) Baumann, M. K.; Swann, M. J.; Textor, M.; Reimhult, E. Pleckstrin Homology-Phospholipase C-δ_1 Interaction with Phosphatidylinositol 4,5-Bisphosphate Containing Supported Lipid Bilayers Monitored *in Situ* with Dual Polarization Interferometry. *Anal. Chem.* **2011**, *83*, 6267–6274.

(106) Shi, X.; Kohram, M.; Zhuang, X.; Smith, A. W. Interactions and Translational Dynamics of Phosphatidylinositol Bisphosphate (PIP_2) Lipids in Asymmetric Lipid Bilayers. *Langmuir* **2016**, *32*, 1732–1741.

(107) Siontorou, C.; Nikoleli, G.-P.; Nikolelis, D.; Karapetis, S. Artificial Lipid Membranes: Past, Present, and Future. *Membranes* **2017**, *7*, 38–61.

(108) Anderson, T. H.; Min, Y.; Weirich, K. L.; Zeng, H.; Fygenson, D.; Israelachvili, J. N. Formation of Supported Bilayers on Silica Substrates. *Langmuir* **2009**, *25*, 6997–7005.

(109) Koster, K. L.; Webb, M. S.; Bryant, G.; Lynch, D. V. Interactions between Soluble Sugars and POPC (1-Palmitoyl-2-Oleoylphosphatidylcholine) during Dehydration: Vitrification of Sugars Alters the Phase Behavior of the Phospholipid. *Biochim. Biophys. Acta BBA - Biomembr.* **1994**, *1193* (1), 143–150.

(110) Obladen, M.; Popp, D.; Schöll, C.; Schwarz, H.; Jähnig, F. Studies on Lung Surfactant Replacement in Respiratory Distress Syndrome. Rapid Film Formation from Binary Mixed Liposomes. *Biochim. Biophys. Acta BBA - Biomembr.* **1983**, *735* (2), 215–224.

(111) Ferrell, J. E. Phosphoinositide Metabolism and the Morphology of Human Erythrocytes. *J. Cell Biol.* **1984**, *98*, 1992–1998.

(112) Hagelberg, C.; Allan, D. Restricted Diffusion of Integral Membrane Proteins and Polyphosphoinositides Leads to Their Depletion in Microvesicles Released from Human Erythrocytes. *Biochem. J.* **1990**, *271*, 831–834.

(113) Ludolphs, M.; Schneeberger, D.; Soykan, T.; Schäfer, J.; Papadopoulos, T.; Brose, N.; Schindelin, H.; Steinem, C. Specificity of Collybistin-Phosphoinositide Interactions: Impact of the Individual Protein Domains. *J. Biol. Chem.* **2016**, *291*, 244–254.

(114) Hannig, G.; Makrides, S. C. Strategies for Optimizing Heterologous Protein Expression in *Escherichia Coli*. *Trends Biotechnol.* **1998**, *16* (2), 54–60.

(115) Baneyx, F. Recombinant Protein Expression in *Escherichia Coli*. *Curr. Opin. Biotechnol.* **1999**, *10* (5), 411–421.

(116) Sørensen, H.; Mortensen, K. Soluble Expression of Recombinant Proteins in the Cytoplasm of *Escherichia Coli*. *Microb. Cell Factories* **2005**, *4* (1), 1.
(117) Chan, W.-T.; Verma, C. S.; Lane, D. P.; Gan, S. K.-E. A Comparison and Optimization of Methods and Factors Affecting the Transformation of *Escherichia Coli*. *Biosci. Rep.* **2013**, *33* (6).
(118) Dubendorff, J. W.; Studier, F. W. Controlling Basal Expression in an Inducible T7 Expression System by Blocking the Target T7 Promoter with *lac* Repressor. *J. Mol. Biol.* **1991**, *219* (1), 45–59.
(119) Studier, F. W.; Moffatt, B. A. Use of Bacteriophage T7 RNA Polymerase to Direct Selective High-Level Expression of Cloned Genes. *J. Mol. Biol.* **1986**, *189* (1), 113–130.
(120) Macherey-Nagel. *Plasmid DNA Purification - User Manual*, 15th ed.; Düren, **2019**.
(121) Chong, S.; Mersha, F. B.; Comb, D. G.; Scott, M. E.; Landry, D.; Vence, L. M.; Perler, F. B.; Benner, J.; Kucera, R. B.; Hirvonen, C. A.; et al. Single-Column Purification of Free Recombinant Proteins Using a Self-Cleavable Affinity Tag Derived from a Protein Splicing Element. *Gene* **1997**, *192* (2), 271–281.
(122) Chong, S.; Montello, G. E.; Zhang, A.; Cantor, E. J.; Liao, W.; Xu, M.-Q.; Benner, J. Utilizing the C-Terminal Cleavage Activity of a Protein Splicing Element to Purify Recombinant Proteins in a Single Chromatographic Step. *Nucleic Acids Res.* **1998**, *26* (22), 5109–5115.
(123) Laemmli, U. K. Cleavage of Structural Proteins during the Assembly of the Head of Bacteriophage T4. *Nature* **1970**, *227* (5259), 680–686.
(124) Schägger, H.; von Jagow, G. Tricine-Sodium Dodecyl Sulfate-Polyacrylamide Gel Electrophoresis for the Separation of Proteins in the Range from 1 to 100 kDa. *Anal. Biochem.* **1987**, *166* (2), 368–379.
(125) Schägger, H. Tricine–SDS-PAGE. *Nat. Protoc.* **2006**, *1* (1), 16–22.
(126) Kyhse-Andersen, J. Electroblotting of Multiple Gels: A Simple Apparatus without Buffer Tank for Rapid Transfer of Proteins from Polyacrylamide to Nitrocellulose. *J BIOCHEM BIOPH METH* **1984**, *10*, 203–209.
(127) Bradford, M. M. A Rapid and Sensitive Method for the Quantitation of Microgram Quantities of Protein Utilizing the Principle of Protein-Dye Binding. *Anal. Biochem.* **1976**, *72* (1–2), 248–254.
(128) Mitchell, D. J.; Ninham, B. W. Micelles, Vesicles and Microemulsions. *J. Chem. Soc. Faraday Trans. 2* **1981**, *77* (4), 601.
(129) Claessens, M. M. A. E.; van Oort, B. F.; Leermakers, F. A. M.; Hoekstra, F. A.; Cohen Stuart, M. A. Charged Lipid Vesicles: Effects of Salts on Bending Rigidity, Stability, and Size. *Biophys. J.* **2004**, *87* (6), 3882–3893.
(130) Maulucci, G.; De Spirito, M.; Arcovito, G.; Boffi, F.; Castellano, A. C.; Briganti, G. Particle Size Distribution in DMPC Vesicles Solutions Undergoing Different Sonication Times. *Biophys. J.* **2005**, *88* (5), 3545–3550.
(131) Hunter, D. G.; Frisken, B. J. Effect of Extrusion Pressure and Lipid Properties on the Size and Polydispersity of Lipid Vesicles. *Biophys. J.* **1998**, *74* (6), 2996–3002.
(132) Ulman, A. Formation and Structure of Self-Assembled Monolayers. *Chem. Rev.* **1996**, *96* (4), 1533–1554.
(133) Bain, C. D.; Evall, J.; Whitesides, G. M. Formation of Monolayers by the Coadsorption of Thiols on Gold: Variation in the Head Group, Tail Group, and Solvent. *J. Am. Chem. Soc.* **1989**, *111* (18), 7155–7164.

(134) Anwander, R.; Nagl, I.; Widenmeyer, M.; Engelhardt, G.; Groeger, O.; Palm, C.; Röser, T. Surface Characterization and Functionalization of MCM-41 Silicas via Silazane Silylation. *J. Phys. Chem. B* **2000**, *104* (15), 3532–3544.

(135) Giovambattista, N.; Debenedetti, P. G.; Rossky, P. J. Effect of Surface Polarity on Water Contact Angle and Interfacial Hydration Structure. *J. Phys. Chem. B* **2007**, *111* (32), 9581–9587.

(136) Stalder, A. F.; Melchior, T.; Müller, M.; Sage, D.; Blu, T.; Unser, M. Low-Bond Axisymmetric Drop Shape Analysis for Surface Tension and Contact Angle Measurements of Sessile Drops. *Colloids Surf. Physicochem. Eng. Asp.* **2010**, *364*, 72–81.

(137) McDonagh, C.; Burke, C. S.; MacCraith, B. D. Optical Chemical Sensors. *Chem. Rev.* **2008**, *108* (2), 400–422.

(138) Gauglitz, G.; Proll, G. Strategies for Label-Free Optical Detection. In *Biosensing for the 21st Century*; Renneberg, R., Lisdat, F., Eds.; Advances in Biochemical Engineering/Biotechnology; Springer Berlin Heidelberg: Berlin, Heidelberg, **2008**; Vol. 109, pp 395–432.

(139) Gauglitz, G. Direct Optical Sensors: Principles and Selected Applications. *Anal. Bioanal. Chem.* **2005**, *381* (1), 141–155.

(140) Atkins, P. W.; De Paula, J.; Keeler, J. *Atkins' Physical Chemistry*, 11th ed.; Oxford University Press: Oxford, United Kingdom; New York, NY, **2018**.

(141) Harvey, A. H.; Gallagher, J. S.; Sengers, J. M. H. L. Revised Formulation for the Refractive Index of Water and Steam as a Function of Wavelength, Temperature and Density. *J. Phys. Chem. Ref. Data* **1998**, *27* (4), 761–774.

(142) Malitson, I. H. Interspecimen Comparison of the Refractive Index of Fused Silica. *J. Opt. Soc. Am.* **1965**, *55* (10), 1205.

(143) Gauglitz, G. Multiple Reflectance Interference Spectroscopy Measurements Made in Parallel for Binding Studies. *Rev. Sci. Instrum.* **2005**, *76* (6), 062224.

(144) Gauglitz, G.; Brecht, A.; Kraus, G.; Mahm, W. Chemical and Biochemical Sensors Based on Interferometry at Thin (Multi-) Layers. *Sens. Actuators B Chem.* **1993**, *11* (1–3), 21–27.

(145) Vörös, J. The Density and Refractive Index of Adsorbing Protein Layers. *Biophys. J.* **2004**, *87* (1), 553–561.

(146) Binnig, G.; Quate, C. F.; Gerber, Ch. Atomic Force Microscope. *Phys. Rev. Lett.* **1986**, *56* (9), 930–933.

(147) Butt, H.-J.; Cappella, B.; Kappl, M. Force Measurements with the Atomic Force Microscope: Technique, Interpretation and Applications. *Surf. Sci. Rep.* **2005**, *59* (1–6), 1–152.

(148) Hapala, P.; Kichin, G.; Wagner, C.; Tautz, F. S.; Temirov, R.; Jelínek, P. Mechanism of High-Resolution STM/AFM Imaging with Functionalized Tips. *Phys. Rev. B* **2014**, *90* (8).

(149) Hansma, P. K.; Cleveland, J. P.; Radmacher, M.; Walters, D. A.; Hillner, P. E.; Bezanilla, M.; Fritz, M.; Vie, D.; Hansma, H. G.; Prater, C. B.; et al. Tapping Mode Atomic Force Microscopy in Liquids. *Appl. Phys. Lett.* **1994**, *64* (13), 1738–1740.

(150) Lichtman, J. W.; Conchello, J.-A. Fluorescence Microscopy. *Nat. Methods* **2005**, *2* (12), 910–919.

(151) Minsky, M. Memoir on Inventing the Confocal Scanning Microscope. *Scanning* **1988**, *10* (4), 128–138.

(152) Schermelleh, L.; Carlton, P. M.; Haase, S.; Shao, L.; Winoto, L.; Kner, P.; Burke, B.; Cardoso, M. C.; Agard, D. A.; Gustafsson, M. G. L.; et al. Subdiffraction Multicolor Imaging of the Nuclear Periphery with 3D Structured Illumination Microscopy. *Science* **2008**, *320* (5881), 1332–1336.

(153) Ramal-Sanchez, M.; Bernabo, N.; Tsikis, G.; Blache, M.-C.; Labas, V.; Druart, X.; Mermillod, P.; Saint-Dizier, M. Progesterone Induces Sperm Release from Oviductal Epithelial Cells by Modifying Sperm Proteomics, Lipidomics and Membrane Fluidity. *Mol. Cell. Endocrinol.* **2020**, *504*, 110723.

(154) Starigazdová, J.; Nešporová, K.; Čepa, M.; Šínová, R.; Šmejkalová, D.; Huerta-Angeles, G.; Velebný, V. *In Vitro* Investigation of Hyaluronan-Based Polymeric Micelles for Drug Delivery into the Skin: The Internalization Pathway. *Eur. J. Pharm. Sci.* **2020**, *143*, 105168.

(155) Urban, P.; Pritzl, S. D.; Ober, M. F.; Dirscherl, C. F.; Pernpeintner, C.; Konrad, D. B.; Frank, J. A.; Trauner, D.; Nickel, B.; Lohmueller, T. A Lipid Photoswitch Controls Fluidity in Supported Bilayer Membranes. *Langmuir* **2020**, *36* (10), 2629–2634.

(156) Macháň, R.; Hof, M. Lipid Diffusion in Planar Membranes Investigated by Fluorescence Correlation Spectroscopy. *Biochim. Biophys. Acta BBA - Biomembr.* **2010**, *1798* (7), 1377–1391.

(157) Jönsson, P.; Jonsson, M. P.; Tegenfeldt, J. O.; Höök, F. A Method Improving the Accuracy of Fluorescence Recovery after Photobleaching Analysis. *Biophys. J.* **2008**, *95*, 5334–5348.

(158) Schäfer, J.; Nehls, J.; Schön, M.; Mey, I.; Steinem, C. Leaflet-Dependent Distribution of PtdIns[4,5]P_2 in Supported Model Membranes. *Langmuir* **2020**, *36* (5), 1320–1328.

(159) Luchini, A.; Nzulumike, A. N. O.; Lind, T. K.; Nylander, T.; Barker, R.; Arleth, L.; Mortensen, K.; Cárdenas, M. Towards Biomimics of Cell Membranes: Structural Effect of Phosphatidylinositol Triphosphate (PIP_3) on a Lipid Bilayer. *Colloids Surf. B Biointerfaces* **2019**, *173*, 202–209.

(160) Schön, M.; Mey, I.; Steinem, C. Influence of Cross-Linkers on Ezrin-Bound Minimal Actin Cortices. *Prog. Biophys. Mol. Biol.* **2019**, *144*, 91–101.

(161) Drücker, P.; Grill, D.; Gerke, V.; Galla, H.-J. Formation and Characterization of Supported Lipid Bilayers Containing Phosphatidylinositol-4,5-Bisphosphate and Cholesterol as Functional Surfaces. *Langmuir* **2014**, *30*, 14877–14886.

(162) Hair, M. L.; Hertl, W. Reaction of Hexamethyldisilazane with Silica. *J. Phys. Chem.* **1971**, *75*, 2181–2185.

(163) *Physical Chemistry of Surfaces*, 6th ed.; Adamson, A. W., Gast, A. P., Eds.; Wiley: New York, **1997**.

(164) Zappone, B.; Rosenberg, K. J.; Israelachvili, J. Role of Nanometer Roughness on the Adhesion and Friction of a Rough Polymer Surface and a Molecularly Smooth Mica Surface. *Tribol. Lett.* **2007**, *26* (3), 191–201.

(165) Levins, J. M.; Vanderlick, T. K. Impact of Roughness on the Deformation and Adhesion of a Rough Metal and Smooth Mica in Contact. *J. Phys. Chem.* **1995**, *99* (14), 5067–5076.

(166) Wenzel, R. N. RESISTANCE OF SOLID SURFACES TO WETTING BY WATER. *Ind. Eng. Chem.* **1936**, *28* (8), 988–994.

(167) Bhushan, B.; Jung, Y. C. Micro- and Nanoscale Characterization of Hydrophobic and Hydrophilic Leaf Surfaces. *Nanotechnology* **2006**, *17* (11), 2758–2772.

(168) Nuzzo, R. G.; Allara, D. L. Adsorption of Bifunctional Organic Disulfides on Gold Surfaces. *J. Am. Chem. Soc.* **1983**, *105* (13), 4481–4483.

(169) Maoz, R.; Sagiv, J. On the Formation and Structure of Self-Assembling Monolayer I. A Comparative ATR-Wettability Study of Langmuir—Blodgett and Adsorbed Films on Flat Substrates and Glass Microbeads. *J. Colloid Interface Sci.* **1984**, *100* (2), 465–496.

(170) Braunger, J. A.; Kramer, C.; Morick, D.; Steinem, C. Solid Supported Membranes Doped with PIP_2: Influence of Ionic Strength and PH on Bilayer Formation and Membrane Organization. *Langmuir* **2013**, *29*, 14204–14213.

(171) Capel-Sanchez, M. C.; Barrio, L.; Campos-Martin, J. M.; Fierro, J. L. G. Silylation and Surface Properties of Chemically Grafted Hydrophobic Silica. *J. Colloid Interface Sci.* **2004**, *277* (1), 146–153.

(172) Fadeev, A. Y.; McCarthy, T. J. Self-Assembly Is Not the Only Reaction Possible between Alkyltrichlorosilanes and Surfaces: Monomolecular and Oligomeric Covalently Attached Layers of Dichloro- and Trichloroalkylsilanes on Silicon. *Langmuir* **2000**, *16* (18), 7268–7274.

(173) Huang, C.; Thompson, T. E. Properties of Lipid Bilayer Membranes Separating Two Aqueous Phases: Determination of Membrane Thickness. *J. Mol. Biol.* **1965**, *13* (1), 183–193.

(174) Ma, C.; Srinivasan, M. P.; Waring, A. J.; Lehrer, R. I.; Longo, M. L.; Stroeve, P. Supported Lipid Bilayers Lifted from the Substrate by Layer-by-Layer Polyion Cushions on Self-Assembled Monolayers. *Colloids Surf. B Biointerfaces* **2003**, *28* (4), 319–329.

(175) Tawa, K.; Morigaki, K. Substrate-Supported Phospholipid Membranes Studied by Surface Plasmon Resonance and Surface Plasmon Fluorescence Spectroscopy. *Biophys. J.* **2005**, *89* (4), 2750–2758.

(176) Boal, D. *Mechanics of the Cell*; Cambridge University Press: Cambridge, **2012**.

(177) Kučerka, N.; Nieh, M.-P.; Katsaras, J. Fluid Phase Lipid Areas and Bilayer Thicknesses of Commonly Used Phosphatidylcholines as a Function of Temperature. *Biochim. Biophys. Acta BBA - Biomembr.* **2011**, *1808* (11), 2761–2771.

(178) Rao, N. M.; Plant, A. L.; Silin, V.; Wight, S.; Hui, S. W. Characterization of Biomimetic Surfaces Formed from Cell Membranes. *Biophys. J.* **1997**, *73* (6), 3066–3077.

(179) Plant, A. L. Supported Hybrid Bilayer Membranes as Rugged Cell Membrane Mimics. *Langmuir* **1999**, *15* (15), 5128–5135.

(180) Wang, J.; Richards, D. A. Segregation of PIP_2 and PIP_3 into Distinct Nanoscale Regions within the Plasma Membrane. *Biol. Open* **2012**, *1* (9), 857–862.

(181) van den Bogaart, G.; Meyenberg, K.; Risselada, H. J.; Amin, H.; Willig, K. I.; Hubrich, B. E.; Dier, M.; Hell, S. W.; Grubmüller, H.; Diederichsen, U.; et al. Membrane Protein Sequestering by Ionic Protein–Lipid Interactions. *Nature* **2011**, *479* (7374), 552–555.

(182) Golebiewska, U.; Nyako, M.; Woturski, W.; Zaitseva, I.; McLaughlin, S. Diffusion Coefficient of Fluorescent Phosphatidylinositol 4,5-Bisphosphate in the Plasma Membrane of Cells. *Mol. Biol. Cell* **2008**, *19* (4), 1663–1669.

(183) Baumann, M. K.; Amstad, E.; Mashaghi, A.; Textor, M.; Reimhult, E. Characterization of Supported Lipid Bilayers Incorporating the Phosphoinositides Phosphatidylinositol 4,5-Biphosphate and Phosphoinositol-3,4,5-Triphosphate by Complementary Techniques. *Biointerphases* **2010**, *5*, 114–119.

(184) McLaughlin, S.; Murray, D. Plasma Membrane Phosphoinositide Organization by Protein Electrostatics. *Nature* **2005**, *438* (7068), 605–611.

(185) Berridge, M. J. Inositol Trisphosphate and Diacylglycerol as Second Messengers. *Biochem. J.* **1984**, *220*, 345–360.

(186) Fehon, R. G.; McClatchey, A. I.; Bretscher, A. Organizing the Cell Cortex: The Role of ERM Proteins. *Nat. Rev. Mol. Cell Biol.* **2010**, *11*, 276–287.
(187) Nöding, H.; Schön, M.; Reinermann, C.; Dörrer, N.; Kürschner, A.; Geil, B.; Mey, I.; Heussinger, C.; Janshoff, A.; Steinem, C. Rheology of Membrane-Attached Minimal Actin Cortices. *J. Phys. Chem. B* **2018**, *122*, 4537–4545.
(188) Hille, B. Diversity of Phosphoinositide Signaling. *Biochem. Mosc. Suppl. Ser. Membr. Cell Biol.* **2012**, *6*, 113–119.
(189) Itoh, T. Role of the ENTH Domain in Phosphatidylinositol-4,5-Bisphosphate Binding and Endocytosis. *Science* **2001**, *291*, 1047–1051.
(190) Lubart, Q.; Vitet, H.; Dalonneau, F.; Le Roy, A.; Kowalski, M.; Lourdin, M.; Ebel, C.; Weidenhaupt, M.; Picart, C. Role of Phosphorylation in Moesin Interactions with PIP_2-Containing Biomimetic Membranes. *Biophys. J.* **2018**, *114*, 98–112.
(191) Senju, Y.; Lappalainen, P. Regulation of Actin Dynamics by $PI(4,5)P_2$ in Cell Migration and Endocytosis. *Curr. Opin. Cell Biol.* **2019**, *56*, 7–13.
(192) Baba, T.; Toth, D. J.; Sengupta, N.; Kim, Y. J.; Balla, T. Phosphatidylinositol 4,5-bisphosphate Controls Rab7 and PLEKHM1 Membrane Cycling during Autophagosome–Lysosome Fusion. *EMBO J.* **2019**, *38*, e100312.
(193) Santagata, S. G-Protein Signaling Through Tubby Proteins. *Science* **2001**, *292*, 2041–2050.
(194) Misra, S.; Miller, G. J.; Hurley, J. H. Recognizing Phosphatidylinositol 3-Phosphate. *Cell* **2001**, *107*, 559–562.
(195) Wang, J.; Arbuzova, A.; Hangyás-Mihályné, G.; McLaughlin, S. The Effector Domain of Myristoylated Alanine-Rich C Kinase Substrate Binds Strongly to Phosphatidylinositol 4,5-Bisphosphate. *J. Biol. Chem.* **2001**, *276*, 5012–5019.
(196) Chandra, M.; Chin, Y. K.-Y.; Mas, C.; Feathers, J. R.; Paul, B.; Datta, S.; Chen, K.-E.; Jia, X.; Yang, Z.; Norwood, S. J.; et al. Classification of the Human phox Homology (PX) Domains Based on Their Phosphoinositide Binding Specificities. *Nat. Commun.* **2019**, *10*, 1528.
(197) Shi, X.; Li, X.; Kaliszewski, M. J.; Zhuang, X.; Smith, A. W. Tuning the Mobility Coupling of Quaternized Polyvinylpyridine and Anionic Phospholipids in Supported Lipid Bilayers. *Langmuir* **2015**, *31*, 1784–1791.
(198) Csúcs, G.; Ramsden, J. J. Interaction of Phospholipid Vesicles with Smooth Metal-Oxide Surfaces. *Biochim. Biophys. Acta BBA - Biomembr.* **1998**, *1369*, 61–70.
(199) Rapuano, R.; Carmona-Ribeiro, A. M. Physical Adsorption of Bilayer Membranes on Silica. *J. Colloid Interface Sci.* **1997**, *193*, 104–111.
(200) Pereira, E. M. A.; Petri, D. F. S.; Carmona-Ribeiro, A. M. Adsorption of Cationic Lipid Bilayer onto Flat Silicon Wafers: Effect of Ion Nature and Concentration. *J. Phys. Chem. B* **2006**, *110*, 10070–10074.
(201) Rapuano, R.; Carmona-Ribeiro, A. M. Supported Bilayers On Silica. *J. Colloid Interface Sci.* **2000**, *226*, 299–307.
(202) Biswas, K. H.; Jackman, J. A.; Park, J. H.; Groves, J. T.; Cho, N.-J. Interfacial Forces Dictate the Pathway of Phospholipid Vesicle Adsorption onto Silicon Dioxide Surfaces. *Langmuir* **2018**, *34*, 1775–1782.
(203) Reimhult, E.; Zäch, M.; Höök, F.; Kasemo, B. A Multitechnique Study of Liposome Adsorption on Au and Lipid Bilayer Formation on SiO_2. *Langmuir* **2006**, *22*, 3313–3319.

(204) Levental, I.; Christian, D. A.; Wang, Y.-H.; Madara, J. J.; Discher, D. E.; Janmey, P. A. Calcium-Dependent Lateral Organization in Phosphatidylinositol 4,5-Bisphosphate (PIP_2)- and Cholesterol-Containing Monolayers. *Biochemistry* **2009**, *48*, 8241–8248.

(205) Carvalho, K.; Ramos, L.; Roy, C.; Picart, C. Giant Unilamellar Vesicles Containing Phosphatidylinositol(4,5)Bisphosphate: Characterization and Functionality. *Biophys. J.* **2008**, *95*, 4348–4360.

(206) Bosk, S. *Dynamische Strukturen Am Zellcortex: Aktivierbarkeit Und Akkumulation von Ezrin in Abhängigkeit von PIP_2: PhD Thesis*; University of Göttingen, **2011**.

(207) Herrig, A. *Wechselwirkung von Ezrin Mit PIP_2-Haltigen Artifiziellen Membransystemen Und Mit F-Aktin: PhD Thesis*; University of Regensburg, **2007**.

(208) Kramer, C. *Verknüpfung Zwischen Plasmamembran Und Zytoskelett: Charakterisierung Der Organisation von Ezrin Und F-Aktin an Artifiziellen Lipidmembranen: PhD Thesis*; University of Göttingen, **2016**.

(209) Kurien, B.; Scofield, R. Western Blotting. *Methods* **2006**, *38* (4), 283–293.

(210) Meloni, G.; Knipp, M.; Vašák, M. Detection of Neuronal Growth Inhibitory Factor (Metallothionein-3) in Polyacrylamide Gels and by Western Blot Analysis. *J. Biochem. Biophys. Methods* **2005**, *64* (1), 76–81.

(211) Gasteiger, E. ExPASy: The Proteomics Server for in-Depth Protein Knowledge and Analysis. *Nucleic Acids Res.* **2003**, *31* (13), 3784–3788.

(212) Gould, K. L.; Cooper, J. A.; Bretscher, A.; Hunter, T. The Protein-Tyrosine Kinase Substrate, p81, Is Homologous to a Chicken Microvillar Core Protein. *J. Cell Biol.* **1986**, *102* (2), 660–669.

(213) Ludolphs, M. *Spezifität Der Wechselwirkung von Collybistin 2 Mit Phosphatidylinositolphosphaten: Einfluss Der Verschiedenen Proteindomänen: PhD Thesis*; University of Göttingen, **2015**.

(214) Naumann, R.; Schmidt, E. K.; Jonczyk, A.; Fendler, K.; Kadenbach, B.; Liebermann, T.; Offenhäusser, A.; Knoll, W. The Peptide-Tethered Lipid Membrane as a Biomimetic System to Incorporate Cytochrome c Oxidase in a Functionally Active Form. *Biosens. Bioelectron.* **1999**, *14* (7), 651–662.

(215) Benesch, J.; Askendal, A.; Tengvall, P. The Determination of Thickness and Surface Mass Density of Mesothick Immunoprecipitate Layers by Null Ellipsometry and Protein ^{125}Iodine Labeling. *J. Colloid Interface Sci.* **2002**, *249* (1), 84–90.

(216) Bosk, S.; Braunger, J. A.; Gerke, V.; Steinem, C. Activation of F-Actin Binding Capacity of Ezrin: Synergism of PIP_2 Interaction and Phosphorylation. *Biophys. J.* **2011**, *100* (7), 1708–1717.

(217) Shabardina, V.; Kramer, C.; Gerdes, B.; Braunger, J.; Cordes, A.; Schäfer, J.; Mey, I.; Grill, D.; Gerke, V.; Steinem, C. Mode of Ezrin-Membrane Interaction as a Function of PIP_2 Binding and Pseudophosphorylation. *Biophys. J.* **2016**, *110*, 2710–2719.

(218) Pace, S.; Seantier, B.; Belamie, E.; Lautrédou, N.; Sailor, M. J.; Milhiet, P.-E.; Cunin, F. Characterization of Phospholipid Bilayer Formation on a Thin Film of Porous SiO_2 by Reflective Interferometric Fourier Transform Spectroscopy (RIFTS). *Langmuir* **2012**, *28* (17), 6960–6969.

(219) Seantier, B.; Breffa, C.; Félix, O.; Decher, G. *In Situ* Investigations of the Formation of Mixed Supported Lipid Bilayers Close to the Phase Transition Temperature. *Nano Lett.* **2004**, *4* (1), 5–10.

(220) Seantier, B.; Breffa, C.; Félix, O.; Decher, G. Dissipation-Enhanced Quartz Crystal Microbalance Studies on the Experimental Parameters Controlling the Formation of Supported Lipid Bilayers. *J. Phys. Chem. B* **2005**, *109* (46), 21755–21765.

(221) Lind, T. K.; Cárdenas, M.; Wacklin, H. P. Formation of Supported Lipid Bilayers by Vesicle Fusion: Effect of Deposition Temperature. *Langmuir* **2014**, *30* (25), 7259–7263.

(222) Harishchandra, R. K.; Neumann, B. M.; Gericke, A.; Ross, A. H. Biophysical Methods for the Characterization of PTEN/Lipid Bilayer Interactions. *Methods* **2015**, *77–78*, 125–135.

(223) Drücker, P.; Pejic, M.; Grill, D.; Galla, H.-J.; Gerke, V. Cooperative Binding of Annexin A2 to Cholesterol- and Phosphatidylinositol-4,5-Bisphosphate-Containing Bilayers. *Biophys. J.* **2014**, *107* (9), 2070–2081.

(224) Richter, R. P.; Maury, N.; Brisson, A. R. On the Effect of the Solid Support on the Interleaflet Distribution of Lipids in Supported Lipid Bilayers. *Langmuir* **2005**, *21*, 299–304.

(225) Reviakine, I.; Brisson, A. Formation of Supported Phospholipid Bilayers from Unilamellar Vesicles Investigated by Atomic Force Microscopy. *Langmuir* **2000**, *16*, 1806–1815.

(226) Andrecka, J.; Spillane, K. M.; Ortega-Arroyo, J.; Kukura, P. Direct Observation and Control of Supported Lipid Bilayer Formation with Interferometric Scattering Microscopy. *ACS Nano* **2013**, *7*, 10662–10670.

(227) van Paridon, P. A.; de Kruijff, B.; Ouwerkerk, R.; Wirtz, K. W. A. Polyphosphoinositides Undergo Charge Neutralization in the Physiological PH Range: A ^{31}P-NMR Study. *Biochim. Biophys. Acta BBA - Lipids Lipid Metab.* **1986**, *877*, 216–219.

(228) Parks, G. A. The Isoelectric Points of Solid Oxides, Solid Hydroxides, and Aqueous Hydroxo Complex Systems. *Chem. Rev.* **1965**, *65*, 177–198.

(229) Tadros, Th. F.; Lyklema, J. Adsorption of Potential-Determining Ions at the Silica-Aqueous Electrolyte Interface and the Role of Some Cations. *J. Electroanal. Chem. Interfacial Electrochem.* **1968**, *17* (3–4), 267–275.

(230) Graber, Z. T.; Jiang, Z.; Gericke, A.; Kooijman, E. E. Phosphatidylinositol-4,5-Bisphosphate Ionization and Domain Formation in the Presence of Lipids with Hydrogen Bond Donor Capabilities. *Chem. Phys. Lipids* **2012**, *165* (6), 696–704.

(231) Graber, Z. T.; Gericke, A.; Kooijman, E. E. Phosphatidylinositol-4,5-Bisphosphate Ionization in the Presence of Cholesterol, Calcium or Magnesium Ions. *Chem. Phys. Lipids* **2014**, *182*, 62–72.

(232) Nagle, J. F.; Tristram-Nagle, S. Structure of Lipid Bilayers. *Biochim. Biophys. Acta BBA - Rev. Biomembr.* **2000**, *1469*, 159–195.

(233) Ohki, S.; Kurland, R. Surface Potential of Phosphatidylserine Monolayers II. Divalent and Monovalent Ion Binding. *Biochim. Biophys. Acta BBA - Biomembr.* **1981**, *645*, 170–176.

(234) Sun, W.-J.; Suter, R. M.; Knewtson, M. A.; Worthington, C. R.; Tristram-Nagle, S.; Zhang, R.; Nagle, J. F. Order and Disorder in Fully Hydrated Unoriented Bilayers of Gel-Phase Dipalmitoylphosphatidylcholine. *Phys. Rev. E* **1994**, *49*, 4665–4676.

(235) Li, Z.; Venable, R. M.; Rogers, L. A.; Murray, D.; Pastor, R. W. Molecular Dynamics Simulations of PIP_2 and PIP_3 in Lipid Bilayers: Determination of Ring Orientation, and the Effects of Surface Roughness on a Poisson-Boltzmann Description. *Biophys. J.* **2009**, *97*, 155–163.

(236) Chiantia, S.; Klymchenko, A. S.; London, E. A Novel Leaflet-Selective Fluorescence Labeling Technique Reveals Differences between Inner and Outer Leaflets at High Bilayer Curvature. *Biochim. Biophys. Acta BBA - Biomembr.* **2012**, *1818* (5), 1284–1290.

(237) Sakuma, Y.; Urakami, N.; Taniguchi, T.; Imai, M. Asymmetric Distribution of Cone-Shaped Lipids in a Highly Curved Bilayer Revealed by a Small Angle Neutron Scattering Technique. *J. Phys. Condens. Matter* **2011**, *23* (28), 284104.

(238) Brian, A. A.; McConnell, H. M. Allogeneic Stimulation of Cytotoxic T Cells by Supported Planar Membranes. *Proc. Natl. Acad. Sci. U. S. A.* **1984**, *81* (19), 6159–6163.

(239) McConnell, H. M.; Watts, T. H.; Weis, R. M.; Brian, A. A. Supported Planar Membranes in Studies of Cell-Cell Recognition in the Immune System. *Biochim. Biophys. Acta BBA - Rev. Biomembr.* **1986**, *864* (1), 95–106.

(240) Jass, J.; Tjärnhage, T.; Puu, G. From Liposomes to Supported, Planar Bilayer Structures on Hydrophilic and Hydrophobic Surfaces: An Atomic Force Microscopy Study. *Biophys. J.* **2000**, *79* (6), 3153–3163.

(241) Contino, P. B.; Hasselbacher, C. A.; Ross, J. B.; Nemerson, Y. Use of an Oriented Transmembrane Protein to Probe the Assembly of a Supported Phospholipid Bilayer. *Biophys. J.* **1994**, *67* (3), 1113–1116.

(242) Salafsky, J.; Groves, J. T.; Boxer, S. G. Architecture and Function of Membrane Proteins in Planar Supported Bilayers: A Study with Photosynthetic Reaction Centers. *Biochemistry* **1996**, *35* (47), 14773–14781.

(243) Reimhult, E.; Kasemo, B.; Höök, F. Rupture Pathway of Phosphatidylcholine Liposomes on Silicon Dioxide. *Int. J. Mol. Sci.* **2009**, *10*, 1683–1696.

(244) Devaux, P. F.; Herrmann, A.; Ohlwein, N.; Kozlov, M. M. How Lipid Flippases Can Modulate Membrane Structure. *Biochim. Biophys. Acta BBA - Biomembr.* **2008**, *1778* (7–8), 1591–1600.

(245) Herrig, A.; Janke, M.; Austermann, J.; Gerke, V.; Janshoff, A.; Steinem, C. Cooperative Adsorption of Ezrin on PIP_2 -Containing Membranes. *Biochemistry* **2006**, *45* (43), 13025–13034.

(246) Janke, M.; Herrig, A.; Austermann, J.; Gerke, V.; Steinem, C.; Janshoff, A. Actin Binding of Ezrin Is Activated by Specific Recognition of PIP_2-Functionalized Lipid Bilayers. *Biochemistry* **2008**, *47* (12), 3762–3769.

(247) Jiang, Z.; Redfern, R. E.; Isler, Y.; Ross, A. H.; Gericke, A. Cholesterol Stabilizes Fluid Phosphoinositide Domains. *Chem. Phys. Lipids* **2014**, *182*, 52–61.

(248) Wu, E. L.; Qi, Y.; Song, K. C.; Klauda, J. B.; Im, W. Preferred Orientations of Phosphoinositides in Bilayers and Their Implications in Protein Recognition Mechanisms. *J. Phys. Chem. B* **2014**, *118* (16), 4315–4325.

(249) Kooijman, E. E.; King, K. E.; Gangoda, M.; Gericke, A. Ionization Properties of Phosphatidylinositol Polyphosphates in Mixed Model Membranes. *Biochemistry* **2009**, *48* (40), 9360–9371.

(250) Kavran, J. M.; Klein, D. E.; Lee, A.; Falasca, M.; Isakoff, S. J.; Skolnik, E. Y.; Lemmon, M. A. Specificity and Promiscuity in Phosphoinositide Binding by Pleckstrin Homology Domains. *J. Biol. Chem.* **1998**, *273* (46), 30497–30508.

(251) Hines, R. M.; Maric, H. M.; Hines, D. J.; Modgil, A.; Panzanelli, P.; Nakamura, Y.; Nathanson, A. J.; Cross, A.; Deeb, T.; Brandon, N. J.; et al. Developmental Seizures and Mortality Result from Reducing $GABA_A$ Receptor α2-Subunit Interaction with Collybistin. *Nat. Commun.* **2018**, *9* (1).

(252) Papadopoulos, T.; Schemm, R.; Grubmüller, H.; Brose, N. Lipid Binding Defects and Perturbed Synaptogenic Activity of a Collybistin R290H Mutant That Causes Epilepsy and Intellectual Disability. *J. Biol. Chem.* **2015**, *290* (13), 8256–8270.

(253) Long, P.; May, M. M.; James, V. M.; Grannò, S.; Johnson, J. P.; Tarpey, P.; Stevenson, R. E.; Harvey, K.; Schwartz, C. E.; Harvey, R. J. Missense Mutation R338W in ARHGEF9 in a Family with X-Linked Intellectual Disability with Variable Macrocephaly and Macro-Orchidism. *Front. Mol. Neurosci.* **2016**, *8*.

(254) Haslam, R. J.; Koide, H. B.; Hemmings, B. A. Pleckstrin Domain Homology. *Nature* **1993**, *363* (6427), 309–310.

(255) Mayer, B. J.; Ren, R.; Clark, K. L.; Baltimore, D. A Putative Modular Domain Present in Diverse Signaling Proteins. *Cell* **1993**, *73* (4), 629–630.

(256) Rebecchi, M. J.; Scarlata, S. PLECKSTRIN HOMOLOGY DOMAINS: A Common Fold with Diverse Functions. *Annu. Rev. Biophys. Biomol. Struct.* **1998**, *27* (1), 503–528.

(257) Lemmon, M. A.; Ferguson, K. M.; O'Brien, R.; Sigler, P. B.; Schlessinger, J. Specific and High-Affinity Binding of Inositol Phosphates to an Isolated Pleckstrin Homology Domain. *Proc. Natl. Acad. Sci.* **1995**, *92* (23), 10472–10476.

(258) Garcia, P.; Gupta, R.; Shah, S.; Morris, A. J.; Rudge, S. A.; Scarlata, S.; Petrova, V.; McLaughlin, S.; Rebecchi, M. J. The Pleckstrin Homology Domain of Phospholipase C-δ_1 Binds with High Affinity to Phosphatidylinositol 4,5-Bisphosphate in Bilayer Membranes. *Biochemistry* **1995**, *34* (49), 16228–16234.

(259) Yu, J. W.; Mendrola, J. M.; Audhya, A.; Singh, S.; Keleti, D.; DeWald, D. B.; Murray, D.; Emr, S. D.; Lemmon, M. A. Genome-Wide Analysis of Membrane Targeting by *S. Cerevisiae* Pleckstrin Homology Domains. *Mol. Cell* **2004**, *13* (5), 677–688.

(260) Ferguson, K. M.; Kavran, J. M.; Sankaran, V. G.; Fournier, E.; Isakoff, S. J.; Skolnik, E. Y.; Lemmon, M. A. Structural Basis for Discrimination of 3-Phosphoinositides by Pleckstrin Homology Domains. *Mol. Cell* **2000**, *6* (2), 373–384.

(261) Lietzke, S. E.; Bose, S.; Cronin, T.; Klarlund, J.; Chawla, A.; Czech, M. P.; Lambright, D. G. Structural Basis of 3-Phosphoinositide Recognition by Pleckstrin Homology Domains. *Mol. Cell* **2000**, *6* (2), 385–394.

(262) Snyder, J. T.; Rossman, K. L.; Baumeister, M. A.; Pruitt, W. M.; Siderovski, D. P.; Der, C. J.; Lemmon, M. A.; Sondek, J. Quantitative Analysis of the Effect of Phosphoinositide Interactions on the Function of Dbl Family Proteins. *J. Biol. Chem.* **2001**, *276* (49), 45868–45875.

(263) Teo, H.; Gill, D. J.; Sun, J.; Perisic, O.; Veprintsev, D. B.; Vallis, Y.; Emr, S. D.; Williams, R. L. ESCRT-I Core and ESCRT-II GLUE Domain Structures Reveal Role for GLUE in Linking to ESCRT-I and Membranes. *Cell* **2006**, *125* (1), 99–111.

(264) Baraldi, E.; Carugo, K. D.; Hyvönen, M.; Surdo, P. L.; Riley, A. M.; Potter, B. V.; O'Brien, R.; Ladbury, J. E.; Saraste, M. Structure of the PH Domain from Bruton's Tyrosine Kinase in Complex with Inositol 1,3,4,5-Tetrakisphosphate. *Structure* **1999**, *7* (4), 449–460.

(265) Essen, L.-O.; Perisic, O.; Katan, M.; Wu, Y.; Roberts, M. F.; Williams, R. L. Structural Mapping of the Catalytic Mechanism for a Mammalian Phosphoinositide-Specific Phospholipase C. *Biochemistry* **1997**, *36* (7), 1704–1718.

(266) Chiou, T.-T.; Long, P.; Schumann-Gillett, A.; Kanamarlapudi, V.; Haas, S. A.; Harvey, K.; O'Mara, M. L.; De Blas, A. L.; Kalscheuer, V. M.; Harvey, R. J. Mutation p.R356Q in the Collybistin Phosphoinositide Binding Site Is Associated With Mild Intellectual Disability. *Front. Mol. Neurosci.* **2019**, *12*.

(267) Hamann, M. J.; Lubking, C. M.; Luchini, D. N.; Billadeau, D. D. Asef2 Functions as a Cdc42 Exchange Factor and Is Stimulated by the Release of an Autoinhibitory Module from a Concealed C-Terminal Activation Element. *Mol. Cell. Biol.* **2007**, *27* (4), 1380–1393.

(268) Mitin, N.; Betts, L.; Yohe, M. E.; Der, C. J.; Sondek, J.; Rossman, K. L. Release of Autoinhibition of ASEF by APC Leads to CDC42 Activation and Tumor Suppression. *Nat. Struct. Mol. Biol.* **2007**, *14* (9), 814–823.

(269) Irie, M. Binding of Neuroligins to PSD-95. *Science* **1997**, *277* (5331), 1511–1515.

(270) Iida, J.; Hirabayashi, S.; Sato, Y.; Hata, Y. Synaptic Scaffolding Molecule Is Involved in the Synaptic Clustering of Neuroligin. *Mol. Cell. Neurosci.* **2004**, *27* (4), 497–508.

(271) Sander, B. *Structural and Biochemical Characterization of Gephyrin and Various Gephyrin-Ligand Complexes: PhD Thesis*; University of Würzburg, 2014.

(272) Grabski, A. C.; Burgess, R. R. Preparation of Protein Samples for SDS-Polyacrylamide Gel Electrophoresis: Procedures and Tips. *Innovations* **2001**, *13*, 11–13.

A Appendix

A.1 List of Figures

A.2 List of Schemes

A.3 List of Tables

A.4 Amino acid Sequences of employed Proteins

A.4.1 *N*-terminal domain of Ezrin (N-ERMAD)

```
MGSSH HHHHH SSGLV PRGSH MASMT GGQQM GRGSE FMPKP INVRV TTMDA    50
ELEFA IQPNT TGKQL FDQVV KTIGL REVWY FGLHY VDNKG FPTWL KLDKK   100
VSAQE VRKEN PLQFK FRAKF YPEDV AEELI QDITQ KLFFL QVKEG ILSDE   150
IYCPP ETAVL LGSYA VQAKF GDYNK EVHKS GYLSS ERLIP QRVMD QHKLT   200
RDQWE DRIQV WHAEH RGMLK DNAML EYLKI AQDLE MYGIN YFEIK NKKGT   250
DLWLG VDALG LNIYE KDDKL TPKIG FPWSE IRNIS FNDKK FVIKP IDKKA   300
PDFVF YAPRL RINKR ILQLC MGNHE LYMRR RK
```

A.4.2 Collybistin 2 wild-type ($CB2_{SH3}$)

```
MQWIR GGSGM LITGD SIVSA EAVWD HVTMA NRELA FKAGD VIKVL DASNK    50
DWWWG QIDDE EGWFP ASFVR LWVNQ EDGVE EGPSD VQNGH LDPNS DCLCL   100
GRPLQ NRDQM RANVI NEIMS TERHY IKHLK DICEG YLKQC RKRRD MFSDE   150
QLKVI FGNIE DIYRF QMGFV RDLEK QYNND DPHLS EIGPC FLEHQ DGFWI   200
YSEYC NNHLD ACMEL SKLMK DSRYQ HFFEA CRLLQ QMIDI AIDGF LLTPV   250
QKICK YPLQL AELLK YTAQD HSDYR YVAAA LAVMR NVTQQ INERK RRLEN   300
IDKIA QWQAS VLDWE GDDIL DRSSE LIYTG EMAWI YQPYG RNQQR VFFLF   350
DHQMV LCKKD LIRRD ILYYK GRIDM DKYEV IDIED GRDDD FNVSM KNAFK   400
LHNKE TEEVH LFFAK KLEEK IRWLR AFREE RKMVQ EDEKI GFEIS ENQKR   450
QAAMT VRKAS KQKVT QRKWH Y
```

A.4.3 Collybistin 2 active mutant ($CB2_{SH3/W24A-E262A}$)

```
MQWIR GGSGM LITGD SIVSA EAVAD HVTMA NRELA FKAGD VIKVL DASNK    50
DWWWG QIDDE EGWFP ASFVR LWVNQ EDGVE EGPSD VQNGH LDPNS DCLCL   100
GRPLQ NRDQM RANVI NEIMS TERHY IKHLK DICEG YLKQC RKRRD MFSDE   150
QLKVI FGNIE DIYRF QMGFV RDLEK QYNND DPHLS EIGPC FLEHQ DGFWI   200
```

```
YSEYC NNHLD ACMEL SKLMK DSRYQ HFFEA CRLLQ QMIDI AIDGF LLTPV   250
QKICK YPLQL AALLK YTAQD HSDYR YVAAA LAVMR NVTQQ INERK RRLEN   300
IDKIA QWQAS VLDWE GDDIL DRSSE LIYTG EMAWI YQPYG RNQQR VFFLF   350
DHQMV LCKKD LIRRD ILYYK GRIDM DKYEV IDIED GRDDD FNVSM KNAFK   400
LHNKE TEEVH LFFAK KLEEK IRWLR AFREE RKMVQ EDEKI GFEIS ENQKR   450
QAAMT VRKAS KQKVT QRKWH Y
```

A.4.4 *C*-terminal PH domain of Collybistin 2 ($CB2_{PH}$)

```
MNIDK IAQWQ ASVLD WEGDD ILDRS SELIY TGEMA WIYQP YGRNQ QRVFF    50
LFDHQ MVLCK KDLIR RDILY YKGRI DMDKY EVIDI EDGRD DDFNV SMKNA   100
FKLHN KETEE VHLFF AKKLE EKIRW LRAFR EERKM VQEDE KIGFE ISENQ   150
KRQAA MTVRK ASKQK VTQRK WHY
```

A.4.5 Intracellular domain of Neuroligin 2 (*cyt*NL2)

```
MKHHH HHHPM SDYDI PTTEN LYFQG AMAYK RDRRQ ELRCR RLSPP GGSGS    50
GVPGG GPLLP TAGRE LPPEE ELVSL QLKRG GGVGA DPAEA LRPAC PPDYT   100
LALRR APDDV PLLAP GALTL LPSGL GPPPP PPPPS LHPFG PFPPP PPTAT   150
SHNNT LPHPH STTRV
```

A.5 Abbreviations and Symbols

µm	Micrometre
Å	Angström
AA	acrylamide
AFM	Atomic force microscopy
ANOVA	Analysis of Variance
APS	Ammonium peroxydisulfate
Asef	APC-stimulated guanine nucleotide exchange factors
BCA	bicinchoninic acid
Bis-AA	N,N´-methylenebisacrylamide
BSA	Bovine serum albumin
Btk	Bruton's tyrosine kinase
Ca^{2+}	Divalent Calcium cation
CAM	Cell adhesion molecule
CB	Collybistin

CBD	Chitin binding domain
CD	circular dichroism
Cdc42	cell division control protein 42 homologue
CLSM	Confocal laser scanning microscope
CMC	Critical micelle concentration
CNS	Central nervous system
CV	Column volume
D	Diffusion coefficient
d	Physical thickness / height
DAG	Diacylglycerol
DGS	1,2-dioleoyl-*sn*-glycero-3-{[*N*-(5-amino-1-carboxypentyl)iminodiacetic acid]succinyl} nickel salt
DH	Dbl homology
DHPE	1,2-dihexadecanoyl-*sn*-glycero-3-phosphoethanolamine
DRIFTS	diffuse reflectance infrared Fourier transform
DTT	dithiothreitol
E	elution fraction
ECL	enhanced chemiluminescence
EDTA	Ethylenediaminetetraacetic acid
ESCRT-II	endosomal sorting complexes required for transport II
F	force
FRAP	Fluorescence recovery after photobleaching
FT	Flow through
GABA	γ-amino butyric acid
$GABA_AR$	γ-amino butyric acid receptor type A
GABAR	γ-amino butyric acid receptor
GAP	GTPase activating protein
GDP	Guanosine 5´-diphosphate
GEF	Guanine nucleotide exchange factor
GLUE	GRAM-like ubiquitin-binding in EAP45

GTP	Guanosine 5′-triphosphate
h	Hour(s)
H_2O	Water
H_2O_2	Hydrogen peroxide
HCl	hydrogen chloride
HEK	human embryonic kidney
HEPES	4-(2-hydroxyethyl)-1-piperazineethanesulfonic acid
His	histidine
His_6	Hexa-histidine
His-*cyt*NL2	His-tagged intracellular domain of neuroligin 2
HMDS	1,1,1-trimethyl-N-(trimethylsilyl)silanamine
hPEM-2	Human homolog of posterior end mark 2
HRP	horse radish peroxidase
Hz	Hertz
I	Intensity
icd	intracellular domain
IEC	Ion exchange chromatography
IMAC	Immobilised metal ion affinity chromatography
$Ins[1,3]P_2$	inositol 1,3-bisphosphate
IP_3	Inositol triphosphate
iSCAT	Interferometric scattering microscopy
ITC	isothermal titration calorimetry
k	Spring constant
KCl	Potassium chloride
K_D	Dissociation constant
kDa	Kilodalton
LB	Lysogeny broth
LED	light-emitting diode
LUV	large unilamellar vesicle
MAC	minimal actin cortex
MD	Molecular Dynamics

$MgCl_2$	Magnesium chloride
$MgSO_4$	Magnesium sulfate
min	Minute(s)
mm	Millimetre
N	Newton
n	Refractive index
Na	Sodium
NaCl	Sodium chloride
NaN_3	Sodium azide
NH_3	Ammonia
Ni^{2+}	Divalent Nickel cation
NL	Neuroligin
nm	Nanometre
NMR	nuclear magnetic resonance
NR	Neutron Reflectometry
NTA	Nitrilotriacetic acid
Osh	oxysterol-binding protein homologue
OT	Optical thickness
PEM-2	posterior end mark 2
PH	Pleckstrin homology
PI	Phosphatidylinositol
PLC-δ_1	phospholipase C-δ_1
PMSF	Phenylmethylsulfonyl fluoride
PNS	Peripheral nervous system
POPS	1-palmitoyl-2-oleoyl-*sn*-glycero-3-phospho-l-serine
POPS	1-Palmitoyl-2-oleoyl-*sn*-glycero-3-phosphatidylserine
PSD	Post synaptic density
PSD	Position-sensitive diode
PtdIns[3,4,5]P_3	Phosphatidylinositol 3,4,5-trisphosphate
PtdIns[3]P	Phosphatidylinositol 3-phosphate

PtdIns[4,5]P_2	Phosphatidylinositol 4,5-bisphosphate
PtdInsP	Phosphatidylinositol phosphate
QCM	Quartz crystal microbalance
QCM-D	Quartz crystal microbalance with Dissipation monitoring
Rho	rat sarcoma homologue
RIfS	Reflectometric interference spectroscopy
ROI	Region of interest
rpm	Rounds per minute
rpm	Rounds per minute
s	Optical path distance
s	Second(s)
SAM	Self-assembled monolayer
SEM	Standard error of the mean
SH3	src homology 3
SHM	Solid-supported hybrid membrane
Si	Silicon
SiO_2	Silicon dioxide
SLB	Solid-supported lipid bilayer
SN	Supernatant
SOC	super optimal broth with catabolite repression
SPR	Surface plasmon resonance
STM	Scanning tunnelling microscope
SUV	Small unilamellar vesicle
t	Time
T	temperature
TEMED	Tetramethyl ethylene diamine
T_M	Main phase transition temperature
TMSCl	trimethylsilyl chloride
TRIS	2-Amino-2-(hydroxymethyl)propane-1,3-diol
TxR	Texas Red®

UV/VIS	Ultraviolet/Visible
V	Volume
V	Volt
Vps36	Vacuolar protein-sorting-associated protein 36
WB	Western blot
WF	Washing fraction
α	Angle of incidence
β	Angle of refraction
γ_0	Mobile fraction
θ	Contact angle
λ	Wavelength
σ	Standard deviation
φ	Phase
χ	Molar fraction

A.6 Chemicals and consumables

Acetic acid	Thermo Fischer Scientific GmbH, Dreieich, Germany
Acrylamid(AA)-mix	Sigma-Aldrich, Taufkirchen, Germany
Agar-agar	Merck KGaA, Darmstadt, Germany
Amber glasses	Ochs GmbH, Göttingen, Germany
Amicon® Ultra	Merck Chemicals GmbH, Darmstadt, Germany
Ampicillin	Sigma-Aldrich, Taufkirchen, Germany
Anti CB Monoclonal mouse purified IgG	Synaptic Systems GmbH, Göttingen, Germany
Anti NL Monoclonal mouse purified IgG	Synaptic Systems GmbH, Göttingen, Germany
Anti-6X His tag®	Abcam, Cambridge, UK
APS	Sigma-Aldrich, Taufkirchen, Germany
Argon	Air Liquide Deutschland GmbH, Düsseldorf, Germany
BODIPY®-TMR PtdIns[3,4,5]P_3	Echelon Biosciences Inc., Salt Lake City, USA
BODIPY®-TMR PtdIns[3]P	Echelon Biosciences Inc., Salt Lake City, USA

BODIPY®-TMR PtdIns[4,5]P_2	Echelon Biosciences Inc., Salt Lake City, USA
Bromophenol blue	VWR International, Darmstadt, Germany
Cantilever	NanoWorld AG, Neuchâtel, Switzerland
Cantilever MSNL-10, MLCT	Bruker AFM Probes, Camarillo, USA
Chitin resin	New England BioLabs Inc., Ipswich, USA
Chloramphenicol	Sigma-Aldrich, Taufkirchen, Germany
Chloroform	VWR International, Darmstadt, Germany
Coomassie Brilliant Blue G-250	Carl Roth GmbH, Karlsruhe, Germany
Cuvettes	Sarstedt, Nürnbrecht, Germany
DGS	Avanti Polar Lipids, Alabaster, USA
Dialysis tubes Visking	Carl Roth GmbH, Karlsruhe, Germany
DTT	Sigma-Aldrich, Taufkirchen, Germany
E. coli BL21(DE3)	Thermo Fischer Scientific GmbH, Dreieich, Germany
E. coli BL21(DE3) Rosetta	VWR International, Darmstadt, Germany
EDTA	Carl Roth GmbH, Karlsruhe, Germany
Eppendorf cups	Eppendorf, Hamburg, Germany
Eppendorf pipettes	Eppendorf, Hamburg, Germany
Ethanol p.a.	VWR International, Darmstadt, Germany
Glycerol	Merck Chemicals GmbH, Darmstadt, Germany
Glycine	Merck Chemicals GmbH, Darmstadt, Germany
H_2O_2 (30 %)	Merck Chemicals GmbH, Darmstadt, Germany
Hellmanex® III	Hellma Materials GmbH, Jena, Germany
HEPES	Carl Roth GmbH, Karlsruhe, Germany
HMDS	VWR International, Darmstadt, Germany
HRP Goat Anti-Mouse Ig	Becton Dickinson Inc., Franklin Lakes, USA
Imidazole	Sigma-Aldrich, Taufkirchen, Germany
IPTG	Sigma-Aldrich, Taufkirchen, Germany
Isopropyl alcohol	Merck Chemicals GmbH, Darmstadt, Germany
Kanamycin	Sigma-Aldrich, Taufkirchen, Germany
KCl	Merck Chemicals GmbH, Darmstadt, Germany
Luminol (≥97 %)	Sigma-Aldrich, Taufkirchen, Germany

Measuring chambers	Custom-made, University workshop, Göttingen, Germany
Methanol	Carl Roth GmbH, Karlsruhe, Germany
Mucasol®	Merck Chemicals GmbH, Darmstadt, Germany
Na-citrate	Merck Chemicals GmbH, Darmstadt, Germany
NaCl	VWR International, Darmstadt, Germany
NaN_3	Merck Chemicals GmbH, Darmstadt, Germany
NH_3 (25 %)	VWR International, Darmstadt, Germany
Nitrocellulose membrane	Bio-Rad Laboratories Inc., Hercules, USA
Parafilm®	American National Can, Chicago, USA
p-Coumaric acid	Sigma-Aldrich, Taufkirchen, Germany
Petri dishes	Sarstedt, Nürnbrecht, Germany
Pipette tips	Sarstedt, Nürnbrecht, Germany
Ponceau S	Sigma-Aldrich, Taufkirchen, Germany
POPC	Avanti Polar Lipids, Alabaster, USA
POPS	Avanti Polar Lipids, Alabaster, USA
Protino®, NTA(Ni^{2+}) agarose	Macherey-Nagel GmbH & Co. KG, Düren, Germany
PtdIns[3,4,5]P_3	Echelon Biosciences Inc., Salt Lake City, USA
PtdIns[3]P	Echelon Biosciences Inc., Salt Lake City, USA
PtdIns[4,5]P_2	Echelon Biosciences Inc., Salt Lake City, USA
Pump tubings	Ismatec, Wertheim-Mondfeld, Germany
QIAprep Spin Miniprep Kit	Qiagen GmbH, Hilden, Germany
SDS	Merck Chemicals GmbH, Darmstadt, Germany
SiO_2 substrates	Silicon Materials Inc., Glenshaw, USA
TEMED	Sigma-Aldrich, Taufkirchen, Germany
Test tubes	VWR International, Darmstadt, Germany
TEV protease	Sigma-Aldrich, Taufkirchen, Germany
TRIS	Carl Roth GmbH, Karlsruhe, Germany
Tryptone	Carl Roth GmbH, Karlsruhe, Germany
Tween-20	Carl Roth GmbH, Karlsruhe, Germany
TxR-DHPE	Sigma-Aldrich, Taufkirchen, Germany

Ultrapure H_2O	Millipore, Billerica, USA
Vivaspin® 500	Sartorius GmbH, Göttingen, Germany
Yeast extract	Carl Roth GmbH, Karlsruhe, Germany
β-mercaptoethanol	Carl Roth GmbH, Karlsruhe, Germany

A.7 Devices

Atomic Force Microscopy (AFM)

MFP-3D classic	Asylum Research, Santa Barbara, USA
MFP-3D infinity	Asylum Research, Santa Barbara, USA

Confocal Laser Scanning Microscopy (CLSM)

LSM 710 Examiner	Carls Zeiss Microscopy GmbH, Oberkochen, Germany
LSM 880 Examiner	Carls Zeiss Microscopy GmbH, Oberkochen, Germany
FluoView 1200	Olympus, Tokyo, Japan

Epifluorescence Microscopy

Olympus BX 51	Olympus, Tokyo, Japan

Reflectometric Interference Spectroscopy (RIfS)

Flame Spectrometer	Ocean Optics GmbH, Ostfildern, Germany
NanoCalc, SD2000 Spectrometer	Ocean Optics GmbH, Ostfildern, Germany
Silver Mirror	Chroma Technology GmbH, Olching, Germany
ADC1000-USB, A/D Converter	Ocean Optics GmbH, Ostfildern, Germany
Dichotomous light fibre	Ocean Optics GmbH, Ostfildern, Germany
Ismatec 795C peristaltic pump	IDEX Health & Science, Wertheim, Germany
HL-2000-LL Light source	Ocean Optics GmbH, Ostfildern, Germany

Other devices

Äkta purification system	GE Healthcare, Little Chalfont, UK
Allegra™ X-22R	Beckman Coulter, Brea, USA
Centricon T-1065, ultracentrifuge	Kontron, Eching, Germany
CP55D, fine scale	Sartorius GmbH, Göttingen, Germany

Galaxy Mini, Minicentrifuge	VWR International, Darmstadt, Germany
Heraeus Fresco 17, table centrifuge	Thermo Fisher Scientific, Darmstadt, Germany
Innova® 44 incubator shaker	New Brunswick Scientific, Ensfield, USA
Microfluidizer™ LM10	Microfluidics, Westwood, USA
Mini-PROTEAN® Tetra Cell, PAGE apparatus	Bio-Rad Laboratories Inc., Hercules, USA
MonoQ 5/50	GE Healthcare, Little Chalfont, UK
MR 3001 K, magnetic stirrer	Heidolph, Schwabach, Germany
NanoDrop2000c	Thermo Fischer Scientific GmbH, Dreieich, Germany
pH-Meter Calimatic 766	Knick, Berlin, Germany
Thermo mixer compact	Eppendorf, Hamburg, Germany
Tip sonifier Sonoplus HD2070	Bandelin, Berlin, Germany
Transblo SD Semi Dry Transfer Cell	Bio-Rad Laboratories Inc., Hercules, USA
Ultrapure Water System, MiliQ Gradient A10	Merck Millipore, Darmstadt, Germany
Ultrasonic bath Sonorex RK 255H	Bandelin, Berlin, Germany
Vacuum drying oven VD23	Binder GmbH, Tuttlingen, Germany
Varian Cary Scan 50, Spectrometer	Agilent Technologies, Santa Clara, USA
Varioklav 135S	Thermo Fischer Scientific GmbH, Dreieich, Germany
Vortexer	Heidolph, Schwabach, Germany
Water bath E38	Dinkelberg Labortechnik, Neu-Ulm, Germany
Zepto LF PC	Diener electronic GmbH & Co. KG, Ebhausen, Germany

A.8 Software

Fiji, ImageJ 1.50i	http://www.fiji.sc
Gwyddion 2.49	http://gwyddion.net
MATLAB 2017b	MathWorks, Natick, USA
Origin Pro 8.5G	OrigonLab Corp., Northhampton, USA
Spectra Suite	Ocean Optics GmbH, Ostfildern, Germany
Zen black 2.3 SP1	Carls Zeiss Microscopy GmbH, Oberkochen, Germany

A.9 Deployed MATLAB-scripts

A.9.1 Deposit diameter determination (DR. JEREMIAS SIBOLD)

```
% testen
clear
close all

Files=dir('*b&w.tif');

clear diameter
Counter=0;
for k=1:numel(Files)
    ImageAnalyse=imread(Files(k).name);
    ImageAnalyse=im2bw(ImageAnalyse(:,:,1),0.5);
    Waterimage=bwconncomp(ImageAnalyse,4);
    %         Waterimage=watershed(ImageAnalyse,4);
    for m=1:Waterimage.NumObjects
        if numel(Waterimage.PixelIdxList{m})>10
            Counter=Counter+1;
            diameter(Counter)=sqrt(4*numel(Waterimage.PixelIdxList{m})/pi);
        end
    end
    Pixelgroesse=input('geben sie manuell die Pixelgröße ihres Bildes ein
[nm]: ');
    diameter=diameter'*Pixelgroesse;
end
hist(diameter)
save('Histodaten.txt','diameter','-ascii')
```

A.9.2 FRAP analysis

```
function frap_analysis

%  Initializes the GUI and creates one panel to the left and two panels to
%  the right

% closes the figures
close(figure(99))
close(figure(98))
close(figure(1))
close(figure(2))
close(figure(3))
close(figure(4))
close(figure(5))
close(figure(6))
close(figure(7))
close(figure(8))

f=figure(99);
clf
set(f,'Visible','off','Position',[0,0,750,500]);
leftPanel = uipanel('bordertype','etchedin',...
    'Position', [0.05*500/750 0.05 0.8*500/750 0.9],...
    'Backgroundcolor','default','Visible','on',...
    'Parent',f);
rightTopPanel = uipanel('bordertype','etchedin',...
    'Position', [0.9*500/750 0.375 1-0.85*500/750-0.1*500/750 0.575],...
    'Backgroundcolor','default','Visible','on',...
```

```
    'Parent',f);
rightBottomPanel = uipanel('bordertype','etchedin',...
    'Position', [0.9*500/750 0.125 1-0.85*500/750-0.1*500/750 0.225],...
    'Backgroundcolor','default','Visible','on',...
    'Parent',f);

% Constructs the components in the gui
sh=uicontrol(leftPanel,'Style','slider',...
    'Max',100,'Min',1,'Value',1,'Visible','off',...
    'SliderStep',[1/(100-1) 5/(100-1)],'Units','normalized',...
    'Position',[0 0 1 (1-0.8/0.9)/2],...
    'Callback',{@sh_Callback});
txt_frm=uicontrol(leftPanel,'Style','text',...
    'String','Frame:','Units','normalized','Visible','off',...
    'Position',[0 1-(1-0.8/0.9)/2 1 (1-0.8/0.9)/2],'FontSize',10,...
    'HorizontalAlignment','left','Backgroundcolor','default');

txt_pre1=uicontrol(rightTopPanel,'Style','text','String','First pre-bleach
frame:',...
    'Units','normalized','FontSize',10,'HorizontalAlignment','left',...
    'Position',[0.05,0.91,0.5,0.06]);
edit_pre1=uicontrol(rightTopPanel,'Style','edit','String','1','Units','nor-
malized',...
    'Position',[0.6,0.91,0.15,0.06],'FontSize',10,'HorizontalAlign-
ment','center');
uicontrol(rightTopPanel,'Style','pushbutton','Units','normalized',...
    'String','Get','Position',[0.8,0.91,0.15,0.06],...
    'Callback',{@btn_pre1_Callback});
uicontrol(rightTopPanel,'Style','text','String','Last pre-bleach
frame:',...
    'Units','normalized','FontSize',10,'HorizontalAlignment','left',...
    'Position',[0.05,0.84,0.5,0.06]);
edit_pre2=uicontrol(rightTopPanel,'Style','edit','String','2','Units','nor-
malized',...
    'Position',[0.6,0.84,0.15,0.06],'FontSize',10,'HorizontalAlign-
ment','center');
btn_pre2=uicontrol(rightTopPanel,'Style','pushbutton','Units','normal-
ized',...
    'String','Get','Position',[0.8,0.84,0.15,0.06],...
    'Callback',{@btn_pre2_Callback});
uicontrol(rightTopPanel,'Style','text','String','Dark count value:',...
    'Units','normalized','FontSize',10,'HorizontalAlignment','left',...
    'Position',[0.05,0.77,0.5,0.06]);
edit_dc=uicontrol(rightTopPanel,'Style','edit','String','','Units','normal-
ized',...
    'Position',[0.6,0.77,0.15,0.06],'FontSize',10,'HorizontalAlign-
ment','center',...
    'Callback',{@edit_dc_Callback});
uicontrol(rightTopPanel,'Style','pushbutton','Units','normalized',...
    'String','Get','Position',[0.8,0.77,0.15,0.06],...
    'Callback',{@btn_dc_Callback});
uicontrol(rightTopPanel,'Style','text','String','First post-bleach
frame:',...
    'Units','normalized','FontSize',10,'HorizontalAlignment','left',...
    'Position',[0.05,0.7,0.52,0.06]);
edit_pb1=uicontrol(rightTopPanel,'Style','edit','String','4','Units','nor-
malized',...
    'Position',[0.6,0.7,0.15,0.06],'FontSize',10,'HorizontalAlign-
ment','center');
uicontrol(rightTopPanel,'Style','pushbutton','Units','normalized',...
    'String','Get','Position',[0.8,0.7,0.15,0.06],...
```

```
    'Callback',{@btn_pb1_Callback});
uicontrol(rightTopPanel,'Style','text','String','Last post-bleach
frame:',...
    'Units','normalized','FontSize',10,'HorizontalAlignment','left',...
    'Position',[0.05,0.63,0.52,0.06]);
edit_pb2=uicontrol(rightTopPanel,'Style','edit','String','','Units','nor-
malized',...
    'Position',[0.6,0.63,0.15,0.06],'FontSize',10,'HorizontalAlign-
ment','center');
uicontrol(rightTopPanel,'Style','pushbutton','Units','normalized',...
    'String','Get','Position',[0.8,0.63,0.15,0.06],...
    'Callback',{@btn_pb2_Callback});
uicontrol(rightTopPanel,'Style','text','String','Omit frame(s):',...
    'Units','normalized','FontSize',10,'HorizontalAlignment','left',...
    'Position',[0.05,0.56,0.32,0.06]);
edit_omit=uicontrol(rightTopPanel,'Style','edit','String','','Units','nor-
malized',...
    'Position',[0.4,0.56,0.35,0.06],'FontSize',10,'HorizontalAlign-
ment','left');
uicontrol(rightTopPanel,'Style','pushbutton','Units','normalized',...
    'String','Get','Position',[0.8,0.56,0.15,0.06],...
    'Callback',{@btn_omit_Callback});
uicontrol(rightTopPanel,'Style','text','String','r_max [pixels]:',...
    'Units','normalized','FontSize',10,'HorizontalAlignment','left',...
    'Position',[0.05,0.49,0.32,0.06]);
edit_rmax=uicontrol(rightTopPanel,'Style','edit','String','','Units','nor-
malized',...
    'Position',[0.4,0.49,0.35,0.06],'FontSize',10,'HorizontalAlign-
ment','center');
uicontrol(rightTopPanel,'Style','pushbutton','Units','normalized',...
    'String','Get','Position',[0.8,0.49,0.15,0.06],...
    'Callback',{@btn_rmax_Callback});
uicontrol(rightTopPanel,'Style','text','String','Pixelwidth [um]:',...
    'Units','normalized','FontSize',10,'HorizontalAlignment','left',...
    'Position',[0.05,0.37,0.7,0.06]);
edit_dx=uicontrol(rightTop-
Panel,'Style','edit','String','0.267','Units','normalized',...
    'Position',[0.65,0.37,0.3,0.06],'FontSize',10,'HorizontalAlign-
ment','center');
txt_dt=uicontrol(rightTopPanel,'Style','text','String','Time between frames
[s]:',...
    'Units','normalized','FontSize',10,'HorizontalAlignment','left',...
    'Position',[0.05,0.30,0.7,0.06]);
edit_dt=uicontrol(rightTopPanel,'Style','edit','String','2','Units','nor-
malized',...
    'Position',[0.65,0.30,0.3,0.06],'FontSize',10,'HorizontalAlign-
ment','center');
cbx_pre=uicontrol(rightTopPanel,'Style','checkbox',...
    'String','  Use pre-bleach frame','Units','normalized',...
    'FontSize',10,'HorizontalAlignment','left',...
    'Value',1,'Position',[0.05 0.18 0.8
0.06],'Callback',{@cbx_pre_Callback});
cbx_times=uicontrol(rightTopPanel,'Style','checkbox',...
    'String','  Define individual time points','Units','normalized',...
    'FontSize',10,'HorizontalAlignment','left',...
    'Value',0,'Position',[0.05 0.11 0.8
0.06],'Callback',{@cbx_times_Callback});
cbx_trc=uicontrol(rightTopPanel,'Style','checkbox',...
    'String','  Track the center of mass','Units','normalized',...
    'FontSize',10,'HorizontalAlignment','left',...
    'Value',0,'Position',[0.05 0.04 0.8 0.06]);
```

```
txt_imin=uicontrol(rightBottomPanel,'Style','text','String','Imin = 1',...
    'Units','normalized','FontSize',10,'HorizontalAlignment','left',...
    'Position',[0.05,0.72,0.35,0.175]);
sh_imin=uicontrol(rightBottomPanel,'Style','slider',...
    'Max',100,'Min',1,'Value',1,'Visible','on',...
    'SliderStep',[1/(100-1) 5/(100-1)],'Units','normalized',...
    'Position',[0.45 0.72 0.5 0.175],...
    'Callback',{@sh_imin_Callback});
txt_imax=uicontrol(rightBottomPanel,'Style','text','String','Imax =
10000',...
    'Units','normalized','FontSize',10,'HorizontalAlignment','left',...
    'Position',[0.05,0.44,0.35,0.175]);
sh_imax=uicontrol(rightBottomPanel,'Style','slider',...
    'Max',100,'Min',1,'Value',100,'Visible','on',...
    'SliderStep',[1/(100-1) 5/(100-1)],'Units','normalized',...
    'Position',[0.45 0.44 0.5 0.175],...
    'Callback',{@sh_imax_Callback});
uicontrol(rightBottomPanel,'Style','pushbutton','Units','normalized',...
    'String','Auto','Position',[0.75,0.12,0.2,0.2],...
    'FontSize',10,'Callback',{@btn_Iauto_Callback});

uicontrol(f,'Style','pushbutton','Units','normalized',...
    'String','Start','Position',[0.73,0.05,0.1,0.05],...
    'FontSize',10,'Callback',{@btn_start_Callback});

% Creates the menus
set(f,'MenuBar','none');
menu_file=uimenu(f,'Label','File');
uimenu(menu_file,'Label','Open','Callback',{@menu_Open_Callback},...
    'Accelerator','O');
uimenu(menu_file,'Label','Exit','Callback',{@menu_Exit_Callback},...
    'Separator','on','Accelerator','Q');

% Assigns the GUI a name to appear in the window title.
set(f,'NumberTitle','off')
set(f,'Name','frap_analysis')

% Moves the GUI to the center of the screen.
movegui(f,'center')

% Makes the GUI visible.
set(f,'Visible','on');

% Creates axes to the images to appear in
ax_f=axes('Units','pixels','Parent',leftPanel,'Units','normalized',...
    'Position',[0 (1-0.80/0.9)/2 1 0.80/0.9],'Visible','off');

% Defines variables
FileName='';    % the name of the image file
file_in=[];     % the filename + directory of the image stack
api=[];         % API associated with the line handle used to determine
rmax
frm_max=1;      % the length of the image stack
I=[];           % matrix consisting of the current image
ib_min=[];      % min intensity in the images
ib_max=[];      % max intensity in the images
Idark=[];       % dark count intensity
Ipb=[];
default_dir='D:\Filmer\FRAP\';   % Default directory for images
```

```
    % btn_pre1_Callback - gets the first pre-bleach frame from the frame
number
    %   of the currently displayed image
    function btn_pre1_Callback(source,eventdata)
        if ~isempty(file_in)
            if get(cbx_pre,'Value')==0
                % the pre-bleach intensity is determined within the region
                % Bpb
                Bpb=roipoly;
                Ipb=mean(I(Bpb));
                set(edit_pre1,'String',num2str(round(Ipb)));
            else
                set(edit_pre1,'String',num2str(get(sh,'Value')));
                Ipb=[];
            end
        end
    end

    % btn_pre2_Callback - gets the last pre-bleach frame from the frame
number
    %   of the currently displayed image
    function btn_pre2_Callback(source,eventdata)
        if ~isempty(file_in)
            set(edit_pre2,'String',num2str(get(sh,'Value')));
        end
    end

    % btn_dc_Callback - determines the value of the dark count intensity
    function btn_dc_Callback(source,eventdata)
        if ~isempty(file_in)
            % the dark count intensity is determined within the region Bdc
            Bdc=roipoly;
            Idark=mean(I(Bdc));
            set(edit_dc,'String',num2str(round(Idark)));
        end
    end

    % btn_pb1_Callback - gets the first post-bleach frame from the frame
number
    %   of the currently displayed image
    function btn_pb1_Callback(source,eventdata)
        if ~isempty(file_in)
            set(edit_pb1,'String',num2str(get(sh,'Value')));
        end
    end

    % btn_pb2_Callback - gets the last post-bleach frame from the frame
number
    %   of the currently displayed image. Left unassigned makes the last
    %   image in the stack being also the last image in the analyzed stack.
    function btn_pb2_Callback(source,eventdata)
        if ~isempty(file_in)
            set(edit_pb2,'String',num2str(get(sh,'Value')));
        end
    end

    % btn_rmax_Callback - determines the maximum radial distance to be used
    %   in the analysis
    function btn_rmax_Callback(source,eventdata)
```

```
        if ~isempty(file_in)
            if isempty(api)
                iml=imline(ax_f,[255 255],[255 255]);
                api=iptgetapi(iml);
            end
            rp=api.getPosition();
            Rp_max=sqrt((rp(2,1)-rp(1,1))^2+(rp(2,2)-rp(1,2))^2);
            set(edit_rmax,'String',num2str(Rp_max))
        end
    end

    % btn_omit_Callback - determines which frames to omit from the analysis
    function btn_omit_Callback(source,eventdata)
        if ~isempty(file_in)
            str_omit=get(edit_omit,'String');
            if isempty(str_omit)
                set(edit_omit,'String',num2str(get(sh,'Value')));
            else
                set(edit_omit,'String',[str_omit,',',num2str(get(sh,'Val-
ue'))]);
            end
        end
    end

    % edit_dc_Callback - uppdates the value of I_dc
    function edit_dc_Callback(source,eventdata)
        str_Idc=get(edit_dc,'String');
        if isempty(str_Idc)
            Idark=[];
        else
            Idark=str2double(str_Idc);
        end
    end

    % btn_start_Callback - calls the routine calc_frap which does the
    %   analysis of the FRAP images to determine the diffusion parameters
    function btn_start_Callback(source,eventdata)
        if ~isempty(file_in)
            dx=str2double(get(edit_dx,'String'));

            if isempty(Idark)
                Idark2=0;
            else
                Idark2=Idark;
            end

            if get(cbx_pre,'Value')==0
                Ipre=ones(size(I))*Ipb-Idark2;
            else
                % A single pre-bleach image is obtained by averaging the
pre-bleach images
                % between the first and last pre-bleach frame selected.
                ipb1=str2double(get(edit_pre1,'String'));
                ipb2=str2double(get(edit_pre2,'String'));
                Ipre=double(imread(file_in,ipb1))-Idark2;
                for i=ipb1+1:ipb2
                    Ipre=Ipre+double(imread(file_in,i))-Idark2;
                end
                Ipre=Ipre/(ipb2-ipb1+1);
            end
```

```
        Ipre(Ipre==0)=1;

        istart=str2double(get(edit_pb1,'String'));
        iend=get(edit_pb2,'String');
        if isempty(iend)
            iend=length(imfinfo(file_in));
        else
            iend=str2double(iend);
        end

        nbr_frames=iend-istart+1;   % Number of post-bleach frames used
        if (istart+nbr_frames-1)>length(imfinfo(file_in))
            nbr_frames=length(imfinfo(file_in))-istart+1;
        end

        % t = frame times
        if get(cbx_times,'Value')==1
            t=str2num(get(edit_dt,'String'));
            t=t-t(1);   % automatically sets the first time to zero
            if length(t)~=nbr_frames
                return
            end
        else
            dt=str2double(get(edit_dt,'String'));
            t=(0:1:nbr_frames-1)*dt;
        end

        if get(cbx_trc,'Value')==1
            trc='y';
        else
            trc='n';
        end

        Rp_max=get(edit_rmax,'String');
        if ~isempty(Rp_max)
            Rp_max=str2double(Rp_max);
        else
            Rp_max=[];
        end

        nr=ones(size(t));
        omit_fr=get(edit_omit,'String');
        if ~isempty(omit_fr)
            omit_fr=str2num(omit_fr);
            for i=1:length(omit_fr)
                nr(omit_fr(i)-istart+1)=0;
            end
        end
        calc_frap(file_in,dx,Ipre,Idark2,istart,t,trc,Rp_max,nr);
    end
end

% sh_Callback - determines which image to show
function sh_Callback(source,eventdata)
    if ~isempty(file_in)
        frm=get(sh,'Value');
        set(sh,'Value',round(frm));
        frm=round(frm);
        I=double(imread(file_in,frm));
        imshow_frap(I,[ib_min,ib_max],ax_f);
```

```
        set(txt_frm,'String',[FileName,' - ',num2str(frm)])
    end
    api=[];
end

% sh_imin_Callback - updates the min intensity settings for the images
%   (coupled to the imin slider)
function sh_imin_Callback(source,eventdata)
    ib_min=round(get(sh_imin,'Value'));
    if ib_min>ib_max
        ib_min=ib_max-1;
        set(sh_imin,'Value',ib_min);
    end
    set(txt_imin,'String',['Imin = ',num2str(ib_min)]);
    if ~isempty(file_in)
        imshow_frap(I,[ib_min,ib_max],ax_f);
    end
end

% sh_imax_Callback - updates the max intensity settings for the images
%   (coupled to the imax slider)
function sh_imax_Callback(source,eventdata)
    ib_max=round(get(sh_imax,'Value'));
    if ib_max<ib_min
        ib_max=ib_min+1;
        set(sh_imax,'Value',ib_max);
    end
    set(txt_imax,'String',['Imax = ',num2str(ib_max)]);
    if ~isempty(file_in)
        imshow_frap(I,[ib_min,ib_max],ax_f);
    end
end

% btn_Iauto_Callback - automatically sets the min and max intensities
% to those in the current image
function btn_Iauto_Callback(source,eventdata)
    if ~isempty(file_in)
        ib_min=min(I(:));
        ib_max=max(I(:));
        set(txt_imin,'String',['Imin = ',num2str(ib_min)]);
        set(txt_imax,'String',['Imax = ',num2str(ib_max)]);
        set(sh_imin,'Value',ib_min);
        set(sh_imax,'Value',ib_max);
        imshow_frap(I,[ib_min,ib_max],ax_f);
    end
end

% cbx_pre_Callback - determines whether to use a pre-bleach frame to
% compensate for uneven illumination or to assume a flat illumination
% with a user specified pre-bleach intensity
function cbx_pre_Callback(source,eventdata)
    if get(cbx_pre,'Value')==0
        set(txt_pre1,'String','Pre-bleach intensity:');
        set(edit_pre2,'Enable','off');
        set(btn_pre2,'Enable','off');
    else
        set(txt_pre1,'String','First pre-bleach frame:');
        set(edit_pre2,'Enable','on');
        set(btn_pre2,'Enable','on');
    end
end
```

```
    % cbx_times_Callback - determines whether to use individual values of
    % the times for all frames or just the time between frames
    function cbx_times_Callback(source,eventdata)
        if get(cbx_times,'Value')==0
            set(txt_dt,'String','Time between frames [s]:');
            set(edit_dt,'Position',[0.65,0.3,0.3,0.06],'HorizontalAlign-
ment','center');
        else
            set(txt_dt,'String','Frame times [s]:')
            set(edit_dt,'Position',[0.45,0.3,0.5,0.06],'HorizontalAlign-
ment','left','String','');
        end
    end

    % menu_Open_Callback - chooses the image stack to analyze
    function menu_Open_Callback(source,eventdata)
        % Displays a dialog box from where to choose the images to be ana-
lyzed
        [FileName,PathName] = uigetfile('*.tif','Select the image-file',de-
fault_dir);
        if FileName==0
            return
        end

        default_dir=PathName;
        file_in=strcat(PathName,FileName);

        if length(imfinfo(file_in))==1
            error('The FRAP data should be a TIF-stack containing atleast 2
frames')
            return
        end

        set(txt_frm,'String',[FileName,' - 1'],'Visible','on')
        I=double(imread(file_in,1));
        set(sh,'Value',1,'Visible','on');

        fw=500/750*size(I,2)/size(I,1);
        set(leftPanel,'Position',...
            [0.05*fw 0.05 0.8*fw 0.9],...
            'Visible','on');
        set(ax_f,'Visible','on')

        frm_max=length(imfinfo(file_in));
        set(sh,'Max',frm_max,'Min',1,...
            'SliderStep',[1/(frm_max-1) 10/(frm_max-1)]);
        axis off

        set(sh_imin,'Max',max(2^14,max(I(:))),'Min',0,...
            'SliderStep',[1/max(2^14,max(I(:))) 10/max(2^14,max(I(:)))],...
            'Value',min(I(:)),'SliderStep',[1/max(2^14,max(I(:)))
50/max(2^14,max(I(:)))]);
        set(sh_imax,'Max',max(2^14,max(I(:))),'Min',0,...
            'SliderStep',[1/max(2^14,max(I(:))) 10/max(2^14,max(I(:)))],...
            'Value',max(I(:)),'SliderStep',[1/max(2^14,max(I(:)))
50/max(2^14,max(I(:)))]);

        ib_min=round(get(sh_imin,'Value'));
        set(txt_imin,'String',['Imin = ',num2str(ib_min)]);
```

```
        ib_max=round(get(sh_imax,'Value'));
        set(txt_imax,'String',['Imax = ',num2str(ib_max)]);
        imshow_frap(I,[ib_min,ib_max],ax_f);
        api=[];
    end

    % menu_Exit_Callback - ends the program
    function menu_Exit_Callback(source,eventdata)

        % closes the figures
        close(f)
        close(figure(98))
        close(figure(1))
        close(figure(2))
        close(figure(3))
        close(figure(4))
        close(figure(5))
        close(figure(6))
        close(figure(7))
        close(figure(8))

    end
end
```

A.9.3 Height analysis of adsorbate (DR. INGO MEY)

```
clear all
close all
[im,map]=imread('Image 9.tif');
l=imshow(im);
[counts,x]=imhist(im);

% min and max heigths and absoulte difference
minh=-2.356e-9;
maxh=5.429e-9;
diffh=maxh-minh;

xh=x./65535.*diffh;
figure
plot(xh,counts);


choice=input('(m)anual or (a)utomatic?','s');
choice


 switch choice
     case {'m'}
         baseh=input('Give Baseheight:', 's')
         baseh=str2num(baseh)
         disp('manual case, baseheight: ')
         baseheight=baseh*65535./diffh
     case {'a'}
         %plot (xh, counts)
         [Val,Ind]=max(counts);
         baseh=xh(Ind)
         disp('automatic case, baseheight: ')
         baseheight=x(Ind)
```

```
 end


im_corr=im-baseheight
figure
k=imshow(im_corr);
%pixelanzahl des Bildes eingeben
pixel=linspace(1,512,512);
im_height=[];
height_abs=[];
im_mark=zeros(size(im,1),size(im,2));

figure
hold on

for i=1:size(im,1);
    heightline=double(im_corr(i,:))./65535.*diffh;
    im_height=[im_height;heightline];
    % Threshold peakdet(xxxx, THRESHOLD
    [MAXTAB, MINTAB] = peakdet(heightline,1.5e-9);
    if isempty(MAXTAB)==0
        im_mark(i,MAXTAB(:,1))=1;
        peakind=MAXTAB(:,1);
        height_abs=[height_abs;MAXTAB(:,2)];
        t=plot(pixel,heightline);
        plot(pixel(peakind),heightline(peakind),'r*')
    else
        im_mark(i,:)=0;
    end

end

xlabel('distance / pixel');
ylabel('height / m');
title('all height lines and Peaks');
hold off

figure
imshow(im)
green = cat(3, zeros(size(im)), ones(size(im)), zeros(size(im)));
hold on
h=imshow(green);
hold off
set(h,'AlphaData',im_mark)


[a,b]=hist(height_abs,100);
figure
m=plot(b,a,'bo');
xlabel('heightabs / m')
ylabel('counts')

saveas(h,'Overlay.jpg','jpg')
saveas(t,'curves_peaks.jpg','jpg')
saveas(k,'image_corr.jpg','jpg')
saveas(l,'image.jpg','jpg')
saveas(m,'hist.jpg','jpg')

save height_abs.txt height_abs -ascii
```

```
clear counts
clear Val
clear baseh
clear diffh
clear green
clear h
clear heightline
clear i
clear map
clear maxh
clear minh
clear peakind
clear pixel
clear x
clear xh
clear a
clear b

save('alldata.mat')
```

A.9.4 Surface coverage analysis (DR. JEREMIAS SIBOLD)

```
Tiffimage=imread('Image x.tif');

figure(1)
imshow(Tiffimage);
figure(2)
hist(double(Tiffimage(:)),1000);



while true
    Threshold=input('Geben Sie manuell den Threshold an oder bei OK
Enter');
    if isempty(Threshold)
        break
    end
    speicherThreshold=Threshold;
    figure(3)
    Thresimage=im2bw(Tiffimage,Threshold./65535);
    imshow(Thresimage)
    figure(2)
    hist(double(Tiffimage(:)),1000);
    hold on
    achsen=axis;
    plot([Threshold,Threshold],[achsen(3),achsen(4)],'r-')
    hold off
    Oberflaechenbelegung=sum(Thresimage(:))/numel(Thresimage)

end

imwrite(Thresimage,[Tiffimage(1:end-4) '_Threshold_' num2str(speicher-
Threshold) '.png'],'png')
```